STUDIES OF THE THERMOSPHERE, IONOSPHERE, AND PLASMASPHERE USING WAVELET ANALYSIS, NEURAL NETWORKS, AND KALMAN FILTERS

by

Adela Florina Anghel

B.S., Technical University of Cluj-Napoca, Romania, 1995

M.S., Technical University of Cluj-Napoca, Romania, 1996

M.S., University of Colorado at Boulder, 2009

A Thesis Submitted to the

Faculty of the Graduate School of the

University of Colorado in partial fulfillment

of the requirements for the degree of

Doctor of Philosophy

Department of Electrical and Computer Engineering

2009

This thesis entitled:
Studies of the Thermosphere, Ionosphere, and Plasmasphere
using Wavelet Analysis, Neural Networks, and Kalman Filters
written by Adela Florina Anghel
has been approved by the Department of Electrical and Computer Engineering

_____
Prof. Albin J. Gasiewski

_____
Prof. George H. Born

Date _____

The final copy of this thesis has been examined by
the signatories, and we find that both the content and the form
meet acceptable presentation standards of scholarly work
in the above mentioned discipline.

Anghel, Adela Florina (Ph.D., Department of Electrical and Computer Engineering)

Studies of the Thermosphere, Ionosphere, and Plasmasphere using Wavelet Analysis, Neural Networks, and Kalman Filters

Thesis directed by Professor Albin J. Gasiewski

This thesis presents a series of studies investigating the Earth's thermosphere, ionosphere, and plasmasphere using continuous wavelet analysis techniques, multi-layer feedforward neural networks, and Kalman filters, along with extensive datasets of satellite and ground-based observations collected during the solar cycle 23.

It is widely accepted that the overall ionospheric and thermospheric variability is primarily influenced by the solar activity, geomagnetic activity, and meteorological processes originating at lower atmospheric layers. While the solar activity influences mostly the long-term variability of the thermosphere-ionosphere system, the geomagnetic activity and meteorological processes tipically induce oscillations with periods ranging from several days to minutes and even seconds. Stemming from the need to understand and predict the behavior of the thermosphere-ionosphere system and its deviations from normal climatological patterns, during both quiet and disturbed geomagnetic conditions, recent modeling and experimental studies have shown an increased interest in the short-period (minutes-to-hours) and day-to-day variability, or weather aspects of the Earth's upper atmosphere and ionosphere. In this context, one of the main objectives of our current studies is to investigate the geomagnetically forced multi-day periodic variations in the thermosphere-ionosphere system, especially those associated with the recurrent geomagnetic activity at the

declining and minimum phases of the solar cycle 23. For this purpose, several ionospheric, thermospheric, and solar wind parameters, along with different geomagnetic and solar activity indices are analyzed using a wide spectrum of wavelet-based analysis techniques.

A large part of this thesis is also dedicated to presenting a variety of neural network-based models developed (1) for estimating the daytime equatorial zonal electric fields using magnetometer observations, (2) for quantifying the relationships between the interplanetary electric field and the daytime penetration electric fields at equatorial latitudes, and (3) for investigating the shielding effect of the ring current at different longitude sectors. In addition, we also examine the periodic variations in the magnetometer-inferred equatorial ionospheric electric fields using wavelet analysis, and relate these variations to periodic fluctuations in the dawn-to-dusk component of the interplanetary electric field, showing that the geomagnetic activity is an important source of periodic oscillations in the ionosphere.

A significant part of this thesis is also dedicated to presenting a Kalman filter-based data assimilation algorithm developed for the near-real time estimation of both the ionospheric and plasmaspheric contributions to the GPS measurements of total electron content (TEC), by combining GPS-TEC observations with background information from an ionospheric model and from a plasmaspheric model. It is shown that the newly-developed algorithm represents a valuable remote sensing technique for investigating both the ionosphere and plasmasphere in near-real time.

Dedicated to

Theotokos

to my family

Narcis, Anna, Maria, Cristian

and

to all my teachers, instructors, professors, and mentors

ACKNOWLEDGEMENTS

I would first of all like to acknowledge and thank my thesis advisor, A.J. Gasiewski, for his continuous support and guidance throughout my graduate studies at the University of Colorado. I would also like to thank C.S. Carrano for sparking my interest in plasmaspheric studies and for collaborating with me on several research papers and to A. Mazzella for his useful comments and suggestions on some of my papers. I would also like to give particular thanks to the committee members A. Richmond, G. Born, N. Zabotin, E. Westwater, D. Smith, and C.T. Mullis for useful discussions and guidance. Many thanks go also to W. Lewis and R. Moore. I owe special thanks to Adina Astilean for her continuous encouragement, support, friendship, dedication, and for always being there for me with good advice. Special thanks to Fr. David Mustian, to the Myrrhbearers, and all the people at St. Luke's. Finally, I would like to thank my husband and children for supporting me and bearing with me through my studies, and my parents for their help.

CONTENTS

Chapter

TABLES

Table

FIGURES

Figure

Chapter 1

Introduction

1.1 General Aspects

This thesis consists of several individual studies that relate to scientific topics of great relevance to the upper atmospheric sciences, and at the same time carries a uniform theme within the general context of ionospheric dynamics and composition. Since the thesis has been developed within an electrical and computer engineering department, our studies are also complemented by advanced signal processing techniques and backed by a suite of originally developed software in MATLAB and C/C++. The content of the thesis is based on nine papers that have been written over the last three years. Four of the papers have already been published in peer-reviewed journals, three of them have been submitted to different journals, and the other two are currently in a manuscript form. In the following, we outline some general aspects regarding the topics covered in this thesis.

1.1.1 The Thermosphere, Ionosphere, and Plasmasphere

The Earth's upper atmosphere consists of the upper mesosphere, thermosphere, and ionosphere, and is the region of the atmosphere where the energy input is dominated by solar extreme ultraviolet (EUV) radiation, electric fields and currents, and energetic particles, and where the motion of the neutral atmosphere is strongly influenced by the motion of plasma. The thermosphere, the neutral component of the upper atmosphere, is a dynamical and multi-constituent system, coupled to the mesosphere at the lower boundary through turbulent mixing and upward propagating atmospheric waves, to the magnetosphere at the upper boundary through particle precipitation and convective electric fields, and directly to the Sun through absorption of solar EUV radiation by the thermospheric constituents.

The ionosphere is the ionized component of the upper atmosphere. It extends roughly within the 90-1000 km altitude region and is the result of interaction between the solar radiation and the Earth's atmosphere and magnetic field. In the ionosphere, the electron density is determined by the relative ratio of recombination and ionization, and is approximately equal to the ion density at any altitude. However, even at ionospheric heights where the ionospheric plasma coexists with the neutral atoms and molecules of the thermosphere, the electrons and ions are only a minor atmospheric constituent and represent about 0.4% of the total atmospheric material (Tascione, 1994). The ionosphere is horizontally stratified and consists of a number of distinct layers, known as the D, E and F regions, with the bulk of plasma typically residing in a relatively thin altitude layer between about 200 and 400 km. The layers

are located at different altitudes and form due to the fact that the atmosphere composition and density change with height (e.g., Kelley, 1988; Kivelson and Russell, 1995; Schunk and Nagy, 2000).

Located above the ionosphere, the plasmasphere is just the high-altitude extension of the ionosphere, with which is in a field-aligned diffusive equilibrium at the ends of the magnetic flux tubes. It is a torus-shaped plasma cloud confined by the Earth's magnetic field that surrounds the Earth at low and mid-latitudes, between about $\pm 60^{o}$ geomagnetic latitude, and extends to equatorial distances of several Earth radii, from the O^{+}/H^{+} transition height up to about 35,000 km. The plasmasphere is primarily populated by ionospheric plasma flows, as in this region of the atmosphere the production and loss processes are essentially absent (e.g., Kersley and Klobuchar, 1978), and consists of relatively dense, cold hydrogen-dominated plasma distributed along the corotating geomagnetic field lines.

1.1.2 The Impact of the Ionosphere and Plasmasphere on GPS Signals

Both the ionosphere and plasmasphere impact the propagation of electromagnetic waves in a wide range of frequencies. They impart a group delay on space-to-ground radio transmissions, which can adversely affect the performance of the technological systems that depend on them, such as navigation, communication, and deep space tracking radars (e.g., Carrano et al., 2008). For the Global Positioning System (GPS) signals, which must travel through the oxygen-dominated plasma of the ionosphere and tenuous hydrogen-dominated plasma of the plasmasphere on their

way to the ground-based GPS receivers, the two ionized regions form a dispersive medium which introduces a frequency dependent path delay proportional to the total electron content (TEC) along the propagation path from where valuable temporal and spatial information about the electron density distribution can be retrieved.

Over the last two decades, several algorithms for estimating the ionospheric TEC from GPS observations have been developed by taking advantage of the dispersive nature of the ionosphere for the GPS signals (e.g., Sardon et al., 1994; Komjathy, 1997; Hansen et al., 1997; Mannucci et al., 1998; Spencer et al., 2004). The GPS system currently consists of a constellation of 31 active satellites that broadcast coded radio signals at the L1 (1675.42 MHz) and L2 (1227.60 MHz) frequencies and more than 2000 dual-frequency GPS receivers in continuous operation worldwide and onboard many Low Earth Orbiting (LEO) satellites, and is considered a unique and reliable source of ionospheric TEC data. It is thus not surprising that monitoring the contribution of the ionosphere to the GPS measurements of TEC has become a widely used and favored remote sensing technique for investigating the ionosphere behavior during both quiet and disturbed geomagnetic conditions (e.g., Mendillo, 2006; Fuller-Rowell et al., 2007).

However, most of the techniques currently used for estimating the ionospheric TEC from GPS observations implicitly assume that all the measured TEC is ionospheric in origin and employ thin-shell approximations for the ionosphere or even more complex ionospheric models that are inappropriate for the plasmasphere, which GPS signals also traverse. As a result, these estimation techniques tend to distribute the group delay imparted by the plasmasphere between the instrumental

biases and the total path delay, which can lead to inaccuracies in the estimation of the biases and total TEC. On the other hand, a number of studies have shown that although the electron densities in the plasmasphere are several orders of magnitude less than in the ionosphere, due to the long propagation distances of the GPS signals through the tenuous plasmasphere compared to the relatively short paths through the ionosphere, the plasmaspheric contribution to the GPS measurements of TEC can become significant under certain conditions and should not be ignored (e.g., Lunt et al., 1999a; Balan et al., 2002).

As shown by Lunt et al. (1999b, c) and Mazella et al. (2002, 2007), to be able to determine the contribution of the plasmasphere to the GPS-derived TEC, it is important that the dynamics and geometry of the plasmasphere, which are inappropriately represented by the models usually employed for the ionosphere, are properly captured by the estimation procedure. Following on these ideas, Carrano et al. (2008) and Anghel et al. (2009a) have developed two Kalman filter-based algorithms for estimating both the ionospheric and plasmaspheric TEC (PEC) by including in the observation equation an additional plasmaspheric term and estimating a scaling factor for this term. In both cases, the plasmaspheric term was obtained by integrating the electron density along GPS ray paths through a plasmaspheric model.

Based on the results reported by Anghel et al. (2009a), in this thesis we present the Kalman filter-based data assimilation algorithm, named WinTEC-IP. The algorithm was originally designed for the near-real time estimation of the ionospheric TEC from ground-based, dual-frequency GPS data and later extended to explicitly account for the PEC. WinTEC-IP is a Windows application written in Borland C++

Builder and features a user-friendly graphical user interface (GUI) based on a Multiple Document Interface (MDI) design. The application can automatically download hourly/daily observation and navigation files from the Internet in the Receiver Independent Exchange Format (RINEX) format to estimate slant and vertical TEC values by processing GPS data from a single site or from several receivers simultaneously in a Kalman filter approach.

In the WinTEC-IP algorithm, the ionosphere is assumed to consist of a set of thin spherical shells located at arbitrary fixed heights, and the vertical TEC on each shell is approximated as polynomials of different orders in a solar-geomagnetic reference frame. The satellite and receiver biases are included in the model as additive terms, with no elevation angle dependency, and the plasmaspheric term is obtained by integrating the electron density predicted by the Gallagher's empirical plasmaspheric model (Gallagher et al., 1988) along actual GPS ray paths from the O^+/H^+ transition height up to the GPS orbital altitude of 20,200 km. The Kalman filter then estimates, in a single site or network solution, the coefficients of a local fit to the vertical ionospheric TEC and a scaling factor for the PEC predicted by the model, as well as the combined receiver and satellite biases.

To evaluate the effect of the plasmaspheric component on the estimated biases and total TEC and to assess the performance of the newly developed algorithm, we compare the WinTEC-IP results, with and without the plasmaspheric term included, at three GPS receivers located at different latitudes in the American sector, during a solar minimum period characterized by quiet to moderate geomagnetic conditions. We also investigate the consistency of our plasmaspheric results by taking advantage

of the specific doughnut-shaped geometry of the plasmasphere and applying the technique at twelve stations distributed roughly over four geomagnetic latitudes and three longitude sectors.

In addition, as a preliminary validation of our technique, we also examine the seasonal changes in the morphology of the GPS-derived PEC by applying the algorithm to GPS data collected from four magnetically conjugate sites located at low and mid-latitudes, within the 65^{o}-90^{o}W longitude range, over two geomagnetically quiet solar minimum periods in August and November 2007. It is shown that the predicted PEC displays diurnal and latitudinal variations which are imposed by our selection of the background plasmaspheric model and the manner in which it has been incorporated into our estimation algorithm, and a seasonal variation and a hemispheric asymmetry which originate from the measurements themselves and are not imposed by the plasmaspheric model. We interpret the variations in the PEC in terms of the ionosphere-plasmasphere interactions in both local and conjugate hemispheres and in terms of the geometry of the plasmaspheric flux tube and tilt of the Earth's magnetic dipole, and show that our results are in excellent agreement with results reported by previous plasmaspheric studies.

1.1.3 Periodic Variations in the Thermosphere-Ionosphere System Induced by Recurrent Geomagnetic Activity

Intimately linked through collisional interactions, the ionosphere and thermosphere form a highly complex and variable system characterized by: (1)

inherent internal interactions occurring inside the system, (2) interactions with the magnetosphere above, where space plasma processes due to magnetosphere-solar wind couplings provide an interface with highly variable inputs of electrodynamic energy and energetic particles, (3) interactions with the middle atmosphere below, itself modulated by the tropospheric weather and surface topology, and (4) variability of the external sources driving the system. In addition, because the ionosphere is closely coupled to the thermosphere via composition, winds, and electrodynamics (e.g., Crowley et al., 2008), changes in the thermospheric composition and dynamics have strong effects on the ionospheric variability and vice versa.

Over the last few decades, there has been an increasing interest in the behavior of the thermosphere-ionosphere system and its deviations from the normal climatological patterns mainly because most of the communication and information systems in our society are based on satellite technology, and space weather plays a critical role in the satellite communication systems and space technologies (GPS, navigation, TV, telephone, information links). It is widely accepted that the overall variability of the thermosphere-ionosphere system with periods ranging from long-term secular changes to days, hours and even minutes and seconds, is influenced by the solar activity, geomagnetic activity, and meteorological processes originating at lower atmospheric layers. While the solar activity influences mostly the long-term (months and years) variability, the geomagnetic activity and the lower atmospheric processes can induce oscillations with periods ranging from about few seconds or minutes to several days or even weeks (e.g., Lastovička, 2006).

One of the main topics of our current studies focuses on examining the multi-day (2-30 days) periodic variations in the thermosphere-ionosphere system, especially those associated with the recurrent geomagnetic activity at the declining and minimum phases of the solar cycle 23. For this purpose, several ionospheric, thermospheric, and solar wind parameters, along with different geomagnetic and solar activity indices are analyzed using a variety of wavelet-based analysis techniques. Recent studies (e.g., Lei et al., 2008a, b, c; Thayer et al., 2008) suggest that, although the recurrent geomagnetic storms are in general characterized by weak-to-moderate geomagnetic activity levels, due to their recurrent nature and characteristic long recovery phases, they can produce significant cumulative effect on the state of the thermosphere-ionosphere system. Our studies are therefore very important and have the potential to provide relevant information about geomagnetically forced periodicities in ionosphere and thermosphere.

1.1.4 Daytime, Equatorial Zonal Electric Fields

The equatorial zonal electric fields are fundamentally important ionospheric parameters that play a significant role in the distribution of ionization from middle to equatorial latitudes and in the dynamics of the thermosphere-ionosphere system at equatorial and low latitudes. They drive the equatorial electrojet (EEJ) and the F-region vertical plasma motion, and affect the morphology of the equatorial ionosphere, the development and evolution of the equatorial ionization anomaly (EIA), also known as the Appleton anomaly, the composition and dynamics of the

low-latitude ionosphere, thermosphere, and plasmasphere, and the generation of the equatorial E and F-region plasma irregularities and instabilities (e.g., Kelley et al., 1989; Fejer, 1997; Anderson et al., 2002; Fejer et al., 2005; Jensen and Fejer, 2007). The equatorial ionospheric electric fields and the associated F-region ExB plasma drifts are also considered important inputs to ionospheric, thermospheric, and plasmaspheric models (e.g., Anderson et al., 1987, 1989; Preble et al., 1994; Heelis et al., 2004; Fejer et al., 2005; Anderson et al., 2006b; Pavlov et al., 2008), and are essential for the development, validation, and improvement of numerical ionospheric models, for testing the predictions of the ionospheric and convection models, for investigating the effects of geomagnetic storms on the ionosphere, and for reliable space weather forecasting.

Currently, there are only sporadic measurements of equatorial ExB plasma drifts, mostly at the Peruvian longitude sector. However, even at these longitudes the drifts are measured only a few times per month using the Incoherent Scatter Radar and the Jicamarca Unattended Long-Term Ionosphere Atmosphere (JULIA) radar located at Jicamarca, Peru (e.g., Chau et al., 2005). Having in view though that the vertical ExB plasma drifts are so critical for ionospheric studies, over the years different techniques for estimating them have been proposed, numerous models have been developed, and several theoretical and experimental studies have investigated their local time, day-to-day, seasonal, longitudinal, latitudinal, altitudinal, solar cycle, and magnetic activity dependency using a variety of radar, satellite, rocket, ionosonde, magnetometer, ground-spaced receiver, and optical imaging technique observations (e.g., Richmond et al., 1980; Scherliess and Fejer, 1997, 1999; Fejer and

Scherliess, 1997, 1998; Abdu et al., 1998; Immel et al., 2004; Arruda et al., 2006; Manoj et al., 2006; Kishore and Mukherjee, 2007; Yao and Makela, 2007; Fang et al., 2008b; Alken, 2009).

Recent studies have shown that realistic daytime, equatorial vertical ExB plasma drifts can be accurately inferred on a day-to-day basis from the difference in the horizontal H component, ΔH, between a magnetometer placed on the magnetic equator and one displaced a few degrees away (Anderson et al., 2002). Based on these previous results, here we present several least-squares regression and neural network-based algorithms for estimating the daytime, equatorial vertical ExB drifts and the corresponding zonal electric fields from magnetometer observations. The algorithms are developed by combining drift measurements from the Jicamarca ISR and JULIA radars with magnetometer H component observations collected at the Peruvian sector between November 2000 and February 2009, and can be applied at any longitude where appropriately-placed magnetometers exist.

We also study the short-period (minutes-to-hours) and day-to-day variability, or the weather aspects of the equatorial zonal electric fields, Ey, at three longitude sectors, Peruvian, Philippine, and Indian, during time intervals of increased geomagnetic activity, and relate this variability to changes in the dawn-to-dusk component of the interplanetary electric field, IEF-Ey. For this purpose, continuous Morlet wavelet and cross-wavelet amplitude spectra with different frequency resolutions are employed to analyze and compare the oscillation activity in the Ey and IEF-Ey spectra in the 10 minute-10 hour and 1.25-12 day period ranges. For the 1.25-12 day period range, the periodicities in the Ey spectrum are compared with similar

periodicities in the IEF-Ey spectrum during 9 February - 9 June 2001, our wavelet results indicating the geomagnetic activity as an important source of Ey variability in this period range. For the 10 minute-10 hour period range, four case studies are examined. We show that the wavelet transform represents a powerful tool to study the frequency dependence of the two specific mechanisms of ionospheric electric field variability which are dominant during geomagnetic storms, namely penetration and disturbance dynamo.

Penetration of the IEF to the low and mid-latitude ionosphere has been extensively studied for more than four decades with radar and magnetometer measurements and numerical simulations (e.g., Nishida, 1968; Gonzales et al., 1979; Kelley et al., 1979; Huang et al., 2005, 2007). However, due to the sporadic nature of the ionospheric electric field measurements, most of the previous studies have primarily focused on correlating the ionospheric response to changes in the orientation of the Bz component of the interplanetary magnetic field, IMF-Bz, for some particular case studies. Very little attention has been given though to establishing quantitative relationships except for some recent reports by Kelley et al. (2003), Huang et al. (2007), and Nicolls et al. (2007). Expanding on their work, in this thesis we present several least-squares regression and neural network-based empirical models developed to quantify the relationship between IEF-Ey and the daytime penetration electric fields at equatorial latitudes and to investigate the shielding effect of the ring current in both time and frequency domains. The models are developed based on several years of simultaneous observations of IEF-Ey data derived from Advanced Composition Explorer (ACE) satellite measurements and

daytime magnetometer H component observations gathered from equatorial stations in Peru and Indonesia. We assess the performance of our models by applying them to IEF-Ey observations and to numerically simulated signals. It is shown that our results are in good to excellent agreement with results reported by previous studies.

1.2 Outline of Thesis

In what follows, the reader will find a collection of ionospheric, thermospheric, and plasmaspheric studies that combine a variety of techniques and data sets. Chapter 2 is based on the work of Anghel (2009f) and presents multi-instrument observations and spectral studies of the thermosphere-ionosphere system over the 2-30 day period range, during the four-year time interval between 2004 and 2007, which covers a large part of the declining and minimum phases of the solar cycle 23. The spectral analysis techniques employed in this chapter are based on the continuous wavelet method presented by Anghel et al. (2008a) and form a unitary collection of wavelet-based spectral analysis tools that include the cross-wavelet analysis, filtering in the wavelet domain, and wavelet bispectral analysis. Chapter 3 describes several least-squares regression and neural network-based algorithms developed for estimating the equatorial zonal electric fields from magnetometer H component observations. This chapter is primarily based on the works of Anghel et al. (2007) and Anghel et al. (2009d). Chapter 4 relates the short-period (minutes-to-hours) and the day-to-day variability of the magnetometer-inferred equatorial zonal electric fields at different longitude sectors to changes in the dawn-to-dusk

component of the interplanetary electric field, during time intervals of increased geomagnetic activity, using a wavelet analysis approach, and is based on the results presented by Anghel et al. (2008a). Chapter 5 presents the analysis of seven years of magnetometer data using finite impulse response (FIR) filters and neural networks-based algorithms. The algorithms are designed to investigate the dynamics and the frequency dependence of the storm-time electric field penetration mechanism between high and low latitudes. This chapter is based on the work of Anghel (2009e). Chapter 6 introduces a Kalman filter-based data assimilation algorithm developed to estimate the ionospheric total electron content (TEC) along GPS ray paths by processing dual-frequency GPS data from a single site or from a network of GPS receivers, and is based on the work of Anghel et al. (2008b) and Anghel et al. (2009c). Chapter 7 describes a newly developed Kalman filter-based algorithm for estimating both the ionospheric and plasmaspheric contributions to the GPS observations of TEC and is based on the results published by Anghel et al. (2009a). Chapter 8 examines the morphology of the GPS-derived PEC and is based on the work of Anghel et al. (2009b). Chapter 8 provides a summary of our studies and highlights some concluding remarks and possible future work.

Chapter 2

Periodic Modulation of the Thermosphere-Ionosphere System by Solar Wind High-Speed Streams and Corotating Interaction Regions at the Declining and Minimum Phases of the Solar Cycle 23

2.1 Background

The sources of variability in the thermosphere-ionosphere system are in general classified into three categories: solar, meteorological, and geomagnetic (e.g., Rishbeth and Mendillo, 2001). The solar sources refer to variations in the solar ultraviolet and extreme ultraviolet (UV/EUV) radiation and generate long-period variations in the neutral composition, neutral temperatures, neutral winds, and ionospheric conductivities. The meteorological sources, on the other hand, refer to upward propagating atmospheric (infrasonic, gravity, tidal, and planetary) waves with periods spanning a range from a few seconds to a few weeks, which originate at lower atmospheric layers and propagate to ionospheric F-region heights via indirect mechanisms (e.g., Forbes et al., 2000; Pancheva, 2000; Lastovička, 2006). The

upward propagating waves and their interactions and modulations play an important role in the variability of the thermosphere-ionosphere system and also in the vertical coupling of the atmosphere by transporting energy and momentum from below to the Earth's upper atmosphere (e.g., Parish et al., 1994; Pancheva and Mukhtarov, 2000; Pancheva et al., 2006). They can produce modifications of the turbulent mixing, changes of the E-region conductivities, modulations of the temperature and wind structures of the thermosphere, and generation of electric fields through dynamo processes (e.g., Forbes, 1996; Altadill and Apostolov, 2003; Haldoupis et al., 2004; Pancheva and Mitchell, 2004). Finally, the geomagnetic sources refer to geomagnetic disturbances which are ultimately caused by disturbances on the Sun that modulate the solar wind and propagate through the interplanetary medium to the geospace environment where they affect the geomagnetic activity and, in turn, impact the state of the upper atmosphere. In this case, variations in the state of the upper atmosphere are primarily linked to changes in the electric fields, neutral composition, neutral densities, neutral temperatures, neutral winds, and energetic particle precipitation.

Short-period, multi-day variations in the solar wind parameters, especially in the solar wind velocity and magnetic field strength, have been shown to represent an important source of planetary wave-like oscillations (periods in the 2-30 day range) in ionosphere and thermosphere (e.g., Rishbeth and Mendillo, 2001; Pancheva et al., 2006; Lastovička, 2006). Multi-day periodic variations in the solar wind are primarily caused by coronal magnetic structures with a certain spatial distribution, which are passed on to interplanetary medium as temporal variations due to the solar rotation and the outflow of solar wind originating from these structures. Several factors can

also affect the periodic fluctuations in the solar wind, including (1) temporal evolution of the dominant polarity regions of the solar magnetic field, (2) heliolatitudinal excursion of the Earth, (3) differential rotation of the Sun, and (4) overlapping effect of the transient solar wind structures (e.g., Nayar et al., 2001; Russell, 2001). In addition, we will show through wavelet bispectral analysis that nonlinear processes in the solar wind, probably associated with the compression of the high-speed solar wind plasma and with wave-shock interactions between fast and slow solar wind flows, can also affect the multi-day periodic fluctuations in the solar wind parameters. In either case, as the modulated solar wind impinges on the Earth's magnetosphere, it modulates the geomagnetic activity and causes fluctuations in the direct forcing of the Earth's upper atmosphere, which in turn modulates the dynamics and composition of the thermosphere and ionosphere.

Variations in the solar wind parameters have been primarily associated with three types of solar wind structures: transient, slow-speed streams, and high-speed streams (HSS). These structures are known as important drivers of recurrent and non-recurrent geomagnetic activity if they reach the Earth with a southward deflection of the interplanetary magnetic field (IMF) (e.g., Emery et al., 2009). The major drivers of non-recurrent geomagnetic activity are the interplanetary extensions of coronal mass ejections (ICMEs) that are Earth-directed, while the main drivers of recurrent geomagnetic activity are the HSSs and the related corotating interaction regions (CIR) that form as the fast solar wind overtakes the ambient slower solar wind. The ICME-driven storms are more frequent around solar maximum, when the sunspot activity reaches its peak and active region complexes randomly distributed on the

solar surface occupy most of the solar corona. The CIR/HSS-driven storms, on the other hand, are more frequent during the declining and minimum phases of a solar cycle, when the sunspot activity is at its lowest levels and the coronal holes (CH) cover a large part of the solar surface.

The history of the recurrent geomagnetic storms and their solar origin goes back more than a century ago (Tsurutani et al., 2006b). Maunder (1904) noted a 27-day recurrence in the geomagnetic activity and speculated to be caused by streams of particles emanating from the Sun. Chree (1912) quantitatively established, for the first time, a 27-day periodicity in the geomagnetic activity using superposed epoch analyses. Bartels (1934) associated the recurrent geomagnetic storms with unseen "M-regions" on the sun (M standing for "magnetically active"), while the first in-situ solar wind measurements obtained from Mariner 2 revealed a 27-day modulation of the solar wind speed (Snyder et al., 1963). Nowadays, the M-regions are identified as CHs, areas of low density and temperature in the Sun's upper atmosphere, characterized by open magnetic field lines and considered the source of the HSSs in the solar wind (Krieger et al., 1973). A more complete historical account on this subject is given by Crooker and Cliver (1994).

Periodic variations in the solar activity and the related changes in the interplanetary medium and terrestrial environment have been studied extensively ever since the discovery of the solar rotation and 11-year periodicity in the sunspot activity. Several authors have shown that both the solar wind parameters and geomagnetic activity indices exhibit a variety of periodicities in the range spanning from a few day to several years (e.g., Fraser-Smith, 1972; Hauska et al., 1973;

Svalgaard and Wilcox, 1975; Mursula and Zieger, 1996; Verma, 2001; Nayar et al., 2001; Emery et al., 2009). Recently, using GOES-12/SXI images, Vršnak et al. (2007) and Temmer et al. (2007) brought compelling evidence that linked a 9-day periodicity in the solar wind parameters (velocity, density, temperature, magnetic field) and geomagnetic activity index Dst in 2005 to a triad of CHs distributed roughly 120^{o} apart in solar longitude. Based on their findings, several authors have investigated the solar-terrestrial connection between rotating solar CHs and multi-day periodic variations in the ionosphere and thermosphere. For example, Emery et al. (2009) found exceptionally strong 7 and 9-day geomagnetically forced oscillations in the 2005 and 2006 time series of global electron hemispheric power which is the area-integrated electron energy deposition and a proxy for the electron auroral precipitation. Mlynczak et al. (2008) also reported a 9-day periodicity in the 2005 data of infrared emissions from carbon dioxide (CO_2) and nitric oxide (NO) in the Earth's thermosphere at altitudes between 100 and 200 km, derived from the Sounding of the Atmosphere using Broadband Emission Radiometry (SABER) instrument on the NASA Thermosphere Ionosphere Mesosphere Energetics Dynamics (TIMED) satellite. Furthermore, Crowley et al. (2008) determined 7 and 9-day periodic variations in the column O/N_2 density ratios, $\Sigma O/N_2$, measured by the Global Ultraviolet Imager (GUVI) on the NASA TIMED spacecraft during 2005 and 2006. Lei et al. (2008a,b) and Thayer et al. (2008) also found 5, 7 and 9-day periodicities in the thermospheric neutral densities at 400 km derived from accelerometer measurements on the Challenging Minisatellite Payload (CHAMP) satellite between 2004 and 2007, and Lei et al. (2008c) reported 7 and 9-day periods

in global observations of ionospheric total electron content (TEC) derived from Global Positioning System (GPS) measurements and in neutral temperature and wind observations between 2005 and 2006. These previous studies showed that there exist strong correlations between the ionospheric and thermospheric parameters and both solar wind speed and Kp index, during the declining and minimum phases of the solar cycle 23. In consequence, they attributed the periodic changes in the ionosphere and thermosphere to recurrent geomagnetic activity and the associated high-speed solar wind streams that modulate the high-latitude Joule and particle heating and, in turn, produce a periodic response in the thermosphere-ionosphere system.

Expanding on these previous studies, our main objective in this chapter is to investigate the multi-day (2-30 days) periodic oscillations in the ionosphere and thermosphere, especially those associated with the recurrent geomagnetic activity at the declining and minimum phases of the solar cycle 23. For this purpose, several ionospheric, thermospheric, and solar wind parameters, along with different geomagnetic and solar activity indices are analyzed using different wavelet-based analysis techniques. For our studies we use twelve solar wind parameters measured by the Solar Wind Electron, Proton, and Alpha Monitor (SWEPAM) and magnetometer (MAG) instruments on board the Advanced Composition Explorer (ACE) satellite, four geomagnetic activity indices (Dst, Kp, AE, PC), and two solar activity indices (SSN, F10.7) between January 1998 and December 2007. In addition, we also use global ionospheric maps of TEC provided by the Center for Orbit Determination in Europe (CODE), CHAMP thermospheric densities, and GUVI ΣO/N2 ratios between January 2001 and December 2007. Our results, along with the

datasets and the techniques employed, are presented in the second part of the chapter after outlining some general theoretical aspects relevant to our studies.

2.2 Theoretical Considerations

2.2.1 Solar Wind-Magnetosphere Interaction

In its motion around the Sun, the Earth is embedded in the solar wind, a continual supersonic outflow of magnetized plasma emitted by the Sun's upper atmosphere and consisting mainly of protons and electrons. Enclosed in the solar wind is a "frozen in" interplanetary magnetic field of about 3-30 nT, at 1AU, which displays a corotating spiral pattern and certain structural properties. Near Earth, the solar wind velocity has a radial component of about 400-1000 km/s and the solar wind density ranges from about 0.1 to 100 cm^{-3}, the two parameters being in general inversely correlated.

As it flows past the Earth, the solar wind distorts and confines the terrestrial magnetic field into a cavity, the magnetosphere. Due to its interaction with the solar wind, the magnetosphere displays a bullet-shaped configuration with an elongated tail that expands hundreds of Earth radii in the anti-sunward direction and a shock front where the solar wind is decelerated, heated, and deflected. The terrestrial magnetosphere is therefore a complex system which acts as a buffer and mediator between the variable solar wind and the Earth's atmosphere (Kivelson and Russell, 1995). Although, to a large extent, the magnetosphere shields the Earth from the solar

wind, some of the solar wind mass, momentum, and energy enter into the magnetosphere powering current systems, geomagnetic storms, and auroral displays.

Several mechanisms (e.g., Echer et al., 2008) have been proposed to explain the transfer of mass, energy and momentum between the solar wind and magnetosphere, among them being the magnetic reconnection of the IMF and geomagnetic field (Dungey, 1961). Nowadays, it is accepted that the solar wind energy transfer into magnetosphere is controlled by the orientation of the IMF, being more efficient for a southern IMF-Bz component, and is modulated by the solar wind speed, density, and magnetic field strength, although other parameters such as temperature are important as well.

The energy flow into magnetosphere is controlled by the *tangential stress* (or drag) exerted by the solar wind on the magnetospheric cavity, whereas the size and shape of the terrestrial magnetosphere and its outer boundary, the magnetopause, are primarily determined by the *normal stress* exerted by the solar wind dynamic and thermal pressures. While the normal stress determines the overall size and shape of the magnetosphere, the tangential stress plays a crucial role in its dynamics, providing the driving force for most magnetospheric processes.

As mentioned previously, the tangential stress is caused by the merging or reconnection of the IMF with the terrestrial field and is controlled by the orientation of the IMF-Bz. However, while the reconnection rate is strong when IMF-Bz is southward and weak when IMF-Bz is northward, there is always reconnection somewhere as the magnetopause has regions of quite diverse field directions, the reconnection site thus depending on the orientation of the IMF-Bz. It is also worth

mentioning that the stresses exerted on the magnetosphere by the solar wind are transmitted to the ionosphere via current systems that flow along magnetic field lines and close in the ionosphere across field lines, and can lead to substantial changes in the thermosphere-ionosphere system.

The magnetospheric response to a southward IMF-Bz is complex and involves several processes, including: magnetic reconnection of the IMF and geomagnetic field lines, erosion of the magnetopause, contraction of the dayside magnetosphere, equatorward movement of the polar cusp, enlargement of the polar cap and geomagnetic tail, increase of the energetic particles precipitation, and overall enhancement of the geomagnetic activity which can give rise to geomagnetic storms and substorms.

Both geomagnetic storms and substorms are aspects of geomagnetic activity associated with southward IMF-Bz. The substorms typically arise in connection with short variations in the IMF-Bz. They are characterized by increased high-latitude currents and involve a rapid release of energy accumulated mostly in the tail, accompanied by a loss of the ring current energy. While the substorms do occur during storms, they do not cause storms and their strength is not predictive of storms either. They occur over intervals of several hours, often repeating every few hours, and produce beautiful and colorful auroras at night. The geomagnetic storms, on the other hand, have longer durations and are characterized by extremely large ring currents caused by prolonged magnetospheric convection.

2.2.2 Predicting the Magnetosphere Activity from Solar Wind Parameters

To predict the magnetospheric response to varying interplanetary conditions, previous studies have used different geomagnetic activity indices in conjunction with in-situ solar wind observations, in a regression analysis approach, and treated the magnetosphere as a black-box whose transfer function remained to be determined. The most commonly used input parameters in such modeling studies were the solar wind density, velocity, and magnetic field strength and direction, while the output was usually taken to be one of the geomagnetic indices (e.g., Arnoldy, 1971, Garrett et al., 1974).

Historically, solar wind density, velocity, and dynamic pressure were among the first solar wind parameters used to describe the interactions between the solar wind and magnetosphere (Chapman and Ferraro, 1931). Over the years though, especially after the published work by Dungey (1961), the importance of the solar wind electric field and magnetic merging in predicting the behavior of the magnetosphere has become more appreciated. Therefore, in an attempt to derive suitable analytical expressions that accurately describe the solar wind-magnetosphere coupling, various combinations of the basic solar wind parameters, including the solar wind electric field, have also been tried (e.g., Burton et al., 1975; Perreaullt and Akasofu, 1978; Kan and Lee, 1979; Papitashvili et al., 2000; Stauning et al., 2008).

A widely used parameter in magnetospheric studies has been the interplanetary "geo-effective" or "merging" electric field $E_m = V_{sw} \cdot B_T \cdot sin^2(\theta/2)$, which is a combination of the solar wind velocity, V_{sw}, transverse component of the IMF,

$B_T=(B_x^2+ B_y^2)^{1/2}$, and the IMF clock angle, $\theta=arctan(B_y/B_z)$. Akasofu (1979) also tested different other combinations of solar wind parameters to describe the energy coupling function in the solar wind-magnetosphere system. They found that the auroral disturbance level correlated the best with $\varepsilon = V_{sw}\cdot|B|^2\cdot sin^4(\theta/2)\cdot l_o^2$, where l_o is about $7\cdot R_E$, with R_E being the radius of the Earth, and $|B|$ is the strength of the IMF.

In a similar effort, Newell et al. (2007) also investigated various combinations of solar wind parameters and showed that $d\Phi_{MP}/dt = V_{sw}^{4/3}\cdot|B|^{2/3}\cdot sin^{8/3}(\theta/2)$, which represents "the rate at which the magnetic flux is opened at the magnetopause", works significantly better in predicting the magnetospheric activity than other solar wind-magnetosphere coupling functions. They showed that several geomagnetic activity indices that characterize the state of the magnetosphere, including Dst, Kp, and AE, can be predicted by $d\Phi_{MP}/dt$ alone without any knowledge of their time history. The apparent physical interpretation is that the merging rate on the dayside magnetopause correlates well with the magnetospheric activity.

2.2.3 Response of the Ionosphere and Thermosphere to Geomagnetic Storms

Geomagnetic storms are large disturbances in the geomagnetic activity caused by enhanced solar wind-magnetosphere energy couplings and associated with different solar and interplanetary phenomena, such as sheath magnetic fields, interplanetary coronal mass ejections, corotating interaction regions, high-speed streams, and Alfvén wave fluctuations. The ionospheric storms represent the response of the ionosphere to geomagnetic storms. They are considered extreme forms of space

weather as they can drastically affect the ground-based and space-based technological systems, disrupting satellite communications and interrupting the flow of electrical energy over power grids. The ionospheric storms are characterized by large disturbances in the ionospheric currents and densities, and are driven by variable magnetospheric energy inputs to the Earth's upper atmosphere. There are two main sources of magnetospheric energy input to the upper atmosphere, the energetic particle precipitation and the convective electric field. The two energy sources increase dramatically during the driven phase of a geomagnetic storm and are considered key drivers in ionospheric and coupled thermosphere-ionosphere models (Fuller et al., 1994, 1996; Buonsanto, 1999).

During geomagnetic storms, the disturbed solar wind compresses the Earth's magnetosphere producing changes in the geomagnetic field. In this process, for a southward IMF-Bz, solar wind magnetic field lines merge with geomagnetic field lines allowing mass, energy, and momentum to be transferred from the solar wind to the Earth's magnetosphere. As a result of magnetic reconnection, intense electric fields map along the connected field lines to high latitudes where they produce a rapid plasma convection that drives the ionosphere and, through collisions, forces the thermosphere into motion. At times, the high-latitude convection electric fields can even penetrate to low latitudes until an opposite shielding electric field develops in the inner magnetosphere. Meanwhile, energetic particles precipitate to the lower thermosphere expanding the auroral zone and increasing the plasma density, and hence the ionospheric conductivity. The strong convective electric fields and the increased conductivities produce substantial electric currents and, through Joule

effects, cause considerable heating and increased temperatures of the ionized and neutral gases over large geographic areas as the Earth rotates. The heating effect can be interpreted as a frictional heating caused by collisions between the accelerated plasma and ambient neutrals (e.g., Buonsanto, 1999).

As a result of the high-latitude Joule and particle heating, the neutral atmosphere undergoes a rapid thermal expansion which causes departures from diffusive equilibrium and increases in the mean molecular mass, i.e., increases in the ratio of molecular nitrogen N_2 and oxygen O_2 concentrations to atomic oxygen O concentration (Rishbeth et al., 1987). The expansion of the heated neutral atmosphere produces pressure gradients which drive significantly divergent neutral winds and modify the global thermospheric circulation. The divergent wind field, in turn, drives upward vertical winds which carry air rich in molecular species across pressure levels to higher altitudes, a process known as upwelling, creating a composition change with increased ratio of molecular to atomic species. The increase in the neutral molecular species at F-region heights increases the recombination rate of O^+ and, consequently, reduces the F-region plasma densities, the recombination rate being proportional to $[N_2]$ and $[O_2]$, and the production rate to [O].

Once created, the composition disturbance zone of increased mean molecular mass is redistributed to lower latitudes by enhanced global-scale equatorward winds driven by the high-latitude heating. Meanwhile, zonal winds develop at mid-latitudes due to the Coriolis effects, and they partially balance the meridional pressure gradients restricting the continuation of the equatorward winds and reducing their divergence, hence limiting the buildup of the composition bulge. In addition,

transport of air parcels from high latitudes also dampens meridional pressure gradients and limits the equatorward winds. When the neutral atmospheric heating events at high latitudes are impulsive, the equatorward winds often take the form of equatorward wind surges or traveling atmospheric disturbances (TAD). These large scale acoustic gravity waves (AGW) can penetrate to low latitudes and even into the opposite hemisphere where they drive poleward winds for a few hours. In the ionosphere they manifest as large-scale traveling ionospheric disturbances (TID) and have been identified as sequential rises in the peak F2-layer height by meridional chains of ionosondes.

The equatorward winds are stronger at night when they superimposed on the background day-to-night circulation and are reinforced by antisunward ion drag due to magnetospheric convection ExB plasma drifts. On the dayside, the equatorward winds compete with the prevailing poleward circulation, while at night the two wind systems work together. Consequently, the composition disturbance zone rich in molecular species reaches lower latitudes at night and then rotates with the Earth into the morning sector. Equatorward of this zone and during the afternoon hours, poleward winds may occur producing a decrease of the mean molecular mass. As a result of this local time dependency of winds and neutral composition changes, at mid-latitudes, negative ionospheric disturbances with depleted plasma densities are more prevalent in the morning sector, while positive ionospheric disturbances with increased plasma densities are more prevalent in the afternoon and evening sectors.

The composition bulge can also penetrate to lower latitudes in summer than in winter due to the fact that the total wind includes a prevailing trans-equatorial

summer-to-winter flow which limits the equatorward motion of the composition bulge in winter, but expands it further equatorward in summer. In winter the composition bulge is thus mostly confined to high latitudes by the flow from the summer hemisphere, while in summer the bulge is advected to lower latitudes and even to the opposite hemisphere. At equinox the bulge is advected to mid-latitudes in some longitude sectors, its diurnal migration being equatorward at night and poleward during the day. As a result of the storm-induced changes in the neutral composition, at mid-latitudes, positive storm effects are more often seen in winter, whereas negative storm effects are more common in summer. After the storm, the background wind field continues to move the bulge poleward during the day and equatorward during the night, thus introducing a diurnal variation in the response. A number of observational and modeling studies have investigated the diurnal and seasonal variations of the positive and negative ionospheric storm effects and of the associated storm-induced composition and ionization perturbations using TEC and NmF2 data.

It is thus clear that the response of the ionosphere to geomagnetic storms is quite complex, the ionosphere being affected by changes in the neutral composition, neutral density, and thermospheric dynamics as the meridional winds push the F-layer to new heights, as well as by plasma convection and energetic particle precipitation. Neutral composition changes alter the balance between production and loss rates in the ionosphere, as increased neutral densities hasten the ion recombination and increase the loss rates, depleting the ionospheric F-region plasma density and leading to the characteristic negative storm effects, while reduced neutral densities lead to the characteristic positive storm effects.

Positive and negative storm effects can also be caused by a disturbed thermospheric circulation, not only by altering the chemical composition of the thermosphere, but also by moving the ionospheric plasma up and down along the magnetic field lines, which then modulates the chemical loss rates by changing the production and loss rates of the ionized species. At mid-latitudes, equatorward winds cause positive ionospheric disturbances by uplifting the plasma to heights where the recombination rates are low, while poleward winds cause negative ionospheric disturbances by pushing plasma to lower altitudes where increased molecular species hasten the ionospheric decay.

A disturbed thermospheric circulation also produces disturbance dynamo electric fields which in addition to the penetration electric fields of magnetospheric origin can affect the production and recombination rates in ionosphere by redistributing the plasma and by producing plasma irregularities and instabilities. Elevated neutral temperatures at storm time can also increase the recombination rates due to the rapid conversion of the O^+ to NO^+, depleting the ionospheric plasma densities. Additionally, another possible chemical loss mechanism, not driven by dynamics, is the production of vibrationally excited molecular nitrogen (e.g., Buonsanto, 1999).

To summarize, at high latitudes, the initial upper-atmospheric response is thermospheric heating, thermal expansion, wave surges, high velocity winds, and changes in the global thermospheric circulation and neutral composition. At low latitudes, the initial response is driven by penetration electric fields of magnetospheric origin. They cause poleward expansions of the equatorial ionization anomaly and

enhanced F-region plasma densities at low and mid-latitudes, as the equatorial plasma moves upward at heights where the recombination rates are low and then diffuses downward along the magnetic field lines to higher latitudes. In the later stages of the storm, the ionospheric plasma responds to changes in the neutral composition and global thermospheric circulation and to disturbance dynamo effects.

Several observational and modeling studies have indicated that multiple physical processes are involved in the response of the thermosphere and ionosphere to geomagnetic storms, the relative importance of these processes being determined by the latitude, local time, season, phase of the storm, and time elapsed since the storm onset. However, due to their complexity, the ionospheric storms and their underlying physical processes are still not fully understood and, at times, are even difficult to interpret (e.g., Fuller-Rowell et al., 2007; Schunk and Zhu, 2008; Mansilla, 2007).

2.2.4 Recurrent and Non-recurrent Geomagnetic Storms

The solar wind is a major driver of space weather near Earth. As mentioned before, it consists of three basic types of flows: (1) ambient slow solar wind flows emitted by regions in or around helmet streamers and active regions on the Sun, (2) high-speed streams originating from solar coronal holes, areas of low density and temperature in the solar corona, and (3) transient ejecta which consist of material emitted during coronal mass ejections (CME), spectacular solar events in which large amounts of solar material are ejected into the solar wind. In addition, the corotating interaction regions, CIRs, are large-scale structures of compressed magnetic field and

plasma in the solar wind that form as corrotating HSSs (750-800 km/s) overtake the ambient slower solar wind streams (300-400 km/s).

The CIRs are therefore closely related to the high-speed solar wind streams and are typically characterized by: (1) high plasma velocities and densities, which make them highly geoeffective over long periods of time, (2) enhanced magnetic fields, and (3) large amplitude Alfvén waves with highly fluctuating IMF-Bz components that propagate radially away from the Sun (e.g., Tsurutani et al. 1995). Their front or leading portion consists of compressed and accelerated slow solar wind, while their trailing portion consists of compressed and decelerated fast solar wind. The "frozen-in" condition of the solar wind plasma prevents the interpenetration of different streams in a CIR structure, and hence interface boundaries separate the fast streams from the ambient plasma streams. Away from the Sun, the CIRs are bounded by fast forward (FS) and fast reverse (RS) shocks, and the fast and slow stream material inside the CIR structures are separated by a stream-stream interface surface (IF). Closer to the Sun and near Earth, at 1 AU, the CIRs typically do not have neither forward nor reverse shocks (Tsurutani and Ho, 1999).

From a space weather perspective, the CIRs and the related HSSs are very important drivers of geomagnetic activity, especially at solar minimum and during the declining phase of a solar cycle. They are stable interplanetary structures that usually recur for several solar rotations, triggering recurrent geomagnetic storms of weak-to-moderate intensity (Dst > -100 nT). When the interplanetary Alfvénic fluctuations within CIRs and HSSs are in the north-south direction, there are significant geophysical consequences as the magnetic reconnection between the IMF and the

terrestrial field allows a significant amount of solar wind energy and particles to enter the magnetosphere/magnetotail system. This results in sporadic energy and particle injection into ionosphere in the form of substorms and auroral particle precipitation. Thus, by impinging upon the Earth's magnetosphere, the periodic CIR/HSSs modulate the energy transfer into the magnetosphere and, in turn, the geomagnetic activity and the state of the thermosphere-ionosphere system, producing chains of consecutive substorms that lead to unusually long recovery phases, known as high-intensity long-duration continuous AE activity (HILDCAA) (e.g., Lavraud et al., 2006; Gonzalez et al., 2007; Echer et al., 2008).

The left panel of Figure 2.1, taken from Tsurutani and Ho (1999), shows the schematic diagram of a CIR structure (looking down from the north pole), where the CIR region is shown as a shaded area and the different regions and interfaces are marked with their corresponding symbols. This panel also illustrates the large amplitude Alfvén waves present in the trailing portion of the CIR structure, and the low amplitude Alfvén waves that fill the fast stream proper (B). The schematics of different solar wind parameters and the resultant geomagnetic activity, represented by the Dst and AE indices, before and during a CIR/HSS interval, are shown in the right panel of Figure 2.1, which is taken from Tsurutani et al. (2006a). In both panels, the different phases of a CIR/HSS-driven geomagnetic storm and the corresponding interplanetary structures that drive them are indicated by numbers, where (1) corresponds to the quiet phase before the storm (AE and Dst near zero) and the slow stream (low speed, low B magnitude, low Bz values), (2) represents the initial phase of the storm and the leading portion of the CIR, which is characterized by increased

plasma densities, (3) indicates the main phase of the storm (low Dst and high AE values) and the trailing portion of the CIR, with large amplitude Alfvén waves and highly-fluctuating Bz components, and (4) corresponds to the recovery phase and the associated fast stream, characterized by continuous Alfvénic fluctuations.

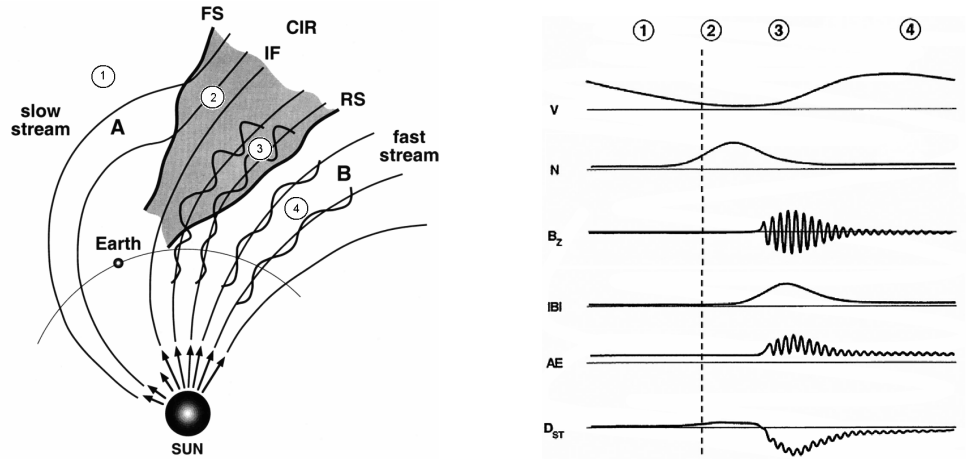

Figure 2.1: (left) Schematic of a CIR/HSS structure (from Tsurutani and Ho, 1999), and (right) schematics of some solar wind parameters and the resultant geomagnetic activity before and during a CIR/HSS interval (from Tsurutani et. al, 2006a)

Unlike the CIR/HSS events which drive recurrent geomagnetic storms, the ICME events drive non-recurrent geomagnetic storms. The ICMEs are more frequent at solar maximum and typically do not persist beyond a solar rotation. They are interplanetary extensions of the CMEs and consist of large amount of solar and coronal material catastrophically ejected from the Sun. Figure 2.2 taken from Tsurutani et al. (2006a) shows schematic profiles of geomagnetic storms driven by ICME (left) and CIR/HSS (right) solar wind structures. It is clear from this figure that both the CIR/HSS and ICME-driven storms are characterized by initial, main, and recovery phases, but, as discussed in Tsurutani et al. (2006a) and as schematically

shown in Figure 2.1, different solar and interplanetary causes are involved during each phase of the two types of storms. The differences between the CIR/HSS and ICME-driven storms are further discussed in the next section. Here we only conclude that the geomagnetic activity during the declining and minimum phases of a solar cycle, when the CIR/HSS activity is dominant, is substantially different than during solar maximum, when the ICME activity is dominant.

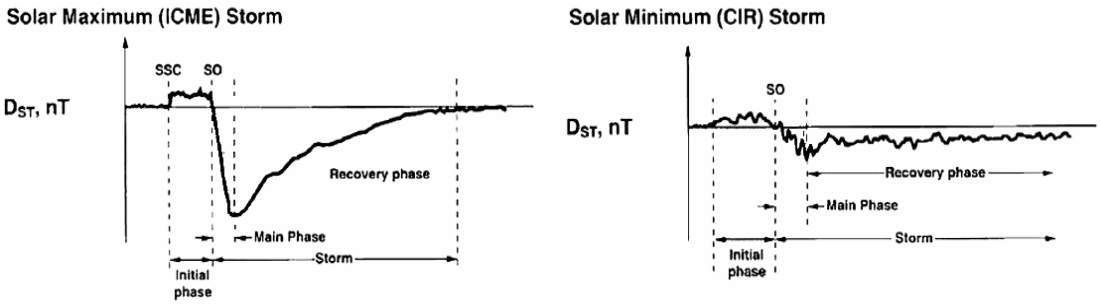

Figure 2.2: Schematic profiles of geomagnetic storms driven by (left) ICME and (right) CIR/HSS structures in the solar wind (from Tsurutani et al., 2006a).

2.2.5 Differences between CIR/HSS-driven Storms and ICME-driven Storms

Several differences between the ICME and CIR/HSS-driven storms have been summarized and discussed by Borovsky and Denton (2006). In a nutshell, the ICME-driven storms are characterized by high geomagnetic activity levels (Dst < -100 nT) and relatively short recovery phases, are brief, do not persist more than a solar rotation, occur randomly, are very different in nature since they depend on the morphology and properties (size, structure, density, etc.) of the associated solar wind structures, are more frequently at solar maximum, have denser plasma sheets and stronger ring currents, and are typified by intense solar energetic particle events. They

can generate new radiation belts, great auroras, and dangerous geomagnetically induced currents (GICs), being thus more hazardous to ground-based systems (e.g., Gonzalez et al., 1994; Kamide et al., 1998; Denton et al., 2006; Xie et al., 2006; Pulkkinen et al., 2007; Kataoka and Pulkkinen, 2008).

On the other hand, the CIR/HSS-driven storms are weak-to-moderate storms (Dst > -100 nT), recur periodically, are similar in nature since CIRs have consistent structures, have initial phases with gradual onset caused by increased ram (dynamic) pressure, have highly-irregular main phases due to highly-fluctuating IMF-Bz components, are epitomized by long recovery phases that usually last for several days or even weeks, display broad and slowly-varying low-intensity diffuse auroral displays covering all local times, prevail during the declining and minimum phases of a solar cycle, are characterized by higher plasma sheet temperatures, have higher and more persistent magnetospheric electron temperature, and produce higher fluxes of relativistic "killer" electrons, bursts of plasma and energy injections into magnetosphere, low but long-lasting subauroral GIC activity in the local pre-noon sector, longer periods of magnetospheric convection, prolonged periods of energetic particle precipitation, continuous high-latitude auroral displays, and severe spacecraft charging which makes them hazardous to space-based assets, particularly at the geosynchronous orbit (e.g., Borovsky and Denton, 2006; Tsurutani et al., 2006a; Vršnak et al., 2007; Longden et al., 2008).

Although the CIR/HSS-driven storms are characterized by weak-to-moderate geomagnetic activity levels, their overall contribution to the geomagnetic activity has been shown to be on average comparable to that of the ICME-driven storms mainly

due to the fact that they usually last much longer than the storms induced by the ICME events. It has been also argued that there is even greater average solar wind energy introduced in the magnetosphere during the declining and minimum phases of a solar cycle when the CIR/HSSs are the dominant structures in the solar wind than at solar maximum when the ICMEs are dominant (Tsurutani et al., 2006a). It can thus be concluded that the space weather effects associated with the CIR/HSS events and their related recurrent geomagnetic activity are also very important to mankind (e.g., Lavraud et al., 2006; Thayer et al., 2008) and deserve careful investigation.

2.2.6 Coronal Holes

Coronal holes are solar features detectable as dark regions in X-ray and EUV images of the Sun, but not in visible light, and represent the Bartels' mysterious M-regions (e.g., Chapman and Bartels, 1940; Crooker and Cliver, 1994). They are characterized by very low densities and temperatures, compared to the typical background corona, and by open and divergent magnetic field configurations. In general, they prevail during the declining and minimum phases of a solar cycle and can persist for several solar rotations. CHs are very important for heliospheric and space weather studies since they are the sources of the high-speed solar wind streams, interplanetary structures that give rise to recurrent geomagnetic storms. In the literature, they have been known under different names: M regions (Bartels, 1932), unipolar magnetic regions, and ghost unipolar magnetic regions in the photosphere (Wilcox and Ness, 1965). Figure 2.3, taken from Tsurutani et al. (2006a), shows a

Yohkoh image of the Sun taken in soft X-rays on 8 May 1992. It illustrates a large polar CH extending over the solar north pole and helmet streamers, which are the sources of the ambient slow solar wind, dominating the solar corona at lower heliographic latitudes.

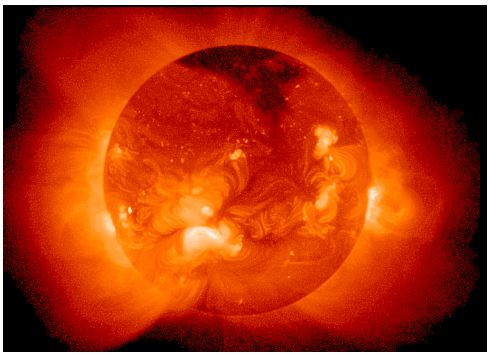

Figure 2.3: Yohkoh image of the Sun taken in soft X rays on 8 May 1992 (from Tsurutani et al., 2006a).

The parameters usually used to characterize the CHs are location, size, and magnetic field polarity. According to their location, CHs have been grouped into three broad categories: polar, non-polar, and transient (Harvey and Recely, 2002). Each category represents certain latitude ranges and lifetime span. The polar coronal holes are located at high heliographic latitudes and have a lifetime that is a significant fraction of the solar cycle, persisting for several years. They are largest at sunspot minimum, when they represent about 15% of the solar surface area, decrease in size during the rise of a cycle, disappear at sunspot maximum around the time of the magnetic field polarity reversal, and reform from mid-latitude isolated coronal holes after the polarity reversal of the magnetic field is completed. Before the solar minimum, the CHs are typically situated at the polar caps but present some tongue-

like extensions into the equatorial regions. The non-polar CHs exist as isolated features within the ±60^{o} latitude range. They are associated with active region and remnant active region magnetic fields and have a lifetime of one to several solar rotations. The transient CHs, on the other hand, have a typical lifetime of several days and are associated with solar eruptive events.

Figure 2.4 illustrates the configuration of the coronal magnetic field lines at solar minimum (left) and at solar maximum (right). It can be seen in this figure that, at solar minimum, the polar CHs are the most dominant features of the solar corona and the activity belt is confined to a narrow latitudinal band at low heliomagnetic latitudes, forming a separatrix between the positive and negative magnetic field lines that originate from CHs of opposite polarity and open into interplanetary space. At solar maximum, the helmet streamers are the dominant features of the Sun's upper atmosphere and are spread all over the solar surface.

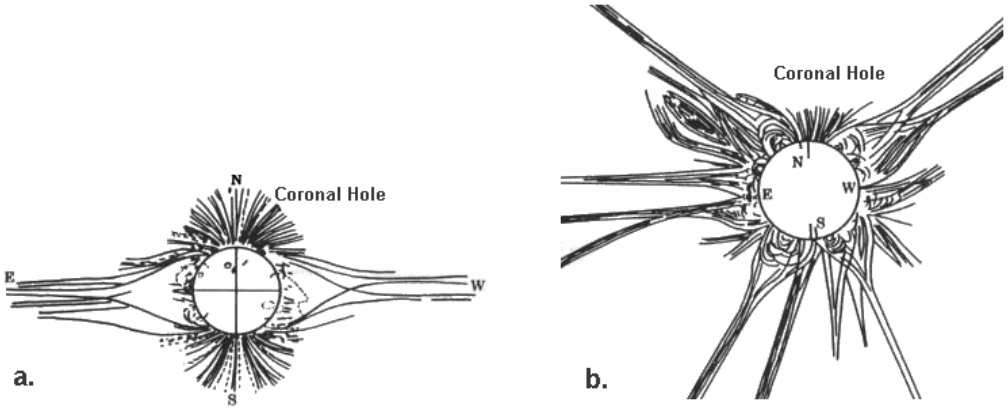

Figure 2.4: Configuration of the coronal magnetic field (a) at solar minimum and (b) at solar maximum (from Prölss, 2004; Bronshtén, 1960; Vsekhsvjatsky, 1963).

2.2.7 Solar Cycle 23

A solar cycle is an 11-year cycle, with periods varying between 7 and 13 years. It starts with a solar (sunspot) minimum and lasts until the following solar minimum. A typical cycle takes about 4 years to rise from minimum to maximum and about 7 years to fall back to minimum. During a solar cycle, the magnetic polarity of the Sun's poles reverses just after the solar maximum. The polarity reversal begins to become apparent within two years following the solar maximum (e.g., Tascione, 1994). The change in the magnetic polarity produces a 22-year solar magnetic cycle, known as Hale cycle (Hale and Nicholson, 1925). A Hale cycle starts with an even cycle and ends with an odd cycle, the geomagnetic activity being in general strongest in the middle of a Hale cycle (e.g., Emery et al., 2009). Figure 2.5 shows the configuration of the coronal magnetic field lines during different phases of an 11-year solar cycle and clearly illustrates the polarity reversal process.

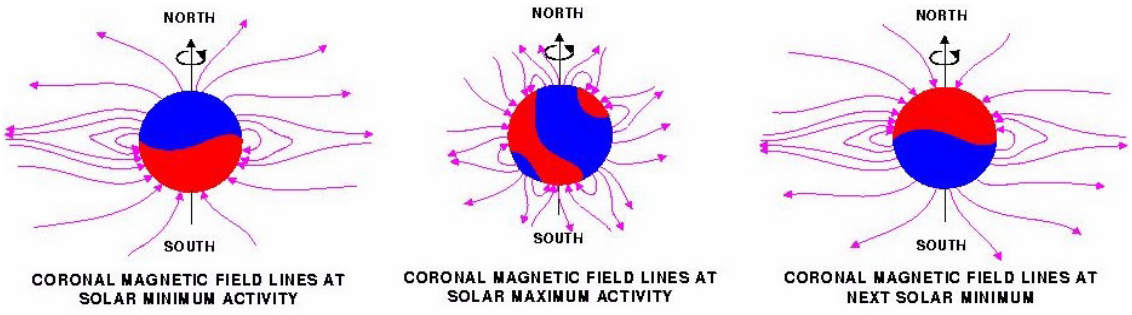

Figure 2.5: Configuration of the coronal magnetic field lines during different phases of a solar cycle.

According to Ishkov (2005), the main developmental stages of the solar cycle 23 are the following: May 1996 - minimum of the solar cycle 22; September 1997 - beginning of the growth phase; April 2000 - maximum of the smoothed relative sunspot number; July to December 2000 - polarity reversal of the solar magnetic field; November 2001 - the second maximum of the sunspot number; February 2002 - maximum of the 10.7 cm radio flux; October 1999 to June 2002 - maximum phase; July 2002 - beginning of the declining phase; and October to November 2003 - the most powerful flare events. The declining phase of the cycle extended from 2002 to 2006, and the solar minimum was reach in 2007. The developmental stages of the solar cycle 23 can be easily identified in Figure 2.6, obtained from http://www.swpc.noaa.gov/SolarCycle/, which shows the sunspot number progression from January 1994 to December 2007.

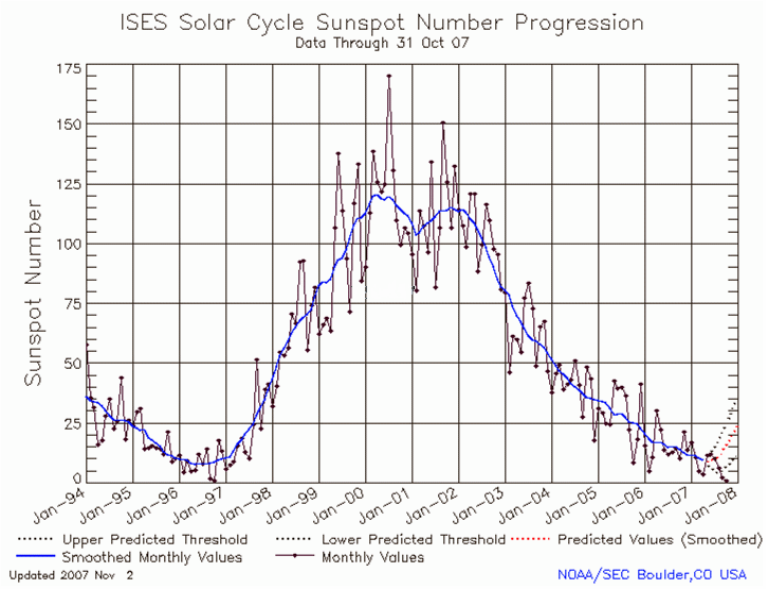

Figure 2.6. Sunspot number progression during solar cycle 23.

2.3 Dataset Description

2.3.1 Global Ionospheric TEC maps

For our studies, we used global ionospheric maps of TEC provided by CODE and available at ftp://ftp.unibe.ch/aiub/CODE/. The maps have a spatial resolution of 2.5^{o} x 5^{o} (latitude x longitude) and are generated every 2 hours based on data from about 200 GPS stations distributed worldwide. The ionosphere is approximated as a thin spherical shell at a fixed height of 450 km and the vertical TEC is modeled using spherical harmonics, in a solar-geomagnetic reference frame. The global vertical TEC is represented with 3328 (13x256) parameters and the instrumental biases for all GPS satellites and ground stations are assumed constant over one day.

2.3.2 Thermospheric Neutral Density Data

The neutral densities were derived from CHAMP accelerometer measurements of non-gravitational accelerations using standard methods described by Sutton et al. (2007). The data are available every 80 km (10 seconds) along the satellite orbit, between 2001 and 2007, and can be downloaded from: http://sisko.colorado.edu/sutton/. Since the ascending and descending orbit data are very similar, here we used only the ascending orbit data. CHAMP was launched into a near-circular orbit with an inclination of 87.3^{o} on 15 July 2000 (Reigber et al., 2000) and the spacecraft orbital altitude decayed from its initial value of 456 km to

about 340 km by the end of 2007. Therefore, to account for changes in the CHAMP orbital altitude, the measured neutral densities at the satellite altitude were mapped to a constant altitude of 400 km using the NRLMSISE-00 empirical model (Picone et al., 2002). The primary objectives of the CHAMP mission were to map the gravity and magnetic fields of the Earth and to monitor the lower atmosphere and ionosphere. More information about the mission can be found at http://www-app2.gfz-potsdam.de/pb1/op/champ/.

2.3.3 GUVI ΣO/N2 Column Density Ratio

It is known that the daytime electron density near the F-region peak is proportional to the local O/N_2 density ratio, as the electron production is primarily by photoionization of atomic oxygen O and the electron loss is proportional to molecular nitrogen N_2 and oxygen O_2 concentrations. For our studies though, we used column O/N_2 density ratios, $\Sigma O/N_2$, defined as the column density of O above the altitude where the N_2 column density is 10^{17} cm^{-2} (at about 135 km) which are only indirectly related to the electron density at any given altitude (e.g., Meier et al., 2005). The $\Sigma O/N_2$ ratios are measured by the GUVI instrument on the TIMED satellite and are available online at http://guvi.jhuapl.edu/guvi_home.html. GUVI was launched on the NASA TIMED satellite on 7 December 2001 (Christensen et al., 2003) and provides a detailed multi-spectral view of a 2000 km-wide swath in a fixed local time every 100 min. The satellite is in a 630 km circular orbit and a 74.1 deg. inclination, and its orbit precesses at a rate of 3^o per day.

2.3.4 Solar Wind Parameters

To describe the interplanetary conditions, we used merged interplanetary magnetic field and solar wind 64-second averages (Level-2 data) available at the Advanced Composition Explorer (ACE) Science Center website http://www.srl.caltech.edu/ACE/. The solar wind parameters are measured by the Solar Wind Electron, Proton, and Alpha Monitor (SWEPAM) and Magnetic Field Experiment (MAG) instruments on board the ACE satellite, which is located at L1 (~1.4 million km from Earth). To fill in the gaps in the solar wind parameters, we applied a linear interpolation procedure.

2.3.5 Geomagnetic Activity Indices

For our studies, we used the following geomagnetic activity indices: AE, Dst, Kp, and PC. The AE index, or the auroral electrojet index, is the most commonly used geomagnetic index at high-latitudes and is obtained from north-south magnetic perturbations recorded at more than ten auroral stations in the northern hemisphere. It is considered a substorm activity index and measures the strength of the currents flowing in the ionosphere over the selected auroral stations. The Dst index, or disturbance storm time index, also known as the ring current index, is more appropriate for low-latitude regions and is obtained from magnetometer stations located near the equator, where the horizontal H component of the magnetic perturbation is dominated by the intensity of the magnetospheric ring current. It is

usually used as a proxy for the ring current intensity, although it contains contributions from both ring current and magnetopause current. However, in a majority of applications, the magnetopause current contribution is neglected and the magnitude of the Dst index is assumed to represent only the kinetic energy of the ring current particles. Dst is expressed in units of nT, with high values indicating a calm magnetosphere and large negative values indicating geomagnetic storms. This index strongly correlates with the solar wind electric field and dynamic pressure.

The Kp index is more representative for middle latitudes and is derived from twelve selected magnetometer stations located in the 48^{o}-63^{o} geomagnetic latitude range. It is a 3-hour quasi-logarithmic index and takes integer values in the 0-9 range. Kp is sensitive to both ring current and auroral activity, and is commonly used to characterize the general level of geomagnetic activity caused by the solar wind, with low Kp values indicating quiet geomagnetic conditions, and high Kp values representing disturbed conditions. Both Kp and Dst are frequently used to indicate the severity of disturbances in near-Earth space. The Dst, Kp, and AE indices are available at the World Data Center for Geomagnetism, Kyoto, Japan (http://swdcwww.kugi.kyoto-u.ac.jp).

The polar cap index, PC, characterizes the polar cap magnetic activity and is indicative of the power input from the solar wind into magnetosphere. In statistical sense, it is equal to the interplanetary geoeffective electric field. This index is considered a measure of the strength of the sheet current flowing sunward across the polar cap and of the penetration of the solar wind electric field into the magnetosphere. Here we use the PC index corresponding to the northern polar cap,

PCN. This index is calculated based on data from the Danish near-polar geomagnetic observatory in Thule (now Qaanaaq), Greenland (geomag. lat. 85.40^{o}N) and is available at http://wdcc1.dmi.dk/pcnu/pcnu.html.

2.3.6 Solar Activity Indices

For monitoring the solar activity, we used the daily F10.7 index (units of 10^{-22} $Wm^{-2}Hz^{-1}$), which represents the 10.7 cm radio flux emission, as a proxy for the solar extreme ultraviolet (EUV) radiative flux, and the daily sunspot number values, SSN, available at ftp://ftp.ngdc.noaa.gov/STP/SOLAR_DATA/. It is important to mention that SSN has no direct relationship with the F-region electron density, but is occasionally used as a convenient index that is assumed to represent the solar EUV emission, although this is not always true. Even the F10.7 index is not always representative of ionizing emission levels, and hence extreme care must be taken in interpreting the correlations between these two indices and the ionospheric response.

2.4 Analysis Techniques

2.4.1 Wavelet Analysis

To examine the periodic fluctuations in our datasets, we employed the Morlet continuous wavelet technique described by Anghel et al. (2008a) and presented also in Chapter 4. The method is appropriate for non-stationary signals, i.e., signals with

variable spectral content, and provides a time-period representation of the "instantaneous" amplitudes and phases of the spectral components in a time series. In addition, to perform filtering in the wavelet domain and reconstruct signals from their continuous wavelet transforms, we developed an inverse continuous wavelet transform algorithm. The inverse transform is performed by first analyzing different reconstructed harmonics and determining their corresponding correction coefficients. The correction coefficients are then used to calculate, through interpolation, a correction profile which is subsequently included in the inversion algorithm.

It is important to mention that, in all the wavelet plots presented in this chapter, the confidence levels are calculated based on a "background" auto-regressive (AR) power spectrum determined individually for each analyzed signal, and the intrinsic frequency, ω_o, of the Morlet wavelet function is 40. The slant thick lines in the wavelet plots mark the cone of influence, the region where the edge effects become significant, and the contour lines indicate the dominant spectral components.

2.4.2 Cross-wavelet Analysis

The cross-wavelet transform is an important tool for determining similar periodicities that are simultaneously present in the wavelet spectra of two or more signals. For the two signal case, the cross-wavelet transform is calculated as:

$$CWT_{xy}(\tau,\omega) = WT_x(\tau,\omega)\cdot WT_y^*(\tau,\omega) \tag{2.1}$$

where $WT_x(\tau,\omega)$ and $WT_y(\tau,\omega)$ represent the wavelet amplitude spectra of *x(t)* and *y(t)*, respectively, τ is the time, and ω is the Fourier angular frequency.

2.4.3 Fourier-based and Wavelet-based Bispectral Analysis

The probability density function of a Gaussian signal is entirely characterized by its first two moments. For a non-Gaussian signal, on the other hand, the first two moments are not sufficient to define the signal and higher-order statistics (HOS), or equivalent higher-order polyspectra, can reveal more information than second order statistics can reveal. Among the higher-order polyspectra, the bispectrum is the most commonly used frequency-domain HOS measure. It has been applied in a variety of areas of science and engineering, including the detection of quadratic phase nonlinear couplings in plasma fluctuations and atmospheric waves, the nonlinear interactions between atmospheric waves being a common feature of the atmospheric dynamics (e.g., Hinich and Clay, 1968; Elgar and Guza, 1988; Pancheva and Mukhtarov, 2000; Larsen et al., 2002). The advantages of using the HOS and the Fourier and wavelet-based polyspectra in signal processing and analysis have been highlighted in several research papers and include the ability to recognize Gaussian and non-Gaussian signals, linear and non-linear systems, minimum and non-minimum phase systems, and (quadratic, cubic, etc.) phase couplings.

Theoretical studies of the nonlinear wave-wave interactions have shown that a nonlinear coupling between two primary waves with frequencies ω_m and ω_n and wavenumbers k_m and k_n yields two secondary waves whose frequencies and

wavenumbers are the sum and difference of the frequencies and wavenumbers of the primary waves (e.g., Teitelbaum et al., 1989). Therefore, in a nonlinear wave-wave interaction process the frequencies ($\omega_m,\omega_n,\omega_s$) and the wavenumbers ($k_m,k_n,k_s$) must satisfy the following selection rules or resonance conditions:

$$\begin{aligned} \omega_m + \omega_n &= \omega_s \\ k_m + k_n &= k_s \end{aligned} \tag{2.2}$$

However, in a system, the same selection rules (2.2) on ω and k can also be satisfied by spontaneously-excited normal modes of the system. One way to discriminate between the two cases is through bispectral analysis, known also as quadratic spectral analysis, as the nonlinear couplings between waves induce non-Gaussian effects that can be captured in general by third order moments. In principle, the bispectrum permits one to distinguish between spontaneously-exited independent modes and coupled modes in a self-excited fluctuation spectrum by measuring the degree of phase coherence between the interacting waves (e.g., Kim and Powers, 1979; Nikias and Raghuveer, 1987).

Mathematically, the bispectrum is the two-dimensional Fourier transform of the third order auto-correlation function:

$$R_{xx}(\tau_1,\tau_2) = \mathrm{E}[x(t)\cdot x(t+\tau_1)\cdot x(t+\tau_2)] \tag{2.3}$$

where E is the expectation operator, and is given by:

$$B_{xx}(\omega_m, \omega_n) = \int_{-\infty}^{\infty} \int R_{xx}(\tau_1, \tau_2) \cdot e^{j(\omega_m \tau_1 + \omega_n \tau_2)} \cdot d\tau_1 \cdot d\tau_2 \quad (2.4)$$

In practice, the bispectrum is usually calculated as:

$$B_{xx}(\omega_m, \omega_n) = X(\omega_m) \cdot X(\omega_n) \cdot X^*(\omega_m + \omega_n) \quad (2.5)$$

where $X(\omega) = \int_{-\infty}^{\infty} x(t) \cdot e^{-j\omega t} \cdot dt$ represents the Fourier transform of the signal *x(t)* and can be easily determined by means of fast-Fourier transform.

It is thus clear from Equation (2.5) that the bispectrum is zero unless the following two conditions are met: (i) waves must be present at the frequencies ω_m, ω_n and $\omega_m+\omega_n$, and (ii) a phase coherence must exist between these waves. In physical terms, waves at ω_m, ω_n and $\omega_m+\omega_n$ are spontaneously-excited normal modes if they exhibit statistically independent random phases, and, in this case, the bispectrum is expected to be zero. Conversely, waves at ω_m, ω_n and $\omega_m+\omega_n$ are generated through nonlinear interactions if they present phase coherence. In this case, the bispectrum is thus expected to take a non-zero value.

Therefore, a non-zero value at the frequency tuple (ω_m,ω_n) in the bispectrum is an indicator of phase-coherent couplings between modes with characteristic frequencies ω_m and ω_n. However, a non-zero value in the bispectrum does not provide any information about the physical nature or origin of the couplings, nor does it reveal anything about the underlying physical processes. It should be also emphasized

that a harmonic generation process is a particular case of nonlinear couplings that corresponds to the case when ω_m equals ω_n, as their nonlinear interactions produce waves with frequency $2 \cdot \omega_m$.

While Equation (2.5) is more appropriate for calculating the bispectra of stationary signals, for nonstationary signals we need to take also into consideration the fact that the spectral properties of the nonstationary signals change with time. Therefore, because the signals we deal with in our analyses are nonstationary, here we employed a wavelet-based bispectral analysis technique to investigate the quadratic nonlinear couplings between the spectral components of a time series and their temporal evolution. The wavelet bispectrum was introduced by van Milligen et al. (1995) and by Dudok de Wit and Krasnosel'skikh (1995) as a valuable tool for studying the nonstationary behavior of the nonlinear plasma fluctuations in chaos and turbulence. Similar to the Fourier bispectrum, the wavelet bispectrum is calculated as:

$$WB_{xx}(\tau, \omega_m, \omega_n) = WT_x(\tau, \omega_m) \cdot WT_x(\tau, \omega_n) \cdot WT_x^*(\tau, \omega_m + \omega_n) \qquad (2.6)$$

where $WT_x(\tau, \omega)$ represents the wavelet amplitude spectrum of the signal *x(t)*. It is clear according to Equation (2.6) that the wavelet bispectrum provides information about the non-Gaussian behavior of the nonstationary time series, and, in addition, it also shows how this behavior and the associated quadratic nonlinear couplings between the spectral components evolve over time.

2.5 Multi-day Periodic Variations in the Solar Wind Parameters during Solar Cycle 23

In this section, we investigate the multi-day periodic fluctuations present in different solar wind parameters and their temporal evolution using the Morlet continuous wavelet transform. For this study, we used twelve solar wind parameters, at a 3-hour temporal resolution, measured by the ACE satellite between 1998 and 2007. The solar wind parameters used here are: proton density, Np; proton temperature, Tp; longitude in radial tangential normal (RTN) coordinates, Long; root mean square (RMS) variation of the solar wind magnetic field, dB; Bx, By, and Bz components of the solar wind magnetic field; magnetic field strength, |B|; proton velocity, Vp; Vx, Vy, and Vz components of the solar wind velocity. The solar wind velocity and magnetic field components are given in geocentric solar magnetospheric (GSM) coordinates, where the x-axis is along the Sun-Earth line with the origin at the center of the Earth and is positive towards the Sun, the y-axis is the cross product of the x-axis and the magnetic dipole axis and is positive towards dusk, and the z-axis completes the right-hand coordinate system.

Figure 2.7 shows the twelve heliospheric parameters and their wavelet amplitude spectra (ω_o=40) for the 2-35 day period range, over the time span between January 1998 and December 2007. This time interval covers most of the solar cycle 23, which started in 1997, reached maximum in 2000-2001 and minimum in 2007. In all the wavelet plots displayed in Figure 2.7, the contour lines delimit regions of high confidence level, as compared to a background AR spectrum, and the slant lines mark

the cone of influence, where the edge effects are significant. The most striking features in these spectra are the predominant oscillations with periods around 5.4, 6.75, 9, 13.5, and 27 days, which are present in most of the solar wind parameters shown in Figure 2.7 except probably in IMF-Bz whose spectrum exhibits a high degree of randomness. However, this is not surprising considering that IMF-Bz is caused by waves and disturbances in the solar wind.

As illustrated in Figure 2.7, the 27-day period is found in most of the solar wind parameters and corresponds to the equatorial rotation period of the Sun as viewed from the Earth (e.g., Emery et al., 2009). This periodicity appears as a dominant and persistent feature in the wavelet amplitude spectra of the Long parameter and of the radial, Bx, and azimutal, By, components of the IMF over the entire ten-year interval. The three spectra are, in fact, very similar over the entire period range, with Bx and By being anti-correlated and representing the large-scale dominant polarity of the Sun. The 27-day periodicity is also significant in the Bz spectrum, where it manifests as a quasi-period spread over a wide range of periods during the ascending, maximum, and descending phases of the solar cycle, but vanishes in 2006 and 2007. In the other solar wind parameters shown in Figure 2.7, the 27-day period seems to be of lesser significance and is not continuous over the considered time interval. It appears during different phases of the sunspot cycle, when it persists for several months or even years.

Another relevant spectral component that can be observed in the wavelet amplitude spectra presented in Figure 2.7 is the 13.5-day period. This periodicity appears as a distinctive feature in the Bx, By and Long spectra, persisting for almost

the entire ten-year interval, except during 2001-2003 when it fades away. This temporal evolution of the 13.5-day period is probably associated with the polarity reversal of the solar magnetic field that occurs just after the sunspot maximum, known to be accompanied by a complete disappearance of the CHs, which reform only after the polarity reversal is completed. Our results seem to confirm previous reports that the 13.5-day period might be due to the occurrence at 1 AU of two high-speed streams per solar rotation, originating from two CHs located roughly 180^{o} apart in solar longitude (e.g., Mursula and Zinger, 1996; Nayar et la., 2001). The 13.5-day period appears also in the Np, Tp, and dB spectra mostly during 2001-2004, but also during other time intervals. It is also present in the spectra of Vx and |B| during different phases of the solar cycle, when it persists for several solar rotations.

As shown in Figure 2.7, oscillations with periods of about 5.4, 6.75 and 9 days occur occasionally in the Np, Tp, dB, |B|, Bx, By, Long, Vp, and Vx spectra throughout the entire ten-year interval, but are in general stronger and more persistent during the declining and minimum phases of the solar cycle. The 9-day periodicity appears in the Bx, By, and Long spectra during 2002-2005, in the dB spectrum, it is almost continuously present from 2001 to 2007, in the Np, Tp, Vp, and Vx spectra, it is present mostly between 2005 and 2007 but also during other phases of the solar cycle, and in |B| spectrum, it shows up intermittently during different phases of the sunspot cycle. The 5.4 and 6.75-day periods are more evident in the Np, Tp, Vp, Vx, and dB spectra and more pronounced near the solar minimum. In fact, a careful inspection of Figure 2.7 indicates that the Np, Tp, Vp, Vx, dB, and |B| spectra present

several common features over the entire analyzed period range, with Vp and Vx being almost identical to each other.

Our results are consistent with previous spectral studies of the solar wind parameters (e.g., Temmer et al., 2007; Emery et al., 2009) and indicate that the occurrence of the 5.4, 6.75, 9 and 13.5-day periodicities in the solar wind is not restricted to the declining and minimum phases of a solar cycle, when rotating CIR/HSS structures dominate the solar wind and drive recurrent geomagnetic activity at Earth, but they can be occasionally observed during other phases of a solar cycle. In addition, these periodicities, which show up as exact fractions of the solar rotation period and persist for several solar rotations, present specific temporal evolutions in each solar wind parameter. This seems to suggest that, although stable patterns of CHs may explain in a straightforward manner the presence of multi-day periodic fluctuations in the solar wind parameters, other processes might be also involved, as it will be discussed later in this chapter.

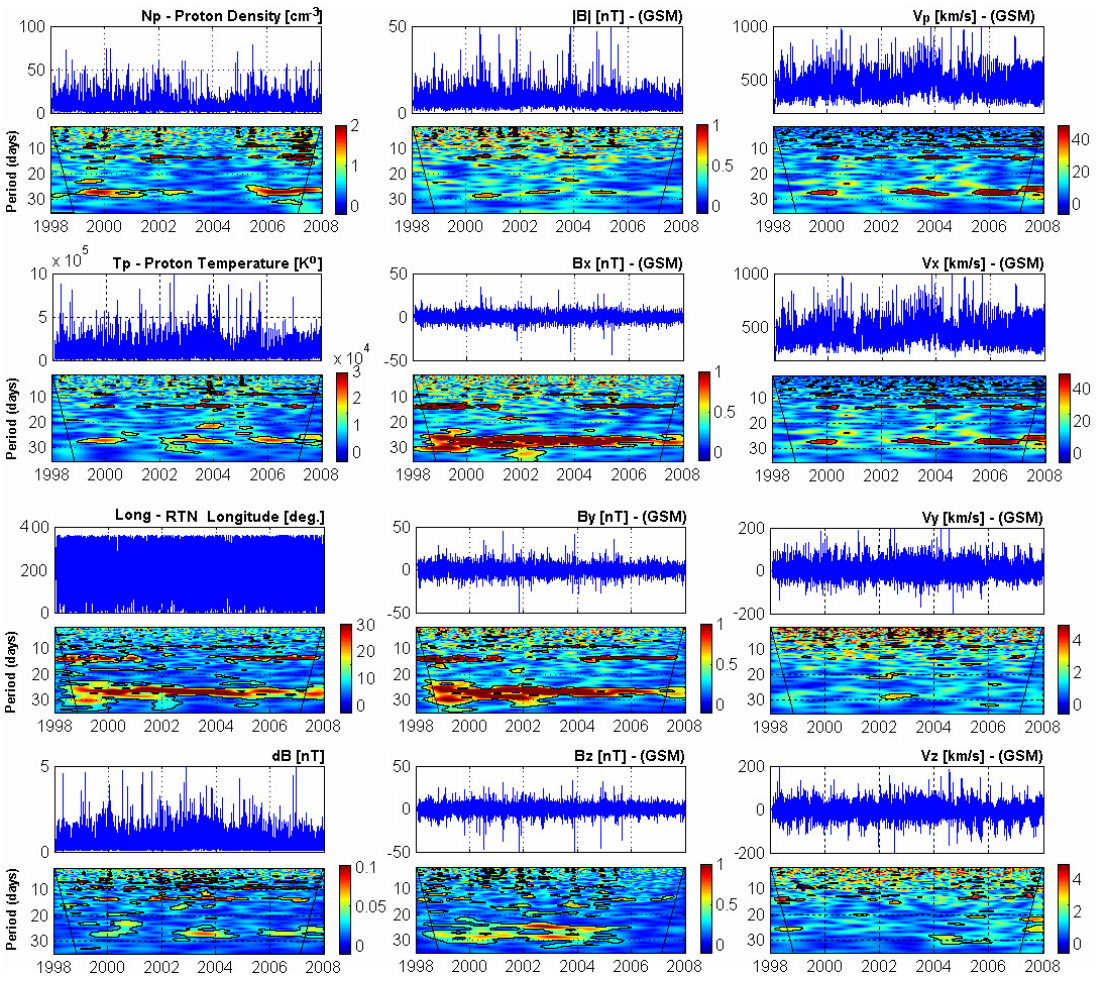

Figure 2.7: Time series and wavelet amplitude spectra (ω_o=40) of twelve solar wind parameters, over the 2-35 day period range, during 1998-2007.

2.6 Multi-day Periodic Variations in the Geomagnetic Activity Indices during Solar Cycle 23

For our studies, we used four 3-hourly geomagnetic activity indices, PC, AE, Kp, and Dst, and two solar activity indices, SSN and F10.7. They are plotted in Figure 2.8 along with their wavelet amplitude spectra (ω_o=40) for the 1.25-35 day period range, over the time interval 1998-2007. As seen in this figure, the wavelet spectra of AE and Kp present several common features: a prominent 9-day period

during 2004-2007, a distinct 6.75-day period in 2006 and 2007, and a 13.5-day period during 1999-2000, 2004, and 2007. In addition, the 27-day period in the AE spectrum is distribute over a wide range of periods, while in the Kp spectrum is confined to a narrower period band. The two spectra present also several similarities with the wavelet spectra of the Np, Tp, Vp, Vx, dB, and |B| parameters of the solar wind. This is in agreement with the fact that the geomagnetic activity is strongly influenced by the solar wind dynamic pressure and interplanetary magnetic field.

The Dst spectrum displays several similarities with the Bz spectrum. It is dominated by periodicities distributed around the 27-day period and by short-lived periodicities, with periods less than about 13.5 days, that coincide with enhanced geomagnetic activity events. Regarding the PC index, our results indicate that it does not show any similarities, over the analyzed period range, with any other geomagnetic activity index or solar wind parameter. PC is usually used to characterize the polar geomagnetic activity resulting from the solar wind-magnetosphere interaction, and is considered to approximate, in statistical sense, the interplanetary electric field.

The wavelet spectra of SSN and F10.7 are displayed in the last column of Figure 2.8. It is clear from this figure that, the two spectra present similar characteristics: dominant periodicities with periods longer than about 10 days during the ascending, maximum, and descending phases of the solar cycle, and no significant periodicities with periods less than 35 days at and near solar minimum, in 2006 and 2007. This is somehow expected considering that the sunspot activity peaks near solar maximum and vanishes at solar minimum.

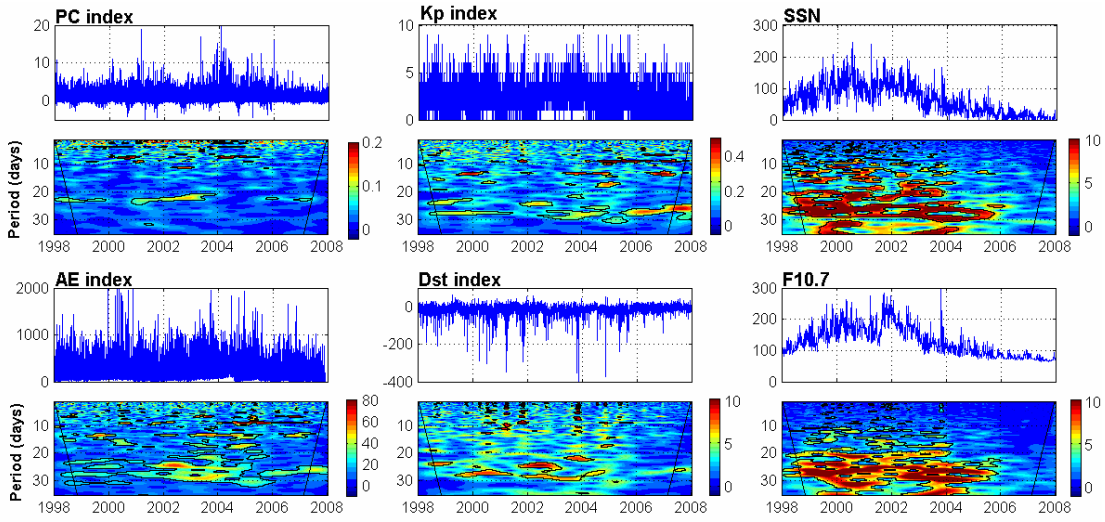

Figure 2.8: Time series and wavelet amplitude spectra (ω_o = 40) of (first two columns) four geomagnetic activity indices and (last column) two solar activity indices, over the 2-35 day period range, during 1998-2007.

2.7 Short-period Oscillations in the Thermosphere and Ionosphere and Their Relationship to Similar Variations in the Solar Wind Parameters and Geomagnetic Activity Indices at the Declining and Minimum Phases of the Solar Cycle 23

The period of interest to our current studies extends from January 2004 to December 2007, and covers a large part of the declining and minimum phases of the solar cycle 23. It has been shown that during this time interval, the solar wind was dominated by periodic HSS and CIR structures, known as important drivers of recurrent geomagnetic activity (Emery et al., 2009). To describe the interplanetary conditions over this time interval, we used the solar wind parameters shown in Figure 2.7, and to represent the geomagnetic and solar activity, we used the indices plotted in

Figure 2.8. Their wavelet amplitude spectra over the 4-14 day period range during 2004-2007, at a temporal resolution of 3 hours, are illustrated in Figure 2.9.

Clearly distinguished in the solar wind spectra shown in Figure 2.9 are oscillations with periods of about 5.4, 6.75, 9 and 13.5 days, which show up as higher harmonics of the solar rotation period and which usually persist for several solar rotations and even years. While these periodicities seem to have similar temporal evolutions in most of the solar wind parameters, there are some particularities about them, from case to case, which are discussed briefly in the following paragraphs.

First, it should be noted in this figure that the dB, Vp, Vx, and Tp spectra are very similar, the Vx and Vp spectra being in fact almost identical. These spectra are dominated by a 9-day period that extends over the entire time interval, except for a short time in 2004, which is strongest in 2005 but decreases to lower amplitudes in 2006 and 2007. Another dominant feature of these spectra is a 6.75-day period. This periodicity is present vaguely for several solar rotations in 2004 and 2005, and reappears reinforced at the beginning of 2006, when it persists until the end of 2007. A significant 5.4-day period can also be observed in these spectra throughout the entire 2004 and 2007, and occasionally for shorter time intervals in 2005 and 2006, but which displays slightly different temporal evolutions in each parameter. The 13.5-day period is also a significant feature of these spectra. It has larger amplitudes in 2004, 2006, and at the beginning of 2007, but smaller amplitudes in 2005. In addition, an 8-day period can also be observed in the dB spectrum during 2005. It also appears in other solar wind parameters but for shorter time intervals.

The spectrum of |B| is very similar with that of dB, but displays a much higher noise level. It presents a 9-day oscillation which is dominant in 2005 and part of 2004, but which has much lower amplitudes in 2006 and 2007. Like the dB spectrum, the spectrum of |B| presents a 6.75-day period in 2006, which also appears sporadically over shorter time intervals in 2004, 2005, and 2007, a weak 5.4-day period in 2004 and 2007, and a 13.5-day period in 2004 and at the beginning of 2007.

The Bx, By, and Long spectra are also very similar. They are characterized by an exceptionally strong 13.5-day period that extends over the entire time interval and a significant 9-day period that has the largest amplitudes in 2004 and 2005. Significant periodicities at 5.4 and 6.75 days can also be observed in these spectra, but they have smaller amplitudes and persist for only a few solar rotations. These periodicities are more distinctive in the By and Long spectra than in the Bx spectrum, where the level of the background noise is much higher.

The Vy and Np spectra also exhibit significant 5.4, 6.75, 9, and 13.5-day periods that display similar temporal evolutions and emerge from noisy background spectra. The Vz spectrum, although very noisy, presents significant 6.75 and 13.5-day periods, in 2005 and at the end of 2006, and weak 5.4 and 9-day periods that appear ocasionally throughout the entire interval. The Bz spectrum, on the other hand, shows a clearly distinguished 9-day period in 2004 and 2005 and a weak 6.75-day period in the first half of 2005.

A visual inspection of the wavelet plots displayed in the last column of Figure 2.9 indicates that the AE and Kp spectra present several common features. The two spectra display a dominant 9-day period that extends over the entire time interval,

from 2004 through 2007, a significant 6.75-day period in 2006, a 5.4-day period during most of 2007 and for short intervals in 2004 and 2006, and a large 13.5-day period in 2004 and at the end of 2006-beginning of 2007. It can also be noted that the two spectra present many similarities with the Vp, Vx, dB, Tp, and |B| spectra but not with the F10.7 spectrum, which exhibits a very weak 9-day period during the first three quarters of 2004 and for a very short time in the middle of 2005. Additionally, it can be remarked that the Dst spectrum presents a strong 9-day period at the end of 2004 and in 2005, which becomes very weak in 2006 and 2007, while the PC spectrum does not show any resemblance with any other spectra shown in Figure 2.9.

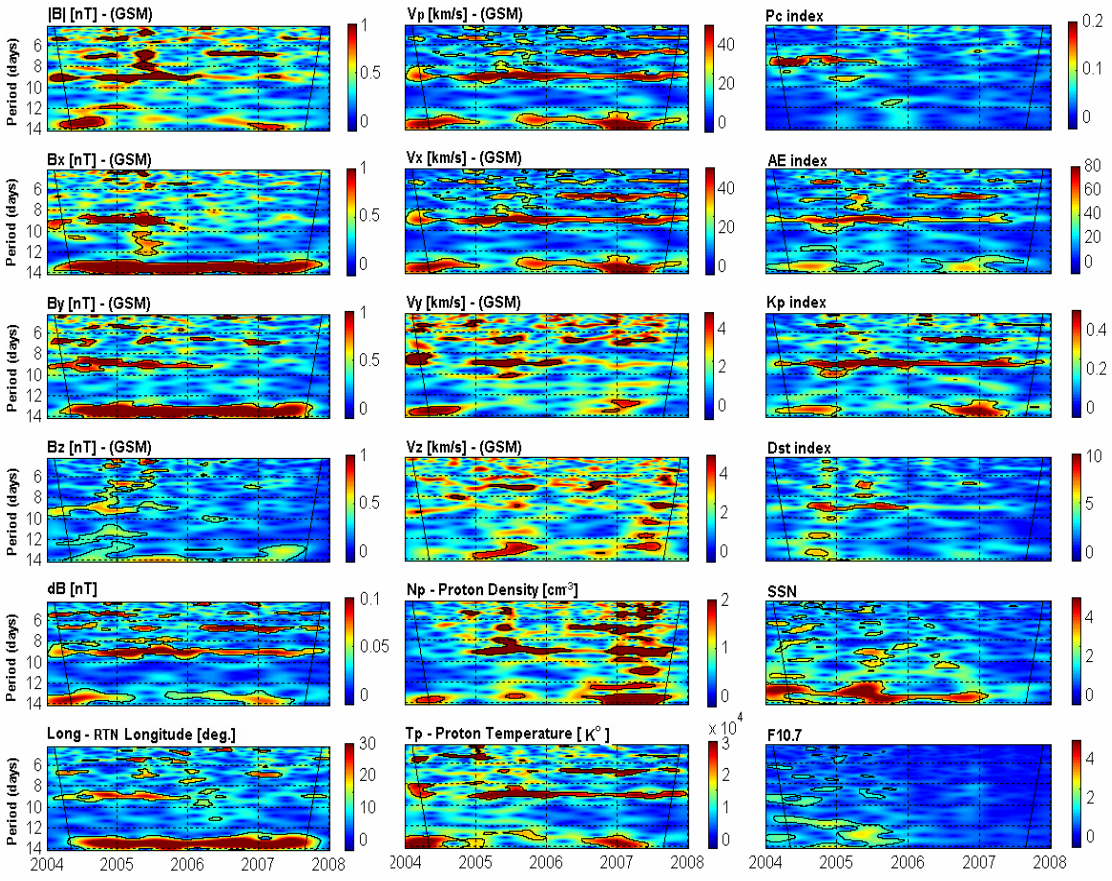

Figure 2.9: Wavelet amplitude spectra (ω_o=40) of twelve solar wind parameters, four geomagnetic indices, and two solar activity indices, over the 4-14 day period range, during 2004-2007.

Figure 2.10 shows, from left to right, the wavelet amplitude spectra (ω_o=40) of the mean values of the CHAMP neutral density, CODE ionospheric TEC (at 0000 UT), and GUVI $\Sigma O/N_2$ ratio at low (0^o-30^o), middle (30^o-60^o), and high (60^o-90^o) latitudes in the southern and northern hemispheres, over the 4-14 day period range and during the time interval between 2004 and 2007. These wavelet spectra are used to examine the latitudinal dependency and temporal evolution of the multi-day periodicities in the three types of observations and to compare these periodicities with similar fluctuations in the solar wind parameters and geomagnetic activity indices.

As seen in Figure 2.10, the wavelet spectra of the CHAMP neutral density are very similar at all latitudes. There is an exceptionally strong 9-day period in 2004 and 2005 which also appears in 2006 and 2007 but at much lower amplitudes, a significant 13.5-day period which is stronger in 2004 but much weaker during the other years, a 6.75-day period at the end of 2006-beginning of 2007 and for shorter time intervals in 2004 and 2005, and 5.4, 10, and 12-day periods at the end of 2004. It can also be remarked in this figure that the 9-day oscillation is slightly stronger at high latitudes than at low latitudes and displays a hemispheric asymmetry, with larger values in the northern hemisphere than in the southern hemisphere, the same being in general true about the other periodicities in the neutral density spectra. The results presented here are consistent with those reported by Lei et al. (2008a,b) and Thayer et al. (2008), where they also observed a similar latitudinal dependency for the 7 and 9-day periods in the CHAMP neutral densities during 2005 and 2006, by using a band-pass filtering technique.

Comparing the neutral density spectra with the spectra of solar wind parameters, geomagnetic activity indices, and F10.7 index, it can be observed that most of the short-period oscillations in the thermospheric neutral density are simultaneously present in several solar wind parameters and in the AE, Kp, and Dst indices, but not in the F10.7 index. The most striking resemblance is with the Kp, Dst, and |B| spectra, especially regarding the 5.4, 6.75, 9, and 13.5-day periodicities and their temporal evolution. Our results thus indicate that these multi-day periodicities in the thermospheric density are a direct response to recurrent geomagnetic activity and the associated CIR/HSS solar wind structures, which by impinging on the Earth's magnetosphere modulate the energy transfer into the magnetosphere-thermosphere-ionosphere system, and are definitely not induced by variations in the solar EUV flux.

Previous studies have shown that the recurrent geomagnetic activity can produce periodic variations in the high-latitude Joule and particle heating and, in turn, can drive global changes in the thermospheric circulation and global increases in the neutral density at F-region heights, larger changes in the thermospheric density occurring at high latitudes than at low latitudes (e.g., Thayer et al., 2008). This is in agreement with our results which clearly show that, although the CIR/HSS-driven storms are characterized by weak-to-moderate geomagnetic activity levels, they can have a significant impact on the global state of the thermosphere.

In addition to recurrent geomagnetic activity, planetary waves propagating from lower atmospheric layers represent an alternative source of periodic fluctuations in the neutral density in the 2-30 day period range. It has been shown though that the planetary waves cannot propagate directly beyond about 100-110 km (e.g., Borries et

al., 2007), and although some indirect mechanisms have been proposed (e.g., Forbes, 1996; Thayer et al., 2008), the manner in which planetary waves can drive periodic oscillations in the thermosphere and ionosphere is still unknown. These aspects further support the idea that the oscillations observed in the CHAMP neutral densities, persisting over several solar rotations and even years, regardless of season and latitude, are a direct response to recurrent geomagnetic forcing.

As shown in the middle column of Figure 2.10, the wavelet spectra of the mean TEC values (at 0000 UT) at low, mid, and high latitudes, in the northern and southern hemispheres, display prominent oscillations with periods of 5.4, 6.75, 9 and 13.5 days and a significant latitudinal dependency. At low latitudes, the TEC spectra in the northern and southern hemispheres are very similar, but also very noisy. They present a significant 9-day period which extends from 2004 to 2007, has larger amplitudes in 2005 and at the beginning of 2004 and 2007, and displays a weak seasonal variation; a strong 13.5-day period at the beginning of 2004 and at the end of 2005; a significant 6.75-day period in 2007 and, for a short time, in 2004 and 2005; and 10 and 11.75-day periods at the end of 2004, mostly in the southern hemisphere.

At mid and high latitudes, the TEC spectra in the southern hemisphere are quite different than those in the northern hemisphere. In both hemispheres, the 9-day periodicity displays a seasonal variation with larger amplitudes in summer than in winter. It can also be observed in this figure that in the southern hemisphere, the TEC oscillations are stronger at high latitudes than at mid latitudes, while in the northern hemisphere, they seem to be stronger at mid latitudes than at high latitudes.

It is evident from Figures 2.9 and 2.10 that several features in the TEC spectra are similar to features in the spectra of different solar wind parameters and of the Ap, Kp, and Dst geomagnetic indices. This therefore suggests that most of the spectral features in the TEC spectra are in fact a direct response to recurrent geomagnetic activity driven by high-speed solar wind streams. In addition, a closer inspection of Figure 2.10 indicates that, despite the fact that there are significant latitudinal differences between the TEC spectra and only small differences between the neutral density spectra, there are several similarities between the TEC and neutral density spectra. They show a strong 9-day period in 2004 and 2005, a 6.75-day period in the second half of 2006 and occasionally in 2004 and 2005, a 13.5-day period mostly in 2004 and 2005, and 5.4, 10 and 11.75-day periods at the end of 2004.

The fact that there are similarities between the TEC and neutral density spectra is not surprising considering that the neutral thermosphere is closely coupled to the F-region ionosphere via composition, winds, and electrodynamics, which can all play a significant role in the ionospheric variability. In fact, variations in the neutral density and the accompanying changes in the neutral winds, temperature, and composition, along with penetration electric fields induced by the transverse Alfvén waves in the CIR/HSS structures and disturbance dynamo electric fields, can modulate the F-region plasma densities by altering the chemical loss rates, the vertical transport, and the height of the ionospheric F-layer, and by redistributing the ionospheric plasma (e.g., Lei et al., 2008c). These more direct ways of modulating the ionosphere can thus explain in a straightforward manner most of the periodicities observed in the TEC spectra displayed in Figure 2.10.

The third column in Figure 2.10 shows the spectra of the mean $\Sigma O/N_2$ ratios at low, mid, and high latitudes in the northern and southern hemispheres. The most prominent periods in these spectra are at 6.75, 9, 10, 11.75, 13.5 days. These periodicities display a significant latitudinal dependency, with much larger amplitudes at high latitudes than at low latitudes in both hemispheres, and a significant hemispheric asymmetry with larger amplitudes in the northern hemisphere than in the southern hemisphere. It can also be noted that at high latitudes, the 9-day periodicity in $\Sigma O/N_2$ exhibits a seasonal variation with larger amplitudes in winter than in summer, which is different than the seasonal variation of the 9-day periodicity in TEC, which is stronger in summer than in winter. The 9-day oscillation in the $\Sigma O/N_2$ ratios correlates very well with similar variations in solar wind parameters and geomagnetic activity indices, but not with variations in F10.7. This basically demonstrates that the 9-day periodicity in $\Sigma O/N_2$ is most probably induced by recurrent geomagnetic activity and not by variations in the solar EUV flux.

It is also interesting to remark in Figure 2.10 that, due to seasonal differences in the TEC and $\Sigma O/N_2$ responses to recurrent geomagnetic activity, the 10-day period present in the spectra of the neutral density and of the Kp and Dst indices at the end of 2004-beginning of 2005, appears in the $\Sigma O/N_2$ spectra only at high and mid latitudes in the northern hemisphere, while in the TEC spectra, it appears only at high and mid latitudes in the southern hemisphere. However, the origin of the 10-day periodicity cannot be completely elucidated at this point as this periodicity does not appear as significant in the solar wind parameters.

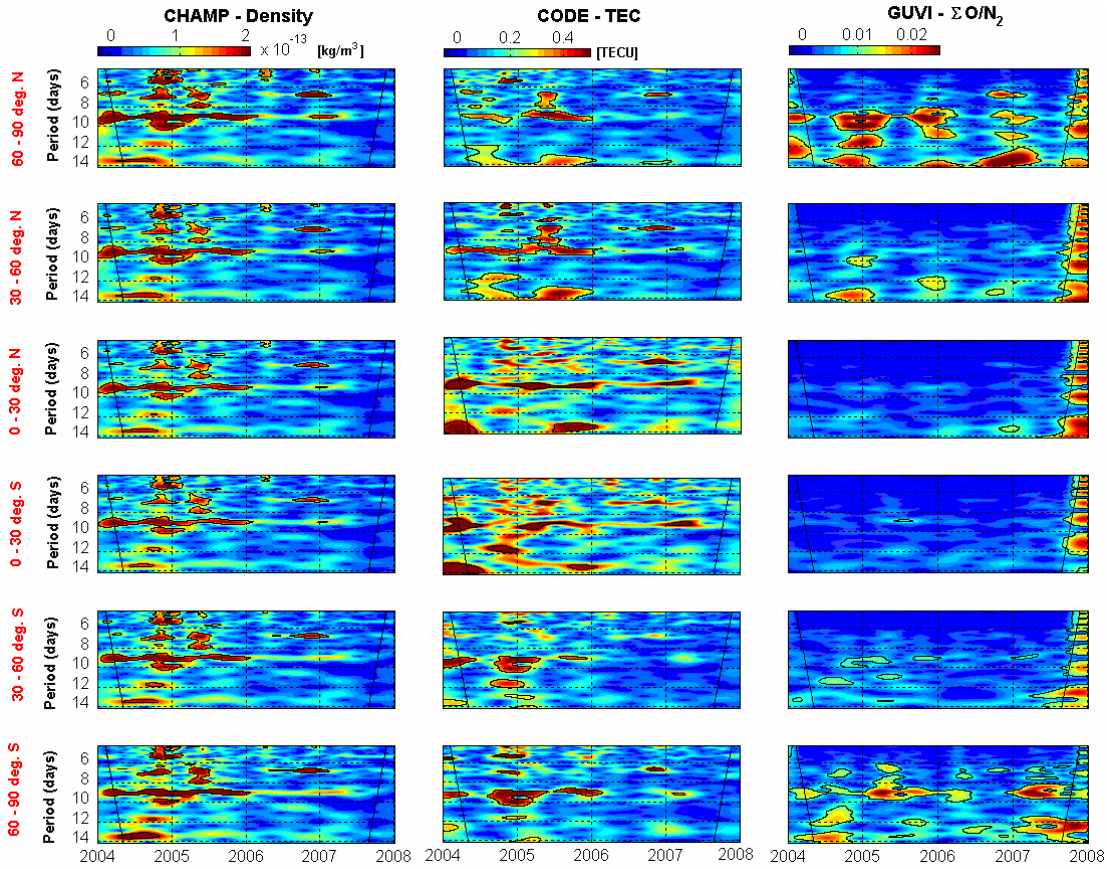

Figure 2.10: Wavelet amplitude spectra (ω_o=40) of the mean values of CHAMP neutral density, CODE-TEC, and GUVI Σ O/N_2 ratio at low (0^o-30^o), middle (30^o-60^o), and high (60^o-90^o) latitudes in the southern and northern hemispheres, over the 4-14 day period range, in 2004-2007.

2.8 Cross-wavelet Analyses between Ionospheric and Themospheric Parameters and Solar Wind Parameters and Geomagnetic Activity Indices

To investigate the correlations between the dominant periodicities in the ionospheric and thermospheric parameters and similar periodicities in the solar wind parameters and geomagnetic activity indices, we employed the cross-wavelet analysis technique presented earlier in this chapter. The cross-wavelet spectrum is a complex number. Here we use its magnitude to determine the similar periodicities that are

simultaneously present in two time series and to assess their significance in the cross-wavelet spectrum, and we use its phase to study the correlations between these periodicities. In all the cross-wavelet spectra presented here, the contour lines indicate the significant periodicities in the cross-wavelet spectrum, and the slant lines, at the edges, mark the cone of influence.

Figure 2.11 shows the absolute phases (values in the 0-π range) corresponding to the cross-wavelet spectra between (a) Kp (at 0000 UT) and (b) F10.7 and the mean values of (left) CHAMP neutral densities, (middle) CODE-TEC (at 0000 UT), and (right) GUVI $\Sigma O/N_2$ ratios, at low (0^o-30^o), middle (30^o-60^o), and high (60^o-90^o) latitudes in the southern and northern hemispheres, over the 4-14 day period range, during 2004-2007. It is clear from this figure that plotting the phase rather than the magnitude of a cross-wavelet spectrum provides an elegant and straightforward way to visualize the correlations between similar spectral components that are simultaneously present in two signals.

A visual inspection of Figure 2.11a reveals that the periodicities in the thermospheric density correlate very well with those in Kp at all latitudes, Kp being a proxy for the magnetospheric energy input. By contrast, the periodicities in the $\Sigma O/N_2$ ratios correlate well with those in Kp only at low latitudes, while at high and mid latitudes they are anti-correlated. On the other hand, the periodicities in TEC and Kp display quite complicated relationships, but in general they correlate relatively well at low latitudes and are anti-correlated at high latitudes. Our results are consistent with theoretical and observational studies of the response of the thermosphere-ionosphere system to geomagnetic storms (e.g., Burns et al., 1995; Mansilla, 2007; Crowley et

al., 2008), which indicate that an increase in the geomagnetic forcing produces a global increase in the thermospheric density and causes high-latitude depletions and low-latitude enhancements in the O/N_2 ratios and F-region plasma densities and TEC.

It is clear from our results that small and continuous changes in the geomagnetic forcing associated with recurrent geomagnetic activity have global effects, which are restricted not only to high latitudes but spread all over the globe, producing continuous changes in the neutral density, neutral composition, and TEC. While there are some similarities between the responses of the neutral density, neutral composition, and TEC to recurrent geomagnetic activity there are also significant differences. Specifically, the neutral density response appears to be global, with small differences between high and low latitudes, and well correlated with Kp. The $\Sigma O/N_2$ response, on the other hand, is much stronger at high latitudes than at low latitudes and is well correlated with Kp at low latitudes but anti-correlated at high and mid-latitudes. The TEC response is also anti-correlated with Kp at high latitudes and relatively well correlated with it at low latitudes. In the following, we discuss what could cause these differences.

During geomagnetic storms, enhanced high-latitude Joule and particle heating causes a rapid thermal expansion of the neutral atmosphere and drives significant vertical winds. Both the thermal expansion and the vertical winds lead to an increase in the neutral density at high latitudes, which is subsequently redistributed globally within about 3-4 hours (e.g., Crowley et al., 2008). However, because here we use only daily values of thermospheric densities, in Figures 2.10 and 2.11, the effect appears as “simultaneously” at all latitudes.

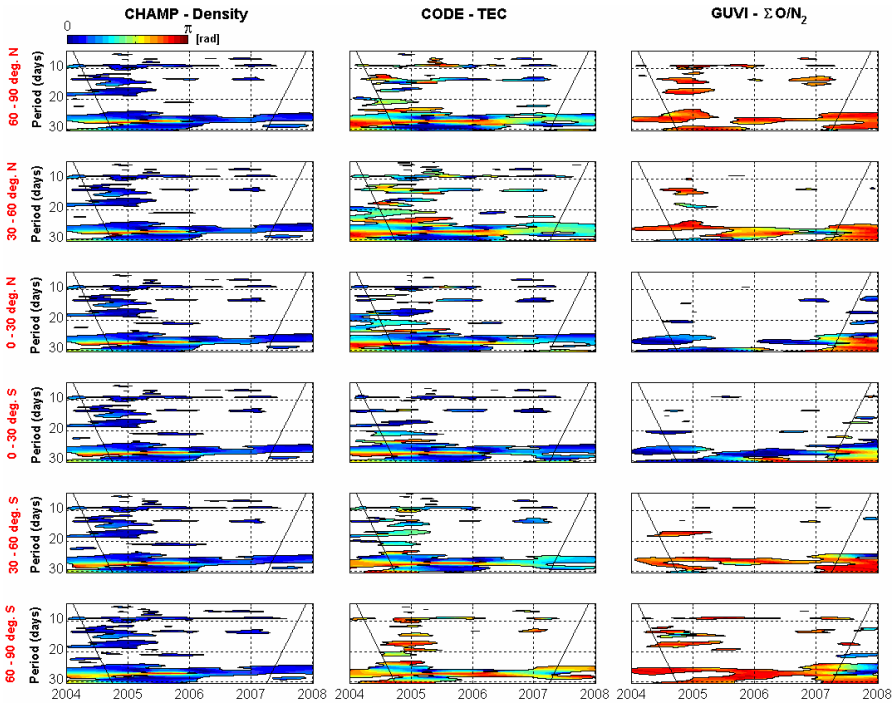

a.

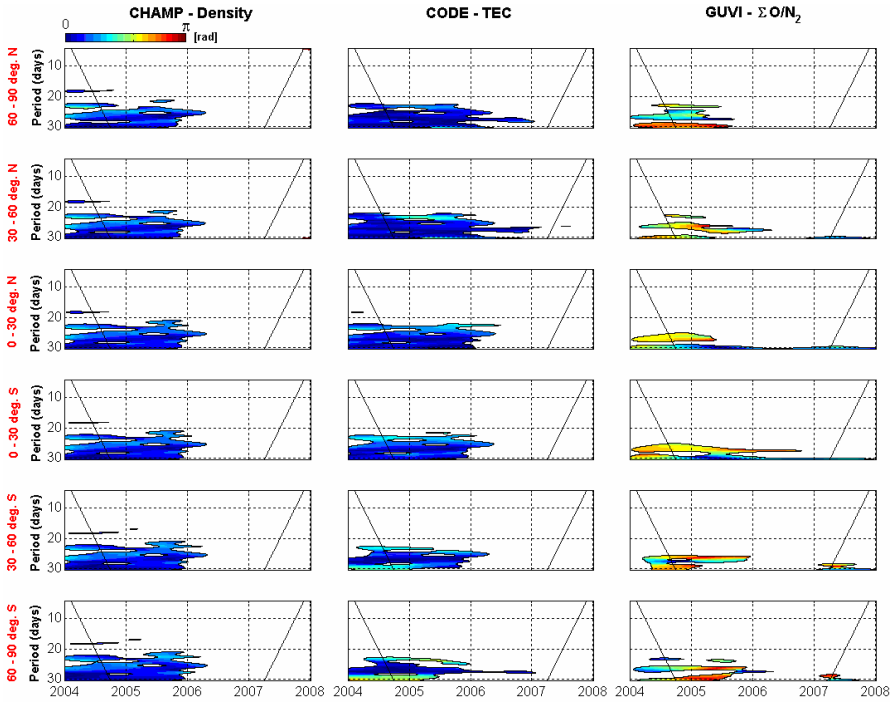

b.

Figure 2.11: Absolute phases of the cross-wavelet spectra (ω_o=40) between (a) Kp (at 0000 UT) and (b) F10.7 and the mean values of the (left) CHAMP neutral densities, (middle) TEC (at 0000 UT), and (right) GUVI $\Sigma O/N_2$ ratios, at low, middle, and high latitudes in the southern and northern hemispheres, over the 4-30 day period range, during 2004-2007.

While the thermal expansion does not cause significant changes in the $\Sigma O/N_2$ ratios, since both O and N_2 are equally affected by the increase in scale height, the upward vertical winds create a composition change of reduced O/N_2 ratio in the polar regions by carrying molecular-rich air across pressure levels to higher altitudes, the large parcels of heated gas from the lower thermosphere drastically altering both the neutral and ion compositions. Strong trans-polar winds then carry the uplifted parcels towards the nightside of the polar cap and out to mid latitudes, creating a disturbance zone in the midnight and early morning sector (e.g., Prölss, 1997).

As the storm progresses, the composition disturbance zone extends to lower latitudes and corotates onto the dayside, where the composition recovers diffusively. In an isolated storm event, the composition recovers on a timescale of several hours, but with continuous high-latitude forcing the recovery can last indefinitely. Also, as the geomagnetic forcing increases or decreases, the disturbance zone correspondingly extends to lower latitudes or retreats to higher latitudes. In addition, zonal winds that develop at mid-latitudes due to the Coriolis effects restrict the continuation of the equatorward winds driven by the high-latitude heating and reduce their divergence, limiting thus the buildup of the composition bulge of reduced O/N_2 ratio at these latitudes. Therefore, unlike the neutral density perturbations, the region of reduced $\Sigma O/N_2$ ratio is not a global effect and extends to equatorial latitudes only during large storms. At low latitudes, the rapid upward motion of the O^+ ions associated with enhanced zonal electric fields causes an increase in the electron density and, in turn, leads to an increase in the thermospheric density as a result of the ion-neutral drag (e.g., Mansilla et al., 2007). It can thus be concluded that the global response of the

neutral density to recurrent geomagnetic activity is the result of the cumulative effect of the thermal expansion and vertical winds, while the $\Sigma O/N_2$ response is the result of the vertical winds, which act mostly at high latitudes (e.g., Crowley et al., 2008).

In addition to recurrent geomagnetic forcing, variations in the solar EUV radiation can also affect the neutral and plasma densities. Figure 2.11b shows strong correlations between F10.7 and the neutral and plasma densities at periods near 27 days during 2004 and 2005, which suggests that the solar EUV radiation, for which F10.7 is a proxy, could be the main source of these periodicities. This is not surprising given that the thermosphere and ionosphere absorb solar EUV radiation and respond by increased neutral and plasma densities. The high correlations observed between the 27-day periodicities in F10.7 and neutral and plasma densities during 2004-2005 can then explain the reduced correlations observed in Figure 2.11a between the 27-day oscillations in Kp and neutral and plasma densities during the same time interval. However, further studies need to be conducted to determine the relative contributions of the recurrent geomagnetic forcing and solar EUV radiation in driving the 27-day oscillations in the neutral and plasma densities.

2.9 Cross-wavelet Analyses between dB and Different Solar Wind Parameters and Geomagnetic Activity Indices

As mentioned previously, during the declining and minimum phases of a solar cycle, the CIR/HSS structures fill much of the solar wind and are characterized by large amplitude Alfvén waves with highly-fluctuating Bz components, which play a

significant role in the weak-to-moderate recurrent geomagnetic activity at Earth. The Alfvén waves, known also as traveling magnetic waves, distinguish themselves by a high correlation between the magnetic field and velocity vectors, the sign of the correlation indicating their direction of propagation, parallel or anti-parallel to the magnetic field (e.g., Tsurutani et al., 1995; Prölss, 2004). In the solar wind, the Alfvén waves propagate predominantly radially away from the Sun along B, and are largely the evolved remnants of fluctuations that originate inside the point where the solar wind flow becomes Alfvénic. The Alfvénic fluctuations are also believed to contribute substantially to the heating and acceleration of the solar wind.

Calculated as the RMS variation of the underlying solar wind magnetic field vector over a 16-second time interval, the dB parameter describes more or less the strength of the Alfvénic fluctuations in the solar wind. We show here using the cross-wavelet analysis that this parameter correlates very well, over a large period band, with several solar wind parameters and with the Kp index. For this purpose, in Figure 2.12 are displayed the absolute phases of the cross-wavelet spectra between dB and different solar wind parameters and between dB and AE, Kp, Dst, and F10.7 indices, over the 4-30 day period range, during 2004-2007. It is clear from this figure that the dominant periodicities in dB correlate very well with similar periodicities in |B|, Vp, Tp, solar wind dynamic pressure (SWDP), and Kp, but are in general anti-correlated with similar periodicities in Dst.

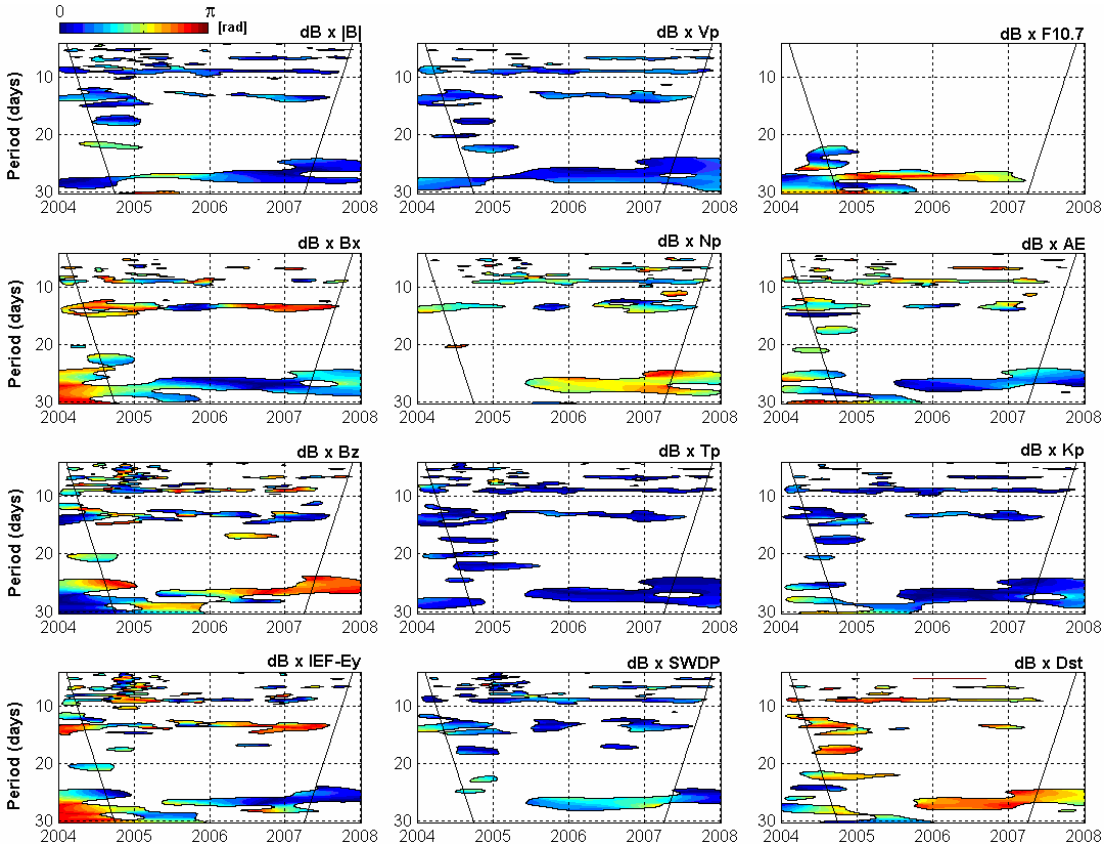

Figure 2.12: Absolute phases of the cross-wavelet spectra (ω_o=40) between dB and (left and middle columns) different solar wind parameters and (right column) different solar and geomagnetic activity indices, over the 4-30 day period range, during 2004-2007.

To better illustrate the excellent correlations between the periodicities in dB, Vp, Tp, and Kp, Figure 2.13 shows the normalized (amplitudes in the [-1,1] range) 27-day periodicities over the 2004-2007 interval, extracted from these parameters using the wavelet-based filtering technique described earlier in this chapter. The figure clearly shows that the four waves not only correlate very well, but also display similar amplitude modulations over the entire time interval. Our results thus indicate that dB could be an excellent candidate for predicting the magnetospheric response to varying interplanetary conditions, and hence for describing the solar wind-magnetosphere interactions. Furthermore, having in view that dB correlates very well

with the thermospheric densities at all latitudes and with the ionospheric TEC at equatorial latitudes, we suggest that dB could be an important parameter for predicting the behavior of the thermosphere-ionosphere system in response to recurrent geomagnetic activity.

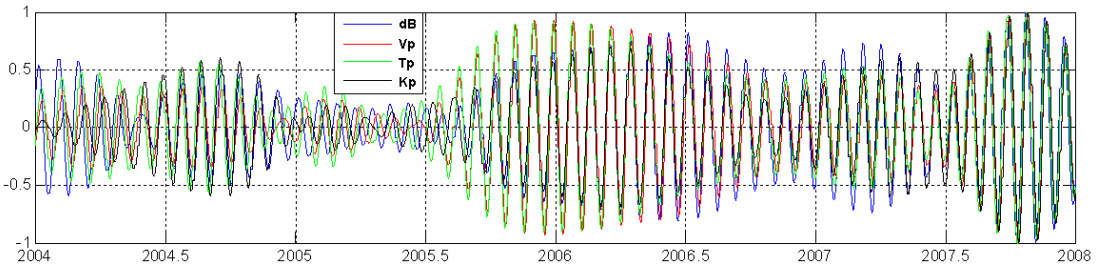

Figure 2.13: Normalized 27-day periodicities in dB, Vp, Tp, and Kp, for 2004-2007.

2.10 The Origin of the Short-period Oscillations in the Solar Wind Parameters

Several studies have reported the presence of multi-day periodic fluctuations in different solar wind parameters and geomagnetic activity indices (e.g., Hauska et al., 1973; Verma and Joshi, 1994; Nayar et al., 2001), but far too little has been done to investigate their underlying physical mechanisms. It is in general assumed that the multi-day periodic oscillations in the solar wind parameters are primarily caused by complex magnetic features on the solar surface, with a certain spatial distribution, that are passed on to the interplanetary medium as temporal variations due to solar rotation and outflow of solar wind (e.g., Nayar et al., 2001).

During the second half of the declining phase of a solar cycle, the CHs are among the most important magnetic structures of the solar corona and are typically situated near the polar caps, presenting some tongue-like extensions to equatorial

latitudes. The streamer belt is confined at low heliospheric latitudes and forms a warped separatrix between magnetic field lines of opposite polarity that open into the interplanetary space carrying an electric current, known as the heliospheric current sheet (Figure 2.4a). Near solar minimum, the streamer belt narrows and the heliospheric current sheet loses its warps becoming flat in close alignment with the solar equatorial plane.

Previous studies (e.g., Nayar et al., 2001, Emery et al., 2009) have suggested that the multi-day periodicities in the solar wind parameters are associated with the evolution of the warping of the heliospheric current sheet, itself modulated by the spatial distribution of the CHs on the solar surface. Typically, there are two CHs of opposite polarity that give rise to a two-stream magnetic sector structure in the ecliptic plane. The two-stream structure produces magnetic disturbances on Earth that recur every 13.5 and 27 days (e.g., Emery et al., 2009). When there are more than two CHs, the magnetic sector structure in the solar wind becomes more complex and produces geomagnetic disturbances that recur more often.

The spatial distribution of the CHs has been shown to depend on the underlying large-scale patterns of the coronal magnetic field, which are related to regions of “giant convective cells” (e.g., Temmer et al., 2007). Thus, the convection layer which completes the transport of energy from the nuclear furnace at the center of the Sun to its radiation into space by the photosphere is considered responsible for setting the temporal and spatial scales of the coronal magnetic field structure, which in turn control the properties of the solar wind (e.g., Russell, 2001).

Recently, Temmer et al. (2007) related in a straightforward manner the periodic longitudinal distribution of three CHs to a 9-day periodic modulation of the solar wind speed, for a time interval in 2005. Lei et al. (2008b) re-examined the relationship between the longitudinal distribution of the CHs and the 9-day periodicity in the solar wind and geomagnetic activity over the same time interval. They suggested that, in addition to the spatial distribution of the CHs, other sources are also required to explain the presence of the 9-day periodicity in the solar wind and geomagnetic activity.

The results reported earlier in this chapter indicate that the 5.4, 6.75, 9, and 13.5-day periods in the solar wind and geomagnetic activity, which appear as exact fractions of the solar rotation period, have specific temporal evolutions in each solar wind parameter and their occurrence is not restricted to the declining and minimum phases of a solar cycle, when the CHs are important features of the solar corona. These results also seem to suggest that, although stable CH patterns can explain in a straightforward manner the presence of the multi-day periodicities in the solar wind and geomagnetic activity, other processes may be also involved.

It has been shown that in addition to large amplitude transverse Alfvénic fluctuations, low intensity mirror modes, presumably generated from a local instability driven by compression of the high-speed solar wind plasma, and other modes, generated by wave-shock interactions between fast and slow flows and even transients, have been also observed in the CIR/HSS solar wind structures (Tsurutani et al., 1995). We therefore suggest that nonlinear interaction processes, as well as turbulent features and instabilities in the solar wind, associated with the compression

of the high-speed solar wind plasma and wave-shock interactions, may be also responsible for the presence of multi-day periodicities in the solar wind.

To test our hypothesis and examine the nonlinear effects in the solar wind, we use the wavelet-based bispectral analysis technique presented earlier in this chapter. The method allows one to detect phase-coherent couplings between spectral components in non-Gaussian and non-stationary signals, and to track the temporal evolution of the couplings. In general, the phase-coherent couplings in a signal are mainly caused by nonlinear interactions between the spectral components. We remind the reader that a non-zero value at the tuple $\{T_1,T_2\}$ in a bispectrum is an indicator of phase-coherent couplings between modes with characteristic periods T_1 and T_2, but it does not reveal anything about the physical nature or the origin of the couplings.

Investigations of the solar wind using bispectral analysis are rather sparse, and to our knowledge this is actually the first time the wavelet bispectral analysis, in the form presented here, has been applied to study the origin of the multi-day periodicities in the solar wind parameters. For our studies, we applied the wavelet bispectral analysis to the following solar wind parameters: |B|, Bx, and Vp. The purpose of this analysis is to detect the phase-coherent couplings between the multi-day periodicities in each considered parameter and to investigate whether or not some of the periodicities are caused, at least partially, by nonlinear processes.

The left column of Figure 2.14 shows, from top to bottom, the wavelet amplitude spectra (ω_o=40) of the |B|, Bx, and Vp parameters (at 0000 UT) over the 4-30 day period range, during 2004-2007. It is clear from this figure, that all four wavelet spectra display significant 5.4, 6.75, 9, 13.5, and 27-day periodicities. One

way to determine if there are any phase-coherent couplings between these harmonics is to calculate the wavelet bispectrum for each parameter. The normalized magnitudes, values between 0 (dark blue) and 1 (red), of the wavelet bispectra calculated from the three wavelet spectra for 1 January 2005, 2006, and 2007, for periods in the 4-30 day range, are shown in the last three columns of Figure 2.14.

In order to interpret these bispectra, we assume that a non-zero point in a bispectrum is indicative of a quadratic nonlinear coupling between two waves with periods corresponding to the coordinates of that point, and that the value of that point is proportional to the strength of the coupling between the two waves. It is also noteworthy that a bispectrum is symmetric with respect to the main diagonal. The main diagonal terms are indicative of harmonic generation processes, $\{T_1,T_1\}\rightarrow T_1/2$, while the off-diagonal terms are indicative of more general phase-coherent couplings, $\{T_1,T_2\}\rightarrow T_1T_2/(T_1+T_2)$.

It can be remarked in the bispectra shown in Figure 2.14 that there are several points with non-zero values, including (27, 27), (27, 13.5), (27, 9), (13.5, 13.5), and (13.5, 9). This thus proves that the 5.4, 6.75, 9, and 13.5-day periodicities in the solar wind parameters could be generated, at least partially, through nonlinear interaction processes. In addition, the fact that the values in the bispectra display specific temporal evolutions indicates that these nonlinear couplings evolve in time. It then remains to be established what is the relative contribution of the nonlinear interaction processes to the generation of these periodicities, but this is beyond the scope of our current studies. It is though possible that the bispectral values might be a good starting point for this purpose, and we plan to explore this idea in future studies.

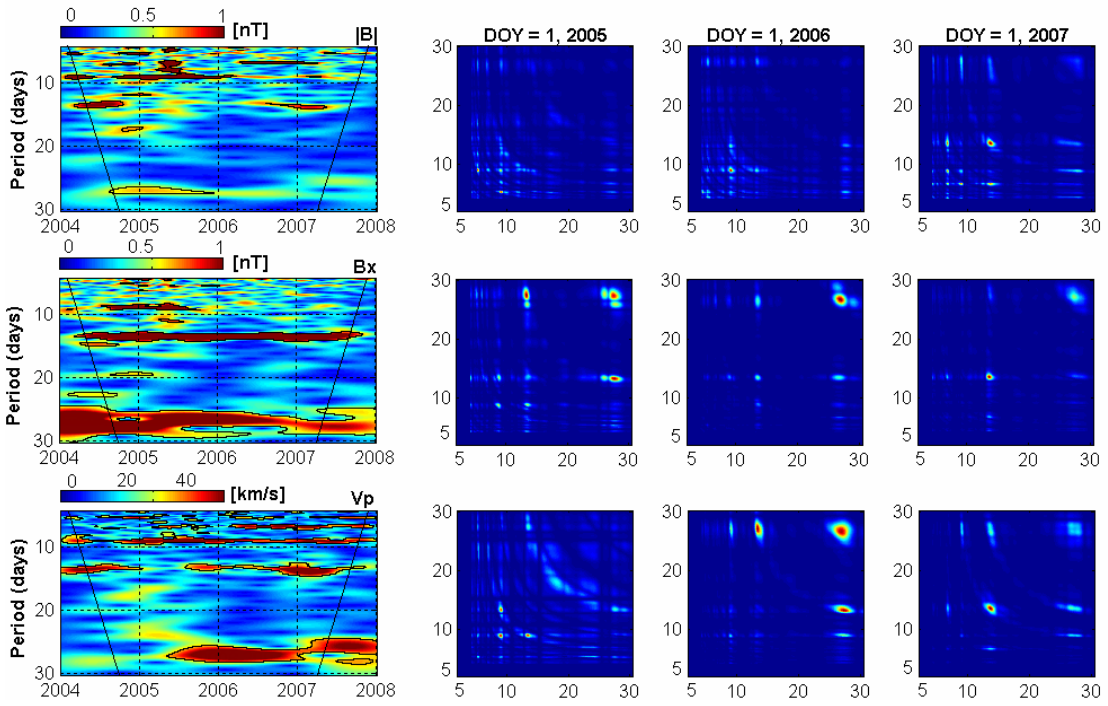

Figure 2.14: (left) Wavelet amplitude spectra (ω_o=40) of the |B|, Bx, and Vp parameters for the 4-30 day period range, during 2004-2007, and (right) their corresponding bispectra (ω_o=40) for 1 January 2005, 2006, and 2007, over the 4-30 day period range.

2.11 Conclusions

Several datasets have been used to study the multi-day periodic oscillations in the solar wind, geomagnetic activity, and thermosphere-ionosphere system using different wavelet-based analysis techniques. We have shown that dominant oscillations with periods of 5.4, 6.75, 9, and 13.5 days occur frequently in the thermosphere density, ionospheric TEC, and $\Sigma O/N_2$ ratios during 2004-2007, and correlate very well with similar periodicities in the geomagnetic activity indices and solar wind parameters. Overall, our results strongly support the idea placed forward by Mlynczak et al. (2008), Lei et al. (2008a,b,c), Thayer et al. (2008), and Crowley et

al. (2008), of the existence of a strong solar-terrestrial connection between rotating solar coronal holes, solar wind, recurrent geomagnetic activity, and periodic fluctuations in the thermosphere-ionosphere system.

There are several important implications of our work. First, the wavelet-based techniques developed here form a set of very powerful spectral analysis tools that can be used to study the periodic features in non-stationary signals and examine their temporal evolution. Then, the periodic nature of the connection determined between solar coronal holes, solar wind, geomagnetic activity, and thermosphere-ionosphere system suggests some element of predictability, and can be used to investigate and predict the behavior of the thermosphere-ionosphere system and to identify and isolate its energy sources (solar, geomagnetic, meteorological). This may have important advantages for various communication, navigation, and surveillance applications that require accurate predictions of the state of the ionosphere.

In addition, our results provide valuable information about the periodic behavior of the thermosphere-ionosphere system, which can be used to improve and validate the existing coupled magnetosphere-thermosphere-ionosphere models and to test their ability to replicate the observed variability. Furthermore, our bispectral analysis results suggest that the periodic oscillations in the solar wind parameters, mostly rooted in rigidly rotating solar coronal holes, may also originate from nonlinear processes taking place in the solar wind, probably as a result of compression of the high-speed solar wind plasma and wave-shock interactions.

Our results also indicate that, although the CIR/HSS-driven storms are in general characterized by weak-to-moderate geomagnetic activity levels, due to their

recurrent nature and characteristic long recovery phases that can last for several days or weeks, they can produce a significant cumulative effect on the state of the thermosphere-ionosphere system. Finally, we also need to mention that additional data sources and model simulations are required to examine the processes at play in modifying the state of the thermosphere-ionosphere system in response to recurrent geomagnetic activity and to evaluate the relative contribution of the periodicities in the neutral density, neutral composition, neutral temperature, neutral winds, and electric fields associated with recurrent geomagnetic activity in driving periodic oscillations in ionosphere.

Chapter 3

Drift-Net: Neural Network-based Algorithms for Estimating the Daytime, Equatorial Vertical ExB drift Velocities from Ground-based Magnetometer Observations

3.1 Background

Recent studies (e.g., Anderson et al., 2002) have demonstrated that realistic daytime, equatorial vertical ExB plasma drifts can be accurately inferred on a day-to-day basis from the difference in the horizontal H component, ΔH, between a magnetometer placed on the magnetic equator and one displaced 6 to 9 degrees away (e.g., Kane, 1973; Yacob, 1977; Gonzales et al., 1979; Rastogi and Klobuchar 1990). Since during daytime the magnetometers respond to both ionospheric currents and remote currents, carrying out this subtraction is necessary in order to separate the equatorial electrojet (EEJ) contribution to the horizontal H component. The resulting ΔH then provides a direct measure of the EEJ and, hence, of the vertical ExB plasma drifts in the ionospheric F-region.

Using different approaches based on linear least-squares regression analysis and neural networks, Anderson et al. (2004, 2006a) established quantitative relationships between ΔH observations and vertical ExB drift velocities at the Peruvian longitude sector. They showed that the same relationships can be applied to estimate the vertical ExB drifts at any longitude where appropriately-placed magnetometers exist. In addition, Anghel et al. (2007) suggested that it is also possible to establish quantitative relationships between H component observations and vertical ExB drifts at Jicamarca, Peru, which eventually can be used to estimate the vertical drifts at other longitude sectors.

Expanding on these previous studies, in this chapter, we present several least-squares regression and neural network-based algorithms, named collectively Drift-Net, developed for estimating the daytime, equatorial vertical ExB drifts and the corresponding zonal electric fields from magnetometer observations. The algorithms were developed by combining vertical drift observations from Jicamarca Unattended Long-term Ionosphere Atmosphere (JULIA) radar and Jicamarca Incoherent Scatter Radar (ISR), with magnetometer H component observations from Jicamarca and Piura, Peru, available between November 2000 and February 2009. In this chapter, we also present vertical ExB drifts obtained by applying the Drift-Net algorithms to magnetometer data collected by stations located in India, Philippines, and Indonesia.

As a first step towards validating our results, we compare the quiet-time magnetometer-inferred drift patterns with drift patterns predicted by the global drift model developed by Scherliess and Fejer (1999) at the four sites, for three seasons. In addition, since under certain conditions the time variability in the interplanetary

electric field (IEF) (minutes to hours) should be reflected in the low-latitude penetration electric fields, we also study the storm-driven penetration effects by examining the relationships between variations in the dawn-to-dusk component of the IEF, IEF-Ey, and those in the daytime, equatorial zonal electric fields, Ey, under disturbed geomagnetic conditions characterized by daily Ap values greater than 20. The zonal electric fields are obtained from vertical ExB drifts knowing that 1 mV/m corresponds to a vertical drift of ~40 m/s in the Peruvian sector, ~28 m/s in the Philippine sector, and ~20 m/s in the Indian sector.

Specific questions that will be addressed are: (1) how well the quiet-time magnetometer-inferred ExB drifts compare with the drifts predicted by the Fejer-Scherliess model at the four longitude sectors, and (2) what are the relationships between the IEF-Ey and the equatorial zonal electric fields Ey during disturbed conditions? Before proceeding to describing our methods and presenting our results, we first review some theoretical aspects regarding the sources of ionospheric electric fields and the low-latitude electrodynamics.

3.2 Theoretical Considerations

3.2.1 Sources of Ionospheric Electric Fields and Currents

The primary sources of electric fields in the ionosphere have been identified as: (1) the neutral winds which blow across the magnetic field lines and generate electric fields through the E and F-region dynamo mechanisms, (2) the interaction

between the solar wind and Earth's magnetic field which drives the magnetospheric plasma into a large-scale convection pattern and produce a plasma motion equivalent to an ExB drift, and (3) the Earth's rotation which induces corotational electric fields in a reference frame that does not rotate with the Earth.

The neutral winds result from the diurnal varying solar heating, upward propagating atmospheric waves, and Ampere force (JxB) and Joule heating (J·E) caused by electric current flows, especially at high latitudes. The Ampere force is the sum of the Lorentz forces on ions and electrons that are transmitted to the neutrals through collisions. Under quiet conditions and in the rotating reference frame of the Earth, the dynamo-driven electric fields are dominant at geomagnetic latitudes lower than about 60^{o}, while the convection electric fields are dominant at higher latitudes.

At high latitudes, the geomagnetic field lines are nearly vertical and the ionospheric currents are joined by field-aligned currents flowing along the geomagnetic field lines into magnetosphere. At these latitudes, the electrodynamics is thus strongly dominated by magnetospheric processes and the total current flow is of the order of 10^{7}A. Associated with these currents are strong nearly horizontal electric fields of the order of several tens of mV/m or more and an electric potential of about 20-200 kV, with a high on the morning side and a low on the evening side. However, the strength and the pattern of the high-latitude potential are strongly dependent on the direction and strength of the interplanetary magnetic field (IMF).

At low and mid latitudes, owing to an increased daytime E-region conductivity, the solar tidal winds cause currents to flow in the 100-130 km altitude region, where the electron mobility is much larger than the ion mobility. This is the

so-called solar quiet (Sq) current system. As shown in Figure 3.1, taken from from http://geomag.usgs.gov/images/ionospheric_current.jpg, the Sq current system is spread within the $\pm 60^{o}$ geomagnetic latitude range and presents two current vortices on the sunlit side of the Earth, counterclockwise in the northern hemisphere and clockwise in the southern hemisphere, with centers at about $\pm 30^{o}$ dip latitudes. The total current flow in each vortex is of the order of 10^{5} A, and the associated electric fields have typical values of a few mV/m during quiet periods. At equatorial latitudes, the two current vortices produce an intense eastward current that flows within a narrow latitudinal band along the dip equator, the EEJ. The two hemispheres are also electrically coupled by currents flowing along the magnetic field lines whenever there is an imbalance in the dynamo forcing between the two hemispheres.

The global characteristics of the Sq current system are in general derived from its magnetic signature on the ground. During quiet times, the Sq magnetic perturbations are of the order of 30 nT at mid-latitudes and display local time, day-to-day, seasonal, and solar cycle variations. They are stronger at solar maximum than at solar minimum due to an increased ionospheric conductivity and stronger atmospheric winds at sunspot maximum. It is also noteworthy that due to the fact that the F-region conductivity is low, the corresponding currents are also very small for their effects to be observed on the ground, such that the ground magnetic perturbations are in general associated with the Sq currents.

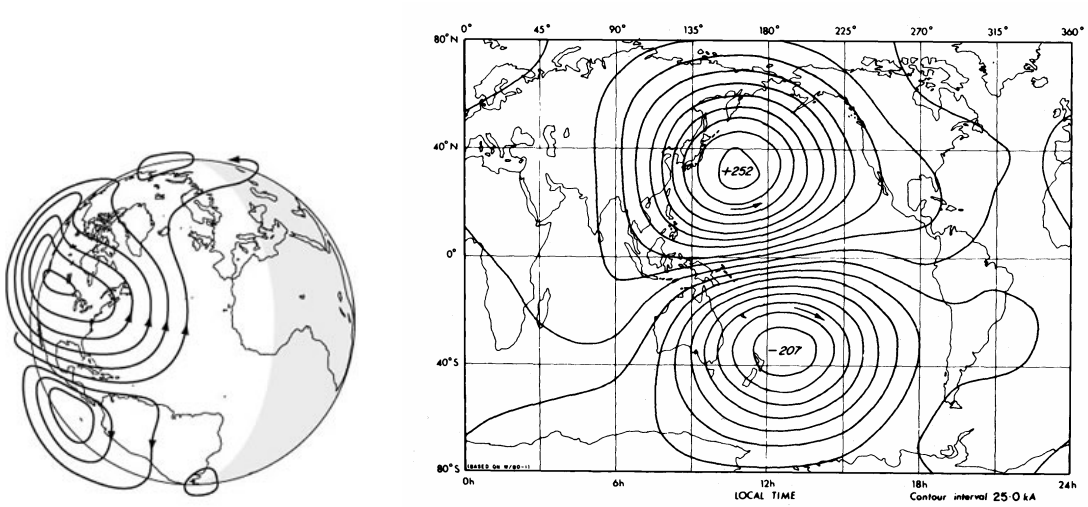

Figure 3.1: Ionospheric currents flowing in the 100-130 km altitude range.

3.2.2 Low-latitude Electrodynamics

At low latitudes, the F-region plasma distribution is determined by the combined physical processes of (1) production by solar EUV radiation, (2) loss through charge exchange with N_2 and O_2, and (3) transport parallel and perpendicular to the geomagnetic field lines by diffusion and neutral winds and respectively by ExB drifts (Anderson et al., 2002). Figure 3.2 shows a schematic diagram of the F-region transport processes in a plane perpendicular to the Earth's surface and along the geomagnetic field lines. As illustrated in this figure, the upward plasma transport, caused by the dayside electrodynamics, and forces parallel to geomagnetic field lines, due to gravity and plasma pressure gradients, produce a plasma "fountain effect" responsible for the development and evolution of the equatorial ionization anomaly (EIA). The EIA consists of ionization crests on either side of the magnetic equator at about $\pm 18^{o}$ dip latitudes. At times, the ionization crests display asymmetries as a

result of the trans-equatorial neutral winds that transport the ionization from one hemisphere to the other (e.g., Tascione, 1994; Anderson et al., 2002).

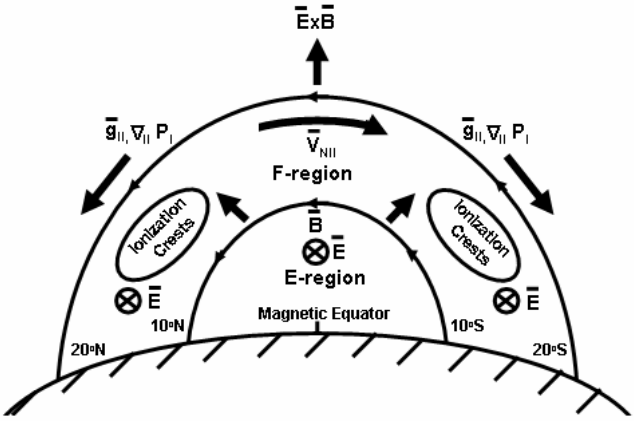

Figure 3.2: Schematic diagram of the daytime F-region ionization transport processes. The forces parallel to B are due to gravity, pressure gradients, and collisions with neutrals, while the forces perpendicular to B are due to the ExB drifts.

The morphology and dynamics of the low-latitude ionosphere are primarily controlled by electrodynamics. During quiet times, the E and F region dynamo processes produce electric fields which are transmitted unaltered along the highly-conductive magnetic field lines, with the E-region dynamo being more effective during daytime and the F-region dynamo being more effective at nighttime and around sunset and sunrise (e.g., Heelis, 2004). The net result is: (1) an eastward electric field during daytime responsible for the formation of the EEJ at E-region heights and of the upward ExB plasma drifts at F-region heights, and for the development and evolution of the EIA, (2) a westward electric field during nighttime responsible for the formation of the downward F-region plasma drifts, and (3) a prereversal enhancement of the F-region vertical ExB drifts near sunset and sunrise.

During disturbed geomagnetic periods, the low-latitude electric fields are significantly altered by high-latitude magnetospheric convection electric fields that penetrate instantaneously to low latitudes (e.g., Fejer et al., 1990) and by disturbance dynamo electric fields caused by drastic changes in the global thermospheric winds as a result of enhanced energy deposition at high latitudes (e.g., Blanc and Richmond, 1980; Fejer and Scherliess, 1995, 1997).

Typically, under quiet geophysical conditions, the daytime equatorial zonal electric field Ey is about 0.5 mV/m and drives an eastward Pederson current along the dip equator. In addition, at equatorial latitudes, where the geomagnetic field lines are horizontal, the eastward electric field in combination with the geomagnetic field drives a downward Hall current at E-region heights, as in this region the electrons drift upward and the ions are locked into the neutral gas. Since the E-region conductivity is bounded in the vertical direction, an upward polarization electric field Ez is established in this region. This vertical electric field is about 5-10 times stronger than the eastward electric field that generated it and drives an eastward Hall current that augments the original Pederson current, producing an increase of the E-region conductivity in the eastward direction. The combined Pederson and Hall conductivity is known as direct or Cowling conductivity and maximizes at E-region heights. At latitudes just off the magnetic equator, the slight tilt of the magnetic field lines allows the polarization charges to drain, significantly reducing the Cowling conductivity (e.g., Tascione, 1994, Schunk and Nagy, 2000; Forbes, 1981; Onwumechili, 1997).

Therefore, the unique horizontal configuration of the geomagnetic field lines at the dip equator favors an abnormal increase of the E-region conductivity and the

formation of the EEJ, which consists of the eastward Pederson and Hall currents. The EEJ is an intense eastward current with a peak current density of the order of 10^{-5} A/m^2. It flows in the 100-120 km altitude region, within a $\pm 2^o$ latitudinal band above the magnetic equator, on the sunlit side of the Earth. A schematic diagram of the EEJ electric fields and current systems is shown in Figure 3.3a, taken from Anderson et al. (2002). While mostly eastward, the EEJ can change its direction during both quiet and disturbed conditions. The rapid reversals during disturbed periods are primarily attributed to magnetospherically-driven changes in the ionosphere, while the quiet time reversals are mainly due to lunar-driven atmospheric tides. Several studies have investigated the EEJ using ground-based, sounding rocket, and low-orbiting satellite observations, and a variaty of EEJ models have been developed (e.g., Forbes, 1981; Reddy, 1989; Richmond, 1989).

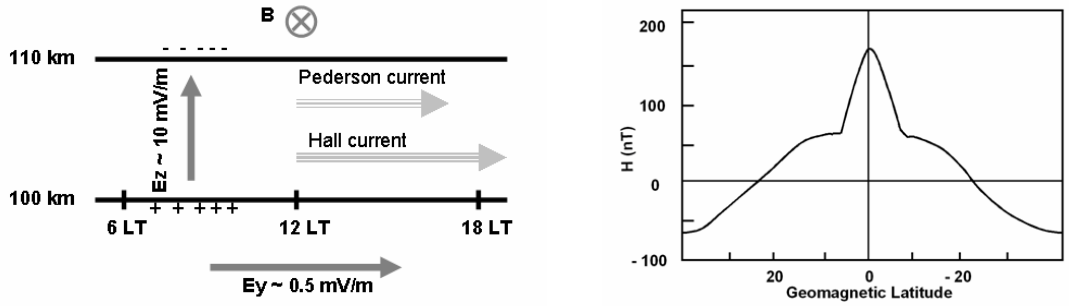

a. b.

Figure 3.3: (a) Schematic of the EEJ electric fields and current systems, and (b) the latitudinal profile of the noontime H component (from Anderson et al., 2002).

Near the geomagnetic equator, the EEJ produces a strong enhancement in the horizontal H component of the Earth's magnetic field, with a peak of ~100 nT around the local noon. Figure 3.3b illustrates a typical latitudinal profile of the noontime H

component, where the magnetic signature of the EEJ can be clearly observed near the dip equator. While the strength of the EEJ is directly proportional to the magnitude of the magnetic field perturbation it produces, interpreting the daytime magnetometer observations is a difficult task since magnetometers respond to both ionospheric currents and remote currents, such as the ring current and magnetopause current. Several studies though have indicated that the strength of the EEJ can be determined by calculating the difference in the horizontal H component, ΔH, between a magnetometer placed on the magnetic equator and one displaced a few degrees away (e.g., Kane, 1973; Yacob, 1977; Gonzales et al., 1979; Rastogi and Klobuchar, 1990; Doumouya et al., 1997; Alex and Mukherjee, 2001; Anderson et al., 2002; Manoj et al., 2006). This procedure is necessary in order to eliminate the contributions in H due to the Sq field and remote currents. The resulting ΔH is then related only to the EEJ, and hence to the equatorial zonal electric field that generated it, and provides a direct measure of the EEJ and of the F-region vertical ExB drifts.

As mentioned previously, at equatorial latitudes, the daytime zonal electric field drives both the EEJ at E-region heights and the F-region vertical ExB plasma drifts. The relative efficiency with which the EEJ and the vertical ExB drifts are driven varies with the time of the day, from day-to-day, with season, solar cycle, and longitude, and during periods of enhanced geomagnetic activity, it is strongly affected by magnetospheric and ionospheric disturbance dynamo effects.

For a steady magnetosphere, the low and mid-latitude ionosphere is shielded from the high-latitude magnetospheric convection electric fields by polarization charges in the Alfvén layer at the inner edge of the ring current (e.g., e.g., Wolf,

1975; Sakharov et al., 1989). However, during disturbed periods, sudden increases in the convection electric field, associated with sudden southward turnings of the Bz component of the IMF, IMF-Bz, cause the polarization charges in the Alfvén layer to get temporarily out of balance. In this case, the high-latitude dawn-to-dusk electric field can leak through the shielding layer and propagate instantaneously to equatorial latitudes until a shielding dusk-to-dawn electric field has time to develop in the inner magnetosphere, a process known as undershielding. When the convection electric field decreases, due to a sudden northward turning of the IMF-Bz, the shielding dusk-to-dawn electric field can promptly penetrate to equatorial latitudes until the shielding layer readjusts, a process termed overshielding.

Besides fast-propagating electric field perturbations caused by sudden changes in the high-latitude convection electric fields, delayed electric field perturbations that lag the auroral inputs by several hours are produced at low latitudes during disturbed periods as a result of drastic changes in the thermospheric neutral winds. The disturbed neutral winds affect both the E and F-region dynamo processes and, consequently, alter the normal electric field patterns of the equatorial ionosphere, producing predominantly westward electric field perturbations on the dayside and eastward electric field perturbations on the nightside. It is thus clear that both the penetration and disturbance dynamo mechanisms play a crucial role in modifying the electrical structure of the equatorial ionosphere during storm times.

3.3 Data Sets and Methodology

3.3.1 Data Sets

Several algorithms based on least-squares regression analysis and neural networks were developed for estimating the equatorial vertical ExB drifts from ground magnetometer observations. To determine the regression coefficients and to train the neural networks, we used vertical ExB drifts measured by the Jicamarca ISR and JULIA radars between November 2000 and February 2009, and magnetometer H component observations from Jicamarca (11.92^{o}S, 76.87^{o}W, geom. 0.8^{o}N) and Piura (5.18^{o}S, 80.64^{o}W, geom. 6.8^{o}N), Peru, at a 5-minute temporal resolution.

Like in Anghel et al. (2007), the input parameters to the neural networks are: year, day of the year (DOY), F10.7 cm flux value, 90-day average F10.7 cm flux (F10.7A), daily Ap, interpolated 3-hourly kp, local time (LT), ΔH or H, and solar zenith angle (SZA). Because only Peruvian data were used for training the neural networks, the SZA was included as an input to the networks in order to account for the seasonal variations attributed to the displacement between the geographic and geomagnetic equators. The SZA is the Sun's angular distance from the vertical, calculated based on the geographic latitude of the site, declination angle, and hour angle, and depends on season and local time.

To test the algorithms at other longitude sectors, we used magnetometer observations, at a 5-minute temporal resolution, from stations in Philippines, Indonesia, and India. At the Philippine sector, the magnetometer observations were

obtained from Davao (7°N, 125.4°E, geom. 1.32°S) and Muntinlupa (14.37°N, 121.02°E, geom. 6.39°N), at Indonesian longitudes, from Yap (9.50°N, 138.08°E, geom. 1.49°N) and Biak (-1.08°, 136.05°, geom. 9.73°S) (Yumoto, 2001), and at the Indian sector, from Thirunelveli (8.7°N, 76.9°E, geom. 0.5°S) and Alibag (18.6°N, 72.9°E, geom. 10°N).

The procedure to calculate ΔH is detailed in Anderson et al. (2002). Specifically, at any longitude where two appropriately placed magnetometers exist, one on the magnetic equator and the other displaced 6°-9° away, the nighttime baselines calculated as a 10-hour average between 1900 and 0500 LT are first determined at each station and then subtracted from the daytime values. These latter values are then further subtracted between the two stations to obtain the ΔH values.

To describe the interplanetary conditions, we used 64-second averages of merged ACE MAG-SWEPAM Level 2 interplanetary magnetic field and solar wind velocity data. The magnetic field experiment MAG on the ACE satellite provides continuous measurements of the local magnetic field in the interplanetary medium, and the solar wind experiment SWEPAM on ACE provides solar wind velocities. The two measurements are used to calculate the dawn-to-dusk component of the IEF (in GSM coordinates), IEF-Ey = $-V_x x B_z$, which can promptly penetrate to equatorial latitudes, during storm times, until a shielding dusk-to-dawn electric field has time to develop in the inner magnetosphere. To analyze the storm-driven penetration effects at equatorial latitudes, we time-shifted the IEF-Ey measured at the spacecraft using the solar wind velocity and added a 10-minute time delay.

3.3.2 Multilayer Feedforward Neural Networks (MLFF-NN)

The multilayer feedforward neural networks (MLFF-NN) are a particular class of neural networks with powerful function-approximation capabilities (e.g., Masters, 1993; Haykin, 1994; Bishop, 1995; Demuth and Beale, 2001). They are widely used in mapping, modeling, regression analysis, pattern recognition, classification, control, and several other types of applications. A multilayer network consists of a set of processing units called neurons which are logically arranged into two or more layers, with the layers being interconnected through a set of weights. There is an input layer and an output layer, each containing at least one neuron, and there are usually one or more hidden layers sandwiched between the input and output layers. The nodes of the input layer are passive, which means that they do not modify the data. They receive a single value on their input, and duplicate the value to their multiple outputs. In comparison, the nodes of the hidden and output layers are active, which means that they modify the data and have associated a nonlinear activation function.

Due to their distributed form of processing, these structures are able to learn highly nonlinear mappings between the input and output spaces. In general, a network with one hidden layer can learn most types of mappings, while a network with two hidden layers can also learn discontinuous mappings and is considered a universal function approximator. It is usually recommended that if any of the nonlinearities between inputs and outputs are known in advance, then a functional link network should be employed in order to improve the learning process.

The neural networks store information within the weights on the connection links. Therefore, training a network consists in adjusting the weights according to a learning algorithm. A MLFF-NN is trained in a supervised way in the sense that several training samples, consisting of a set of inputs and the corresponding desired outputs, are used as exemplars and presented to the network. For training, a subset of the original training set is selected randomly and presented to the network. After all the samples from the selected subset are presented to the network, the weights are adjusted according to a learning algorithm in order to minimize the mean-square error (MSE) between the outputs predicted by the network and the desired outputs. Thus, a learning algorithm uses the training samples to calculate an optimized set of weights based on the statistics of the exemplars. One pass through the subset of training samples along with an update of the weights is called an epoch, and the number of samples in the subset is called the epoch size. The learning and generalization capabilities of MLFF-NNs are impressive. In general, few hidden neurons are required and with proper design of the network architecture and of the training set, the training time is manageable.

3.4 Estimating the Equatorial Vertical ExB Drifts at the Peruvian Longitude Sector

In this section, we present the Drift-Net algorithms and provide analytical formulas, derived via multiple regression analysis, for estimating the daytime, equatorial vertical ExB drifts from magnetometer observations. Figures 3.4a and 3.4b

show the scatterplots of the ΔH (Jicamarca-Piura) observations and, respectively, of the Jicamarca H component (after subtracting the nighttime baseline), H_J, observations as functions of the vertical ExB drifts measured by the Jicamarca ISR (red dots) and JULIA (blue dots) radars. The plots were produced based on about 60,000 samples of concurrent daytime (0700-1700 LT) magnetometer and radar observations between November 2000 and February 2009, corresponding to about 600 days of JULIA drifts and 150 days of ISR drifts. Shown in these figures are also the linear least-squares straight lines through the data points and the corresponding regression equations and correlation coefficients, R. It is clear from these figures that the correlation coefficients are about the same in all four cases, which further suggests that H_J, like ΔH, could be an excellent candidate for estimating the daytime, equatorial vertical ExB drifts, as previously pointed out by Anghel et al. (2007).

Therefore, to estimate the vertical ExB drifts at Peruvian longitudes, we used both H_J observations from Jicamarca and ΔH observations from Jicamarca and Piura, and employed techniques based on the least-squares regression analysis and neural networks. The regression analysis was performed for the four cases presented in Table 3.1, where the regression equations derived for the data sets displayed in Figure 3.4 are shown along with the corresponding root-mean-squares (RMS) errors. In all four cases presented in Table 3.1, we applied the polynomial regression analysis in order to capture the nonlinearities between the ΔH and H observations and the vertical ExB drifts. It is also important to mention that, as discussed in Anderson et al. (2006a), the derived equations are general and can be used to estimate the vertical ExB drifts at any longitudes where appropriately placed magnetometers exist.

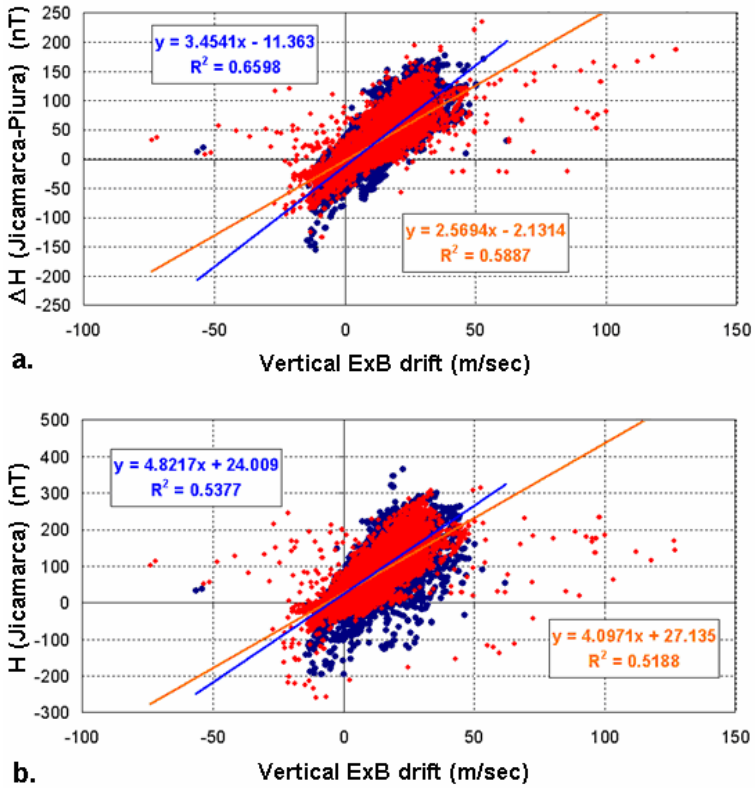

Figure 3.4: Scatterplots of (a) ΔH and (b) H_J versus ExB drift observations from Jicamarca ISR (red) and JULIA (blue) radars between November 2000 and February 2009.

$ExB = 14.47 - 0.03428 \cdot F10.7 + 0.02824 \cdot DailyAp - 0.44436 \cdot LT + 0.2469 \cdot \Delta H + 0.0001196 \cdot \Delta H^2 - 0.00000379 \cdot \Delta H^3$ [1]	RMS = 4.7410 (m/s)
$ExB = 1290.378 - 0.6344 \cdot Year - 0.00328 \cdot DOY - 0.03323 \cdot F10.7 - 0.0308 \cdot F10.7A + 0.01044 \cdot ApDaily + 0.1865 \cdot kp - 0.42708 \cdot LT - 0.01644 \cdot SZA + 0.24496 \cdot \Delta H + 0.0001055 \cdot \Delta H^2 - 0.0000036 \cdot \Delta H^3$ [2]	RMS = 4.6943(m/s)
$ExB = 4.63376 - 0.05189 \cdot F10.7 + 0.0509 \cdot DailyAp + 0.0806 \cdot LT + 0.14998 \cdot H + 0.0002131 \cdot H^2 - 0.000001323 \cdot H^3$ [3]	RMS = 5.3378 (m/s)
$ExB = -1299.32517 + 0.64577 \cdot Year + 0.001666 \cdot DOY - 0.041607 \cdot F10.7 - 0.0010876 \cdot F10.7A + 0.011432 \cdot ApDaily + 0.94867 \cdot kp + 0.1198 \cdot LT + 0.121946 \cdot SZA + 0.1665 \cdot H + 0.00031 \cdot H^2 - 0.000001699 \cdot H^3$ [4]	RMS = 5.0210 (m/s)

Table 3.1: Analytical formulas for estimating the daytime, equatorial vertical ExB drifts.

For the Drift-Net algorithms, we chose MLFF-NN structures with 15 hidden neurons. As mentioned before, these types of neural networks are known for their powerful function approximation capabilities, being able to learn highly nonlinear mappings between input and output parameters without any prior knowledge about the nature of the input-output relationships. Currently, Drift-Net consists of two MATLAB neural networks trained in a supervised way using the data sets shown in Figure 3.4. The main difference between the two networks lies in the fact that they have either ΔH or H as inputs. Training the networks was performed for 200 training epochs, at the end of the training process the RMS error reaching a value of 4.0611 m/s when ΔH was used as input, and a value of 4.2694 m/s when H was used as input.

Figure 3.5 shows the daytime (0700-1700 LT) ΔH and H-inferred vertical ExB drifts at Jicamarca between 2001 (top) and 2008 (bottom) as a function of day number and local time. The blue bands of even color in the plots indicate periods of missing data. It is clear from these plots that the ΔH and H-inferred drifts share many features and display a significant short-term and day-to-day variability similar to that of the magnetometer data used for their calculation. They are mostly upward during daytime, maximize at late morning hours around 1100 LT on most days, have a large day-to-day variability, and display a seasonal variation with peaks at equinox, but they do not exhibit a significant solar cycle variation, which is consistent with previous studies (e.g., Fejer et al., 1991, 1995). Moreover, the excellent agreement between the estimated ExB drifts and the Jicamarca ISR and JULIA drifts during 2001-2008 is clearly illustrated in Figure 3.6, where the drifts are plotted versus LT.

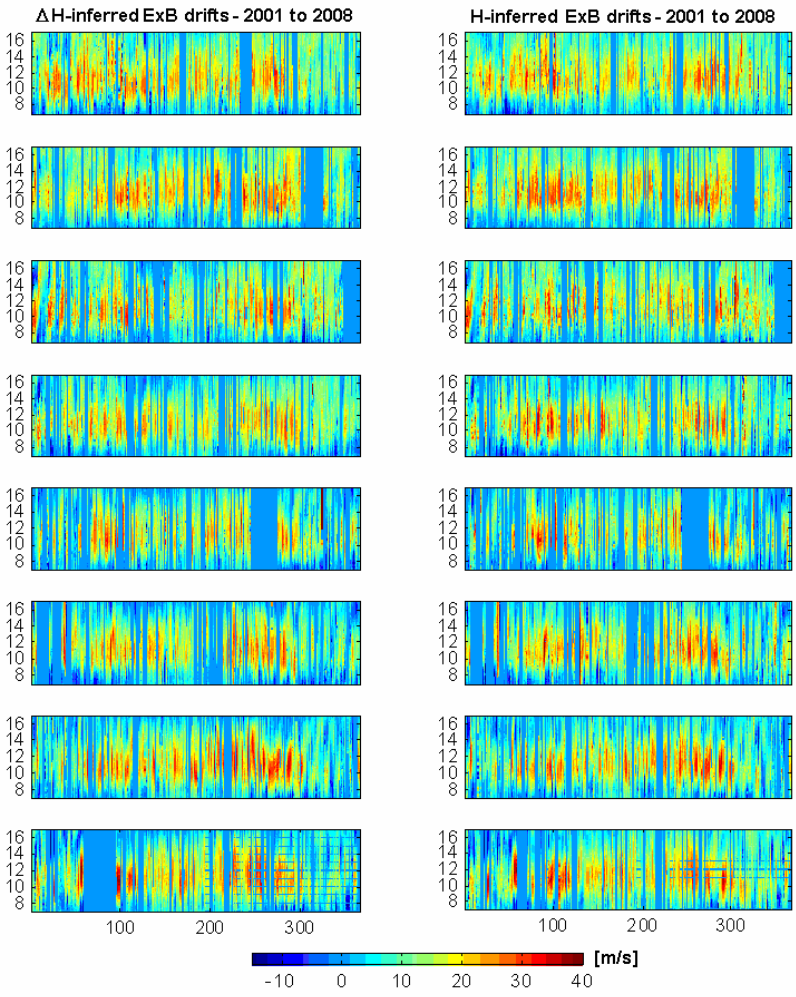

Figure 3.5: Daytime (0700-1700 LT) vertical ExB drifts inferred from (left) ΔH and (right) H_J observations as a function of day number and LT, for 2001-2008.

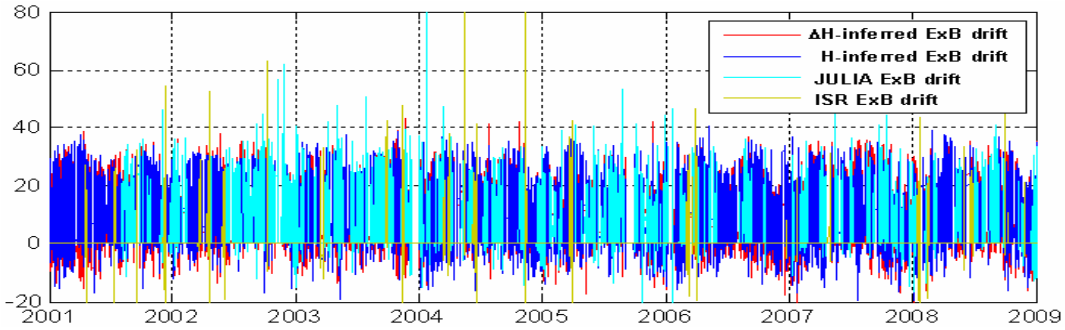

Figure 3.6: Daytime (0700-1700 LT) vertical ExB drifts inferred from ΔH (red) and H_J (blue) observations, and measured by JULIA (cyan) and ISR (green) radars, during 2001-2008.

As part of the validation process, we compare the average quiet-time ΔH and H-inferred drift patterns with the corresponding Fejer-Scherliess drift patterns, for three seasons: December solstice (January, February, November, and December - JFND), Equinox (March, April, September, and October - MASO), and June solstice (May, June, July, and August - MJJA). For each season the averages were performed over about 400 quiet days, characterized by daily Ap values less than 10.

The comparative results are presented in Figure 3.7, where the average quiet-time drift curves are shown versus local time. The vertical bars in the plots represent the standard deviations associated with the average drift patterns and indicate the variability in the drifts caused by changes in the geophysical conditions over the eight-year time interval. As shown in this figure, there is an excellent agreement between the ΔH and H-inferred ExB drift patterns, which further suggests that the Jicamarca H component can be successfully used as input parameter to ExB drift estimation algorithms. The comparative results with the Fejer-Scherliess quiet-time drift curves are also excellent for the Equinox and June solstice conditions and good for the December solstice, which is in agreement with the results reported by Anderson et al. (2006a) and Anghel et al. (2007).

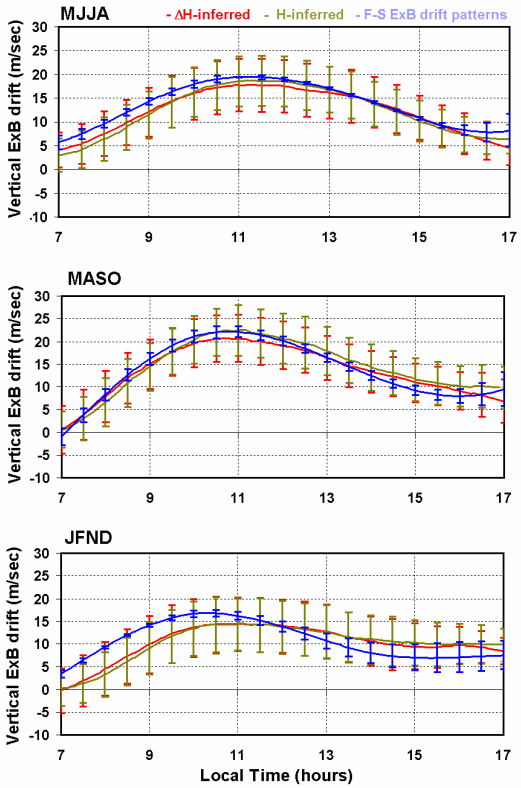

Figure 3.7: Quiet-time vertical ExB drift patterns versus LT for (upper panel) June solstice, (middle panel) Equinox period, and (bottom panel) December solstice.

3.5 Global Models of Daytime, Equatorial Vertical ExB Drifts

In their recent studies, Anderson et al. (2006a) and Anghel et al. (2007) showed that the same neural network-based drift model trained only with Peruvian data can also be used to estimate the vertical ExB drifts at other longitude sectors. To test their hypothesis, they trained a neural network with magnetometer ΔH and ExB drift observations from Jicamarca, between August 2001 and February 2005, and applied the trained network to ΔH observations from Peruvian, Philippine, and Indian longitudes. They compared then the seasonal, quiet-time drift patterns predicted by their algorithm at each site with drift patterns predicted by the Fejer-Scherliess model.

Figure 3.8, taken from Anghel et al. (2007), shows the ΔH-inferred drifts and the corresponding seasonal drift patterns (thick red lines) at the three longitude sectors, while Figure 3.9 taken also from Anghel et al. (2007) shows the ΔH-inferred seasonal drift patterns (thick red lines) and the associated standard deviations. The Fejer-Scherliess drift patterns are displayed in both figures as thick blue lines and the number of days used in each averaging is indicated on the panels. As seen in these figures, an excellent agreement between the ΔH-inferred and Fejer-Scherliess drift patterns was found at the Peruvian sector and a very good agreement at the Philippine and Indian sectors. The implications of their results are significant, suggesting that realistic daytime, equatorial vertical ExB plasma drifts can now be obtained globally and on a day-to-day basis wherever appropriately placed magnetometers exist.

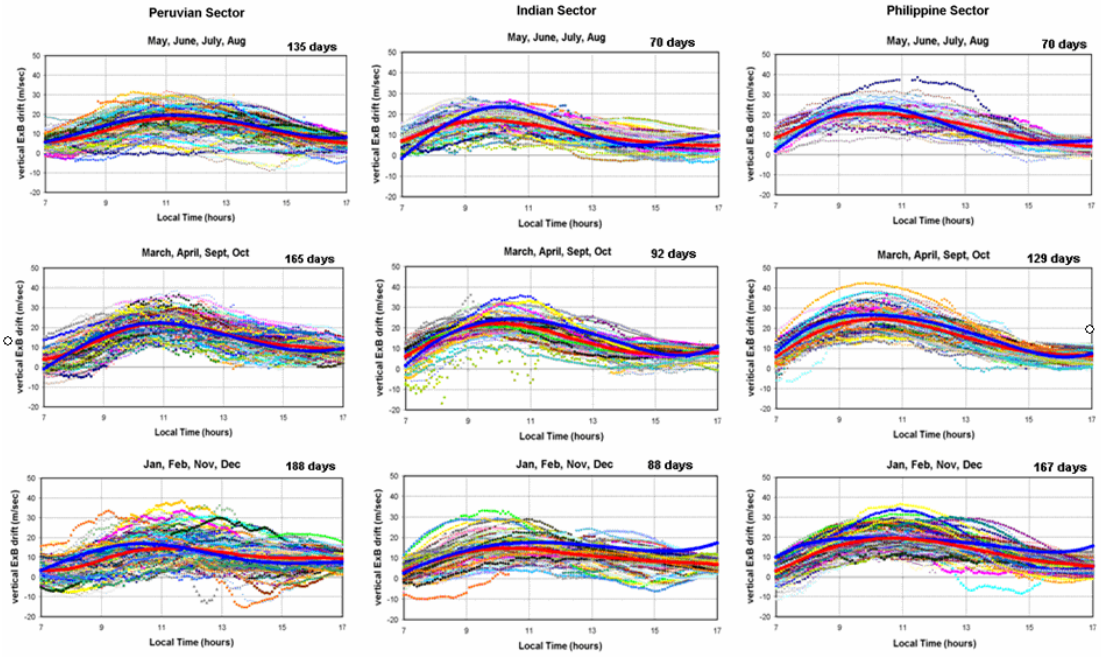

Figure 3.8: ΔH-inferred vertical ExB drifts at the Peruvian, Indian, and Philippine sectors (from Anghel et al., 2007).

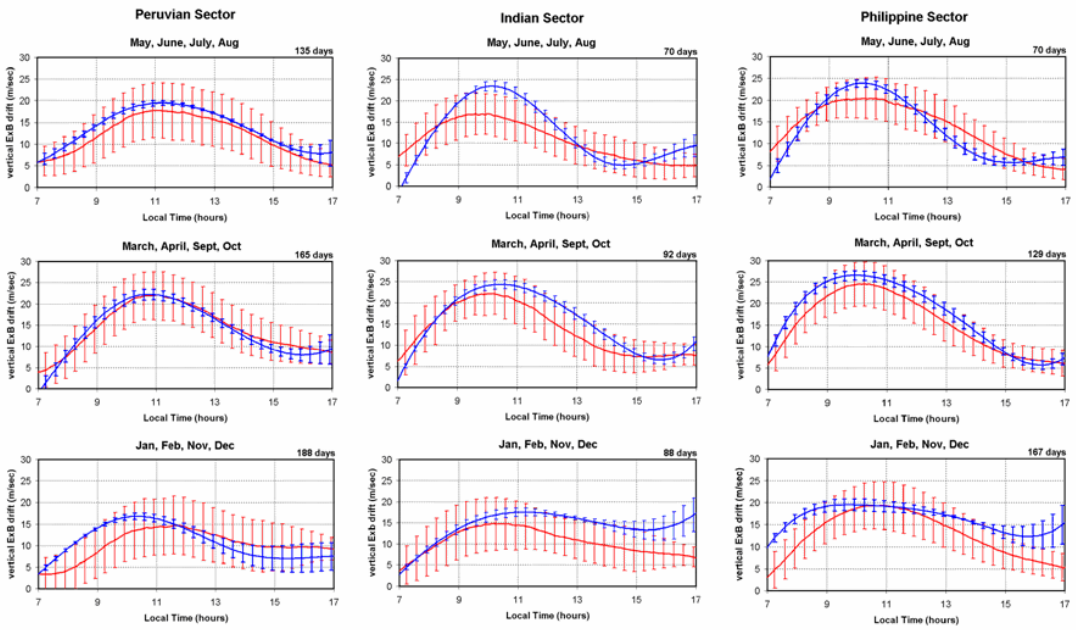

Figure 3.9: Vertical ExB drift patterns at the Peruvian, Indian, and Philippine sectors (from Anghel et al., 2007).

3.5.1 Quiet-time Studies

Like in Anderson et al. (2006a) and Anghel et al. (2007), we applied the Drift-Net algorithms trained with Peruvian data to magnetometer observations from Peruvian, Indian, Philippine, and Indonesian longitudes. Then, to investigate the performance of our algorithms, we calculated the seasonal patterns of the quiet-time ΔH and H-inferred drifts at each site by binning the drifts into three seasonal periods, namely December solstice (JFND), Equinox (MASO), and June solstice (MJJA), and compared them with seasonal drift patterns predicted by the Fejer-Scherliess model.

Figure 3.10 shows the seasonal drift patterns at the four longitudes as a function of local time, with the number of days used in each averaging being indicated on the panels. In this figure, the solid red lines represent the quiet-time ΔH-

inferred drift patterns, the solid green lines are the quiet-time H-inferred drift patterns, and the solid blue lines are the quiet-time Fejer-Scherliess drift patterns. The vertical bars represent the standard deviations associated with these average drift patterns and reflect the day-to-day variability of the estimated drifts.

As seen in Figure 3.10, the standard deviations corresponding to the magnetometer-inferred ExB drift patterns are close to 5 m/s around the noontime hours and to about 2.5 m/s at early morning and late afternoon hours. It can also be observed in this figure that there is excellent agreement between the ΔH and H-inferred drift patterns at the Peruvian and Indonesian longitudes, but a large discrepancy at the Indian and Philippine sectors. A large discrepancy can also be observed between the magnetometer-inferred drift patterns at the Philippine and Indonesian sites. This is somehow surprising given that the two sites are only about 10^{o} apart in longitude.

We suggest that the factors responsible for the observed differences between the magnetometer-inferred drift patterns at the two closely-spaced sites could be the relative location of the stations with respect to the magnetic equator, the amount of data used for calculating each pattern, and the quality of the data used in each case. However, further studies including model simulations are necessary to systematically investigate the causes of the observed differences between the magnetometer-inferred drift patterns, but this is beyond the purpose of our current study.

As illustrated in Figure 3.10, at the Peruvian longitudes, there is an excellent agreement between the magnetometer-inferred drift patterns and the drift patterns predicted by the Fejer-Scherliess model for Equinox and June solstice conditions, and

a good agreement for December solstice conditions. At the Indian and Philippine longitudes, the best agreement is obtained at Equinox, while at the Indonesian site there is in general a poor agreement between the magnetometer-inferred and Fejer-Scherliess drift patterns. At this latter site, the differences between the magnetometer-inferred and Fejer-Scherliess drift patterns are both in amplitude and shape. However, this is not surprising given that the Fejer-Scherliess model was developed based on Jicamarca ISR drifts and a limited number of satellite observations, while the magnetometer-inferred drifts follow closely the shape and variability of the magnetometer observations they were derived from. A more complete discussion on the ExB drift patterns predicted by the Fejer-Scherliess model and those estimated from ΔH magnetometer observations can be found in Anghel et al. (2007).

The results presented in this section are in excellent agreement with those reported by Anderson et al. (2006a) and Anghel et al. (2007) and further demonstrate that the H and ΔH versus ExB drift relationships developed for the Peruvian longitudes can also be used to obtain realistic vertical ExB drifts at other longitude sectors. This is an important and significant result, which means that we now have the ability to investigate the day-to-day, "weather" aspects of daytime ExB drifts at different longitudes and relate them to the IEF conditions.

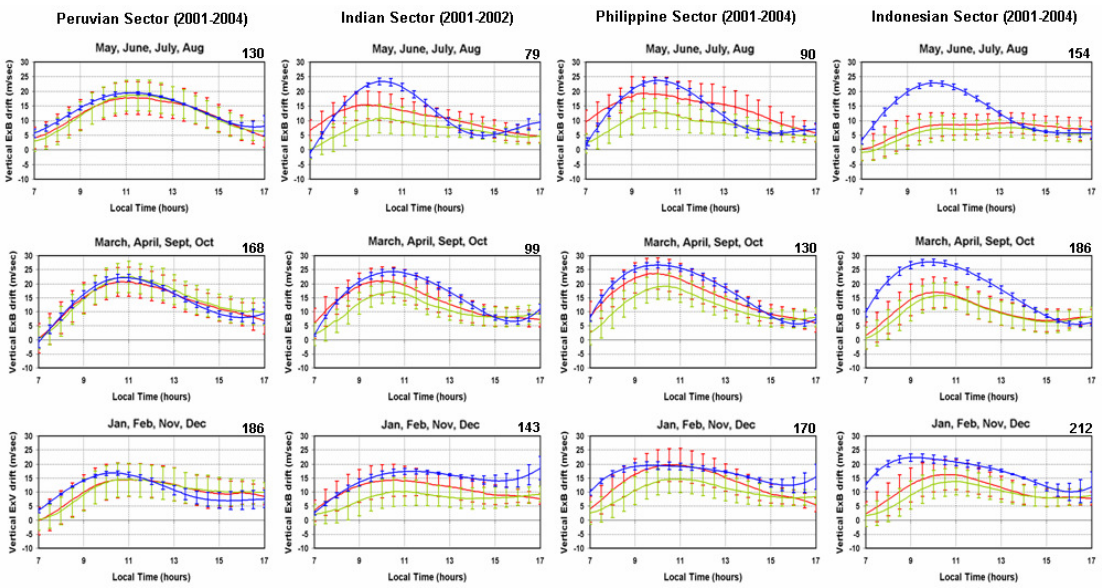

Figure 3.10: Vertical ExB drift patterns at the Peruvian, Brazilian, Indian, Philippine, and Indonesian longitude sectors.

3.5.2 Disturbed-time Studies

Compared with the quiet-time ExB drift patterns, the low-latitude plasma drifts and currents respond quite differently during geomagnetically disturbed periods, as magnetospheric and ionospheric disturbance dynamo effects become significant under such conditions. As mentioned before, there are two major sources of low-latitude electric field perturbations during disturbed periods. One originates from the magnetosphere and the other is due to the ionospheric disturbance dynamo. The latter results from the dynamo action of the storm time winds driven by enhanced energy deposition at high-latitudes.

Under steady-state conditions, the low and mid-latitude ionosphere is shielded from the high-latitude convection by shielding charges at the inner edge of the ring current. However, during disturbed periods when the high-latitude convection

patterns are undergoing large changes, the high-latitude electric fields “leak through” the shielding layer. In this case, the cross polar cap potential suddenly increases as a result of an increase in the dawn-to-dusk, cross-tail electric field, and this electric field can promptly penetrate to the equatorial region (undershielding) until a shielding dusk-to-dawn electric field develops in the inner magnetosphere. The dusk-to-dawn electric field shields the inner magnetosphere from strong convection fields. When the strong convection field decreases, due to a northward turning of the IMF, the dusk-to-dawn electric field can promptly penetrate to low-latitudes (overshielding) until the shielding layer and the overall magnetospheric configuration readjust.

In the following two figures, we compare the IEF conditions observed by the ACE satellite with the low-latitude zonal electric fields Ey inferred from magnetometer observations in the Peruvian, Philippine and Indian longitude sectors. For each figure, the various quantities are plotted as a function of universal time (UT). In the Peruvian sector, 0000 UT is 1900 LT, in the Philippine sector, 0800 LT, and in the Indian sector, 0500 LT. In each figure, the orange line represents the daytime (0700-1700 LT), ΔH-inferred vertical ExB drift and the corresponding zonal electric field in the Peruvian sector. The red line corresponds to the daytime values in the Philippine sector, while the light blue line represents the daytime values in the Indian sector. The green line represents the Jicamarca ISR drift and zonal electric field observations. In the two figures the notation in the legends of the panels are: ISR - Jicamarca ISR drift/electric field observations, Est.(DM) - estimated drift/electric field values at the Philippine sector using magnetometer observations from Davao and Muntinlupa, Est.(TA) - estimated drift/electric field values at the Indian sector

using magnetometer observations from Thirunelvelli and Alibag, and Est.(JP) - estimated drift/electric field values at the Peruvian sector using magnetometer observations from Jicamarca and Piura.

Figure 3.11 illustrates the IEF conditions and the ΔH-inferred drifts for 17-19 April 2001. The thin lines in the second panel of this figure represent the Fejer-Scherliess drifts for this period, at the three longitude sectors. During April 17, the IEF conditions are quiet, with daily Ap less than 20, and the Peruvian, Philippine and Indian sectors reflect quiet-time drifts of about 20 m/sec. As shown in Figure 3.11, at 0100 UT on April 18, IMF-Bz suddenly turns southward leading to a strong, positive value for IEF-Ey of about 10 mV/m. This occurs when the Philippine sector is in daylight and the ΔH-inferred ExB drift begins to respond to the IEF-Ey conditions.

Referring to the bottom panel of Figure 3.11, between 0200 and 0400 UT on April 18, marked by two black arrows, the low-latitude zonal electric field in the Philippine sector matches the IEF-Ey/10 curve almost exactly for the entire period. This is a period of extended IMF-Bz south condition that corresponds to an extended penetration electric field (e.g., Huang et al., 2005). During this period, when IMF-Bz turned southward and remained stably southward for more than 2 hours, the low-latitude zonal electric field at Philippines maintained enhanced and stable amplitudes.

At 0430 UT on April 18, which is a fairly disturbed day with a daily Ap of 50, there is a sudden northward turning of the IMF-Bz and a sudden decrease in the upward ExB drift velocity in both Philippine and Indian sectors (second black arrow). Simultaneously, in the nighttime Peruvian sector, there is a sudden increase in the vertical ExB drift. This is consistent with the idea that, for overshielding, the electric

fields at low latitudes are directed from dusk-to-dawn which means that the daytime ExB drifts are downward and the nighttime ExB drifts are upward.

The third black arrow at 29 UT, points to the sudden turning of the IEF-Ey from negative to positive values and to the prompt penetration electric fields in the Peruvian, Philippine, and Indian sectors. For this case, the penetrating electric field is dawn-to-dusk, which means that, in the Peruvian nighttime sector, the electric field is westward and the ExB drift is downward and, in the daytime Philippine and Indian sectors, the electric field is eastward and the ExB drift is upward. The fact that the daytime drifts are so small in the Philippine and Indian sectors implies that the disturbance dynamo electric fields are fairly strong and act to cancel the penetration electric fields at these two longitude sectors.

Figure 3.12 shows the IEF-Ey and the low-latitude zonal electric fields Ey for 6 July 2002. It is clear from this figure that the IEF-Ey fluctuations between 0200 and 0600 UT, with amplitudes in the ±5 mV/m range, are mirrored in the Ey values at the Indian sector. Also, the positive increases of about 3 mV/m in the IEF-Ey, between 1500 and 1900 UT, are reflected in the Ey increases of about 0.3 mV/m at the Peruvian sector. Both Figures 3.11 and 3.12 demonstrate that the “weather” signatures in the vertical ExB drift velocities can be realistically studied at any longitude sector where appropriately placed magnetometers exist.

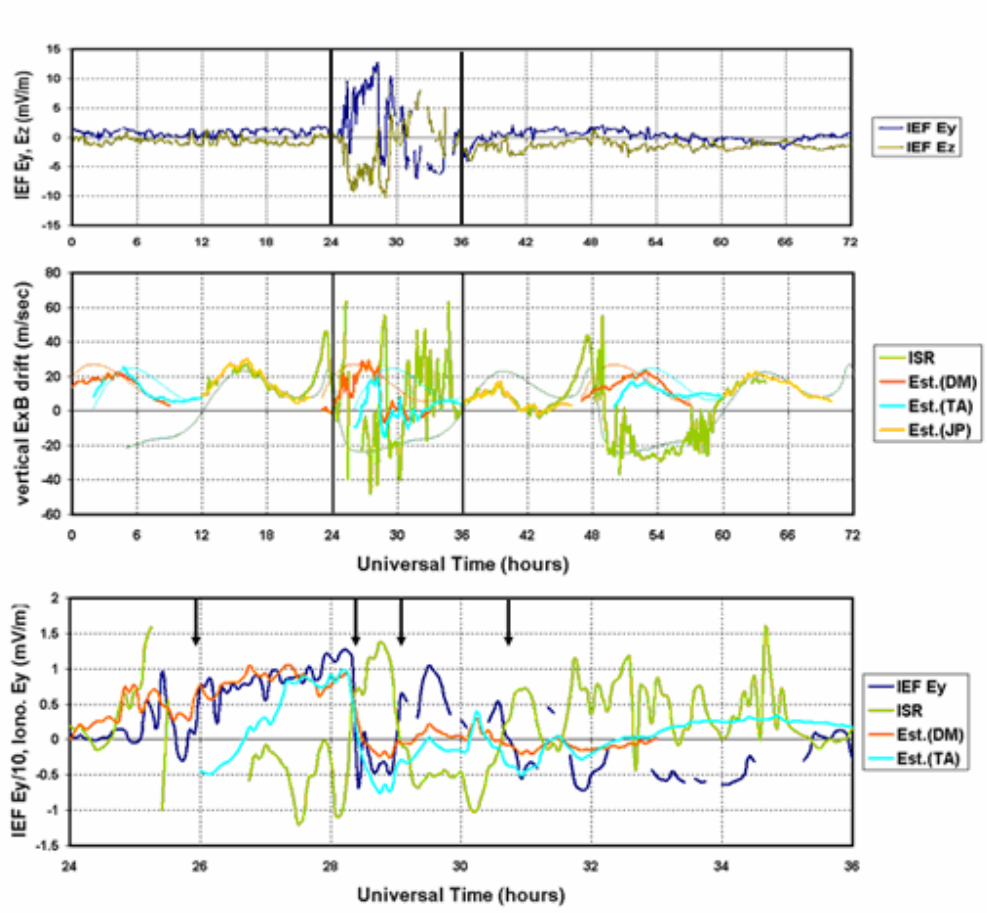

Figure 3.11: (top) IEF-Ey and IEF-Ez, (middle) vertical ExB drifts at the Peruvian, Philippine and Indian longitude sectors during 17-19 April 2001, and (bottom) IEF-Ey/10 and the zonal electric fields Ey between 0000 and 1200 UT on 18 April 2001 (from Anghel et al., 2007).

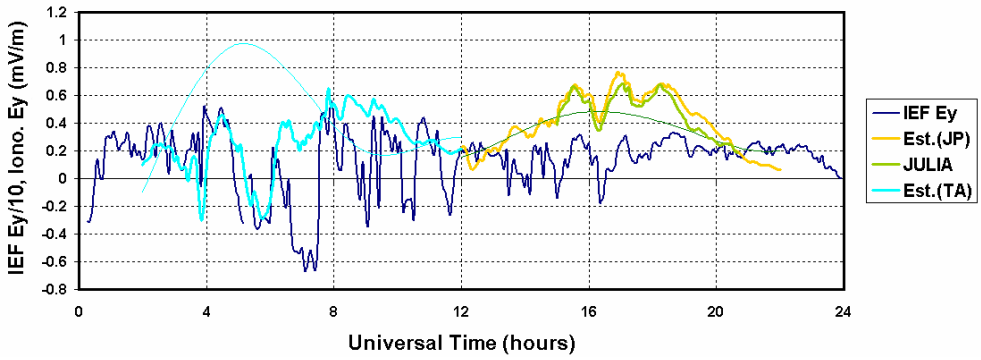

Figure 3.12: IEF-y/10 and the low-latitude zonal electric fields Ey versus UT for 6 July 2002 at the Peruvian and Indian longitude sectors, with the thin lines representing the Fejer-Scherliess drift values.

3.6 Algorithm for Estimating the Evening ExB Drifts Using Ionosonde Data

In the previous sections, we have presented different algorithms for estimating the daytime, equatorial vertical ExB drifts from magnetometer observations. Since the magnetometer data can be used to calculate only the daytime (0700-1700 LT) drifts, to estimate the vertical drifts at evening hours, we developed an algorithm based on Jicamarca digital sounder data. In this algorithm, the vertical ExB plasma drifts between 1700 and 2100 LT are determined as the time rate of change of the height of the $2x10^5$ el/cm^3 contour density (~4 MHz) at the bottomside ionosphere (e.g., Fagundes, 2004). We tested the algorithm for the entire 2000-2007 dataset of Jicamarca ISR vertical ExB drifts and the results are impressive, showing an excellent agreement between the measured ISR drifts and the estimated drifts.

As an example, Figure 3.13 displays the estimated drifts for 10-12 November 2004 as a function of LT. This is a highly disturbed period, with daily Ap values ranging between 23 and 181. In Figure 3.13, the green lines represent the vertical drifts predicted by the Fejer-Scherliess model, the blue lines are the ΔH-estimated drifts, the red lines are the Jicamarca ISR drifts, and the gray dots are the drifts estimated using ionosonde data from Jicamarca. It is clear from this figure that, for all three days, there is an excellent agreement between the evening (1700-2100 LT) drifts measured by the ISR radar and those estimated from ionosonde observations.

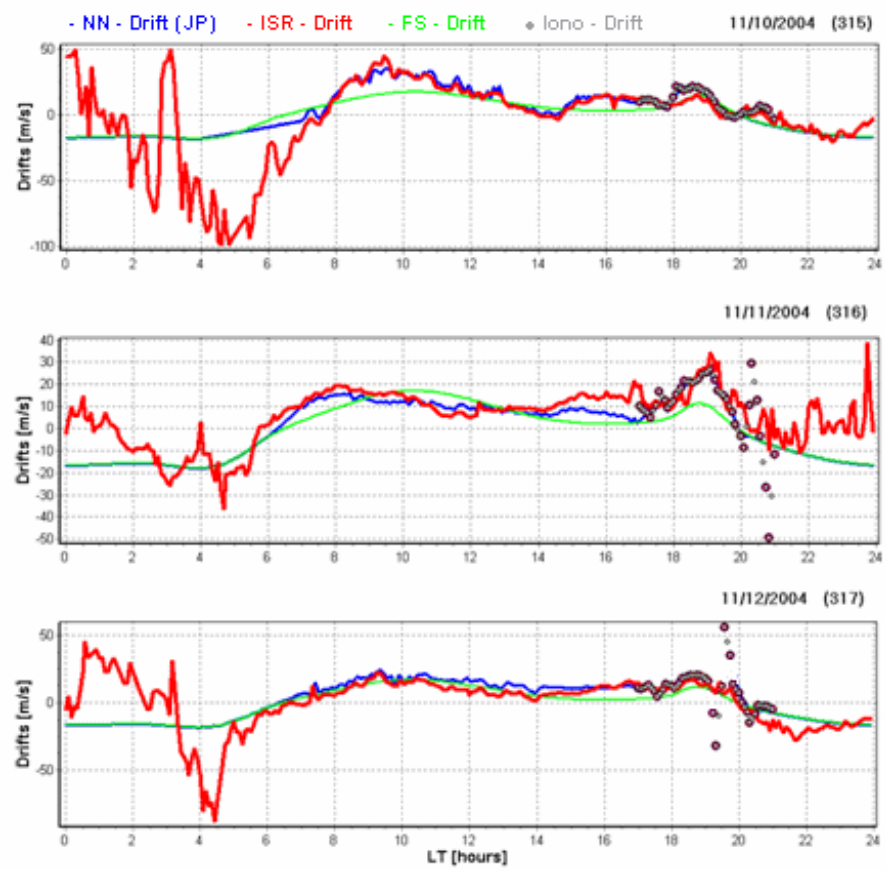

Figure 3.13: The vertical ExB drifts versus LT for 10-12 November 2004.

Using an ionospheric model, Yue et al. (2008) investigated the local time dependency of the relationship between the vertical ExB drifts and the time rate of change of the peak height of the F-layer, dHmF2/dt, for two seasons and three solar activity levels, under quiet geomagnetic conditions. As shown in Figure 3.14, taken from Yue et al. (2008), they obtained the best correlations around sunrise and sunset. Their results are in agreement with statistical observational studies reported by other authors (e.g., Bertoni et al., 2006; Oyekola et al., 2007a, b; Woodman et al., 2006).

Woodman et al. (2006) showed that the ionosonde-derived vertical ExB drifts include the actual vertical drifts but they are also affected by changes in the shape of the electron density profiles caused by photochemical processes. Speciffically, during

daytime, the ionosphere reaches an equilibrium state under the combined effect of electrodynamics and chemistry, such that the shape of the electron density profiles does not undergo significant changes, and consequently the derived plasma drifts are small. An equilibrium state is also reached during nighttime, when the vertical drift is downward and the recombination processes dominate. In this case, the derived drifts are also small. However, during sunrise, sunset, and early evening hours, the strength and direction of the zonal electric fields undergo large changes, such that the above mentioned ionospheric equilibrium is disrupted and the dynamics becomes dominant. In consequence, at these hours, the ionosonde-derived drifts are also more accurate.

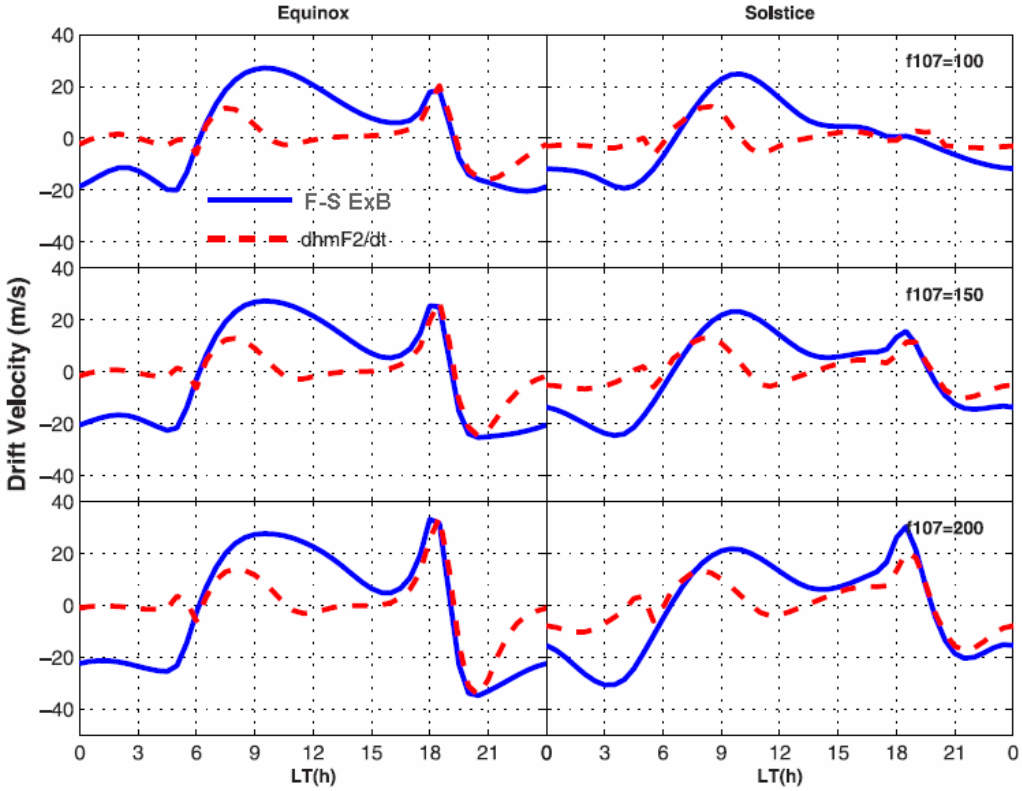

Figure 3.14: The Fejer-Scherliess drifts (blue) and the dHmF2/dt-inferred drifts (red) versus LT (from Yue et al., 2008).

3.7 ΔH-inferred Vertical ExB Drifts as Inputs to Ionospheric Models

Previous studies have shown that the accuracy in the ionospheric parameter specification can be significantly improved by using more realistic vertical ExB drifts as inputs to ionospheric models (e.g., Preble et al., 1994). In a recent study, Anderson et al. (2006b) used ΔH-inferred vertical ExB drifts as inputs to the Low-Latitude Ionospheric Sector (LLIONS) model and found a better agreement between the theoretically calculated electron densities and vertical total electron content (TEC) values and the ground-based and satellite observations, than when using drifts predicted by the Fejer-Scherliess model. LLIONS is a single-sector ionospheric model capable of incorporating data-determined drivers, and can be used to calculate electron and ion densities as a function of altitude (90-1600 km), latitude (±35^o dip latitude), and local time (24 hours) for specified ExB drift values.

Similar with the results presented by Anderson et al. (2006b), Figure 3.15 shows the LLIONS results for 28 October 2003 obtained by applying the ΔH-inferred and Fejer-Scherliess vertical ExB drifts as inputs to the model. The ΔH-inferred (blue) and Fejer-Scherliess (green) drifts for this day are shown in Figure 3.15a, while the theoretically calculated vertical TEC values for the two types of drifts are plotted in Figures 3.15b and 3.15c as a function of local time and geomagnetic latitude. The vertical TEC values predicted by LLIONS were obtained by integrating the electron densities along vertical ray paths from 90 to 1600 km altitude, every 2^o in latitude and every 15 minutes in local time, over a 24-hour period. In running the model, the drifts were assumed independent of latitude. Figure 3.15d shows the actual TEC values for

the same day obtained from a chain of ground-based, dual-frequency GPS receivers. It can be concluded from Figure 3.15 that the TEC values predicted by the LLIONS model are very sensitive to and critically dependent on the drift values used as inputs to the model. Our results are consistent with those presented by Anderson and et al. (2006b), and support the idea that by incorporating more realistic drifts into ionospheric models the theoretically calculated ionospheric parameters show in general a better agreement with the observations.

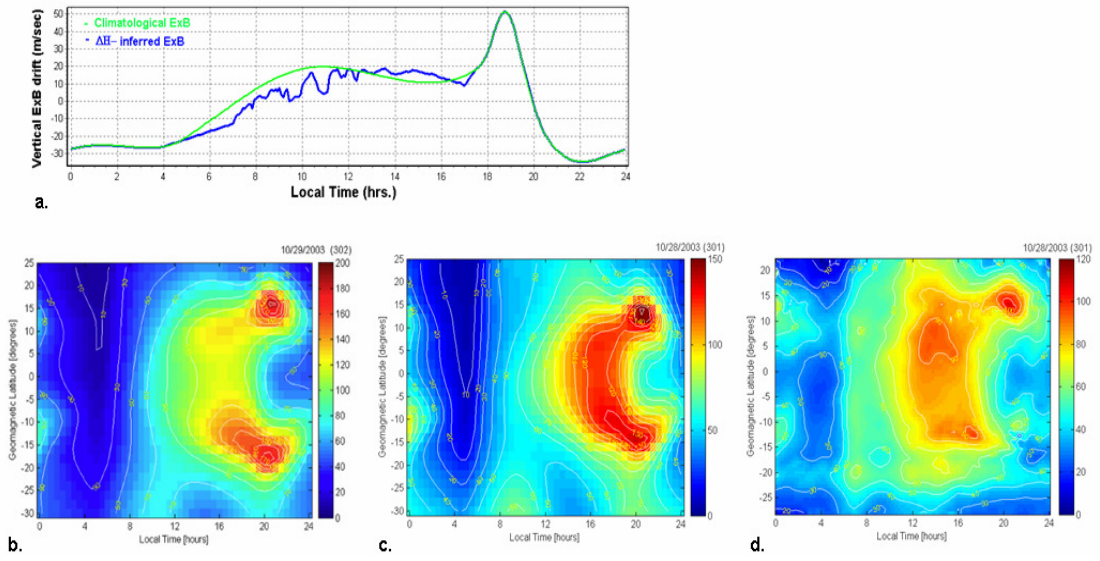

Figure 3.15: (a) ΔH-inferred and Fejer-Scherliess vertical ExB drifts, (b) LLIONS-calculated TEC using Fejer-Scherliess drift, (c) LLIONS-calculated TEC using ΔH-inferred drift, and (d) the observed GPS-derived TEC for 28 October 2003.

3.8 Conclusions

We have presented several least-squares regression and neural network-based algorithms, named Drift-Net, for estimating the daytime, equatorial vertical ExB drifts from magnetometer observations. The Drift-Net algorithms represent a

successful attempt to use MLFF-NNs for the development of empirical drift models. We chose the neural network approach, since the neural networks have the ability to learn nonlinear, complex relationships between the input and output parameters without any apriori knowledge about those relationships. Another major advantage of employing a neural network is the relative ease with which it can be retrained should more data become available.

The validation results reported in this chapter show that, at Peruvian longitudes, the ΔH and H-inferred drift patterns are very similar with the drift patterns predicted by the Fejer-Scherliess model. These results indicate that the Jicamarca H component, like ΔH, can also be used to estimate the daytime vertical ExB drifts at Peruvian longitudes. However, at this point it is not clear whether or not the algorithms trained with H_J observations can be applied at other longitude sectors, and further experimental and theoretical studies are required in this regard. Using H as input parameter to drift estimation algorithms could be very important given that, as shown by Richmond et al. (1973) and Fang et al. (2008a), the H component away from the magnetic equator is much more affected by zonal neutral winds than the H component on the magnetic equator. This could be also very useful at longitudes where a single equatorial magnetometer station is available, and could also eliminate the uncertainty surrounding the position of the off-equatorial station.

From our quiet-time studies, the fact that there is a reasonable agreement between the magnetometer-inferred and Fejer-Scherliess drift patterns at the Peruvian, Philippine and Indian longitudes suggests that realistic, vertical ExB drifts can be obtained from ground-based magnetometer observations at any longitude

where appropriately placed magnetometers exist. However, the large discrepancies between the magnetometer-inferred and Fejer-Scherliess drift patterns at the Indonesian site, which is only about 10^{o} away in longitude from the Philippine site, require further studies. The large differences between the ΔH and H-inferred drift patterns at the Philippine and Indian sectors are also inexplicable at this point and may also constitute an interesting research topic, worthy of further investigation.

The disturbed-time studies presented here demonstrate that we now have the capability to investigate the "weather" aspects of the daytime, equatorial vertical ExB drifts at different longitudes and to relate them to IEF conditions. Our results indicate that promptly penetrating and overshielding electric fields produce opposite day/night effects in the equatorial vertical ExB drifts that substantiate current magnetosphere-ionosphere coupling theories (e.g., Kelley et al., 1979; Gonzales et al., 1979).

In addition, since the ground-based magnetometer observations can be used to estimate only the daytime (0700-1700 LT) drifts, we have also presented an algorithm for estimating the evening (1700-2100 LT) vertical ExB drifts using digital sounder data. It is noteworthy that, although the results presented here are based on Jicamarca sounder observation, the algorithm is general and can be applied to any equatorial station. We have also shown that using more realistic drifts as inputs to ionospheric models can in general improve the predictions from these models, which is in agreement with results reported by other previous studies.

Chapter 4

Relating the Interplanetary Electric Field with the Low-Latitude Zonal Electric Fields under Disturbed Geomagnetic Conditions

4.1 Background

Stemming from the need to understand and predict the behavior of the ionosphere under both quiet and disturbed conditions, recent modeling and experimental studies have shown an increased interest in the short-period (minutes-to-hours) and day-to-day variability of the upper atmosphere and ionosphere (e.g., Mendillo and Schatten, 1983; Forbes et al., 2000; Pancheva et al., 2002; Mendillo, 2006). As mentioned in Chapter 1, the thermosphere-ionosphere system is a highly-variable and complex system, its complexity being determined by: (1) inherent internal interactions, (2) interactions with the magnetosphere above, (3) interactions with the middle atmosphere below, and (4) variability of the external sources driving the system. Consequently, the ionosphere displays variations from its normal climatological pattern that affect the ionospheric predictions on time scales ranging

from secular to days, hours and even minutes and seconds. These variations have been observed in different ionospheric parameters (e.g., Parish et al., 1994; Rishbeth and Mendillo, 2001; Pancheva et al., 2006; Fagundes et al., 2005; Abdu et al., 2006; Hocke, 2008) and are in general induced by wave activity originating in the lower regions of the atmosphere, quasi-periodic oscillations in the geomagnetic activity, or periodic variations in the solar EUV flux. While changes in the solar EUV flux influence mostly the long-period, secular (months to years) variability of the ionosphere, the geomagnetic activity and the lower atmospheric processes induce in general oscillations with periods ranging from about few seconds or minutes to several days or even weeks (e.g., Lastovička, 2006).

The main purpose of this chapter is to investigate the variability of the low-latitude zonal electric fields (LLZEF) in response to changes in the dawn-to-dusk component Ey of the interplanetary electric field (IEF-Ey) during time intervals of increased geomagnetic activity. During storm times, large ionospheric electric field and current perturbations travel from high to equatorial latitudes, changing the ionization distribution over large areas and controlling the storm-time dynamics and electrodynamics of the low and mid-latitude ionosphere. The most important sources of low-latitude electric field disturbances under these conditions are: (1) the prompt penetration electric fields of solar wind/magnetospheric origin, and (2) the disturbance dynamo electric fields caused by high-latitude Joule and particle heating. The penetration electric fields are associate with changes in the field-aligned current system, which is responsible for shielding the inner magnetosphere and the low and mid-latitude ionosphere from the high-latitude magnetospheric convection electric

fields, and propagate instantaneously to equatorial latitudes in response to changes in the high-latitude convection (e.g., Fejer and Scherliess, 1997; Huang et al., 2005). On the other hand, the disturbance dynamo electric fields are associated with enhanced deposition of energy and momentum in the auroral zone. At equatorial latitudes, they are predominantly westward on the dayside and eastward on the nightside (e.g., Blanc and Richmond, 1980; Scherliess and Fejer, 1997).

Equatorial electric field measurements are rather sporadic, but as shown in the previous chapter, realistic vertical ExB drifts and zonal electric fields can be inferred on a day-to-day basis from ground magnetometer observations at any longitude sector where appropriately placed magnetometers exist. In addition, we also showed in the previous chapter that the magnetometer-inferred drifts can be used to investigate the variability of the F-region drifts at different longitudes and to relate this variability to the IEF-Ey conditions. Expanding on these studies, in this chapter we use wavelet and cross-wavelet spectral analysis techniques to compare the oscillation activity in the LLZEF and IEF-Ey spectra in the 10 min.-10 hour and 1.25-12 day period ranges.

The purpose of this chapter is therefore twofold: (1) to study the variability of the LLZEF in the 1.25-12 day period range at three longitudes, Peruvian, Philippine, and Indian, over a time interval of relatively increased geomagnetic activity, 9 February-9 June 2001, and relate this variability to similar changes in the IEF-Ey, and (2) to analyze and relate the oscillation activity in the LLZEF and IEF-Ey in the 10 min.-10 hour period range for three case studies characterized by enhanced geomagnetic activity, 17-19 April 2001, 15-18 April 2002 and 9-12 November 2004, using concurrent observations of Jicamarca ISR zonal electric field and IEF-Ey data.

A fourth case, 29 March - 2 April 2004, is also considered for comparison purposes and is used as a quiet-time reference.

The chapter is organized as follows: in the next section, we describe the data sets and the wavelet analysis approach, then we examine the 1.25-12 day and 10 min.-10 hour periodicities in the LLZEF and IEF-Ey wavelet spectra, and finally, we present succinctly our conclusions.

4.2 Data Sets and Analysis Techniques

4.2.1 Data sets

For our studies, we used magnetometer data, with a 5-minute temporal resolution, from three pairs of equatorial stations located in Peru, Philippines, and India. The magnetometer observations at the Peruvian sector were obtained from Jicamarca (11.9^{o}S, 283.1^{o}E, geom. 0.8^{o}N) and Piura (5.2^{o}S, 279.4^{o}E, geom. 6.8^{o}N), at the Philippine sector, from Davao (7^{o}N, 125.4^{o}E, geom. 1.32^{o}S) and Muntinlupa (14.37^{o}N, 121.02^{o}E, geom. 6.39^{o}N) (Yumoto, 2001), and at the Indian sector, from Thirunelveli (8.7^{o}N, 76.9^{o}E, geom. 0.5^{o}S) and Alibag (18.6^{o}N, 72.9^{o}E, geom. 10^{o}N). The daytime LLZEFs at the three longitudes were obtained using the neural network drift model presented by Anderson et al. (2004), knowing that 1 mV/m corresponds to a vertical drift of ~40 m/s at the Peruvian sector, ~28 m/s at the Philippine sector, and ~25 m/s at the Indian sector.

To describe the interplanetary conditions, we used 64-second averages of merged ACE MAG-SWEPAM Level 2 interplanetary magnetic field and solar wind velocity data. First, we calculated the dawn-to-dusk component of the IEF (in GSM coordinates), IEF-Ey = $-V_x x B_z$, at the spacecraft location (~1.4 million km). Then, we time-shifted the IEF-Ey values to the magnetopause using the solar wind velocity and included an additional 10-minute time delay (e.g., Kelley et al., 2003).

4.2.2 Continuous Morlet Wavelet Analysis

Over the last several years, the continuous wavelet transform (e.g., Kumar and Foufoula-Georgiou, 1997; Torrence and Compo, 1998) has become one of the favored tools to analyze oscillations that occur in the atmosphere (e.g., Pancheva, 2000; Abdu et al., 2006). The wavelet transform is suitable for non-stationary signals, signals with variable frequency content, like the ones we deal with in our analysis. For our current studies, we use the continuous Morlet wavelet transform. The Morlet wavelet is a complex-valued function of the form:

$$\psi(t) = \frac{1}{\pi^{1/4}} \cdot \exp\left(-\frac{t^2}{2}\right) \cdot \exp(j\omega_o t) \tag{4.1}$$

where ω_o is the intrinsic frequency of the wavelet function and controls the frequency resolution in the wavelet domain, larger values corresponding to an increased frequency resolution.

As mentioned in Chapter 2, an important advantage of the wavelet method used in our studies consists in its ability to extract the "instantaneous" amplitudes and phases of the periodicities present in a signal. Here we also use the method for cross-wavelet spectral analysis. The cross-wavelet spectrum is calculated as the geometric mean of different wavelet spectra and provides information about similar periodicities that occur simultaneously in those spectra (e.g., Manson et al., 2005).

It is important to mention that, in all the wavelet plots presented in this chapter, the slant lines mark the cone of influence, the region where the edge effects are significant, and the contour lines indicate the significant spectral components. The statistical significance levels are calculated based on a first order auto-regressive (AR) parametric spectral estimate of the power spectrum (Roberts and Mullis, 1987), considered as a background spectrum.

In the following, we present three examples of simulated wavelet amplitude spectra in order to familiarize the reader with our wavelet technique. The first example refers to Figure 4.1a, which shows the wavelet amplitude spectra of a 1-year long signal obtained by superimposing harmonics of amplitude one at different time intervals. The wavelet spectrum shown in the left panel of this figure was obtained for ω_o=6 and is characterized by a relatively low frequency resolution. In this case, as a result of the reduced frequency resolution, the wavelet spectrum presents strong beatings between the relatively close spectral components, which appear as amplitude modulations. On the other hand, in the wavelet spectrum shown in the right panel of this figure, ω_o=12, the frequency resolution is higher, and consequently the spectral components appear as distinct lines well localized in time.

The second example refers to Figure 4.1b and represents an amplitude modulation case. In this case, a 30-day long signal of 1-day period is modulated by a 5-day period signal:

$$x(t) = \cos\left(2\pi t / T_{p1}\right) \cdot \left[1 + \cos\left(2\pi t / T_{p2}\right)\right] = \\ = \cos\left(2\pi t / T_{p1}\right) + 0.5 \cdot \cos\left(2\pi t / T_{s}\right) + 0.5 \cdot \cos\left(2\pi t / T_{d}\right) \tag{4.2}$$

where T_{p1}=1 day and T_{p2}=5 days are the primary periods, and $T_s=T_{p1}\cdot T_{p2}/(T_{p1}+T_{p2})$ = 0.833 days and $T_d=T_{p1}\cdot T_{p2}/(T_{p2}-T_{p1})$ = 1.25 days are the sum and difference secondary periods.

In the wavelet spectrum shown in the left panel of Figure 4.1b, ω_o=6 and the two secondary periods beat with the primary 1-day period, producing a 1-day period modulated in amplitude by a 5-day period. Conversely, the wavelet spectrum shown in the middle panel of this figure was obtained for ω_o=30 and consists of three distinct spectral components that correspond to the two secondary periods and to the primary 1-day period. For this latter case, the wavelet amplitudes of the three spectral components on day 15 are displayed in the right panel of the figure, which clearly illustrates that our wavelet method is able to determine the exact amplitudes of the spectral components in a signal. An important conclusion that can be drawn from these two examples is that, in a wavelet spectrum with reduced frequency resolution, two simultaneous and relatively close periods, T_1 and T_2, can beat with each other, with the beating period $T = T_1\cdot T_2/|T_1-T_2|$, and produce an amplitude modulation effect, which may appear as distinct and unrelated bursts of oscillation activity.

The third example refers to Figure 4.1c. In this case, the signal is given by:

$$x(t) = 2 \cdot \cos(2\pi t / T_{p1}) \cdot \cos(2\pi t / T_{p2}) = \cos(2\pi t / T_s) + \cos(2\pi t / T_d) \quad (4.3)$$

where T_{p1}= 1 day, T_{p2}= 10 days, T_s= 0.9091 days, and T_d = 1.11 days. The wavelet spectrum of this signal for ω_o=6 is shown in the left panel of Figure 4.1c and consists of two periods, T_s and T_d, that beat with each other with a 5-day beating period. Therefore, the beating between the two secondary periods produces, like in our second example, a 1-day period modulated in amplitude by a 5-day period, although different spectral components are present in the two cases. The middle panel of Figure 4.1c shows the wavelet spectrum of the signal for ω_o=30, where the two periods appear as distinct spectral components of amplitude one. To further demonstrate that our method is able to determine the correct amplitudes of the spectral components in a signal, the wavelet amplitudes of the two periodicities on day 15 are displayed in right panel of the figure.

It is thus clear from the examples presented here that, in most situations, a time domain analysis of a non-stationary signal by itself, which is very similar with our wavelet analysis for ω_o=6, might not be sufficient. At the other extreme a Fourier analysis might not help much either, as in this case the time information is completely lost. We therefore conclude that a better choice for analyzing non-stationary signals is to use the wavelet analysis, which provides an accurate way of representing a signal in the time-frequency domain, over a large frequency band.

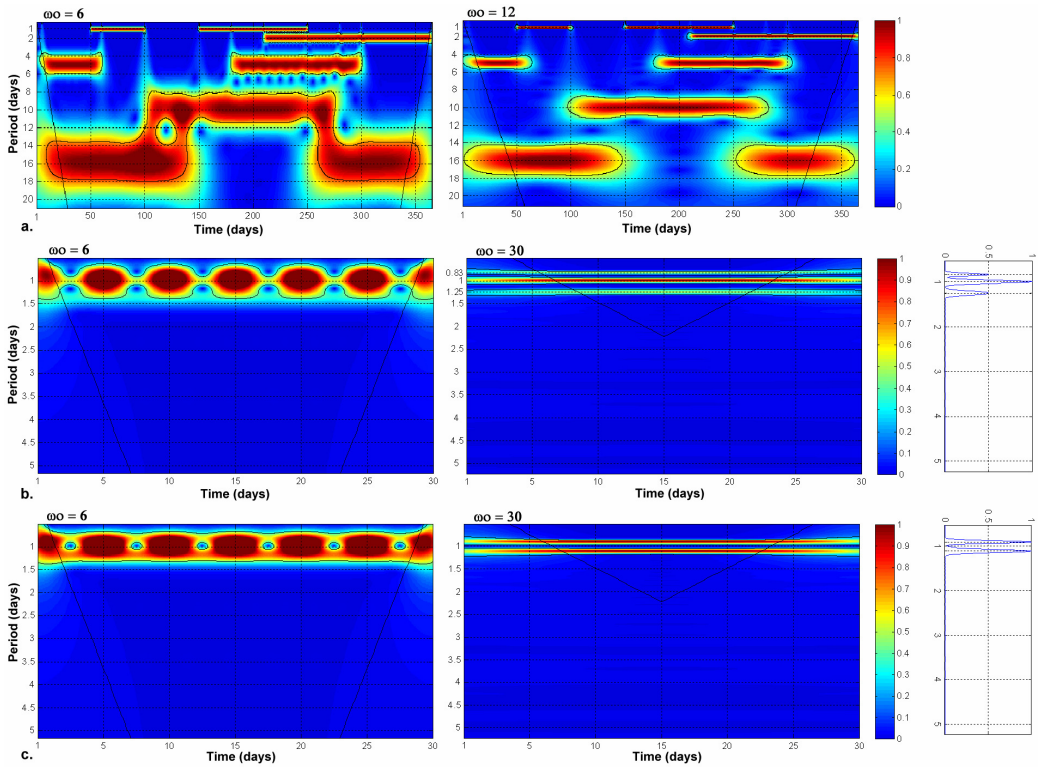

Figure 4.1: Wavelet amplitude spectra for the (a) first, (b) second, and (c) third example.

4.3 Low-latitude Zonal Electric Field Perturbations of Geomagnetic Origin

4.3.1 LLZEF Perturbations in the 1.25-12 day Period Range

Previous studies have shown that the geomagnetic activity is an important driver of planetary wave-like oscillations (periods in the 2-30 day range) in the ionosphere (Altadill and Apostolov, 2001; Forbes et al., 2000; Rishbeth and Mendillo, 2001; Pancheva, 2002). Therefore, in this section, we relate periodicities in the 1.25-12 day range that are present in the LLZEF spectra at Peruvian, Philippine, and Indian longitudes, with similar periodicities in the IEF-Ey spectrum, using the continuous wavelet approach presented in the previous section. The LLZEFs at the

three longitude sectors were obtained from magnetometer ΔH observations via a neural network-based vertical drift model (Anderson et al., 2004).

Figure 4.2a shows the daytime ΔH observations from the Peruvian, Philippine and Indian sectors as a function of local time and day number, for the entire year 2001, indicating a large day-to-day variability and seasonal changes, with peaks at equinox. The wavelet spectra of the ΔH observations at the three sectors, for the 0.2-1.8 day and 1.5-33 day period ranges, are shown in Figures 4.2b and 4.2c. Similar wavelet spectra for the LLZEF are displayed in Figure 4.3. It can be seen in Figures 4.2 and 4.3 that the main spectral features of the ΔH data in the 0.2-33 day period range are in general preserved by the neural network processing procedure of inferring the LLZEFs.

Referring to Figure 4.3b, some general characteristics are worth mentioning: (1) oscillations with periods in 1.5-33 day range in the LLZEF spectra at all three longitudes during 2001, (2) continuous and strong bursts of oscillation activity with periods less than about 5 days throughout the entire year at all three locations, (3) enhanced oscillation activity over a wide range of periods, mostly at the equinoxes, (4) intense oscillation activity at the Indian sector and low activity at the Philippine sector, and referring to Figure 4.3a, (5) stronger 8, 12, and 24-hour periods at the Philippine sector than at the other two sectors.

Figure 4.4 shows the wavelet spectrum (ω_o=6) of the IEF-Ey/15, over the entire year 2001. A scaling factor of 15 was used to obtain comparable amplitudes in the IEF-Ey and LLZEF spectra. The main features that can be remarked in this figure are: (1) continuous and strong bursts of oscillation activity with periods less than

about 5 days throughout the year, (2) enhanced oscillation activity over a large range of periods during November, December and at equinoxes, (3) small amplitude periodicities with periods less than about 5 days during January, February, and summer solstice, and (4) significant periodicities with periods less than about 10 days.

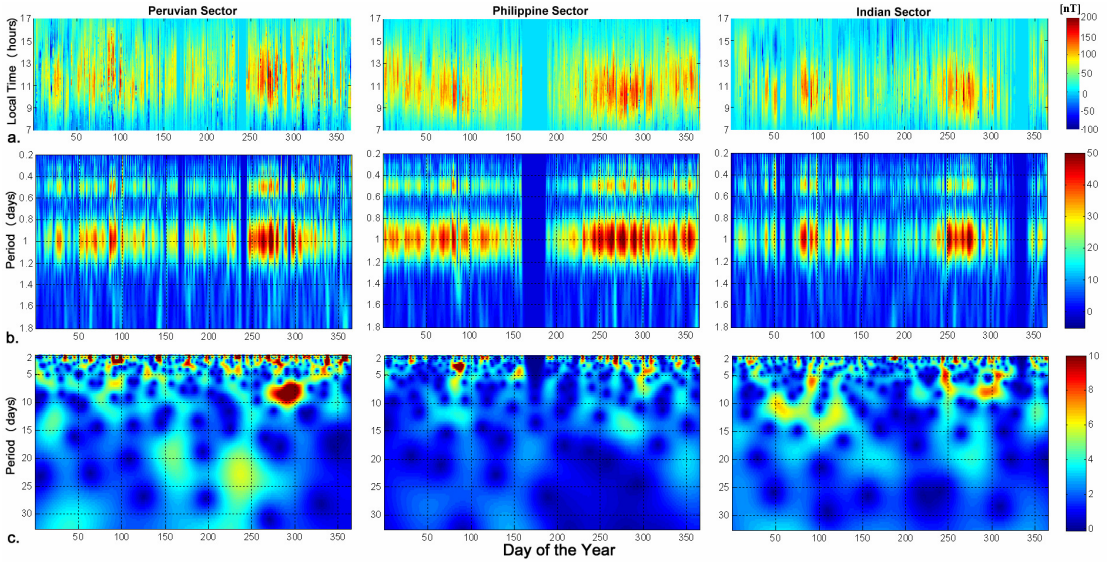

Figure 4.2: (a) ΔH observations at the three longitude sectors as a function of LT and day number, over the entire year 2001, (b) wavelet amplitude spectra (ω_o=6) for the 0.2-1.8 day period range, (c) wavelet amplitude spectra (ω_o=6) for the 1.5-33 day period range.

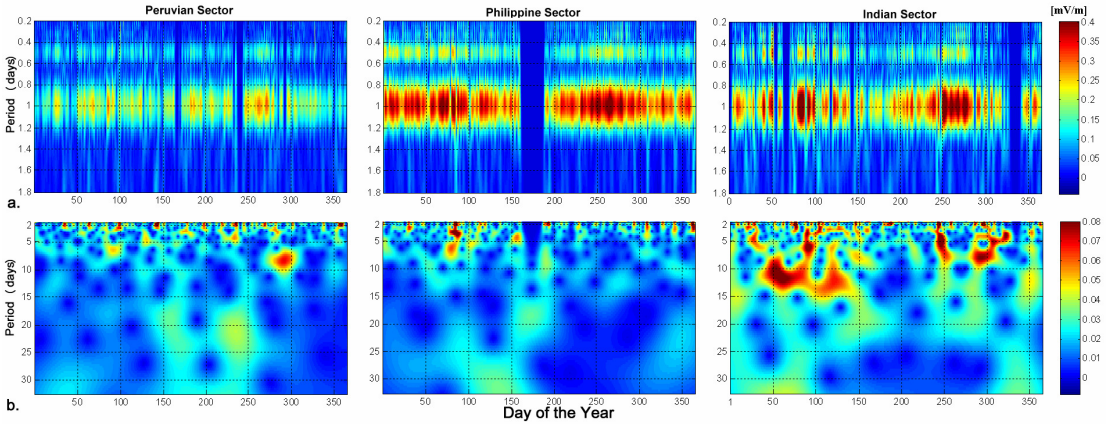

Figure 4.3: Wavelet amplitude spectra (ω_o=6) of the ΔH-inferred LLZEF for the (a) 0.2-1.8 day and (b) 1.5-33 day period ranges, at the three longitude sectors.

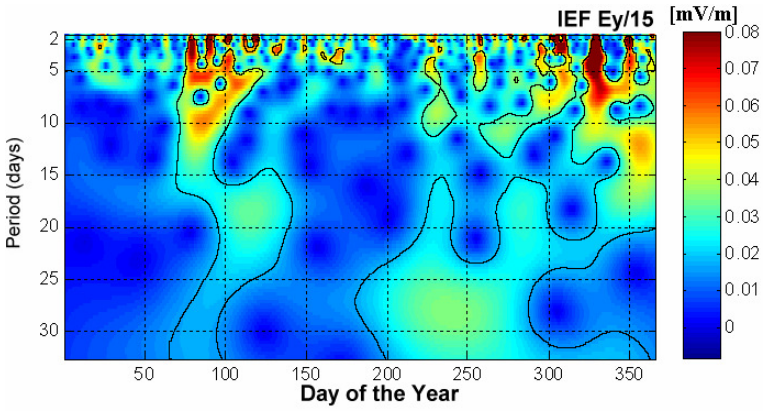

Figure 4.4: Wavelet amplitude spectrum of the IEF-Ey for the 1.5-33 day period range.

Subsequently, we focus our discussion on periods in the 1.25-12 day range in the LLZEF and IEF-Ey spectra, during the 9 February - 9 June (40-160) 2001 interval characterized by enhanced geomagnetic activity. The wavelet spectra of the LLZEF at the three longitudes and of the IEF-Ey/15 are shown in the left (ω_o=6) and middle (ω_o=30) columns of Figure 4.5, and their cross-wavelet spectra (ω_o=30) in the right column of this figure. As shown in the left panel of Figure 4.5a, in the 70-120 day interval, the IEF-Ey spectrum displays ongoing bursts of activity, which appear as amplitude modulations of the 1.25-5 day periods by a 10-day period. However, the plots shown in the middle panel of this figure reveal that the IEF-Ey spectrum is in fact relatively constant over this interval and presents distinct spectral components.

Figures 4.5b, 4.5c, and 4.5d show the LLZEF spectra corresponding to the Peruvian, Philippine and Indian sectors. It is clear from these figures that the LLZEF spectra (ω_o=30) at the three sectors present some common features. This is more evident at the Philippine and Indian sectors, which are separated by only 3 UT hours. To relate the oscillation activity in the LLZEF and IEF-Ey spectra, we employed the

cross-wavelet method described in the previous section. The cross-wavelet spectra are shown in the right column of Figure 4.5. The upper panel of this column shows the global cross-wavelet spectrum between IEF-Ey/15 and all three LLZEFs. It indicates similar periodicities that are simultaneously present in the IEF-Ey and LLZEF spectra. Several periodicities can be observed in the cross-wavelet spectra mostly near the 3, 4, 6, 7, and 9-day periods. We suggest that these periodicities in the LLZEF are most probably induced by geomagnetic disturbances and are probably associated with the penetration of the IEF-Ey to equatorial latitudes.

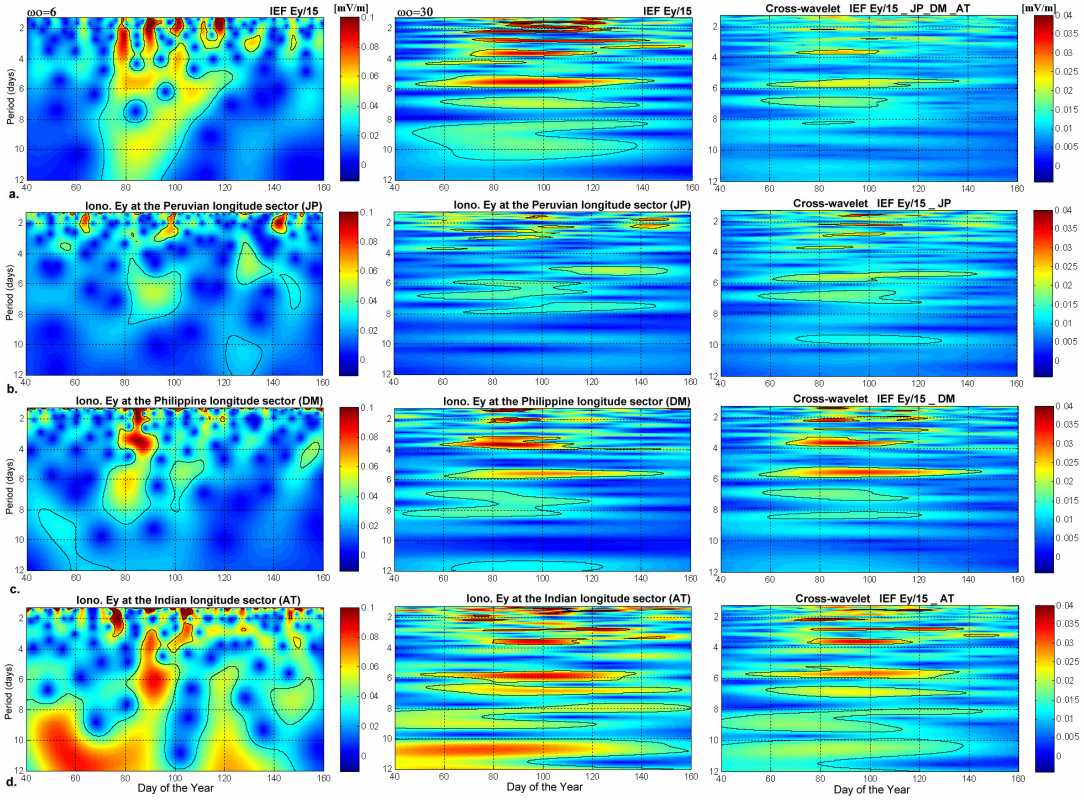

Figure 4.5: Wavelet amplitude spectra of the LLZEFs at the three longitude sectors, and of the IEF-Ey/15, in the 1.25-12 day period range and during the 40-160 day time interval in 2001, for (left) ω_o=6 and (middle) ω_o=30, and (right) cross-wavelet spectra for ω_o=30.

4.3.2 LLZEF Perturbations in the 10 min.-10 hour Period Range

In this section, we analyze the oscillation activity in the LLZEF and IEF-Ey spectra in the 10 min.-10 hour period range, for three storm-time cases and a quiet-time case. The three storm events examined are 17-19 April 2001, 15-18 April 2002 and 9-12 November 2004, and the quiet-time case is 29 March-2 April 2004, which is included here for comparison purposes, as a quite-time reference. In all four cases, concurrent observations of Jicamarca ISR zonal electric field and IEF-Ey data were available for at least three days. Time and frequency domain analyses of the three storm events have been reported previously in the literature (e.g., Kelley et al., 2007; Nicolls et al., 2007; Maruyama et al., 2007; Anghel et al. 2007), but this is the first time, to our knowledge, when the wavelet analysis in the form presented here has ever been used to study the relationships between the LLZEFs and IEF-Ey conditions.

During storm times, the most important sources of ionospheric electric field disturbances are the prompt penetration electric fields of solar wind/magnetospheric origin and the disturbance dynamo electric fields caused by the dynamo action of the storm-time winds. To identify the sources of ionospheric electric field perturbations during disturbed conditions, previous studies have used different Fourier-based spectral analysis techniques. Earle and Kelley (1987) performed Fourier analyses in the 1-10 hour period range, to identify the sources of ionospheric electric fields at equatorial latitudes and to study the frequency dependence of the penetration of the high-latitude convection electric fields to low latitudes. They found that for Kp greater than 3 and periods less than about 5 hours, the magnetospheric electric field

sources dominate the atmospheric sources, the entire system acting as a high-pass filter with a peak in the 3-5 hour period range and a roll-off near the 10-hour period.

More recently, Nicolls et al. (2007) using large data sets of concurrent IEF-Ey and ΔH-inferred LLZEF data, studied the frequency dependence of the electric field penetration mechanism using a frequency response/transfer function approach. They showed that the system, with IEF-Ey as input and LLZEF as output, behaves as a band-pass filter, which passes periodicities in the 30 min.-5 hour range, attenuates the longer periodicities, drops off at periodicities shorter than about 30 min., and peaks near the 2-hour period. In this section, we show that the wavelet analysis is a better tool for identifying the sources of period fluctuations in the LLZEFs, and that the filtering effect of the ring current is more complex than predicted by a time or a Fourier domain analysis, the wavelet analysis revealing in each of our case studies some peculiarities regarding the relationships between the IEF-Ey and LLZEFs.

Figure 4.6a shows the wavelet results for the 18 April 2001 storm event. The upper panel displays the LLZEF (red line) and IEF-Ey (blue line), scaled by a factor of 5, as a function of local time, during 17-19 April (107-109) 2001, when concurrent Jicamarca ISR zonal electric field and IEF-Ey data were available for several days. This storm event, characterized by a daily Ap value of 50, commenced and developed mostly during the nighttime at Jicamarca on April 17, which explains the strong anti-correlation between the two time series. The days before and after the event were quiet, with a daily Ap value of 7. This storm period was also analyzed in the previous chapter, and here we compare the corresponding IEF-Ey and LLZEF spectra in a wavelet domain with increased frequency resolution.

The wavelet amplitude spectra (ω_o=30) of the IEF-Ey and LLZEF, for periods ranging from 10 min. to 10 hours, are plotted in the middle and bottom panels, respectively, as functions of local time and period. The ratio between the maximum amplitudes in the two spectra is about 7, but for plotting purposes we used a scaling factor of 5. The wavelet spectrum of the IEF-Ey shows: (1) strong periodicities with periods less than about 1-hour confined to a time interval of increased IEF-Ey activity, (2) significant periodicities in the 1.5-3 hour range developing few hours in advance to the onset of increased IEF-Ey activity, persisting over the entire time interval of increased IEF-Ey, and then fading away about 4 hours after the increased IEF-Ey activity halts, and (3) a less significant 4-hour period persisting for several hours. As seen in the IEF-Ey spectrum, periodicities longer than about 1.5 hours form a background spectrum on which high-frequency components, with periods less than about 1-hour, superimpose during the interval of increased IEF-Ey activity.

The LLZEF spectrum presents some significant spectral components with periods less than about 3 hours that appear also in the IEF-Ey spectrum. There are two significant spectral components near the 1-hour period and one near the 2-hour period, each having a correspondent in the IEF-Ey spectrum. Of lesser significance are two spectral lines near the 3-hour period, a 4-hour period, a 5-hour period, and an 8-hour period. The 2.75-hour period seems to be associated with a strong and similar periodicity in the IEF-Ey spectrum, while the 3.2 and 5-hour periods cannot be directly linked with similar periodicities in the IEF-Ey spectrum. They stretch over long time intervals and may be caused with disturbance dynamo effects. The 4-hour

period is very weak and narrow banded, but appears also in the IEF-Ey spectrum, while the 8-hour period has relative constant amplitude over the entire interval.

The results for the 17 April 2002 storm event are presented in Figure 4.6b. The upper panel shows the Jicamarca zonal electric field (red line) and the IEF-Ey (blue line), scaled by a factor of 10, as a function of local time, for 15-18 April (105-108) 2002. During this time interval, the daily Ap varied from 7, on April 15, to 41 and 54, on April 17 and 18. The storm commenced and developed on April 17 during the daytime hours at Jicamarca, which explains the strong correlation between the two signals. We have, in this case, a scenario when both IEF-Ey and LLZEF evolved from quieter to more fluctuating values.

The IEF-Ey and LLZEF spectra are shown in the middle and bottom panels, respectively, the ratio between their maxima being about 7. The IEF-Ey spectrum presents several significant periods less than about 1-hour during daytime on April 17 when the IEF-Ey is highly fluctuating. Some predominant spectral components with periods longer than 1-hour can also be distinguished in the IEF-Ey spectrum: a 1.5-hour period, a 2-hour period, a 3.5-4 hour period, a 6-hour period, and a 9-hour period. The 1.5-hour period is present in the spectrum for about 24 hours, between the midnights on April 17 and 18, and the 2-hour period persists between noontime on April 16 and midnight on April 18, both periodicities being very strong during these time intervals. The other periodicities have smaller amplitudes and extend from early morning on April 16 to noontime on April 18. Conversely, the LLZEF spectrum is dominated by a strong 8-hour period over the entire time interval. It can be also remarked that on April 17, the periodicities less than 1-hour in the LLZEF spectum

appear also in the IEF-Ey spectrum. Other significant periodicities in the LLZEF spectrum are the 1.5, 2, and 4-hour periods, which are also present in the IEF-Ey spectrum, where they extend over wider period bands.

Our third case is presented in Figure 4.6c and refers to the 9 November 2004 event, which is part of a more complex storm event that commenced on 7 November 2004. The upper panel shows the LLZEF (red line) and IEF-Ey (blue line), scaled by a factor of 10, for 9-12 November (314-317) 2004. The daily Ap values for November 9 and 10 were 120 and 181, respectively, and the ratio between the maxima of the IEF-Ey and LLZEF spectra is about 7. The wavelet spectrum of the IEF-Ey is displayed in the middle panel and shows significant periodicities less than about 2 hours, mostly confined to an interval of strong and highly fluctuating IEF-Ey. A dominant 3-hour period is also observed between early hours on November 9 until about noon on November 10. There are also other significant spectral components in the IEF-Ey spectrum, which extend over long time intervals of more than 4-5 days, but possibly developed even earlier on November 6 or 7.

The LLZEF spectrum for this storm event is not as spectacular as the IEF-Ey spectrum and does not show any significant periodicities in the 4-8 hour period band. There are some significant periodicities less than about 2-hours and a strong 3-hour period, similar with those in the IEF-Ey spectrum, and two less significant and narrow-banded 4 and 6-hour periods. The LLZEF spectrum is dominated by two strong and persistent 8 and 9.5-hour periods. The two periods might be associated with disturbance dynamo effects and/or upward propagating waves since they do not have a direct correspondent in the IEF-Ey spectrum. The 8-hour period, most

probably attributed to the terdiurnal tide, appears in all three storm events and also in the quiet-time case shown in Figure 4.6d. Since it presents different amplitudes in each case, this might suggest that its magnitude dependents on the strength of the storm, although seasonal variations might be also involved.

It is thus clear from Figure 4.6 that, for the 18 April 2001 and 17 April 2002 storm events, characterized by daily Ap values of about 50, the IEF-Ey spectra display significant periodicities with periods less than about 4 hours that emerged from a noisy background spectrum. For the 9 November 2004 event, characterized by daily Ap values greater than 120 for three consecutive days, the IEF-Ey spectrum also presents distinct period bands of large amplitudes that superimpose on a noisy background spectrum.

In the storm cases considered here, some of the significant periodicities in the IEF-Ey spectrum, especially those with periods less than about 4 hours, are also present in the LLZEF spectrum, but as very narrow bands compared to their counterparts in the IEF-Ey spectrum. Also, the LLZEF spectrum for the 9 November 2004 event does not show any significant periodicities in the 4-8 hour range, except for two weak and narrow spectral bands, although there is a quite strong oscillation activity in the IEF-Ey spectrum in this period range. Our results also indicate that, in general, periodicities with periods longer than about 1.5 hours appear in both IEF-Ey and LLZEF spectra several hours in advance of a visible storm onset, as in the case of the 17 April 2002 event, and usually persist for several hours after the main phase of a storm, as in the case of the 18 April 2001 and 9 November 2004 events.

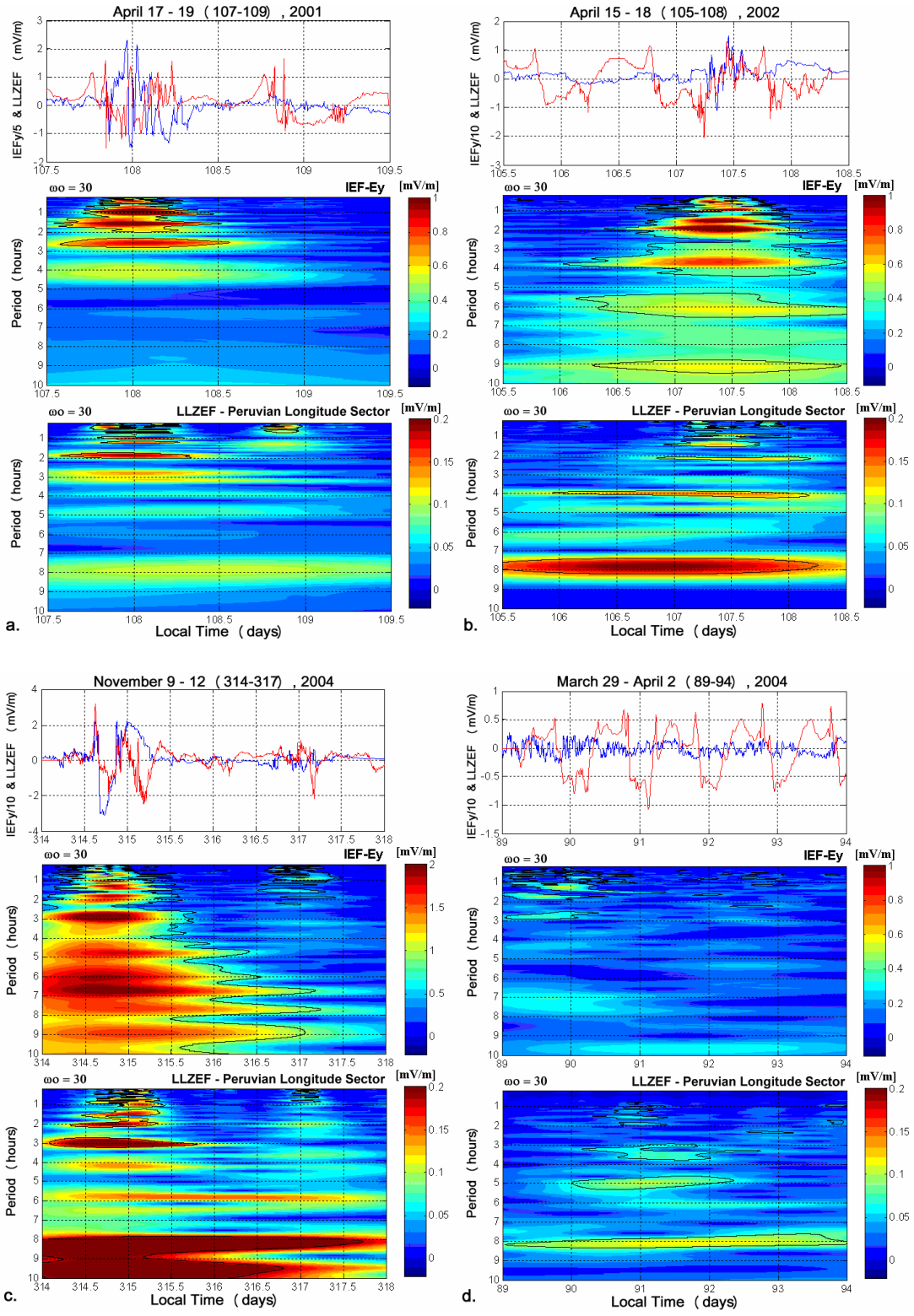

Figure 4.6: The LLZEF (red line) and IEF-Ey (blue line), and their wavelet amplitude spectra, over the 10 min.-12 hour period range, for (a) 17-19 April 2001, (b) 15-18 April 2002, (c) 9-12 November 2004, and (d) 29 March - 2 April 2004.

We conclude that, in the 10 min.-10 hour period range, the system with IEF-Ey as input and LLZEF as output behaves as a highly-nonlinear time-varying filter, which seems to attenuate more periodicities longer than about 4 hours, as seen in the 9 November 2004 event. Also, we suggest that similar periodicities that occur simultaneously in both LLZEF and IEF-Ey spectra are most probably caused by penetration effects, while periodicities with periods longer than ~3 hours, which are present in the LLZEF spectrum but not in the IEF-Ey spectrum, might be attributed to disturbance dynamo effects, although some other processes may be also involved.

4.4 Conclusion

In this chapter, we have used the Morlet wavelet transform in order to relate the oscillation activity in the LLZEF and IEF-Ey spectra, in the 10 min.-10 hour and 1.25-12 day period ranges, during time intervals of enhanced geomagnetic activity. The wavelet method described here provides accurate "instantaneous" amplitude and phase values for the periodicities present in a signal and can be easily tuned to different frequency resolutions in the wavelet domain. Three examples of simulated wavelet spectra have been presented to familiarize the reader with the method.

We have shown that the continuous wavelet transform represents a powerful tool to study the frequency dependence, in the 10 min.-10 hour period range, of the two specific mechanisms of equatorial electric field variability which are dominant during disturbed periods, namely penetration and disturbance dynamo mechanisms. In separating out the two contributions, we associated a periodicity longer than about

3 hours in the LLZEF spectrum with disturbance dynamo effects if it were not simultaneously present in the LLZEF and IEF-Ey spectra, and considered that a periodicity in the LLZEF spectrum was due to electric field penetration effects if it were simultaneously present in both LLZEF and IEF-Ey spectra, although other processes could also be involved. In doing so, we considered that fact that previous studies associated a periodicity in the LLZEF spectrum with the penetration effects if it were present in both LLZEF and IEF-Ey Fourier spectra (e.g., Earle and Kelley, 1987; Nicolls et al., 2007), although there was no information about its occurrence time in the two spectra. It is also important to mention that our wavelet-based techniques described here can also be used to study the penetration efficiency and the characteristic time scales of the electric field penetration effects via wavelet-based transfer function approaches.

We have also shown that wavelet and cross-wavelet analyses indicated significant periodicities that occurred simultaneously in both LLZEF and IEF-Ey spectra in the 1.25-12 day period range, during 9 February-9 June 2001. It is thus possible that these periodicities may have been caused by electric field penetration effects, but it is not excluded that other processes could have been also involved.

We conclude that wavelet analysis in conjunction with physics-based models and ground and satellite observations can provide a deeper understanding of the sources of variability in the LLZEF and of the system that links the IEF-Ey and LLZEFs. Here we have provided new methods of analysis and presented a few case studies, but separating out the sources of ionospheric electric field variability still remains a task that requires further investigations.

Chapter 5

Empirical Models of the Penetration Electric Fields at Peruvian and Indonesian Longitudes

5.1 Background

The equatorial ionospheric electric fields are important ionospheric parameters that play a crucial role in plasma distribution at low and mid-latitudes. Their quiet-time and storm-time behavior has been studied for decades using radar, magnetometer, ionosonde, and satellite observations (e.g., Fejer and Scherliess, 1995; Batista et al., 1996) and useful models describing their morphology under different geophysical conditions have been developed (e.g., Richmond et al., 1980; Fejer and Scherliess, 1997; Scherliess and Fejer, 1997, 1999). In this context, our main purpose in this chapter is to investigate the storm-related changes in the electrical structure of the equatorial ionosphere caused by the penetration of the interplanetary electric field (IEF) to equatorial latitudes, namely the penetration electric fields.

The penetration electric fields are electric fields of solar wind/magnetospheric origin observed equatorward of the shielding layer, located at the inner edge of the ring current. Under geomagnetically quiet and steady conditions, the shielding layer acts to shield the low and mid-latitude ionosphere from the high-latitude magnetospheric convection electric fields through the action of the region-2 field aligned currents (e.g., Huang et al., 2005). Consequently, during quiet times, the low and mid-latitude ionospheric electric fields are primarily generated through the dynamo action of the neutral winds.

During disturbed conditions though, two main sources of perturbation electric fields have been identified at equatorial latitudes: (1) the penetration electric fields caused by the penetration of the high-latitude electric fields of solar wind/ magnetospheric origin to equatorial latitudes, and (2) the disturbance dynamo electric fields, caused by the dynamo action of the storm time winds. The latter have long lifetimes, of up to 30 hours, and usually manifest a few hours after a storm onset. Their net effect is to suppress the normal quiet-time pattern of the daytime, equatorial ionospheric electric fields during the main phase of a storm. On the other hand, the former operate on relatively short time scales, of less than a few hours, and propagate instantaneously to equatorial latitudes. They are dominant during the main phase of a storm and are in general attributed to the development of asymmetric ring currents, to the undershielding and overshielding effects, fossil winds, and magnetospheric reconfiguration (e.g., Fejer and Scherliess, 1995).

Of relevance to our current studies is the penetration of the dawn-to-dusk component of the IEF, IEF-Ey, to equatorial latitudes. According to the physics of the

solar wind-magnetosphere-ionosphere coupling, the penetration of the IEF-Ey to the low and mid-latitude ionosphere is mainly controlled by the sign and magnitude of the north-south component of the interplanetary magnetic field, IMF-Bz, as more negative (southward) IMF-Bz values imply a faster rate of reconnection and flux transfer into magnetosphere, while positive (northward) IMF-Bz values cause a reduction in the reconnection rate.

Two mechanisms have been proposed to explain the penetration of the IEF-Ey to the equatorial ionosphere: the undershielding and the overshielding mechanisms. The undershielding effect is produced by polarization charges that accumulate at the inner edge of the ring current during enhanced magnetospheric convection associated with a sudden southward turning of the IMF-Bz (which corresponds to a dawn-to-dusk IEF-Ey). The role of the shielding charges is to create a dusk-to-dawn electric field in order to cancel out the effect of the primary dawn-to-dusk electric field. Conversely, the overshielding effect occurs when the magnetospheric convection is suddenly weakened as a result of a sudden northward turning of the IMF-Bz (which corresponds to a dusk-to-dawn IEF-Ey). In this latter case, the dusk-to-dawn electric field generated by the shielding charges produces an eastward electric field on the nightside and a westward electric field on the dayside.

It is important to remark that an eastward (westward) electric field on the dayside and a westward (eastward) field on the nightside are both in the dawn-to-dusk (dusk-to-dawn) direction in a sun-fixed system, such that the fluctuations in the equatorial zonal electric field Ey and IEF-Ey are positively correlated during daytime and anti-correlated during nighttime. It is also noteworthy that besides penetration

effects associated with fluctuations in the IEF-Ey, the substorms are also important sources of magnetospheric electric field perturbations which can as well penetrate to equatorial latitudes.

An important aspect regarding the electric field penetration mechanism is the penetration efficiency, defined by Huang et al. (2007) as the ratio between the change in the IEF-Ey and the corresponding change in the Ey. Huang et al. (2007) conducted statistical studies of the IEF-Ey penetration efficiency using vertical ExB drifts measured by the JULIA system at Jicamarca, Peru, and derived an empirical linear formula based on 73 daytime (1000-1300 LT) events, between 2001 and 2005, characterized by rapid (0.5-1 hour) southward turnings in the IMF-Bz. They determined an approximate ratio of about 10 between the fluctuating IEF-Ey and the penetration electric fields at equatorial latitudes. A similar value for the penetration efficiency was determined by Burke (2007) using the Volland-Stern model, while Kelley et al. (2003) found a value of 15 in a single storm event study.

Spectral studies of the ionospheric and interplanetary electric fields using Fourier and continuous wavelet transforms showed that the penetration mechanism and hence the penetration efficiency are in fact frequency dependent (e.g., Earle and Kelley, 1987; Nicolls et al., 2007; Anghel et al., 2008a). Nicolls et al. (2007) determined an average frequency response function between IEF-Ey and the daytime Ey at Peruvian longitudes, with a broad maximum centered near the 2-hour period. Earle and Kelley (1987) also presented a measure of the transfer function for electric field penetration between high and low-altitude L-shells, with peaks in the 3-5 hour period range and roll-off near the 10-hour period.

Another important aspect regarding the electric field penetration mechanism is the characteristic time scale within which IEF-Ey can penetrate to low latitudes without significant shielding. Previous theoretical and modeling studies provided estimates of the shielding time ranging from about 10-30 min up to about 5 hours (e.g., Jaggi and Wolf, 1973; Senior and Blanc, 1984; Fejer and Scherliess, 1995). More recent studies, though, showed that IEF-Ey can in fact continuously penetrate to low latitudes for several hours without effective shielding during the main phase of a magnetic storm as long as IMF-Bz remains southward (e.g., Huang et al., 2005; Huang et al., 2007).

In this chapter, we present several least-squares and neural network-based algorithms developed to quantify the relationship between IEF-Ey and the daytime penetration electric fields at equatorial latitudes, and to investigate the shielding effect of the ring current in both time and frequency domains. The models were developed based on several years of IEF-Ey data derived from ACE satellite measurements and on daytime (0700-1700 LT), equatorial ΔH observations collected from magnetometers in Peru and Indonesia. We assess the performance of our models by applying them to IEF-Ey observations and to numerically simulated signals. We show that our results are in good to excellent agreement with results reported by previous studies (e.g., Earle and Kelley, 1987; Huang et al., 2007; Nicolls et al., 2007).

5.2 Dataset Description

5.2.1 Equatorial Zonal Electric Field Data

We showed in Chapter 3 that the equatorial zonal electric field Ey can be inferred from the difference in the horizontal H component, ΔH, between two magnetometers, one located on the magnetic equator and the other located slightly off the magnetic equator. In the two-site magnetometer method, the concept is that the magnetic field perturbations produced by the ring current affect both sites equally, whereas the magnetic field caused by the equatorial electrojet is confined to the near equatorial site. The main contribution to ΔH is then attributed to the equatorial electrojet, although other sources, such as wind-driven currents and other current systems, can become significant under certain circumstances and add some limitations to this approach. This idea has been successfully extended to other longitudes, assuming that any remaining ring current effects are removed from the neural network output since it learns from the measured electric field at Jicamarca.

For our studies, we used concurrent observations of IEF-Ey and ΔH-inferred Ey fields from Peru and Indonesia, at a temporal resolution of 5 minutes. The daytime (0700-1700 LT) Ey fields were obtained by applying the neural network-based algorithm described in Chapter 3 to ΔH observations collected from Peru and Indonesia between 2001 and 2007 and, respectively, between 2001 and 2004, knowing that 1 mV/m corresponds to about 40 m/s at Peruvian longitudes and to about 28 m/s at Indonesia. The network consists of 15 hidden neurons and is

parameterized in terms of year, day of the year (DOY), F10.7, 90-day average F10.7A, daily Ap index, 3-hourly Kp index, local time (LT), solar zenith angle (SZA), and ΔH. It was trained with daytime vertical ExB plasma drifts from the Jicamarca ISR and JULIA radars and with magnetometer observations from Jicamarca (11.9^{o}S, 283.1^{o}E, geom. 0.8^{o}N) and Piura (5.2^{o}S, 279.4^{o}E, geom. 6.8^{o}N), Peru, between 2000 and 2009. At Indonesia, the magnetometer data were obtained from Yap (9.5^{o}N, 138.08^{o}E, geom. 1.49^{o}N) and Biak (-1.08^{o}, 136.05^{o}, geom. 9.73^{o}S).

5.2.2 Solar wind data

To describe the inteplanetary conditions, we used ACE satellite data and calculated the IEF-Ey based on the formula:

$$E_y = -V_z \cdot B_x + V_x \cdot B_z \tag{5.1}$$

where V and B are the solar wind velocity and magnetic field, respectively, in Geocentric Solar Magnetospheric (GSM) coordinates, measured by the MAG and SWEPAM instruments on ACE. In the GSM system the x-axis is along the Sun-Earth line and is positive towards the Sun, the y-axis is the cross product of the x-axis and the geomagnetic dipole axis, being positive towards the dusk, and the z-axis is the cross product appropriate for a right-hand coordinate system, being positive in the same sense as the magnetic north. The IEF-Ey calculated at the spacecraft was delayed by the transit time from the ACE satellite to the magnetopause using the solar

wind velocity, and an additional 10 minute time delay was added to account for the solar wind travel through the magnetosheath.

5.3 Modeling Techniques

To quantify the relationship between IEF-Ey and the storm-induced equatorial electric field perturbations and to investigate the shielding effects associated with the ring-current, we have developed several algorithms based on multiple linear regression (MR) analysis, finite impulse response (FIR) filters, and neural networks. The methods are described subsequently.

5.3.1 Multiple Linear Regression (MR) Analysis

In this approach, the purpose is to establish quantitative relationships between a set of inputs and an output variable. For our particular case, the inputs are Kp, LT, IEF-Ey, and IEF-Ey^2, and the output is the deviation of the equatorial zonal electric field Ey from a quiet-time reference, dEy. The method consists in determining some regression coefficients from a set of input/output pairs by casting the problem into a simple algebraic equation and applying the linear least-squares algorithm.

5.3.2 Finite Impulse Response (FIR) Filter Approach

We use an FIR filter as a system identification tool in order to investigate the dynamics of the shielding mechanism associated with the ring-current. The method assumes that the system to be identified is linear and time-invariant. Although, this is not quite our case, we use an FIR filter to obtain general information about the system's dynamics.

An N^{th} order FIR filter is a type of digital filter characterized by a difference equation of the form:

$$y(n) = b_o \cdot x(n) + b_1 \cdot x(n-1) + \cdots + b_N \cdot x(n-N) = \sum_{k=0}^{N} b_k \cdot x(n-k) = B^T \cdot X(n) \quad (5.2)$$

where x is the input, y is the output, $\{b_i\}_{i=0..N}$ are the coefficients of the filter, and **B** is the vector containing the filter coefficients. It is thus clear from Equation (5.2) that the output of an FIR filter is just the weighted sum of the inputs. In our case, the input is IEF-Ey and the output is dEy.

The *impulse response* of an FIR filter can be determined by setting $x(n) = \delta(n)$, where $\delta(n)$ is the Kronecker data impulse:

$$h(n) = \sum_{k=0}^{N} b_k \cdot \delta(n-k) = b_n \text{ for } n = 0,..,N. \quad (5.3)$$

Therefore, the impulse response of an N[th] order FIR filter is represented by the set of coefficients $\{b_i\}_{i=o,..,N}$ and can last for only (N+1) samples. The Z-transform of the impulse response is the *transfer function* of the FIR filter:

$$H(z) = Z\{h(n)\} = \sum_{k=-\infty}^{\infty} h(k) \cdot z^{-k} = \sum_{k=-\infty}^{\infty} b_k \cdot z^{-k} \tag{5.4}$$

while its Fourier transform represents the *frequency response function* of the filter:

$$H(j\omega) = F\{h(n)\} = \sum_{k=-\infty}^{\infty} h(k) \cdot e^{-j\omega k} = \sum_{k=-\infty}^{\infty} b_k \cdot e^{-j\omega k} \tag{5.5}$$

where ω is the Fourier angular frequency.

Both the impulse response and frequency response function contain complete information about the system. Therefore, the main purpose is then to determine the filter coefficients from a set of input/output pairs. According to Equation (5.2), once the training samples are selected and the order of the filter established, the coefficients of the filter can be easily calculated in a straightforward manner by solving the algebraic equation $\mathbf{Y} = \mathbf{B}^{\mathbf{T}} \cdot \mathbf{X}$ in a least-squares sense, where **Y** is the output vector and **X** is a matrix whose rows contain the current and the N previous input values for each component in **Y**.

5.3.3 Neural Network (NN) Approach

The neural networks have been employed here since they do not impose any constraints on the linearity of the system to be studied. Hence, they are expected to provide more accurate solutions to the system identification and regression problems at hand than the methods discussed above.

Two multilayer feedforward neural network structures, schematically depicted in Figure 5.1, have been chosen: one to quantify the relationship between IEF-Ey and the penetration electric fields at equatorial latitudes (Figure 5.1a), and the other to investigate the system's dynamics (Figure 5.1b). In both cases, x_k is IEF-Ey and y_k is dEy, at the time instant k. In the first case, shown in Figure 5.1a, the network's inputs are Kp, LT, and IEF-Ey, while in the second case, shown in Figure 5.1b, the inputs are the current and the N previous values of IEF-Ey. It is interesting to remark that in the second case the network acts as a nonlinear N^{th} order FIR filter.

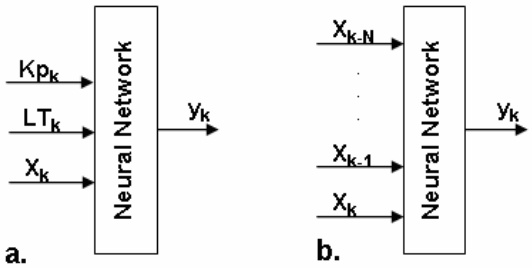

Figure 5.1: Schematics of the neural networks used in the analysis.

For our studies, N is 120 since we use 10 hours of daytime Ey observations, between 0700 and 1700 LT, at a temporal resolution of 5 minutes, which corresponds to 120 samples of Ey values.

5.4 Selecting the Training Samples

The training samples used in our studies consist of simultaneous observations of IEF-Ey and dEy, corresponding to Kp values greater than 4. This selection criterion was imposed by the fact that according to Earle and Kelley (1987), for Kp values greater than 4, the fluctuations in the zonal electric field at Jicamarca with periods less than10 hours are primarily caused by fluctuations in the high-latitude magnetospheric electric field, while for Kp values less than 3, the equatorial field fluctuations are primarily due to fluctuating atmospheric winds.

The dEy values were obtained by detrending the equatorial electric field using representative quiet-time values. Such a quiet-time field component was determined for each training sample by averaging the Ey values, characterized by Kp values less than 3 and same local time as the training sample, over a 21-day interval centered on the day corresponding to the training sample. The purpose of this procedure is to isolate the penetration electric fields from the quiet background conditions and to correct, up to some extent, for the disturbance dynamo effects. It needs though to be specified that this procedure is not effective in eliminating the substorm-induced penetration effects and the effects of the gravity waves, which too are considered important sources of periodic fluctuations in the equatorial zonal electric fields in this period range.

5.5 Modeling the Relationship between IEF-Ey and the Penetration Electric Fields at Peruvian Longitudes

For the studies presented in this section, we used seven years of IEF-Ey observations and ΔH-inferred zonal electric fields from the Peruvian longitude sector, between 2001 and 2007. Figure 5.2 shows, from top to bottom, the wavelet amplitude spectra (ω_o=40) of the Ey predicted by the Fejer-Scherliess model (Fejer and Scherliess, 1997) and inferred from ΔH observations, only for those days with available ΔH observations, and of the IEF-Ey/10, for the 1-10 hour period range and between 2001 and 2007.

It is clear from the spectra shown in Figure 5.2 that the most dominant features in the modeled and observed equatorial Ey fields are the 6 and 8-hour periods corresponding to the quarterdiurnal and terdiurnal tides. The two dominant spectral components display significant annual and semiannual variations over the entire seven year interval and amplitudes of up to ~0.08 mV/m. Other significant spectral components but of much smaller amplitudes can be also noticed near the 3 and 4-hour periods, and they too may represent some higher harmonics of the diurnal tide.

In general, the two Ey spectra are similar and display dominant horizontal features. However, there are also significant differences between the two Ey spectra which motivate the chosen detrending procedure adopted to calculate dEy, instead of using the drifts predicted by the Fejer-Scherliess model. The vertical features in the Fejer-Scherliess Ey spectrum are caused by gaps in the data, which means that some of the vertical features in the ΔH-inferred Ey spectrum are also caused by data gaps.

Other vertical features in the ΔH-inferred Ey spectrum are due to solar wind/magnetosphere phenomena and gravity wave activity, which are also responsible, at least partially, for the random aspect of this spectrum. By contrast to the Ey spectra, the IEF-Ey spectrum exhibits a high degree of randomness and dominant vertical features, which are probably associated with sudden variations in IEF-Ey. Several of the vertical features in the IEF-Ey spectrum coincide with those in the ΔH-inferred Ey spectrum and are most probably indicative of penetration effects.

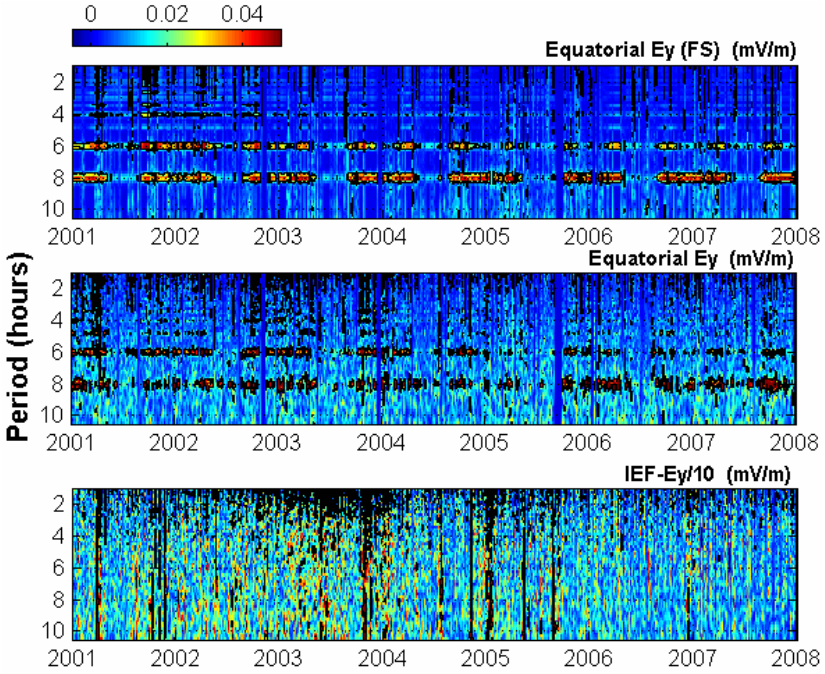

Figure 5.2: Wavelet amplitude spectra (ω_o=40) of the equatorial Ey (top) predicted by the Fejer-Scherliess model and (middle) inferred from ΔH observations at the Peruvian sector, and (bottom) of IEF-Ey/10 for the 1-10 hour period range, from 2001 to 2007.

To investigate the dynamics of the system that has IEF-Ey as input and the variations in the equatorial zonal electric field, dEy, as output, we employed an FIR filter and a neural network approach. We remind the reader that an FIR filter assumes

that the system is linear and time-invariant, while a neural network does not make any assumptions about the system to be identified. Thus, by using an FIR filter we obtain information about the general linear behavior of the system, while by using a neural network we can also capture non-linear features of the system's dynamics. However, given that the neural networks are very sensitive to the quality of the training set, some caution is required in interpreting their results, as it will be shown later. In both approaches, the filter and the network have 120 inputs consisting of the current and the previous 10 hours of IEF-Ey values. This allows us to determine the impulse response of the system over a 10 hour interval, which is exactly the length of our daytime observations.

As discussed earlier, dEy is calculated for Kp greater than 4 by subtracting a quiet-time component from Ey. About 37000 of such dEy values were obtained and used to build the training set. Both models were trained with the same training set, and the training root mean square (RMS) errors for the neural network model and FIR filter were about 0.1709 mV/m and 0.1780 mV/m, respectively. To assess the consistency of our results, and also for comparison purposes, we developed additional FIR filter and neural network models with IEF-Ey as input and the variations in ΔH, $d(\Delta H)$, as output. In this latter case, the training RMS errors associated with the neural network model and FIR filter were 33.723 nT and 33.819 nT, respectively. Once trained, we tested the models for different simulated signals in order to extract information about the system's dynamics. The results are presented in the following.

The frequency response functions and the impulse responses of the FIR filters (green lines) and neural network models (red lines) are shown at the top of Figures

5.3a and 5.3b. In these plots, the normalized magnitudes of the frequency response functions are plotted as a function of period over the 10 min-24 hour period range, while the impulse responses are plotted as a function of local time, for 0700-1700 LT. In addition to the frequency and impulse responses, Figure 5.3 also shows the models' responses, as a function of local time, to six simulated inputs that resemble to some degree the types of fluctuations usually observed in the IEF-Ey. The first, second, and third cases correspond to 10, 4 and 2-hour long pulse waves of amplitude one, starting at 0700 LT. The fourth and fifth cases are ramp and triangular waves, respectively, and the sixth case is a sinusoidal wave with a 2-hour period. It is clear from these plots that the FIR filters predict similar behavior whether dEy or d(ΔH) is used as output, while the neural network models predict slightly different responses.

To determine the sources of these differences, we need to take a look at the frequency response functions of the FIR filters and neural network models. First, it is important to remark that the frequency response functions of the FIR filters indicate a band-pass filter with a roll-off just before the 10-hour period and peaks near the 4 and 6-hour periods, periodicities shorter than about 1 hour and longer that about 10 hours being attenuated by the system. For the case shown in Figure 5.3b, the frequency response functions of the FIR filter and neural network model, and also their responses to all six test signals, are very similar. For the case shown in Figure 5.3a though, the frequency response functions of the neural network model and FIR filter display large discrepancies in the 3-5 hour period range and so do their responses to some of the test signals. In this case, the frequency response function of the neural network model shows a suppression of the periodicities in the 3-5 hour range, which

may explain the gradual decay in the pulse and ramp responses, which settle to zero after about 6 hours. We suggest that the observed suppression of the periodicities in the 3-5 hour range may be due to the nonlinear character of the neural network model and also to the quality of the training data set. Here we will explain the dynamics of the system based on the FIR filter responses since they are in general more consistent.

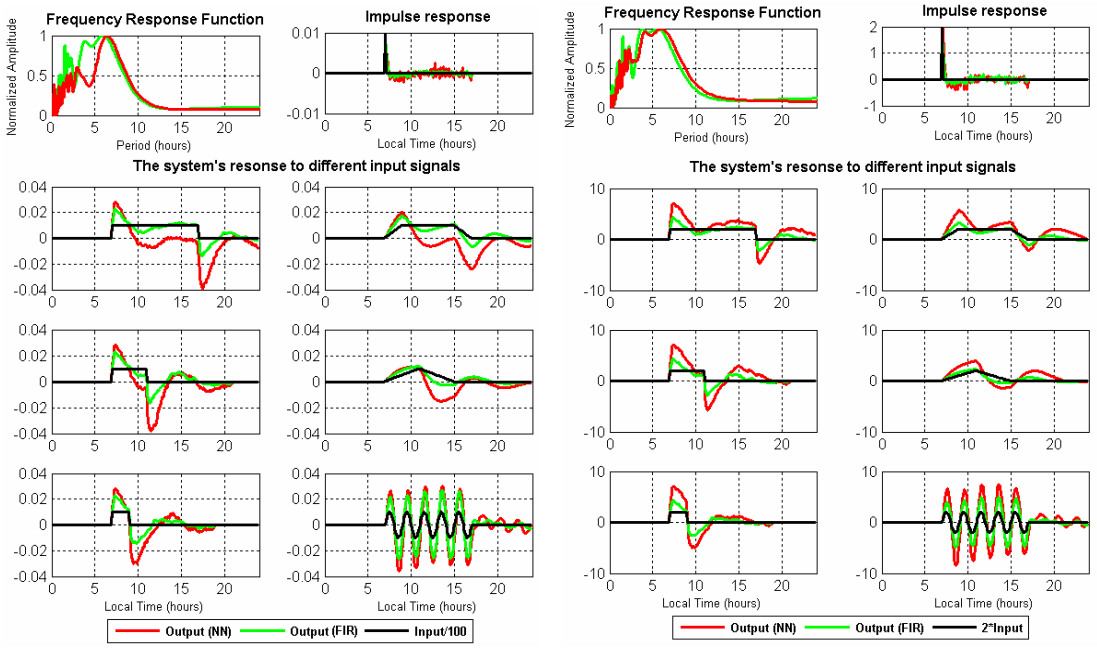

a. b.

Figure 5.3: (top) The frequency response functions and the impulse responses of the FIR filters (green) and neural network models (red) with IEF-Ey as input and (a) dEy and (b) d(ΔH) at the Peruvian sector as outputs. (bottom) The responses of the FIR filters (green) and neural network models (red) to different test signals.

As shown in Figure 5.3a, the impulse and step responses of the FIR filter indicate an oscillatory system with a natural period of about 6 hours, a rise time less than 30 minutes, a settling time of about 6 hours, a damping ratio of about 0.2 corresponding to about 50% overshoot in the step response, and an amplification factor of about 1% of the input for steady-state conditions. Our results are consistent

with those reported by Nicolls et al. (2007), where they explained that the weakly resonant behavior predicted by the models may indicate that, in addition to the self-inductance of the ring current and the resistance of the ionosphere, there exists some capacitance in the system, but the physical mechanisms behind such an equivalent circuit have not been investigated.

The long-duration responses to pulse and ramp signals also support the notion that the response of the equatorial zonal electric field to long-duration IEF-Ey polarities can last for many hours, which is in agreement with the long-duration penetration events presented by Huang et al. (2007). It is also interesting to remark that both rising and falling edges of the pulse and ramp signals produce enhanced responses, which in our case are symmetrical due to the fact that FIR is a linear phase filter. This basically means that the equatorial ionospheric electric field responds to both southward and northward turnings of the IMF-Bz in very similar ways, which is consistent with the results reported by Nicolls et al. (2007). It can be also added that the system's response to a triangular wave is typical of an oscillatory system and the response to a sinusoidal wave is a sinusoidal wave of the same frequency and phase as the input wave.

To assess the validity of the two FIR filters discussed above, we calculated the average standard deviations associated with their coefficients. The values we found are around 0.0011 and 0.22 nT/mV/m. They were determined by estimating the FIR filter coefficients for 20 individual cases, and then by calculating the standard deviation and the mean values for those 20 cases. In each case, the coefficients were estimated based on two-thirds of randomly selected samples from the total training

set. It was found that the coefficients of the two FIR filters were almost identical with the mean values of the estimated coefficients for the 20 cases. The estimated coefficients for each individual case along with the coefficients of the two FIR filters (thick cyan lines) are shown in Figure 5.4. Given that there is a high variability in the penetration events from case-to-case, we consider that the observed variability in the coefficients of the two filters is reasonable.

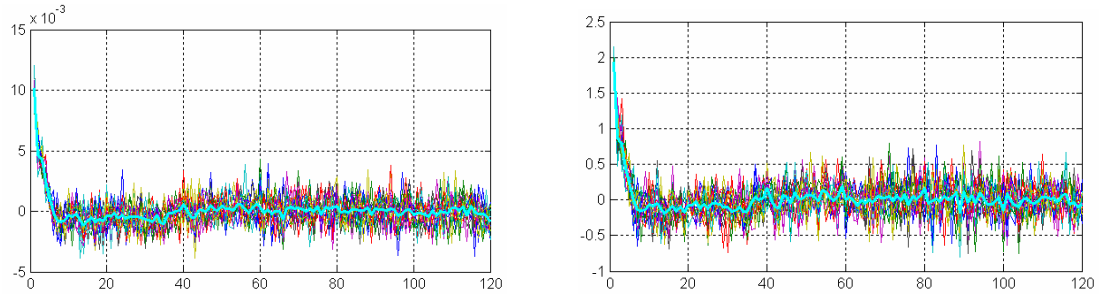

a. b.

Figure 5.4: Distribution of the FIR filter coefficients for the (a) dEy and (b) d(ΔH) inputs.

Besides analyzing the behavior of the system in response to different input signals, our purpose here is also to establish quantitative relationships between IEF-Ey and the penetration electric fields. The models described above can serve such a purpose but they require much more information than needed to establish an input-output mapping. In consequence, two additional methods based on multiple regression analysis and neural networks are employed for this purpose. In both approaches the inputs are Kp, LT, and IEF-Ey, and the output is either dEy or d(ΔH).

The first approach consists in determining some regression coefficients in a least-squares sense, and the latter approach consists in adjusting the weights of a

neural network according to a learning algorithm based on a training set. For the neural network approach the training RMS errors were about 0.17887 mV/m and 33.2571 nT, while for the multiple regression approach, the regression equations and the training RMS errors are given in Table 5.1. It is noteworthy that these relationships apply to penetrating electric fields and were developed based on samples characterized by Kp values larger than 4. It can be also remarked that the training RMS errors are very similar with those obtained with the FIR filters and neural network models discussed above. This indicates that using only the current IEF-Ey value should be sufficient to predict the corresponding dEy and d(ΔH) values.

$dEy = -0.0764 - 0.0031 \cdot kp + 0.0062 \cdot LT + 0.0148 \cdot IEF\text{-}Ey + 0.0002 \cdot IEF\text{-}Ey^2$	0.1800 [mV/m]
$d(\Delta H) = -20.2978 - 0.1842 \cdot kp + 1.5281 \cdot LT + 2.9152 \cdot IEF\text{-}Ey + 0.0447 \cdot IEF\text{-}Ey^2$	33.9836 [nT]

Table 5.1: Regression equations and the associated RMS errors.

5.6 Case Studies

Figure 5.5 illustrates the Ey fields inferred from ΔH observations (thick black lines), the Ey fields predicted by the FIR filter (thick green lines) and the neural network model (thick red lines) that have the current and the past 10 hours of IEF-Ey values as inputs, along with the Ey predicted by the Fejer-Scherliess model (dashed blue line) and IEF-Ey/15 (thin blue line), for eight days characterized by Kp values greater than 4. As seen in this figure, some of the events are more oscillatory in nature, others are characterized by square wave inputs, while others are quite unique.

These storm cases were also examined by Nicolls et al. (2007), where they provided a more complete description of each event. Overall, our results are in excellent agreement with their results and many of their conclusions apply to our Ey estimates.

As seen in Figure 5.5, the Ey fields predicted by the FIR filter and neural network model are in general smoother than the observed fields. The predicted fields are also able to capture the equatorial responses quite well although the edges on the data are a bit sharper than predicted by our models, showing a rise time of about 30 min. Both effects are due to the suppression of the high-frequency components in the frequency response functions shown in Figure 5.3. The attenuation of the high-frequencies might be due to the fact that the highly fluctuating fields display large variability from one penetration event to another, and hence they are not well represented by the training samples. Another reason might be that the training samples were selected based on the Kp index, which is not quite appropriate to identify penetration events. A more appropriate index would be obtained by calculating the integrated power within a certain period range in the wavelet domain, which is similar with the integrated fluctuation power index defined by Nicolls et al. (2007). This procedure then provides index values at a desired sampling rather than on a daily basis. However, given that the substorm-induced penetration electric fields and the gravity waves are important sources of high-frequency electric field fluctuations, and the existing indices are not sufficient to fully isolate their effects, an even better approach would be to investigate the high-frequency components on a case-by-case basis as shown by Nicolls et al. (2007) and Anghel et al. (2008a).

Another aspect that can be observed in Figure 5.5 is that both southern and northern IMF-Bz turnings cause the Ey field estimates to overshoot, which is typical of an oscillatory system. Other features of the estimated fields consist in their ability to reproduce oscillatory and ramping effects, slow decays in the ionospheric fields, and long-duration penetration effects. Also, like in Nicolls et al. (2007), there is a general tendency our models to underestimate the ionospheric field fluctuations by a factor of about 2-3, although many of the features are recovered. This is kind of expected given the quality of the data, the way the training samples were selected based on the Kp index, the effect of the gravity waves and substrom-induced penetration fields, and also the fact that both approaches tend to learn the most significant and frequent patterns embedded in the training set. It is also worth mentioning that similar results like those in Figure 5.5 are obtained with the multiple regression equation given in Table 5.1 and with neural network algorithm that has Kp, LT, and IEF-Ey as inputs and dEy as output.

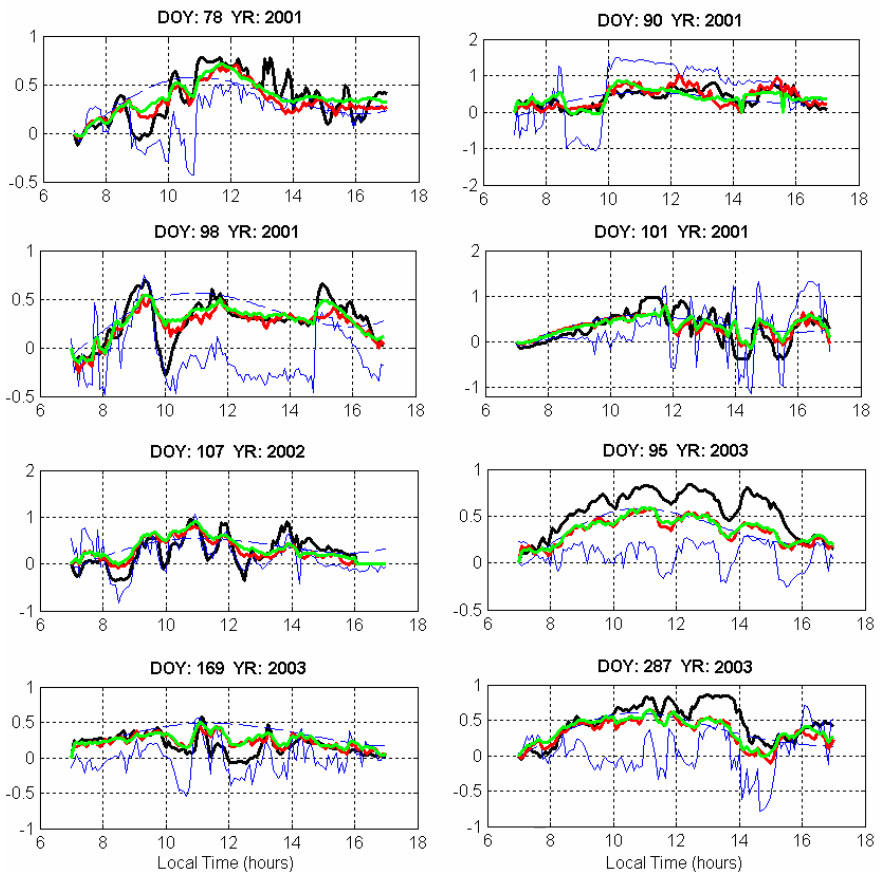

Figure 5.5: A series of eight case studies where the thick black line is the ΔH-inferred Ey at Jicamarca, the thick red line is the Ey predicted by the NN, the thick green line is the Ey predicted by the MR algorithm, the thin blue line is the IEF-Ey divided by 15 and the dashed blue line is the Ey field predicted by the Fejer-Scherliess model.

5.7 Modeling the Relationship between IEF-Ey and the Penetration Electric Fields at Indonesian Longitudes

Magnetometer observations from Yap and Biak, Indonesia, between 2001 and 2004, have been used to estimate the zonal electric fields at these longitudes using the neural network approach described in Chapter 3. The estimated Ey fields are used here: (1) to establish quantitative relationships between IEF-Ey and the penetration

electric fields, and (2) to investigate the electric field penetration mechanism associated with the ring-current, using the methods discussed earlier in this chapter.

The wavelet amplitude spectra (ω_o=40) of the Fejer-Scherliess Ey and ΔH-inferred Ey at Indonesia, calculated only for those days when ΔH observations are available, and of the IEF-Ey/10, over the 1-10 hour period range and between 2001 and 2004, are shown in Figure 5.6. Here again the most dominant features in the two Ey spectra are the 6 and 8-hour periods, corresponding to the quarterdiurnal and terdiurnal tides. It is clear from this figure that the two spectral components are much stronger than at Peruvian longitudes and reach amplitudes of up to about 0.2 mV/m. Other higher harmonics of the diurnal tide can be also distinguished but they have much smaller amplitudes. As shown in this figure, the 8-hour period in the ΔH-inferred Ey spectrum exhibits a distinct seasonal variation, while in the Fejer-Scherliess Ey spectrum the amplitude of the 8-hour period is constant over the entire interval. On the other hand, the 6-hour period in the two Ey spectra does not display any seasonal variation and maintains high amplitudes throughout the entire interval.

It is thus clear from the two Ey spectra that the quantity obtained by subtracting the Ey predicted by the Fejer-Scherliess model from the observed Ey is not quite appropriate for studies that involve equatorial electric fluctuations with periods less than 10 hours. As stated previously, the vertical features in the two Ey spectra are due to missing data records. But, in the ΔH-inferred Ey spectrum, they are also due to solar wind/magnetospheric phenomena and gravity wave activity, which are in addition responsible for some of the random features in this spectrum. The IEF-Ey spectrum displayed in Figure 5.6 is the same one from Figure 5.1.

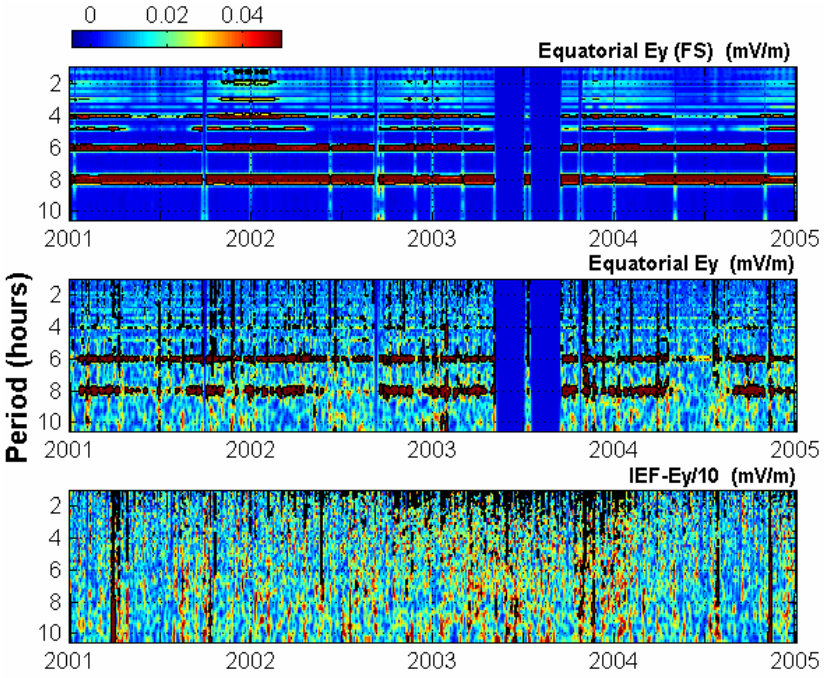

Figure 5.6: Wavelet amplitude spectra (ω_o=40) of the equatorial Ey (top) predicted by the Fejer-Scherliess model and (middle) inferred from ΔH observations at Indonesia, and of (bottom) of IEF-Ey/10 for the 1-10 hour period range and for 2001-2004 time interval.

We further analyze the penetration mechanism of the IEF-Ey to equatorial latitudes by investigating the dynamics of the system that has IEF-Ey as input and dEy as output. For this purpose, we also employed an FIR filter and a neural network model with 120 inputs, that represent the current and the previous 10 hours of IEF-Ey values. The training set in this case consisted of about 26000 samples and the training RMS errors for the neural network model and FIR filter were about 0.1727 mV/m and 0.1806 mV/m, respectively. The responses of the two models to different input signals are shown in Figure 5.7a. Again, for comparative purposes and also to test the consistency of our results, we developed additional FIR filter and neural network models with IEF-Ey as input and d(ΔH) as output. Their responses to the same test signals are shown in Figure 5.7b. In this latter case, the training RMS errors

associated with the neural network model and FIR filter were about 22.650 nT and 23.544 nT, respectively.

The plots in Figure 5.7 are in the same format as those in Figure 5.3, with the impulse responses and the frequency response functions at the top of the figure and the responses to the six test inputs described earlier in the chapter in the lower part of the figure. It is clear from these plots that the two FIR filters predict similar behaviors whether dEy or d(ΔH) is used as output with the exception of a negative offset in the responses to pulse, ramp and triangular waves when dEy is used as output. The observed offset might be due to the neural network algorithm employed to estimate the vertical ExB drifts from ΔH observations, having in view that only Peruvian data were used for its training. The frequency response functions of the two FIR filters are also very similar and indicate a band-pass filter with a roll-off near the 10-hour period, peaks near the 4 and 6-hour periods, and a significant attenuation of the periodicities outside the 1-10 hour period range.

As compared to the frequency response functions shown in Figure 5.3, there is a significant attenuation of the 5-hour period relative to the 4 and 6-hour periods, which may be due to the fact that there are stronger 6 and 8-hour tidal components at Indonesian longitudes than at Peruvian sector. We speculate that this relative suppression of the 5-hour period with respect to the 4 and 6-hour periods could be responsible for the gradual decay in the step responses which settle to zero in one case and to a negative value in the other after about 2 hours from the beginning of the step signal. A similar situation is observed in Figure 5.3a, where the neural network response to a step input also reaches zero after about 2 hours. In that case too, the 5-

hour period is significantly attenuated relative to the 6-hour period. However, further investigations are required to clarify the role played by the strength of the tidal components and the relative suppression of the 5-day period in the rapid decay of the pulse responses.

As shown in Figure 5.7, the pulse responses of the FIR filters are characterized by a rise time less than 30 minutes, enhanced responses to both rising and falling edges, and a settling time of about 3 hours, while the impulse responses are slightly oscillatory and reveal a natural period of about 6 hours. The FIR filter responses to triangular waves are also typical of an oscillatory system, and their responses to sinusoidal waves are sinusoids of the same frequency and phase as the input waves. It can be also remarked that the responses predicted by the neural network models slightly overestimate the responses predicted by the FIR filters and exhibit some peculiarities.

Comparing Figures 5.3 and 5.7, it is clear that there are significant differences between the FIR filter responses to pulse signals of duration longer than 2 hours, at Indonesian and Peruvian longitudes. Also, the FIR filter responses at Indonesia have slightly lower amplitudes than at the Peruvian sector, which is more evident for the sinusoidal input. All these point out that there exists a longitudinal dependency of the penetration effects which remains to be further investigated in our future studies.

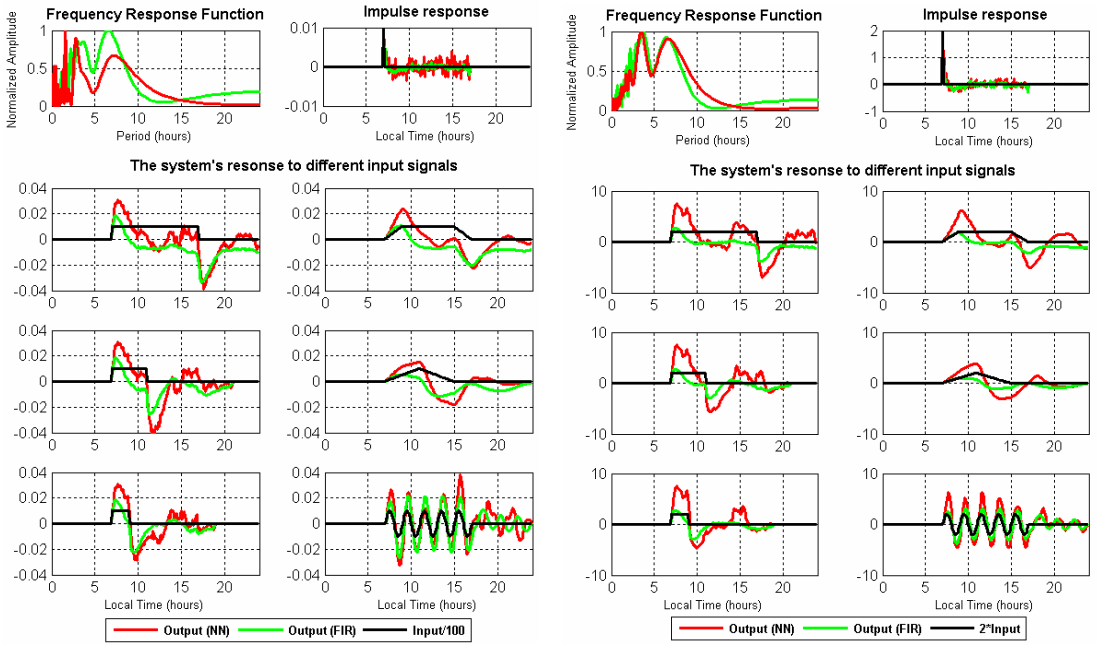

a. b.

Figure 5.7: Same as Figure 5.3 but for Indonesia.

Using multiple regression and neural network approaches, we also established simple quantitative relationships between IEF-Ey and dEy and between IEF-Ey and d(ΔH). For the multiple regression approach, the regression equations and the RMS errors associated with the training set are shown in Table 5.2, while for the neural network approach the training errors are about 0.17995 mV/m and 23.986 nT. The relationship can be used to estimate the penetration electric fields at Indonesian longitudes directly from IEF-Ey measurements.

$dEy = 0.0687 - 0.0191 \cdot kp - 0.0008 \cdot LT + 0.0082 \cdot IEF\text{-}Ey + 0.0003 \cdot IEF\text{-}Ey^2$	0.1871 [mV/m]
$d(\Delta H) = 2.9579 - 2.9945 \cdot kp + 0.4974 \cdot LT + 1.5906 \cdot IEF\text{-}Ey + 0.0310 \cdot IEF\text{-}Ey^2$	24.1963 [nT]

Table 5.2: Regression equations and the associated RMS errors.

5.8 Conclusions

In this chapter, we have investigated the shielding effect of the ring current, in both time and frequency domains, and established quantitative relationships between IEF-Ey and the fluctuations in the zonal component Ey of the daytime equatorial electric fields at both Peruvian and Indonesian longitudes. Several techniques based on neural networks, multiple regression analysis, and FIR filters have been employed for this purpose and have been discussed in this chapter.

We have shown that our models developed for the Peruvian sector predict smoother responses as compared to the observations and display a tendency to underestimate the fluctuations in the observed Ey field by a factor of 2-3. Their frequency response functions are very similar and indicate a band-pass filter with peaks near the 4 and 6-hour periods, roll-off near the 10 hour period, and a significant attenuation of the periodicities outside the 1-10 hour period band. Our results thus support the ideas that the ring current behaves as a band-pass filter and that the shielding effect is more effective for periods longer than about 10 hours (e.g., Earle and Kelley, 1987). Their step responses are typical of a weakly resonant system characterized by a natural period of about 6 hours, a positive and negative overshoot of about 50%, that corresponds to a damping rate of 0.2, a rise time less then 30 minutes, a settling time of about 6 hours, and an amplification factor of about 1% of the input for steady-state conditions. As explained by Nicolls et al. (2007) the self-inductance of the ring current coupled with some capacitance and the ionospheric resistivity may provide such oscillatory responses, but the physical mechanisms

behind such an equivalent circuit have not been investigated. In addition, their long-duration responses to pulse signals are in agreement with the results reported by Huang et al. (2007) and Nicolls et al. (2007) and support the notion that the response of the equatorial field to long-duration IEF-Ey polarities can last for many hours.

We have also shown that the models developed for the Indonesian site present some particularities, especially regarding their response to long-duration pulses, as these responses settle to zero in one case and to a negative value in the other after about 2 hours from the beginning of the pulse. We speculate that the observed decay in the pulse responses may be caused by the presence of strong 6 and 8-hour tidal components in the Ey field at these longitudes as illustrated in Figure 5.5. The two tidal components are also deemed to be responsible for the relative suppression of the 5-hour period with respect to the 4 and 6-hour periods in the frequency response functions shown in Figure 5.7. However, further investigations are needed to elucidate the impact of the 6 and 8-hour periods on interpreting the penetration effects at these longitudes. In addition, the pulse responses of these models are characterized by a rise time less than 30 minutes, enhanced responses to both rising and falling edges, and a settling time of about 3 hours, while their impulse responses are slightly oscillatory and reveal a natural period of about 6 hours. Overall, our results indicate that the penetration mechanism presents a longitudinal dependency which remains to be further investigated in future studies.

Chapter 6

WinTEC - A Kalman Filter-based Algorithm for Near Real-Time Monitoring of the Ionosphere Using Dual-Frequency GPS Data

6.1 Background

Consisting currently of a constellation of 31 active satellites that broadcast coded L-band radio signals at the L1 (1675.42 MHz) and L2 (1227.60 MHz) frequencies and more than 2000 dual-frequency Global Positioning System (GPS) receivers in continuous operation worldwide and onboard many Low Earth Orbiting (LEO) satellites, the GPS system represents a unique and reliable source of ionospheric total electron content (TEC) data. The ionosphere is the ionized component of the Earth's upper atmosphere that impacts the propagation of electromagnetic waves in a wide range of frequencies (e.g., Tascione, 1994). For the GPS signals, the ionosphere is a dispersive medium which introduces a frequency dependent path delay proportional to the integrated electron density along the signal path from where valuable temporal and spatial information about the electron density

distribution in the ionosphere can be retrieved. Over the last two decades, several algorithms for estimating the ionospheric TEC from GPS observations by taking advantage of the dispersive nature of the ionosphere in the microwave region of the electromagnetic spectrum have been developed (e.g., Sardon et al., 1994; Komjathy, 1997; Mannucci et al., 1998; Spencer et al., 2004). In this context, the main purpose of this chapter is to introduce the mathematics behind our GPS-TEC estimation algorithm, named WinTEC, developed for near real-time monitoring of the ionospheric TEC using ground-based, dual-frequency GPS data.

WinTEC has been developed as a Windows application in Borland C++ Builder and features a user-friendly Graphical User Interface (GUI) based on a Multiple Document Interface (MDI) design. The application can automatically download hourly/daily observation and navigation files in the Receiver Independent Exchange Format (RINEX) format from Internet, and is able to estimate slant and vertical ionospheric TEC values by processing GPS data from a single site or from several receivers simultaneously in a Kalman filter approach. The estimation procedure in WinTEC consists of two phases. The first phase is a data pre-processing phase where, at each epoch, the algorithm calculates the coordinates of all the satellites in view (e.g., Grewal et al., 2007), the differential pseudoranges and carrier phases, and then, after checking and correcting for the potential cycle slips in the differential carrier phases within a 30-minute observation arc centered on the current epoch, the phase-leveled slant TEC for each satellite in view. In the second phase, the phase-leveled TEC values are fed to a Kalman filter after detecting and eliminating the anomalous data points. To detect and correct for the bad data points, at each

iteration step, the algorithm compares the measured TEC with the previously estimated TEC and eliminates those values that exceed a certain threshold.

To assess the performance of our algorithm, we provide some comparative results between the vertical TEC values predicted by the WinTEC and USTEC techniques (Spencer et al., 2004) at five North American stations and for three time intervals, 5-11 November 2004, 2-11 January 2005, and 20-26 August 2005, characterized by enhanced geomagnetic activity conditions. We selected USTEC for our validation studies, since it employs a more complex TEC estimation technique than the one used in WinTEC. USTEC produces ionospheric TEC estimates over the contiguous United States (CONUS), within the 10^{o}-60^{o}N latitude range and 50^{o}-150^{o}W longitude range, with a spatial resolution of 1^{o}x1^{o} in latitude and longitude, at a latency of 15 minutes. It uses dual-frequency GPS data from about 100 ground-based receivers in a data-assimilation scheme that combines Kalman filtering and tomography, with IRI95 (Bilitza, 1995) as a background ionospheric model. As reported by Minter et al. (2007), the USTEC uncertainty is of about 2-3 TECU for quiet geomagnetic conditions, and possibly higher for moderate and enhanced geomagnetic activity levels. For our studies, we use USTEC data available at http://www.ngdc.noaa.gov/stp/IONO/USTEC/products/.

In the following sections of the chapter, we introduce the mathematical formalism behind the WinTEC algorithm by: (1) providing relevant information about the ionospheric effects on the GPS signals, (2) examining the GPS observables, (3) reviewing the thin-shell ionospheric model, and (4) describing the sequential Kalman processor and its governing equations. We then present several comparative

results between WinTEC and USTEC and conclude the chapter with a succinct description of our results.

6.2 Estimation Strategy

Several authors have already published the basic mathematical equations that describe the impact of the ionosphere on the GPS signals and the GPS observables (e.g., Komjathy, 1997; Hoffmann-Wellenhof et al., 1998, Haykin, 2001; Grewal et al., 2007). Here we include these fundamental equations for completeness along with the Kalman filter equations (Tapley et al., 2004).

6.2.1 Ionospheric Refraction. GPS Observables. Thin-Shell Ionospheric Model.

The ionosphere is a dispersive medium for the GPS signals, which presents frequency dependent phase, n_{ph}, and group, n_{gr}, refractive indices. Neglecting the collision and magnetic field effects, n_{ph} and n_{gr} for an electromagnetic wave propagating through the ionosphere are in general approximated as:

$$n_{ph} = \frac{c}{f_{ph}} = 1 - \frac{f_p^2}{f^2} \cong 1 - \frac{40.3 \cdot N_e}{f^2} \tag{6.1a}$$

$$n_{gr} = \frac{c}{f_{gr}} = 1 + \frac{f_p^2}{f^2} \cong 1 + \frac{40.3 \cdot N_e}{f^2} \tag{6.1b}$$

where f is the carrier frequency, f_p is the plasma frequency, f_{ph} and f_{gr} are the phase and group frequencies, respectively, N_e is the electron density, and c is the speed of light. It is clear from Equations (6.1a) and (6.1b) that the ionosphere impacts the GPS signals by introducing a frequency dependent group delay given by (in meter units):

$$\Delta^{Iono} = \frac{40.3}{f^2} \cdot TEC \tag{6.2}$$

where TEC is the total electron content along the propagation path, in TEC units (1 TECU $=10^{16}$ electron/m^2 and corresponds to a time delay of 0.54 ns and and a range delay of 0.16 m at the L1 frequency).

For a receiver-satellite (RS) pair, the quantity in Equation (6.2) affects both the measured code P and phase Φ ranges. The two ranges are in general expressed in distance units as:

$$P(L) = \rho + c \cdot \Delta\tau + \Delta^{Iono}(L) + \Delta^{Trop} + b^R_{P,L} + b^S_{P,L} + m_{P,L} + \varepsilon_{P,L} \tag{6.3a}$$

$$\Phi(L) = \rho + c \cdot \Delta\tau + \lambda \cdot N - \Delta^{Iono}(L) + \Delta^{Trop} + b^R_{\Phi,L} + b^S_{\Phi,L} + m_{\Phi,L} + \varepsilon_{\Phi,L} \tag{6.3b}$$

where ρ is the actual satellite-receiver geometric range, $\Delta\tau$ is the satellite-receiver clock error, L is the carrier frequency, λ is the wavelength, c is the speed of light, N is an integer phase ambiguity number, Δ^{Iono} is the frequency dependent ionospheric path delay, Δ^{Trop} is the non-dispersive tropospheric path delay, $b^R_{P,L}$, $b^S_{P,L}$, $b^R_{\Phi,L}$, and $b^S_{\Phi,L}$ are the satellite and receiver instrumental biases, $m_{P,L}$ and $m_{\Phi,L}$ are the multipath

errors, and $\varepsilon_{P,L}$ and $\varepsilon_{\Phi,L}$ are random noise processes. Since the two measured ranges are affected by both random and systematic errors, they are usually known as code and phase pseudoranges, or simply as pseudorange and carrier phase, respectively. Also, having in view that there are different tracking loops for the code and phase measurements, the receiver and satellite instrumental biases for P and Φ are different.

By combining Equations (6.2), (6.3a), and (6.3b) for the L1 and L2 frequencies, one can express the differential pseudorange TEC_P and the differential carrier phase TEC_Φ observables, in TECU, as:

$$TEC_P = 9.52 \cdot (P_2 - P_1) \tag{6.4a}$$

$$TEC_\Phi = 9.52 \cdot (\Phi_1 - \Phi_2) \tag{6.4b}$$

where TEC_P is a noisy and biased measure of the actual TEC due to multipath effects and instrumental biases, while TEC_Φ is a very precise but ambiguous measure of it due to the phase-cycle ambiguity. TEC_Φ is less sensitive to multipath that TEC_P and has a noise level of about 2-3 orders of magnitude below the noise level in TEC_P. Taking advantage of the properties of the two independent TEC estimates given by Equations (6.4a) and (6.4b), here we use a phase-leveling technique that combines TEC_Φ and TEC_P measurements collected over phase-connected arcs of data. The technique consists in adjusting the TEC_Φ measurements by a constant value calculated as the elevation-weighted average of the TEC_Φ-TEC_P measurements for each phase-connected arc. Although still affected by the satellite and receiver

instrumental biases, the new line-of-sight phase-leveled TEC observable is a precise and unambiguous measure of the actual TEC and, at a certain epoch *k*, is given by:

$$TEC_{RS}^{k} = TEC_{\Phi}^{k} - \frac{\sum_{j=i-n}^{i+n} p_j \cdot \left(TEC_{\Phi}^{j} - TEC_{P}^{j}\right)}{\sum_{j=i-n}^{i+n} p_j}, \quad p_j = \left(e_{RS}^{j}\right)^2 \tag{6.5}$$

where e^{j}_{RS} is the elevation angle at epoch *j*. In our analysis, the summation in Equation (4) is performed over a 30 minute arc length centered at the current epoch *k*, after detecting and correcting the cycle slips in TEC_{Φ} within this time interval. Also, in the results presented here, the cutoff elevation angle is chosen at 10^{o} and the sampling time is 30 seconds, which is also the update time in our Kalman filter-based algorithm.

Moreover, to estimate the actual TEC from the phase-leveled TEC measurements, we employed a thin-shell model for the ionosphere and a bilinear spatial representation, in a solar-geomagnetic reference frame, for the vertical TEC above the monitoring stations. In the thin-shell model the ionosphere is approximated as a thin spherical shell at a fixed height, assumed to correspond to the peak electron density in the ionosphere. In WinTEC, we chose a solar-geomagnetic reference frame based on sun-fixed longitude and geomagnetic latitude because the ionosphere is the result of interaction between the solar radiation and the Earth's atmosphere and magnetic field, and is assumed to vary more slowly in a Sun-fixed reference frame than in an Earth-fixed one (e.g., Tascione, 1994). A mathematical model is then set

up that takes into account that the ionospheric path delay is a function of elevation angle, whereas the satellite and receiver biases are elevation angle independent, according to the following observation equation:

$$TEC_{RS}^{k} = M\left(e_{RS}^{k}, h\right) \cdot \left[a_{0,R}^{k} + a_{1,R}^{k} \cdot \Delta\lambda_{RS}^{k} + a_{2,R}^{k} \cdot \Delta\varphi_{RS}^{k}\right] + b_{R}^{k} + b_{S}^{k} \tag{6.6}$$

In Equation (6.6), the additive terms b^{k}_{S} and b^{k}_{R} are the slowly varying satellite and receiver instrumental biases, the parameters $a^{k}_{0,R}$, $a^{k}_{1,R}$, and $a^{k}_{2,R}$ are the coefficients of a first-order polynomial fit to the vertical TEC above the receiver, $\Delta\lambda^{k}_{RS}$ is the difference between the longitude of the ionospheric piercing point (IPP) and that of the mean sun, and $\Delta\varphi^{k}_{RS}$ is the difference between the geomagnetic latitude of the IPP and that of the receiver. Finally, $M(e^{k}_{RS}, h)$ is an elevation angle-dependent mapping function that relates the line-of-sight and vertical TEC values at the IPP:

$$M\left(e_{RS}^{k}, h\right) = \sec\left(\arcsin\left(\frac{R_e}{R_e + h}\right) \cdot \cos\left(e_{RS}^{k}\right)\right) \tag{6.7}$$

where R_e is the radius of the Earth, e_{RS} is the elevation angle, and h is the ionospheric shell height, taken here at 350 km. It is noteworthy that by using Equation (6.6), the satellite and receiver biases cannot be determined separately unless an additional assumption is made, and consequently here we estimate only the combined satellite and receiver biases. It is also important to mention that, as it will be shown in the next

chapter, the WinTEC algorithm can also accommodate for multi-shell representations of the ionosphere and for more elaborated polynomial structures for the vertical TEC.

6.2.2 Kalman Filter

The Kalman filter provides an alternative way of formulating the least-squares filtering problem using state-space methods (e.g., Kalman, 1960; Haykin, 2001; Tapley et al., 2004), with the dynamical system to be estimated being modeled as:

$$\mathbf{X}_k = \Phi_{k,k-1} \cdot \mathbf{X}_{k-1} + \mathbf{w}_{k-1} \tag{6.8}$$

$$\mathbf{Y}_k = \mathbf{H}_k \cdot \mathbf{X}_k + \mathbf{v}_k \tag{6.9}$$

where $\mathbf{X}_k$ is the state vector, $\mathbf{\Phi}_{k,k-1}$ is the state transition matrix, $\mathbf{w}_k$ is the process noise (a zero-mean white Gaussian noise with the covariance matrix $\mathbf{Q}$), $\mathbf{Y}_k$ is the measurement vector, $\mathbf{H}_k$ is the measurement matrix, and $\mathbf{v}_k$ is the measurement noise (a zero-mean white Gaussian noise with the covariance matrix $\mathbf{R}$). The main idea behind the Kalman filter is that, as new measurements become available, both the state estimate and the error of that estimate are updated or refined. The recursive equations of the Kalman filter, grouped as time and measurement update equations, are given below for convenience:

1. time update equations

$$\bar{\mathbf{X}}_k = \Phi_{k,k-1} \cdot \hat{\mathbf{X}}_{k-1} \tag{6.10}$$

$$\bar{\mathbf{P}}_k = \Phi_{k,k-1} \cdot \mathbf{P}_{k-1} \cdot \Phi_{k,k-1}^T + \mathbf{Q} = E\left[\left(\mathbf{X}_k - \bar{\mathbf{X}}_k\right) \cdot \left(\mathbf{X}_k - \bar{\mathbf{X}}_k\right)^T\right] \tag{6.11}$$

2. measurement update equations

$$\mathbf{K}_k = \bar{\mathbf{P}}_k \cdot \mathbf{H}_k^T \cdot \left(\mathbf{H}_k \cdot \bar{\mathbf{P}}_k \cdot \mathbf{H}_k^T + \mathbf{R}\right)^{-1} \tag{6.12}$$

$$\hat{\mathbf{X}}_k = \bar{\mathbf{X}}_k + \mathbf{K}_k \cdot \left(\mathbf{Y}_k - \mathbf{H}_k \cdot \bar{\mathbf{X}}_k\right) \tag{6.13}$$

$$\mathbf{P}_k = \left(\mathbf{I} - \mathbf{K}_k \cdot \mathbf{H}_k\right) \cdot \bar{\mathbf{P}}_k = E\left[\left(\mathbf{X}_k - \hat{\mathbf{X}}_k\right) \cdot \left(\mathbf{X}_k - \hat{\mathbf{X}}_k\right)^T\right] \tag{6.14}$$

where "^" indicates estimated values and "-" apriori values at the k^{th} iteration.

In the Equations (6.10)-(6.14), **P** is a symmetric positive-definite matrix and represents the estimation error covariance matrix, being thus usually used as a measure of the estimation accuracy. Instead of using Equation (6.14), in WinTEC we use the equivalent Joseph's formulation which always yields a symmetric result for **P** during the estimation process regardless of the round-off computer errors:

$$\mathbf{P}_k = \left(\mathbf{I} - \mathbf{K}_k \cdot \mathbf{H}_k\right) \cdot \bar{\mathbf{P}}_k \cdot \left(\mathbf{I} - \mathbf{K}_k \cdot \mathbf{H}_k\right)^T + \mathbf{K}_k \cdot \mathbf{R}_k \cdot \mathbf{K}_k^T \tag{6.15}$$

Also, as indicated by Equation (6.13), the Kalman gain **K** provides a relative weighting between the apriori data and the new observations. Basically, when the measurements are very noisy with respect to the apriori state, as reflected by the **R** and **P** matrices, the Kalman gain makes the estimation algorithm less sensitive to the new observations, and vice versa, when the apriori state is less accurate relative to the

measurements, the Kalman gain makes the estimation algorithm more sensitive to the new measurements (e.g., Tapley et al., 2004).

6.2.3 Single-site and Multi-site Estimation Procedures

In the following, we further detail the WinTEC processing algorithm for the single receiver case and for the case of an arbitrary number of receivers. For the single-site case, according to Equation (6.6), the state vector consists of three ionospheric fit coefficients that describe the vertical TEC above the site, one receiver bias, and N satellite biases:

$$\mathbf{X}_k = \left[a_{0,R}^k \;\; a_{1,R}^k \;\; a_{2,R}^k \;\; b_R^k \;\; b_{S_1}^k \ldots b_{S_N}^k\right]^T \tag{6.16}$$

and the measurement vector contains the slant phase-leveled TEC observations:

$$\mathbf{Y}_k = \left[TEC_{RS_1}^k \;\; TEC_{RS_2}^k \ldots TEC_{RS_N}^k\right]^T \tag{6.17}$$

In WinTEC, the state transition matrix $\mathbf{\Phi}_{k,k-1}$ is the identity matrix and the state variables are modeled as stochastic random walk processes, while according to Equation (6.6) the $\mathbf{H}_k$ matrix is given by:

$$\mathbf{H}_k = \begin{bmatrix} M\left(e^k_{RS_1},h\right) & M\left(e^k_{RS_1},h\right)\cdot\Delta\lambda^k_{RS_1} & M\left(e^k_{RS_1},h\right)\cdot\Delta\varphi^k_{RS_1} & 1 & 1 & \cdot & 0 \\ M\left(e^k_{RS_2},h\right) & M\left(e^k_{RS_2},h\right)\cdot\Delta\lambda^k_{RS_2} & M\left(e^k_{RS_2},h\right)\cdot\Delta\varphi^k_{RS_2} & 1 & 0 & \cdot & 0 \\ \cdot & \cdot & \cdot & \cdot & \cdot & \cdot & \cdot \\ M\left(e^k_{RS_N},h\right) & M\left(e^k_{RS_N},h\right)\cdot\Delta\lambda^k_{RS_N} & M\left(e^k_{RS_N},h\right)\cdot\Delta\varphi^k_{RS_N} & 1 & 0 & \cdot & 1 \end{bmatrix} \quad (6.18)$$

It can be remarked in Equations (6.17) and (6.18) that each component in $\mathbf{Y}_k$ and each row in $\mathbf{H}_k$ correspond to a particular GPS satellite, and if the satellite is not in view then its corresponding components in $\mathbf{Y}_k$ and $\mathbf{H}_k$ are set to zero.

Also, in WinTEC, both **Q** and **R** are diagonal matrices and are kept constant throughout the entire estimation process. For the single-site case, they are taken to be:

$$\mathbf{Q} = \begin{bmatrix} 1 & 0 & 0 & 0 & . & 0 \\ 0 & 1 & 0 & 0 & . & 0 \\ 0 & 0 & 1 & 0 & . & 0 \\ 0 & 0 & 0 & 0 & . & 0 \\ . & . & . & . & . & . \\ 0 & 0 & 0 & 0 & . & 0 \end{bmatrix} \cdot 10^{-6} \qquad \text{and} \qquad \mathbf{R} = 0.04 \cdot \mathbf{I} \qquad (6.19)$$

where **I** is the identity matrix. As seen in Equation (6.19), in the specification of **Q**, we imposed non-zero values for the diagonal elements corresponding to the ionospheric state variables and zero values for the elements corresponding to the instrumental biases, having in view that the ionosphere varies on much shorter timescales than the instrumental biases.

For the network approach, the state vector contains N satellite biases and a set of three ionospheric fit coefficients and a receiver bias for each station. Thus, for a

network of M receivers and N satellites there are 4·M+N state variables. In this case, Equations (6.16)-(6.19) modify accordingly, and the state and measurement vectors become:

$$\mathbf{X}_k = \left[a^k_{0,R_1} \;\; a^k_{1,R_1} \;\; a^k_{2,R_1} \;\; b^k_{R_1} \;\; . \;\; . \;\; . \;\; a^k_{0,R_M} \; a^k_{1,R_M} a^k_{2,R_M} \;\;\; b^k_{R_M} \;\; b^k_{S_1} \;\; . \;\; b^k_{S_N} \right]^T \tag{6.20}$$

$$\mathbf{Y}_k = \left[TEC^k_{R_1S_1} \;\; TEC^k_{R_1S_2} \;\; . \;\; TEC^k_{R_1S_N} \;\; . \;\; . \;\; . \;\; TEC^k_{R_MS_1} \;\; TEC^k_{R_MS_2} \;\; . \;\; TEC^k_{R_MS_N} \right]^T \tag{6.21}$$

The algorithm can also use predefined satellite biases, and in this case the size of the state vector reduces to 4·M (e.g., Carrano et al., 2008, 2009). Several studies conducted with the WinTEC algorithm, for different solar and geomagnetic conditions, have indicated that both single and multi-site approaches are robust with the Kalman filter stabilizing after about one day, as the geometry of the GPS satellite configuration repeats every 24 hours.

6.2.4 Validation Procedure using Simulated Data

During its first stages of development, we validated WinTEC by using predefined ionospheric coefficients and instrumental biases, while using actual configurations of the GPS satellites. Specifically, we tested the algorithm for predefined ionospheric coefficients that captured the diurnal variation of the vertical TEC and constant instrumental biases, but also for different process and measurement noise levels and for state variables with sophisticated temporal evolutions. We found

that, in most of the considered cases, the algorithm was able to produce accurate estimates of the state vector.

6.3 Results

In this section, we present several comparative results between WinTEC and USTEC with the purpose of assessing the performance level of our algorithm. The two algorithms are compared in terms of the root mean square error (RMSE) between vertical TEC values predicted by WinTEC and USTEC at different North American sites and for different geomagnetically disturbed periods. As mentioned earlier in the chapter, we chose USTEC for validation since it employs a more complex TEC estimation technique than WinTEC, combining Kalman filtering and tomography in a data assimilation scheme that uses IRI95 in the background. For the comparative studies presented here, we used data from five North American dual-frequency GPS receivers from the Continuously Operating Reference Stations (CORS) network. The codes and names of the stations are listed in Table 6.1, along with their geographic coordinates. For our analyses, the DSRC station was arbitrarily chosen, while the other stations were selected since they also provide data for USTEC.

The comparisons were conducted for three solar minimum periods, 5-11 November 2004, 2-11 January 2005, and 20-26 August 2005, characterized by increased geomagnetic activity levels. During the three time periods, the daily Ap values were greater than 20 for most of the time, as clearly shown in Figure 6.1, where the corresponding daily Ap values for each interval are plotted as a function of

day of the month. We selected these periods because USTEC data are only available starting with October 2004 and also because these periods have been among the most disturbed periods since then. During the three periods, USTEC produced regional maps of vertical TEC over the 20^{o}-50^{o}N latitude range and 60^{o}-130^{o}W longitude range, with a spatial resolution of 1^{o}x1^{o} (lat. x long.) and at a latency of 15 minutes, by using GPS data from about 60 North American stations including the first four stations given in Table 6.1. Conversely, the WinTEC-derived vertical TEC values for the three periods were obtained, at a 30-second sampling rate, by individually processing the GPS data from each receiver listed in Table 6.1, for a cutoff elevation angle of 10^{o} and for an ionosphere approximated as a thin-shell located at a fixed altitude of 350 km.

Before proceeding with presenting our results, we need to mention that several sources of RMSEs between the vertical TEC values predicted by the two algorithms have been considered. One main source of errors may arise from the fact that, although based on Kalman filter estimation, the two algorithms are substantially different as they imply different processing techniques. While USTEC assumes the satellite biases and solves for the receiver biases and for the coefficients of three IRI95-based empirical orthogonal functions (EOFs) at each latitude-longitude grid point (Spencer, et al., 2004), WinTEC estimates the combined satellite and receiver biases and the ionospheric coefficients of a polynomial fit to the vertical TEC at each site. Also, since neither algorithm accounts explicitly for the plasmaspheric contribution to the GPS measurements of TEC, the plasmaspheric TEC is distributed differently by each algorithm between the estimated quantities, the two algorithms

being thus prone to producing different ionospheric TEC estimates. In addition, the WinTEC algorithm in a single-site approach may be more susceptible to corruption from the plasmasphere, whereas errors due to plasmasphere may partially cancel in USTEC due to the fact that it uses observations from a network of GPS receivers located over a large range of latitudes. On the other hand, in a network solution the estimated state variables for a certain receiver may also be strongly influenced by measurements from other receivers nearby. Other sources of errors may be related to the fact that different types of receivers are used to provide GPS data for the two estimation techniques, and also to the simple fact that the comparisons are performed by taking the closest grid points in the USTEC maps to the GPS receivers listed in Table 6.1.

GPS Stations - WinTEC/USTEC	**Latitude**	**Longitude**
CCV3/CCV4 (CAPE CANAVERAL, FL)	28.46	279.45
CME1/CME2 (CAPE MENDOCINO, CA)	40.44	235.60
ANP1/ANP2 (ANNAPOLIS, MD)	39.01	283.39
SPN1/SPN2 (SPOKANE,WA)	47.62	242.58
DSRC (BOULDER, CO)	39.99	254.74

Table 6.1: List of CORS stations used in the analysis.

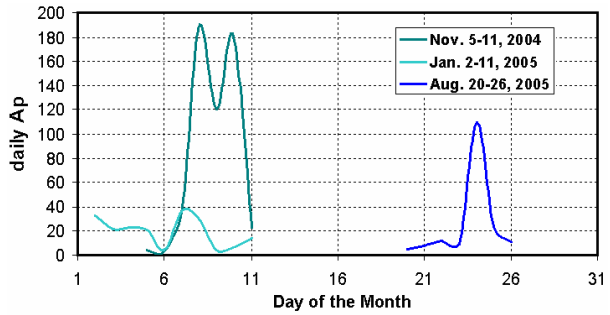

Figure 6.1: Daily Ap values for 5-11 November 2004, 2-11 January 2005, and 20-26 August 2005, plotted as a function of day of the month.

a. 5-11 November (310-316) 2004

Figure 6.2a displays the vertical TEC values predicted by WinTEC (red lines) and USTEC (blue lines) at the five stations, for 5-11 November 2004, the corresponding RMSE being indicated on each panel. This is an extremely disturbed period and, as shown in Figure 6.1, the daily Ap increased to values of about 180 on two occasions during this time interval. Overall, the plots in Figure 6.2a indicate a good agreement between the two algorithms, although a few discrepancies can be also remarked. For instance, during the daytime hours on November 10, there is a relatively large difference of about 6 TECU between the estimated TEC values at CME1, although on the previous days the two time series track each other quite well. A similar situation can be also noticed at SPN1 and DSRC. In all three cases the vertical TEC values predicted by WinTEC are smaller than those predicted by USTEC. To examine the causes of the observed differences, in Figure 6.3, we show the WinTEC plots for CME1 over the entire seven-day interval. The figure displays, from top to bottom, the slant phase-leveled TEC, the estimated slant and vertical (thick red line) TEC, and the combined satellite and receiver biases as a function of day of the year and universal time (UT), the slant TEC values and the biases being color-coded. As seen in this figure, the estimated biases are relatively constant over the entire period, whereas the measured TEC values undergo a decrease on November 10. This basically demonstrates that the decrease in TEC at CME1 on November 10 is not an artifact of the WinTEC algorithm and corresponds to an actual depletion of the TEC at this site which is not captured by USTEC. Additionally, the WinTEC plots for DSRC and SPN1 (not shown here) also confirm our conclusion.

Another aspect that can be remarked in Figure 6.3 is that there are slight variations in the estimated biases at early UT hours on November 8. The variations are caused by the fact that the strong gradients in the measured TEC are not properly captured by the thin-shell linear ionospheric model employed here, which is more appropriate for a quiet ionosphere with smooth temporal variations. Several solutions can be adopted in order to eliminate the bias drifting effect. Here we suggest the following: (1) keep the biases constant over the storm interval, (2) eliminate those measured TEC values from the estimation procedure that exceeded a certain gradient threshold, or (3) represent the vertical TEC above the stations as higher order polynomials.

It is also important to mention that, as shown in Figure 6.2a, during the positive phase of the November 7 storm event, characterized by large TEC values and gradients, the two algorithms predict similar vertical TEC values. Moreover, as seen in this figure, the RMSEs between the vertical TEC predicted by the two algorithms are about 2.5-4 TECU, being thus comparable with the USTEC quiet-time uncertainty values. These indicate that there is a good to excellent agreement between WinTEC and USTEC over the entire time interval, and suggest that the WinTEC algorithm is a reliable TEC estimation technique even during storm-time conditions.

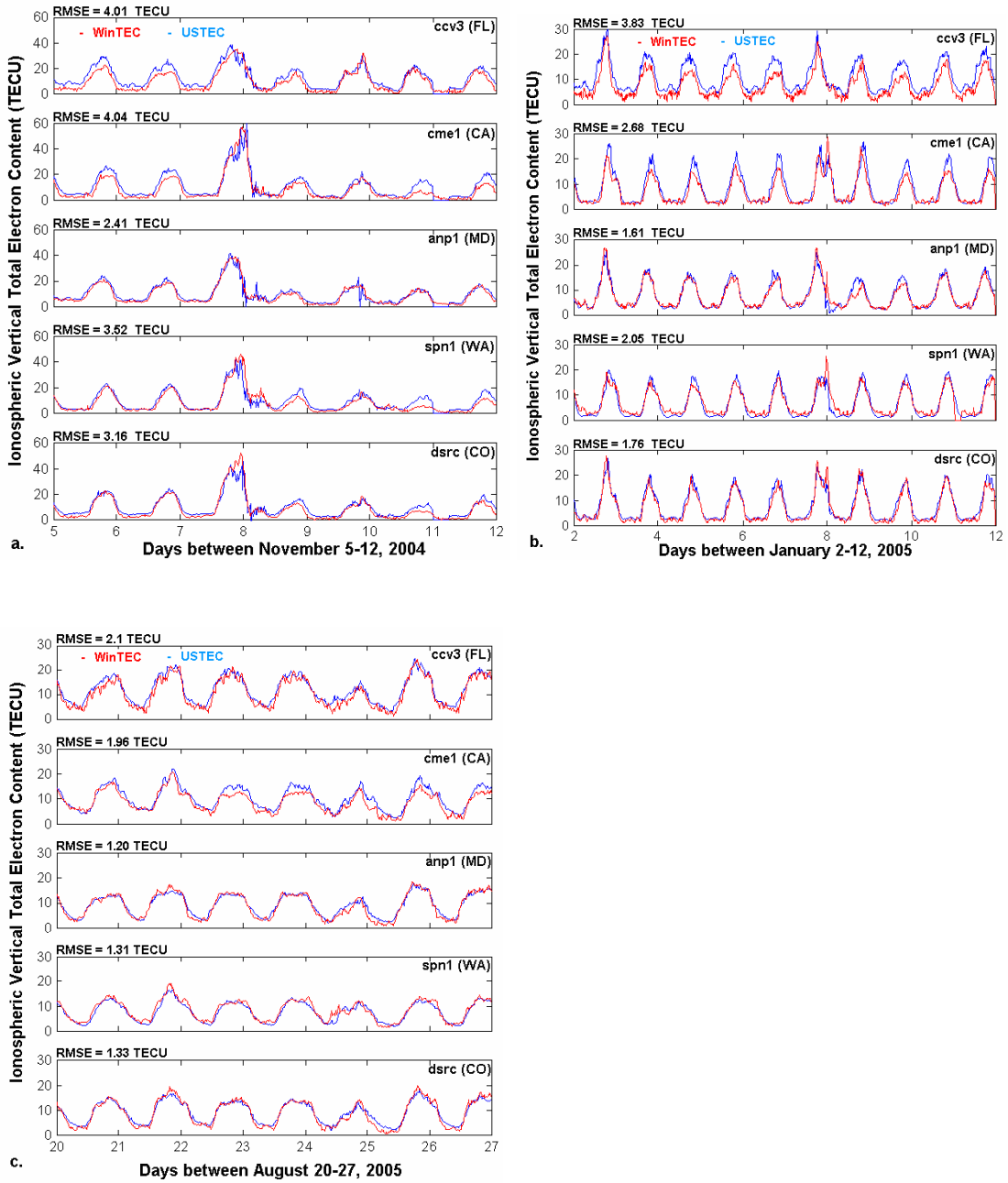

Figure 6.2: Vertical TEC values predicted by WinTEC (red lines) and USTEC (blue lines) at five GPS stations, for three time intervals. The codes of the stations, the time intervals in day of the month and UT, and the RMSE values are indicated on each plot.

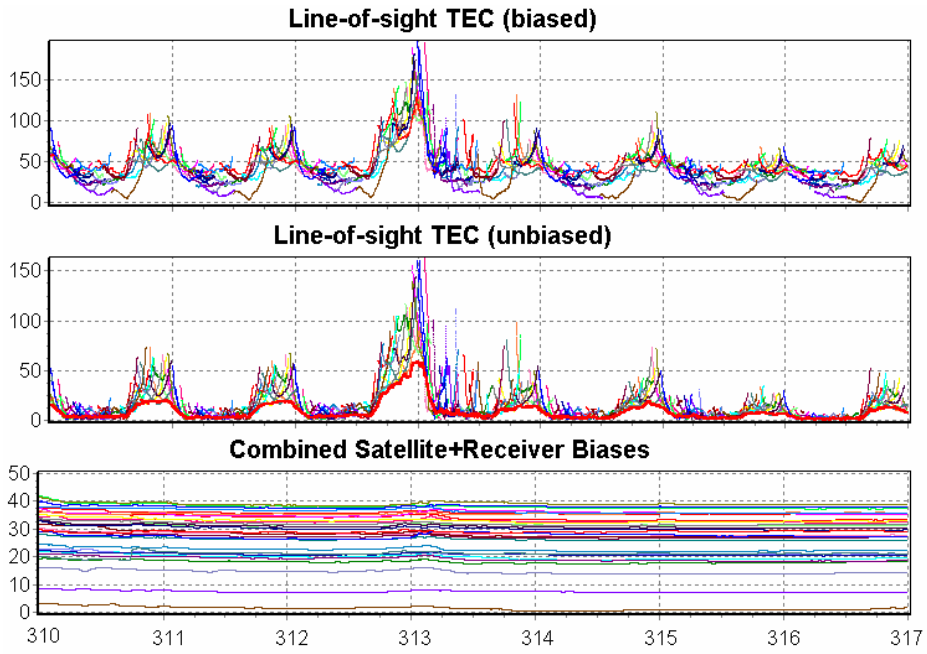

Figure 6.3: WinTEC plots at CME1 for 5-11 November 2004: (top) the biased slant TEC, (middle) the estimated slant and vertical (thick red line) TEC, and (bottom) the combined instrumental biases as a function of day of the year and UT.

b. 2-11 January 2005

The WinTEC and USTEC comparative results for 2-11 January 2005 are illustrated in Figure 6.2b. This is a moderately disturbed period and, as shown in Figure 6.1, the daily Ap values during this time interval were between 20 and 40, except for three days, January 6, 9 and 10, when the daily Ap values were less than 10, and for January 11, when the daily Ap value was 14. The results presented in Figure 6.2b indicate that there is an excellent agreement between the two algorithms at DSRC, SPN1 and ANP1, with RMSEs less than about 2 TECU, and a good agreement at CCV3 and CME1, with RMSEs of 3.83 and 2.68 TECU, respectively. Some systematic differences can be also observed between the vertical TEC values predicted by the two algorithms and are discussed subsequently.

It can be observed in Figure 6.2b that, at CCV3, WinTEC systematically underestimates the USTEC-derived vertical TEC values throughout the entire period, except on January 2 and 7, which are two storm events characterized by increased TEC values. The differences are around 2-5 TECU and persist during both daytime and nighttime, larger differences being recorded during daytime than during nighttime. Like in the previous case, to examine the causes of the observed differences, we need to look at the WinTEC-estimated biases for this station. The WinTEC results for CCV3 are displayed in Figure 6.4, in the same format as in Figure 6.3, and show that the estimated biases are approximately constant over the entire ten-day period. Therefore, the fact that the biases are nearly constant and the WinTEC and USTEC algorithms predict similar daytime vertical TEC values on January 2 and 7, suggests that the estimated biases, and hence the WinTEC-derived TEC values, are correct. A similar situation is encountered at CME1. As shown in Figure 6.2b, at this station, WinTEC underestimates the daytime vertical TEC values predicted by USTEC throughout the entire time interval, except on January 7, while the nighttime vertical TEC values predicted by the two algorithms are very similar. Figure 6.5 displays the WinTEC results for CME1 and shows that the estimated biases are relatively constant over the entire period. Again, the fact that the biases are almost constant and the two algorithms predict similar nighttime vertical TEC values, suggests that the estimated biases at CME1, and hence the WinTEC-derived TEC values, are also correct. Since the WinTEC estimates are good in both cases, we speculate that the main cause for the observed differences between the WinTEC and USTEC-estimated vertical TEC values is the background ionospheric model in

USTEC. However, other factors may be also involved, such as variations in the biases that are not correctly account for by the two estimation algorithms and differences in the measured TEC at CCV3 and CCV4.

Another interesting aspect that can be observed in Figure 6.2b is the double-crest TEC feature (e.g., Mendillo, 2004) on January 7, with enhanced TEC values during late morning and early evening hours. The feature is predicted by WinTEC at four of the sites, except at CCV3, and by USTEC only at CME1. At SPN1, it is most pronounced during early evening hours, when the vertical TEC values predicted by WinTEC exceed those predicted by USTEC by about 7 TECU. To show that the predicted TEC enhancement at SPN1 is a real feature and not an artifact of our algorithm, it is sufficient to look at the WinTEC plots in Figure 6.6. The plots clearly indicate that the estimated biases are relatively constant over the entire period, thus proving that the WinTEC-predicted TEC enhancement, although not captured by USTEC, is a real feature. Similar results (not shown here) were also obtained for the CME1, ANP1, and DSRC stations. Overall, our results suggest that WinTEC could be a better choice for applications that require finer TEC values than those predicted by a regional or global TEC algorithm.

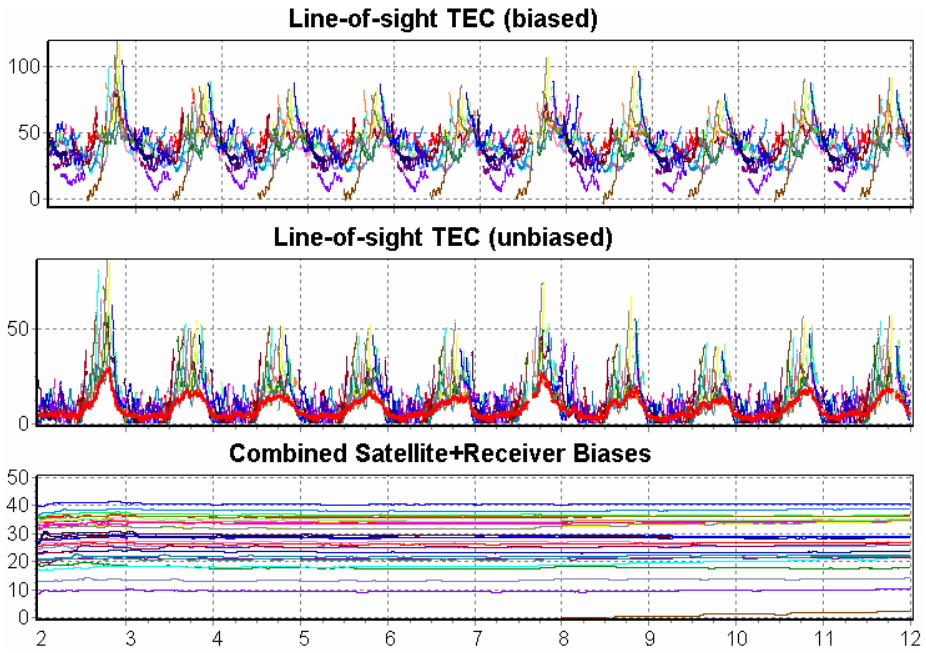

Figure 6.4: Same as Figure 6.3 at CCV3 for 2-11 January 2005.

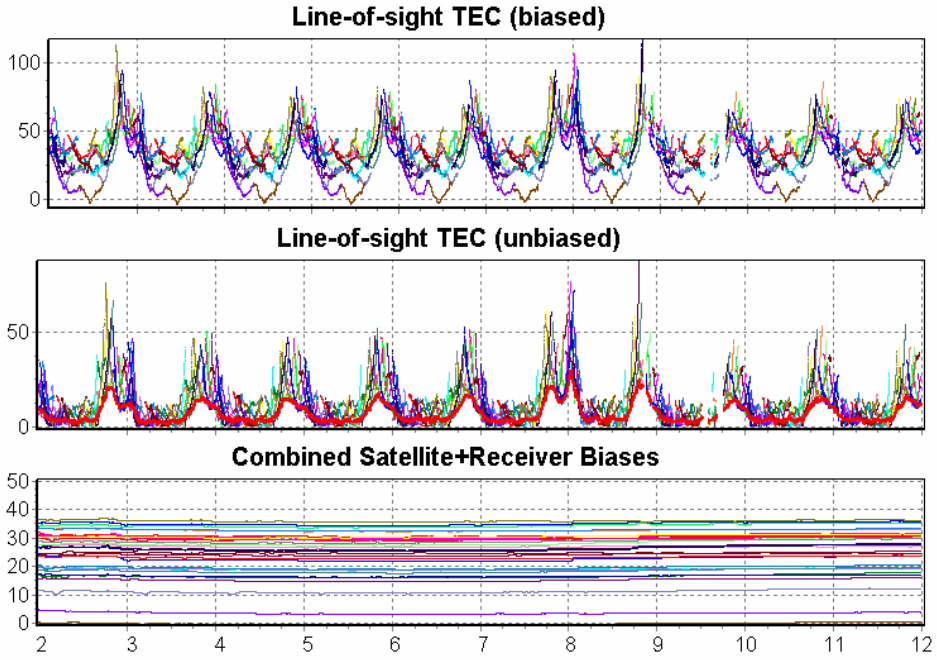

Figure 6.5: Same as Figure 6.3 at CME1 for 2-11 January 2005.

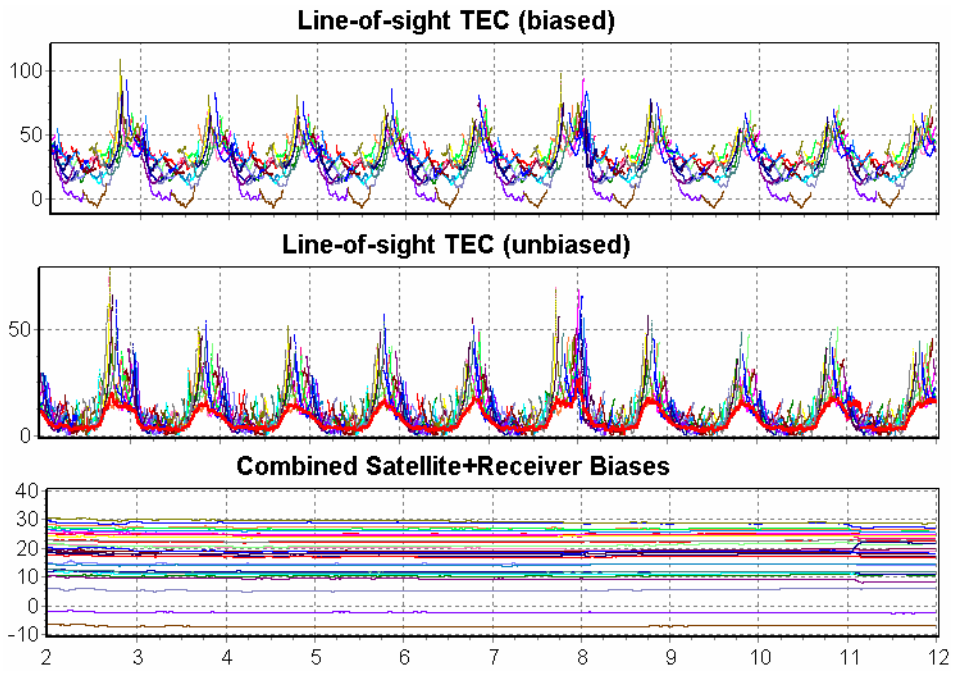

Figure 6.6: Same as Figure 6.3 at SPN1 for 2-11 January 2005.

c. 20-26 August (232-238) 2005

Our last set of comparative results between WinTEC and USTEC is shown in Figure 6.2c and corresponds to 20-26 August 2005. This is a very disturbed period and, as shown in Figure 6.1, the daily Ap reached a value of 110 on August 24. Figure 6.2c indicates that there is an excellent agreement between the two algorithms at all five stations, throughout the entire period, with RMSEs less than about 2 TECU. An example of WinTEC results for this period is given in Figure 6.7, which shows the WinTEC plots for the DSRC station. Specific for this station during all three periods are the predominantly negative line-of-sight phase-leveled TEC measurements, which for 20-26 August 2005 are displayed in the upper panel of Figure 6.7. It is important to remark that, as shown in Figure 6.2, at this station the two algorithms are in excellent agreement during all three periods, although USTEC

does not use GPS data from DSRC to produce TEC values. This further confirms that, although based on a simple estimation technique, WinTEC is a powerful tool for estimating the ionospheric TEC from GPS observations that can rise to the performance level of a more complex algorithm like USTEC.

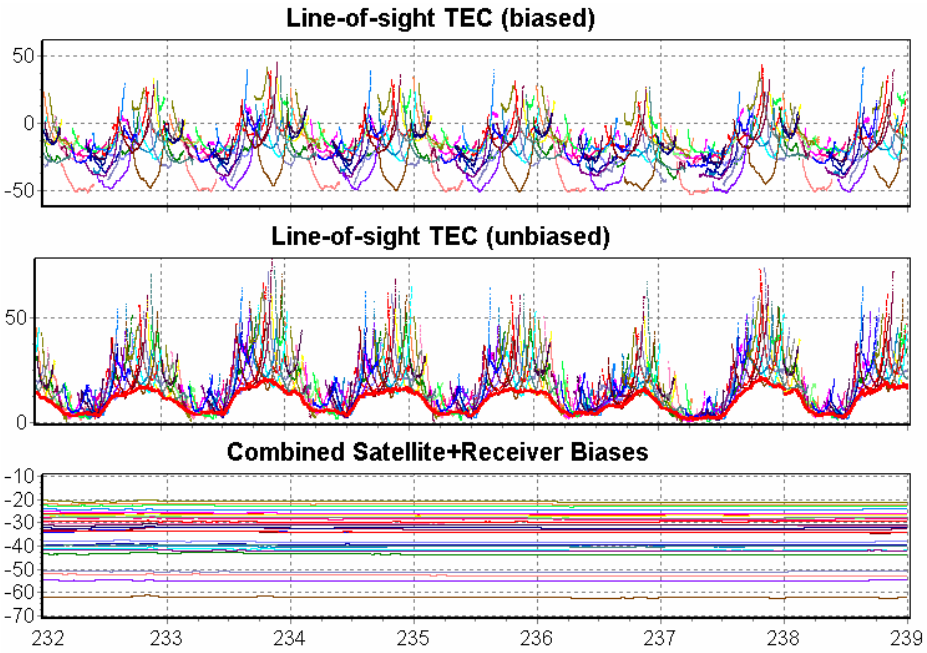

Figure 6.7: Same as Figure 6.3 at DSRC for 20-26 August 2005.

6.4 Conclusions

In this chapter, we have introduced the Kalman filter-based WinTEC algorithm developed for near real-time estimation of the ionospheric TEC using data from a single site or from a network of ground-based dual-frequency GPS receivers. In WinTEC, the ionospheric TEC and the combined satellite and receiver biases are estimated at the sampling rate of the GPS data (30 seconds) by using hourly/daily RINEX observation and navigation files. The estimation procedure assumes a simple

model for the ionosphere, approximated as a thin spherical shell at a fixed height of 350 km, and a first-order polynomial fit for the vertical TEC above the monitoring stations. Although these approximations are more appropriate for a quiet ionosphere with smooth variations in the electron densities, the results presented here show that our estimation algorithm provides accurate TEC estimates even during disturbed periods characterized by enhanced geomagnetic activity levels. In addition, the excellent comparison results between WinTEC and USTEC confirm that, although based on a simple mathematical formalism, WinTEC is a powerful tool for ionospheric studies that can reach the performance level of a more complex and computationally expensive algorithm like USTEC, being able to retrieve accurate TEC values in near real-time, during both quiet and disturbed periods.

Chapter 7

WinTEC-IP: A Kalman Filter-based Algorithm for Monitoring the Ionosphere and Plasmasphere with GPS in Near-real Time

7.1 Background

The ionized atmosphere surrounding the Earth at altitudes beyond about 90 km represents a dispersive medium for the GPS signals which must travel through the oxygen-dominated plasma of the ionosphere and the tenuous hydrogen-dominated plasma of the plasmasphere on their way to the ground-based GPS receivers. The ionosphere extends from about 90 to 1000 km in altitude, with the bulk of plasma typically residing in a relatively thin altitude layer (~200-400 km) in the F-region. On the other hand, the plasmasphere, denoted also as protonosphere due to its composition, is just the continuation of the ionosphere into the magnetosphere and and consists of relatively dense (~100-1000 cm^{-3}), cold (~1-2eV) hydrogen-dominated plasma distributed along the corotating geomagnetic field lines (e.g., Prölss, 2004). It is a torus-shaped plasma cloud confined by the Earth's magnetic

field that surrounds the Earth at low and mid-latitudes, between about ±60^{o} magnetic latitudes, and extends to equatorial distances of several Earth radii, from the O^{+}/H^{+} transition height, where the concentration of hydrogen becomes comparable with that of oxygen, up to about 35,000 km, the height of the plasmapause.

In the plasmasphere, the diurnal motion of plasma is controlled by an electric field induced by the Earth's rotation which forces the plasma to corotate with the Earth, while at higher L-shells the plasma motion is driven by a convection electric field caused by the solar wind interaction with the Earth's magnetic field. The plasmapause, the outer boundary of the plasmasphere, is the boundary that forms between the regions dominated by corotation and convection. It encloses the magnetic flux tubes that corotate with the Earth and is in general characterized by sharp density gradients and plasma densities of about 10-100 cm^{-3}. The position of the plasmapause changes with the strength of the convective electric field, such that a strong convection moves the plasmapause to lower L-shells, while a weak convection moves the boundary to higher L-shells. In the absence of geomagnetic disturbances the plasmapause is located at L~5.6 (e.g., Carpenter and Anderson, 1992; Gallagher et al., 1995).

Several studies have investigated the azimuthal density profile of the plasmapause in the magnetic equatorial plane reporting both symmetric and asymmetric shapes (e.g., Gallagher et al., 2000, Carpenter et al., 2004). In general, the plasmapause is considered to be roughly circular with a pronounced bulge of plasma at larger radial distances (L>3), at dusk, which causes a dawn-dusk asymmetry of the plasmapause in the magnetic equatorial plane (e.g., Gallagher et al., 1995).

Traditionally, the plasma bulge is considered part of the plasmasphere, resulting from the opposition at local dusk of the corotation flow near the Earth and the sunward solar wind-driven convection of the magnetosphere (e.g., Lunt et al, 1999a). But, recent studies (e.g., Kotova, 2007) suggest that the bulge and the plasmasphere are distinct regions, as the bulge plasmas are mostly influenced by convection and the plasmasphere is mostly influenced by corotation.

During quiet geomagnetic conditions, the corotation dominates the near-Earth plasma flow and the plasmasphere becomes gradually saturated with upflowing ionospheric plasma which accumulates in the corotating flux tubes until a diffusive equilibrium is established with the underlying ionosphere. Conversely, during disturbed geomagnetic conditions, the enhanced convection erodes the outer plasmasphere by transporting the plasma outward and sunward toward the magnetopause, causing a reduction in the size of the plasmapause and a rapid depletion of the plasmaspheric flux tubes on the day of the storm. The replenishment of the plasmasphere by upward ionospheric plasma fluxes is a very slow process that usually last longer than the recurrence time between storms, such that the plasmasphere is in general considered as in a state of partial replenishment (e.g., Kersley and Klobuchar, 1980; Lunt et al. 1999c; Belehaki et al., 2004). Also, during disturbed periods, the plasma bulge rotates sunward to earlier hours and decreases in size, whereas for decreasing magnetic activity the bulge moves antisunward.

Although the electron densities in the plasmasphere are several orders of magnitude less than in the ionosphere, due to the long propagation distances of the GPS signals through the tenuous plasmasphere compared to the relatively short paths

through the ionosphere, the plasmaspheric contribution to the total electron content (TEC) along the entire signal path can become significant under certain conditions (e.g., Lunt et al., 1999a; Balan et al., 2002). There are several studies that investigate the plasmasphere using GPS data (e.g., Ciraolo and Spalla, 1997; Lunt et al., 1999c,d; Law, 1999; Mazzella et al., 2002; Otsuka et al., 2002; Belehaki et al., 2004; Izengaw et al., 2008; Manju et al., 2008; Carrano et al., 2008). Lunt et al. (1999a) used model simulations to examine the plasmaspheric electron content (PEC) at European and North American mid-latitude sites for solar minimum and maximum conditions and quiet geomagnetic activity levels. At 40^{o}N geographic latitude and for solar minimum conditions, they determined vertical PEC values of about 2 TECU at European longitudes and of about 0.5 TECU at American longitudes, the lesser significance of the plasmasphere to GPS-TEC observations in the American sector being attributed to the tilt of the Earth's magnetic dipole. Their modeling studies also indicate that the vertical PEC displays a latitudinal dependency, decreasing with increasing geomagnetic latitude of the monitoring station, and that the slant PEC at mid-latitude stations exhibits a latitudinal asymmetry due to the geometry of the plasmaspheric flux tubes and distribution of the plasmaspheric plasma (e.g., Lunt et al., 1999d). In addition, Lunt et al. (1999c) and Belehaki, et al. (2004) observed a weak diurnal variation in the vertical PEC derived from GPS data at some European sites, with a morning minimum around 0800-1200LT and an evening maximum around 1800-2000 LT. For solar minimum conditions, Ciraolo and Spalla (1997) reported an average slant PEC of 2-4 TECU at sites in southern Italy, Lunt et al. (1999c) estimated slant PEC values of 1-2 TECU on ray paths to the south at a mid-latitude

European station, but negligible PEC values above the station and on ray paths to the north, and Kersley and Klobuchar (1978) determined slant PEC values of 3-5 TECU at a European site. For solar maximum conditions, Mazzella et al. (2002) presented GPS-derived PEC results at a near-equatorial site. However, while very important, the previous studies provide only limited statistical information about the plasmaspheric contribution to the GPS measurements of TEC on vertical and slant ray paths, at a limited number of sites and for specific geomagnetic and solar conditions.

In this chapter, we show that the GPS system represents an important source of PEC and a useful remote sensing technique for monitoring the plasmasphere. For this purpose we use the WinTEC algorithm presented in the previous chapter. WinTEC estimates the ionospheric TEC values along the GPS signal paths and the combined satellite and receiver biases using a Kalman filter approach in a single-site or network solution. In the original version of the algorithm, we adopted a thin-shell model for the ionosphere and a spatial linear approximation for the vertical TEC above the monitoring stations, but we did not account for the plasmasphere. As shown by Lunt et al. (1999b, c) and Mazella et al. (2002), to be able to estimate the contribution of the plasmasphere to the GPS-derived TEC, one needs to explicitly account for the PEC by properly capturing in the estimation procedure the dynamics and geometry of plasmasphere which are inappropriately represented by the models usually employed for the ionosphere. Based on their ideas, Carrano et al. (2008) extended the WinTEC algorithm by explicitly accounting for the plasmasphere contribution to the GPS-TEC measurements. They determined the plasmasphere contribution by integrating the electron density predicted by the Carpenter-Anderson

plasmaspheric model (Carpenter-Anderson, 1992) along GPS ray paths and allowing the Kalman filter to scale the PEC predicted by the model to fit the observations. In a similar approach, we extended the WinTEC algorithm by incorporating the Gallagher empirical plasmaspheric model (Gallagher et al., 1988) into our data assimilation scheme and estimating a scaling factor for the PEC predicted by the model. We named the newly developed algorithm WinTEC-IP because it is able to estimate both the ionospheric and plasmaspheric TEC.

Since it is important to have an adequate model for the ionosphere before explicitly accounting for the plasmasphere contribution to the GPS-TEC observations, in the first part of the chapter we present several WinTEC results obtained by employing different models for the ionosphere and for the vertical TEC above the monitoring stations. For this purpose, we tested four different ionospheric modeling techniques and compare them in terms of post-fit residuals using GPS data from the low-latitude station Managua, Nicaragua, for two solar minimum and maximum periods, 8-17 August 2000 and 15-24 November 2007. The four modeling techniques are: (1) the single-shell linear, (2) quadratic, and (3) cubic approaches, and (4) the multi-shell linear approach. These approaches have been also adopted by other authors to model the ionosphere in different GPS-based TEC estimation techniques (e.g., Juan et al., 1997; Rho et al., 2002; Komjathy et al., 2002) and have proven to provide reliable TEC estimates. Here we show that the single-shell cubic approach is more appropriate for describing the ionospheric vertical TEC and that the multi-shell linear structure does not improve significantly the performance of the algorithm compared to the single-shell linear approach, in terms of post-fit residuals. Like in the

previous chapter, as part of the validation process, we also present comparative results between WinTEC, with the single-shell cubic approach, and USTEC (Spencer et al., 2004) at the five stations listed in Table 6.1, for 15-24 November 2007, which is a relatively quiet solar minimum period.

The second part of the chapter is dedicated to presenting some results obtained with the WinTEC-IP algorithm. First, we compare the results of the algorithm, with and without the plasmaspheric term included in the observation equation, for three stations located at different geomagnetic latitudes in the American sector, for 15-24 November 2007. It is shown that the algorithm is effective in retrieving both the ionospheric and plasmaspheric TEC from the GPS measurements, and that the combined satellite and receiver biases are only slightly affected by the plasmaspheric term. Then, to test the method and assess the consistency of our results at different latitudes and longitudes, we took advantage of the symmetric, doughnut-shaped geometry of the plasmasphere and applied the algorithm to data collected during 15-24 November 2007 from twelve GPS stations distributed roughly over four geomagnetic latitudes and three longitude sectors. We show that the estimated PEC patterns are similar at all three longitude sectors during this period, with vertical PEC values decreasing with increasing geomagnetic latitude, large PEC values at mid-latitudes on ray paths to the south, but much smaller values overhead and to the north, and comparable slant and vertical PEC values at low and equatorial latitudes.

The chapter is organized as follows: (1) in the next section, we present the WinTEC-IP algorithm and the four ionospheric modeling techniques, then (2) we introduce our PEC estimation technique and briefly (3) describe the Gallagher

empirical plasmaspheric model, and finally, (4) we present succinct results and conclusions.

7.2 The WinTEC and WinTEC-IP Algorithms

As mentioned before, the WinTEC algorithm is a Windows application written in Borland C++ Builder, developed to estimate the slant and vertical ionospheric TEC and the combined satellite and receiver instrumental biases by processing GPS data from a single site or from several receivers simultaneously in a Kalman filter approach. The application is solely driven by GPS data and assumes a simple structure for the ionosphere and for the vertical TEC above the monitoring stations. Four ionospheric modeling techniques have been adopted for WinTEC and are presented in the following:

1. ***single-shell linear approach*** - the ionosphere is approximated as a thin spherical shell located at a fixed height and the vertical TEC is represented as a first order polynomial in a solar-geomagnetic reference frame:

$$TEC_{RS} = M\left(e_{RS}, h\right) \cdot \left[a_{0,R} + a_{1,R} \cdot \Delta\lambda_{RS} + a_{2,R} \cdot \Delta\varphi_{RS}\right] + b_R + b_S \tag{7.1}$$

2. ***single-shell quadratic approach*** - the vertical TEC is represented as a second order polynomial:

$$TEC_{RS} = M\left(e_{RS}, h\right) \cdot \begin{bmatrix} a_{0,R} + a_{1,R} \cdot \Delta\lambda_{RS} + a_{2,R} \cdot \Delta\varphi_{RS} + \\ a_{3,R} \cdot \Delta\lambda_{RS}^2 + a_{4,R} \cdot \Delta\varphi_{RS}^2 + a_{5,R} \cdot \Delta\varphi_{RS} \cdot \Delta\lambda_{RS} \end{bmatrix} + b_R + b_S \quad (7.2)$$

3. ***single-shell cubic approach*** - the vertical TEC is represented as a third order polynomial:

$$TEC_{RS} = M\left(e_{RS}, h\right) \cdot \begin{bmatrix} a_{0,R} + a_{1,R} \cdot \Delta\lambda_{RS} + a_{2,R} \cdot \Delta\varphi_{RS} + \\ a_{3,R} \cdot \Delta\lambda_{RS}^2 + a_{4,R} \cdot \Delta\varphi_{RS}^2 + a_{5,R} \cdot \Delta\varphi_{RS} \cdot \Delta\lambda_{RS} + \\ a_{6,R} \cdot \Delta\lambda_{RS}^3 + a_{7,R} \cdot \Delta\varphi_{RS}^3 + a_{8,R} \cdot \Delta\varphi_{RS}^2 \cdot \Delta\lambda_{RS} + \\ a_{9,R} \cdot \Delta\varphi_{RS} \cdot \Delta\lambda_{RS}^2 \end{bmatrix} + b_R + b_S \quad (7.3)$$

4. ***multi-shell linear approach*** - the ionosphere is assumed to consist of three thin spherical shells located at fixed heights and the vertical TEC corresponding to each shell is represented as a first order polynomial:

$$TEC_{RS} = \sum_{m=1}^{M} M\left(e_{RS,m}, h_m\right) \cdot \left[a_{0,R,m} + a_{1,R,m} \cdot \Delta\lambda_{RS,m} + a_{2,R,m} \cdot \Delta\varphi_{RS,m}\right] + b_R + b_S \quad (7.4)$$

In Equations (7.1)-(7.4), b_S and b_R are the slowly varying satellite and receiver instrumental biases, $\{a_{j,R}\}_{j=0,..,9}$ are the coefficients of a polynomial fit to the vertical TEC, $\Delta\lambda_{RS}$ is the difference between the longitudes of the ionospheric piercing point (IPP) and the mean sun, and $\Delta\varphi_{RS}$ is the difference between the geomagnetic latitudes of the IPP and the station. In all the above observation equations, $M(e_{RS},h)$ represents a standard mapping function that relates the slant and the vertical TEC at the IPP

(e.g., Mazzella et al., 2002), where e_{RS} is the elevation angle and h is the ionospheric shell height, and is given by Equation (6.7).

In the single-shell approaches adopted here, the ionosphere is approximated as a thin shell located at the fixed altitude of 350 km, whereas in the multi-shell approach, the ionospheric electron content is considered to be distributed on three thin shells located at the fixed altitudes of 200 km, 350 km, and 500 km. A similar multi-shell approach was adopted by Juan et al. (1997), where they included a second shell at 5000 km in order to account for the electrons in the outer part of the ionosphere. We also tested the WinTEC algorithm for different numbers of shells located at different heights. However, our results indicate that the estimated TEC for an individual shell does not represent the actual TEC for the respective shell, and in fact, it does not have any significance by itself. We thus concluded that by using our TEC estimation algorithm, it is not possible to estimate the plasmaspheric contribution to the total TEC along GPS ray paths just by including additional shells at heights above the transition height, thereby the thin-shell models usually adopted for ionosphere are not adequate to describe the plasmasphere.

However, to be able to determine the PEC, we explicitly accounted for the plasmasphere by including an additional term, $a_p \cdot sPEC$, in the observation equation (7.3). *sPEC* represents the slant PEC obtained by integrating the electron density predicted by the Gallagher's plasmaspheric model (Gallagher et al., 1988) along GPS ray paths from the O^+/H^+ transition height, taken here at 1000 km (Balan et al., 2002), up to the GPS orbital altitude of 20,200 km. The parameter a_p, on the other hand, is a scaling factor for the *sPEC* predicted by the model and is estimated by the Kalman

filter along with the other state variables. The observation equation in this case is given by:

5. ***single-shell cubic approach + Gallagher plasmaspheric model - WinTEC-IP***

$$TEC_{RS} = M\left(e_{RS}, h\right)\cdot \begin{bmatrix} a_{0,R} + a_{1,R}\cdot\Delta\lambda_{RS} + a_{2,R}\cdot\Delta\varphi_{RS} + \\ a_{3,R}\cdot\Delta\lambda_{RS}^2 + a_{4,R}\cdot\Delta\varphi_{RS}^2 + a_{5,R}\cdot\Delta\varphi_{RS}\cdot\Delta\lambda_{RS} + \\ a_{6,R}\cdot\Delta\lambda_{RS}^3 + a_{7,R}\cdot\Delta\varphi_{RS}^3 + a_{8,R}\cdot\Delta\varphi_{RS}^2\cdot\Delta\lambda_{RS} + \\ a_{9,R}\cdot\Delta\varphi_{RS}\cdot\Delta\lambda_{RS}^2 \end{bmatrix} + \tag{7.5}$$

$$a_p \cdot sPEC_{RS} + b_R + b_S$$

As previously mentioned, the new algorithm that incorporates the observation equation (7.5) has been named WinTEC-IP, where IP stands for Ionosphere-Plasmasphere, since it is able to estimate both the ionospheric and plasmaspheric electron contents along the GPS ray paths.

7.3 Gallagher's Empirical Plasmaspheric Model

The empirical plasmaspheric model presented by Gallagher et al. (1988) was developed from measurements taken by the Retarding Ion Mass Spectometer (RIMS) on the Dynamics Explorer 1 (DE 1) and consists of an analytical expression that describes the plasmaspheric electron density as a function of magnetic local time (MLT), height, and geomagnetic coordinates. The model is applicable to a wide range of altitudes, from the bottom side of the ionosphere to beyond the plasmapause, and is

able to reproduce the large scale features of the plasmasphere and plasmapause, for low to moderate geomagnetic activity levels. The model equations are given below for convenience:

$$
\begin{aligned}
&Log_{10}(n) = a_1 \cdot F(L) \cdot G(L) \cdot H(L) \\
&F(L) = a_2 - e^{a_3 \cdot \left(1 - a_4 \cdot e^{-h(L,\lambda)/a_5}\right)}, \quad with \quad L = (1 + h/R)/\cos^2(\lambda) \;\; and \;\; R = 6370\,km \\
&G(L) = a_6 \cdot L + a_7 \\
&H(L) = \left(1 + \left(\frac{L}{a_8}\right)^{2\cdot(a_9 - 1)}\right)^{-\left(\frac{a_9}{a_9 - 1}\right)}
\end{aligned}
\tag{7.6}
$$

$$a_1 = 1.4; \quad a_2 = 1.53; \quad a_3 = -0.036; \quad a_4 = 30.76; \quad a_5 = 159.9; \quad a_7 = 6.27$$

$$a_6 = -0.87 + 0.12 \cdot e^{-x^2/9}, \quad with \quad x = \begin{cases} MLT, & for \;\; 0 - 12 \;\; MLT \\ MLT - 24, & for \;\; 12 - 24 \;\; MLT \end{cases}$$

$$a_8 = 0.7 \cdot \cos(2 \cdot \pi \cdot (MLT - 21)/24) + 4.4$$

$$a_9 = 15.3 \cdot \cos(2 \cdot \pi \cdot MLT/24) + 19.7$$

where L is the McIlwain parameter (McIlwain, 1961), h is the height above the Earth's surface, and λ is the geomagnetic latitude. In the model, a_6 represents the slope of the logarithmic plasmaspheric density and varies from -0.87 at noon MLT to -0.75 at midnight MLT, a_8 defines the location of the midpoint of the plasmapause falloff, and a_9 controls the plasmapause gradient.

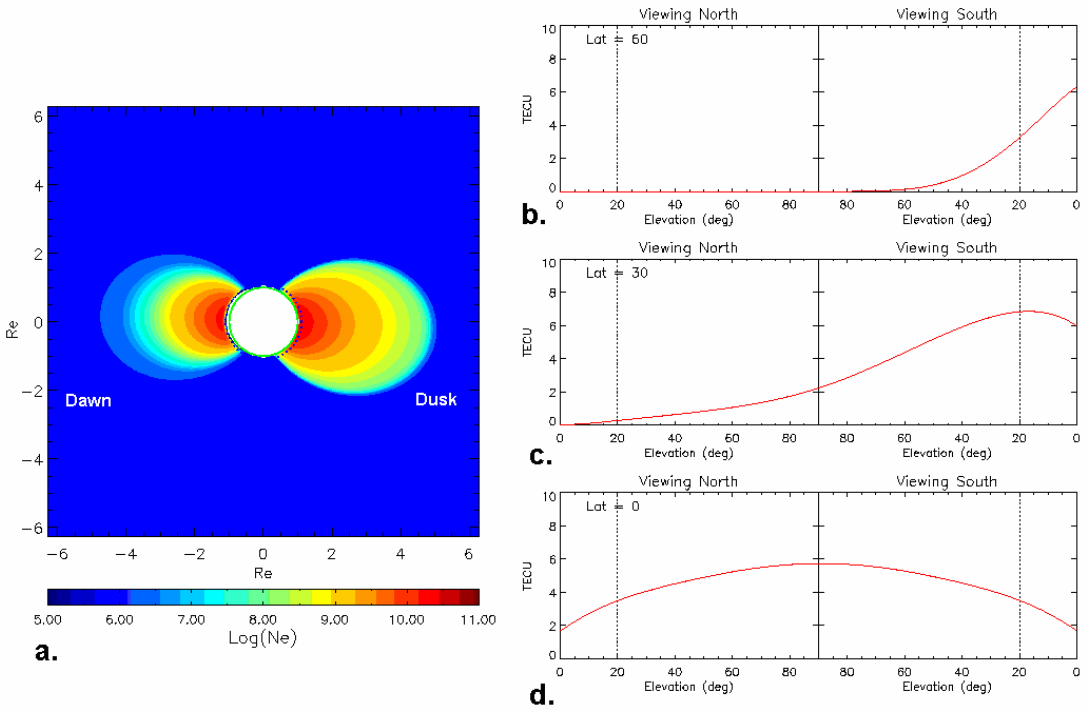

Figure 7.1: a. Plasmaspheric electron density predicted by the Gallagher model in a plane containing the Earth's rotation axis. The dotted line represents the base of the plasmasphere, taken here at 1000 km. b.-d. Modeled PEC as a function of northward and southward-viewing elevation angles, at 60°N, 30°N, and 0° geomagnetic latitudes.

Figure 7.1a illustrates the spatial distribution of the plasmaspheric electron densities predicted by the Gallagher model. It clearly shows that the plasmasphere predicted by the model displays an approximate azimuthal symmetry at lower distances (L<3) and an extension at larger radial distances (L>3), at dusk. Figures 7.1b-d show the modeled PEC as a function of northward and southward-viewing elevation angles for receivers located at 60°N, 30°N, and 0° geomagnetic latitudes. The plots indicate that, at mid and high latitudes in the northern hemisphere, the modeled PEC presents a meridional asymmetry with larger values on ray paths to the south than to the north, while at equatorial latitudes, it is independent of the northward/southward-viewing direction and exhibits a weak elevation angle

dependency. It can be also observed in Figure 7.1 that the vertical PEC decreases with increasing geomagnetic latitude. This is due to the fact that there are shorter vertical path lengths through the plasmasphere at higher latitudes than at lower latitudes and, in addition, at higher latitudes, higher L-shells with consequent lower electron densities are encountered at lower altitudes on vertical ray paths.

7.4 Results

7.4.1 Ionospheric Modeling Techniques - Comparative Results

In this section, the four ionospheric modeling techniques described in Section 7.2 are compared in terms of post-fit residuals. For this purpose, we used GPS data collected during 8-17 August 2000 and 15-24 November 2007 from the MANA station (12.08^{o}N, 273.86^{o}E) located at Managua, Nicaragua. The post-fit residuals, calculated as the difference between the measured and the estimated biased slant TEC values, are used here as an indicator of modeling accuracy. The daily Ap values for the two periods are plotted in Figure 7.2 as a function of day of the month, and indicate that 8-17 August 2000 was in general a geomagnetically disturbed period with Ap values over 100, while 15-24 November 2007 was characterized by relatively quiet geomagnetic conditions.

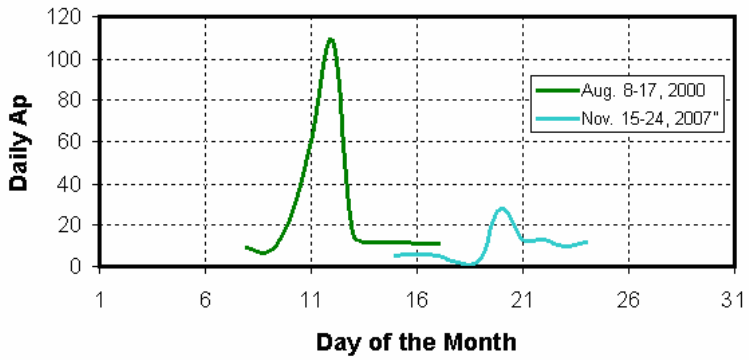

Figure 7.2: The daily Ap values for 8-17 August 2000 (221-230) and 15-24 November 2007 (319-328).

Figure 7.3 displays the WinTEC results for MANA obtained with the linear, quadratic, cubic, and multi-shell linear approaches, for 15-24 November 2007. In all four panels of this figure, the plots represent from top to bottom: the biased slant TEC observations, the unbiased slant and vertical (solid red line) TEC values obtained after subtracting the biases from the TEC measurements, the combined satellite and receiver biases, and the post-fit residuals. As seen in this figure, the biases are relatively constant over the entire interval in all four cases, but there are slight differences between individual biases from case to case. It is clear from these plots that, in terms of post-fit residuals, the worst modeling results are obtained with the single-shell linear approach, while the best results are obtained with the cubic approach, the standard deviation of the residuals in the cubic approach being about four times smaller than in the linear approach. On the other hand, the standard deviation of the residuals in the multi-shell linear approach is only slightly small than in the single-shell linear approach, and in the quadratic approach is about two times smaller than in the linear case.

Similar conclusions can be drawn from Figure 7.4 for 8-17 August 2000, where the best results in terms of post-fit residuals are also obtained with the cubic approach. However, during this time interval, although expected to be constant, the biases exhibit a relatively large variability in each of the four cases, which may indicate a poor modeling quality, and from one case to another. Also, the residuals in Figure 7.4 are much larger than those in Figure 7.3 in each of the considered cases. This may be due to the fact that there are larger TEC values during August 2000 than during November 2007, but it may also reflect a poor modeling accuracy, indicating that the storm-time ionospheric TEC gradients during 8-17 August 2000 are not correctly represented by the ionospheric models used. In Figures 7.3 and 7.4, the WinTEC plots were produced at a 30-second sampling rate and after one day of simulation to allow the Kalman filter to stabilize.

It is thus clear from our analysis that a multi-shell structure does not improve significantly the modeling results in terms of post-fit residuals as compared to a single-shell structure, for the same representation of the vertical TEC, but on the contrary, it can make the Kalman filter algorithm computationally more expensive and eventually numerically unstable due to the increased size of the state vector. For example, in the single-shell linear approach there are only three ionospheric coefficients to be estimated, whereas in the multi-shell linear approach there are nine, but, as seen in Figures 7.3 and 7.4, the results are not much improved in terms of post-fit residuals. Much better results, in terms of post-fit residuals, are obtained though with the single-shell quadratic and cubic approaches, where there are six and respectively ten coefficients to be estimated. It is also found that, in the multi-shell

approach, the estimated TEC for an individual shell does not have a clear significance by itself, but only when considered together with the contributions from all the other shells in the structure. This further indicates that, using the WinTEC algorithm, it is not possible to estimate the contribution of the electrons in the outer part of the ionosphere by placing shells at protonospheric heights, and more complex approaches need to be employed for this purpose.

Our comparative studies between different ionospheric modeling techniques suggest that, when using GPS data from a single site, at least a third order polynomial is needed to model the vertical TEC in the WinTEC algorithm in order to obtain an improved modeling accuracy with reduced post-fit residuals, especially when dealing with solar maximum conditions and increased geomagnetic activity levels. Using higher order polynomials though reduces the post-fit residuals even more but also produces a substantial increase in the size of the state vector, which in turn can lead to the instability of the estimation algorithm. Therefore, for our current studies, from both computational efficiency and modeling accuracy perspectives, we selected a third order polynomial to represent the vertical ionospheric TEC above the monitoring stations throughout the remainder of the chapter.

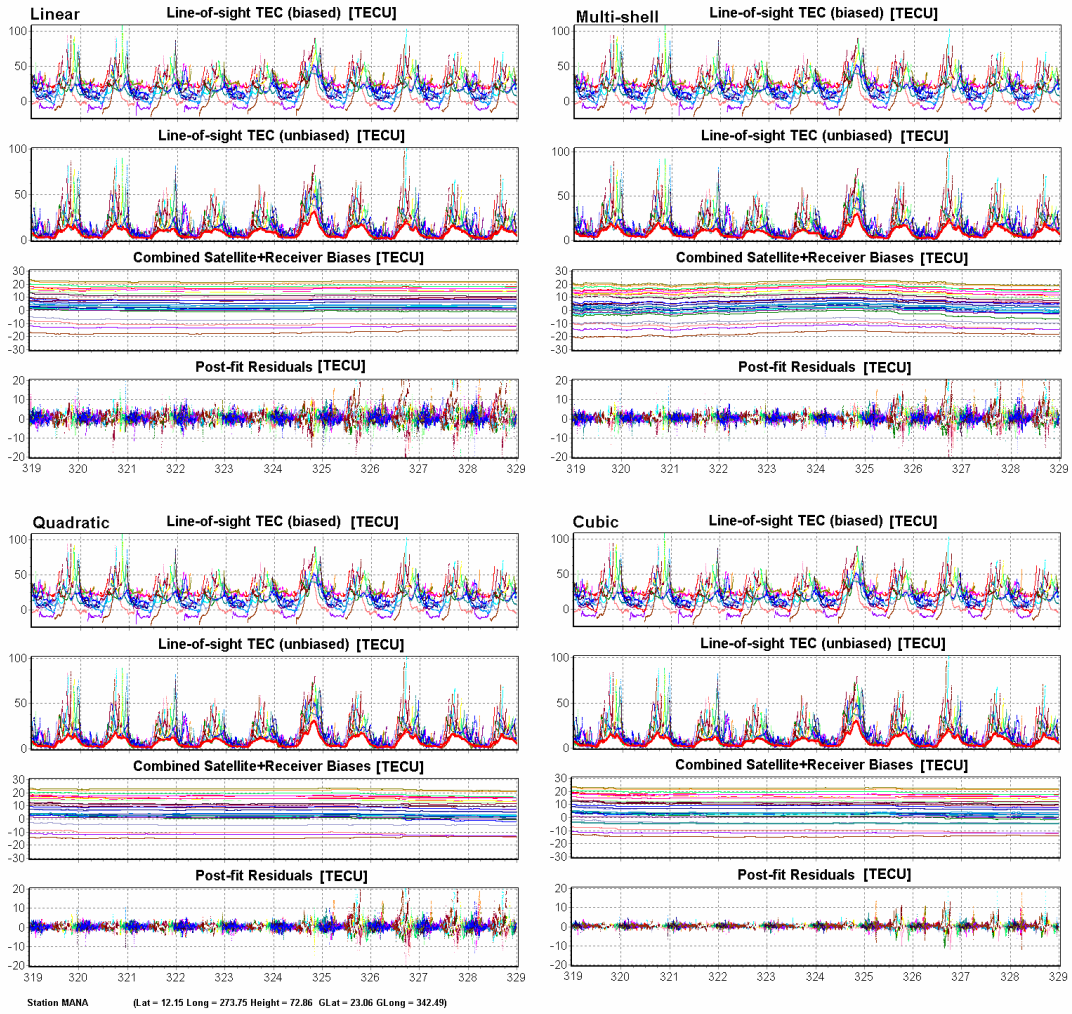

Figure 7.3: WinTEC results at MANA, for 15-24 November 2007, using the single-shell linear, quadratic, and cubic approaches and the multi-shell linear approach.

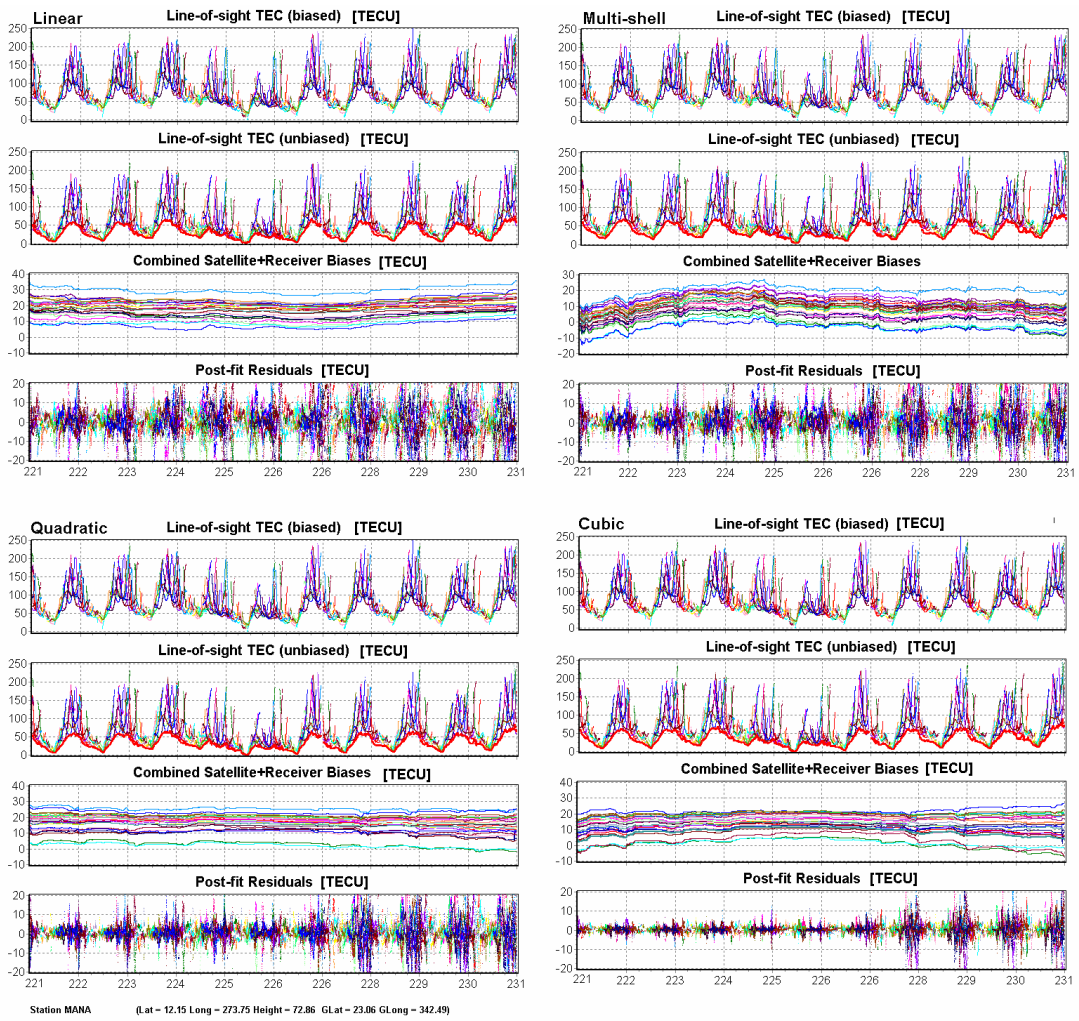

Figure 7.4: WinTEC results at MANA, for 8-17 August 2000 (221-230), using the single-shell linear, quadratic, and cubic approaches and the multi-shell linear approach.

7.4.2 Comparative Results between WinTEC and USTEC

For validation purposes, in this section, we compare the WinTEC-estimated vertical TEC values obtained with the cubic approach with those predicted by USTEC (Spencer et al., 2004), for 15-24 November 2007. For our analysis, we selected the same five North American stations that were also used in the previous chapter, their

codes, names, and geographic coordinates being listed, for convenience, in Table 7.1. Four of the stations were selected since they also provide data for USTEC, while the DSRC station was chosen arbitrarily. Also, as indicated by the daily Ap values plotted in Figure 7.2, this solar minimum period was characterized by quiet to moderate geomagnetic conditions.

GPS Stations for WinTEC/USTEC	*Latitude*	*Longitude*
CCV5/CCV4 (CAPE CANAVERAL, FL)	28.46	279.45
CME5/CME2 (CAPE MENDOCINO, CA)	40.44	235.60
ANP5/ANP2 (ANNAPOLIS, MD)	39.01	283.39
SPN1/SPN2 (SPOKANE,WA)	47.62	242.58
DSRC (BOULDER, CO)	39.99	254.74

Table 7.1: List of GPS stations used for the WinTEC - USTEC comparative analysis.

Figure 7.5 displays the WinTEC results for four of the stations after one day of simulations, for the Kalman filter to stabilize, whereas the results for DSRC are included in the ensemble of plots in Figure 7.7. As shown in these plots, the daytime vertical TEC values (the solid red curves in the unbiased TEC plots) were in general less than 15 TECU and the slant TEC values were less than 40 TECU, but larger TEC values were obtained during the positive phase of the storm that commenced on November 20. Displayed in these plots are also the combined satellite and receiver biases, which appear relatively constant over the entire period, and the post-fit residuals, with standard deviations less than 0.5 TECU. Together they indicate that there is a high modeling accuracy in all five cases. The upper panels in the WinTEC plots show the biased slant TEC values prior to the Kalman filter processing.

The vertical TEC values predicted by WinTEC (red) and USTEC (blue) at the five stations, for 15-24 November 2007, are displayed in Figure 7.6, with the corresponding root mean square errors (RMSE) being marked on the panels. As shown in this figure, the largest RMSE values, of about 2 TECU, are obtained at CCV5 in Florida and CME5 in California, but these values are below the USTEC uncertainty level, estimated to be about 2-3 TECU for quiet geomagnetic conditions (Minter et al., 2007). It can thus be concluded that there is an excellent agreement between the two algorithms at all five stations, over the considered time interval. The excellent comparative results between WinTEC and USTEC bring also new evidence that, although based on a simple mathematical formalism, WinTEC is a powerful tool for estimating the ionospheric TEC, which can rise to the performance level of a more complex and computationally expensive algorithm like USTEC. With WinTEC providing accurate ionospheric TEC estimates, in the next two sections, we present some results obtained with WinTEC-IP, which is basically a modified version of the WinTEC algorithm with an additional plasmaspheric term included in the observation equation.

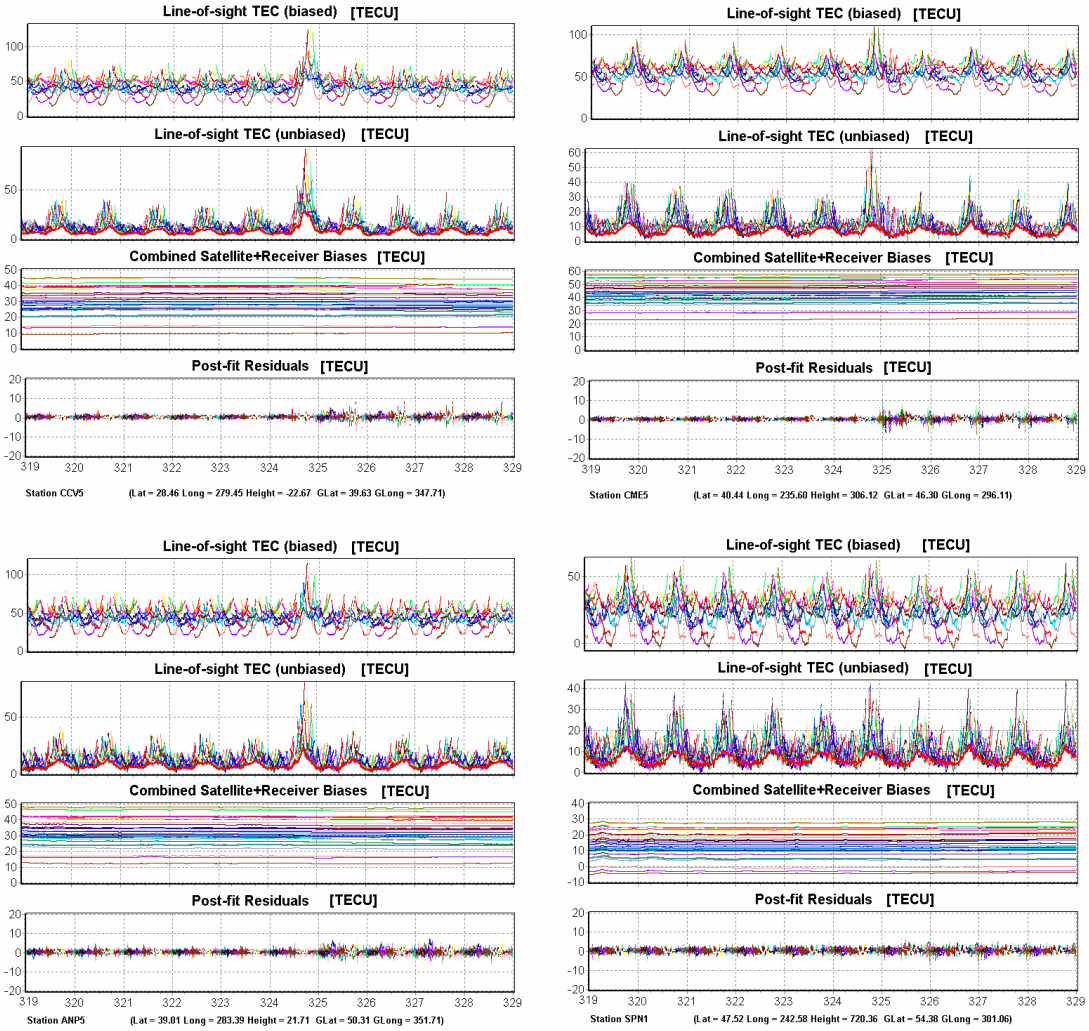

Figure 7.5: WinTEC results at CCV5, ANP5, CME5 and SPN1, for 15-24 November 2007 (319-328), using the cubic approach. The solid red lines in the unbiased slant TEC plots represent the estimated vertical TEC above the stations.

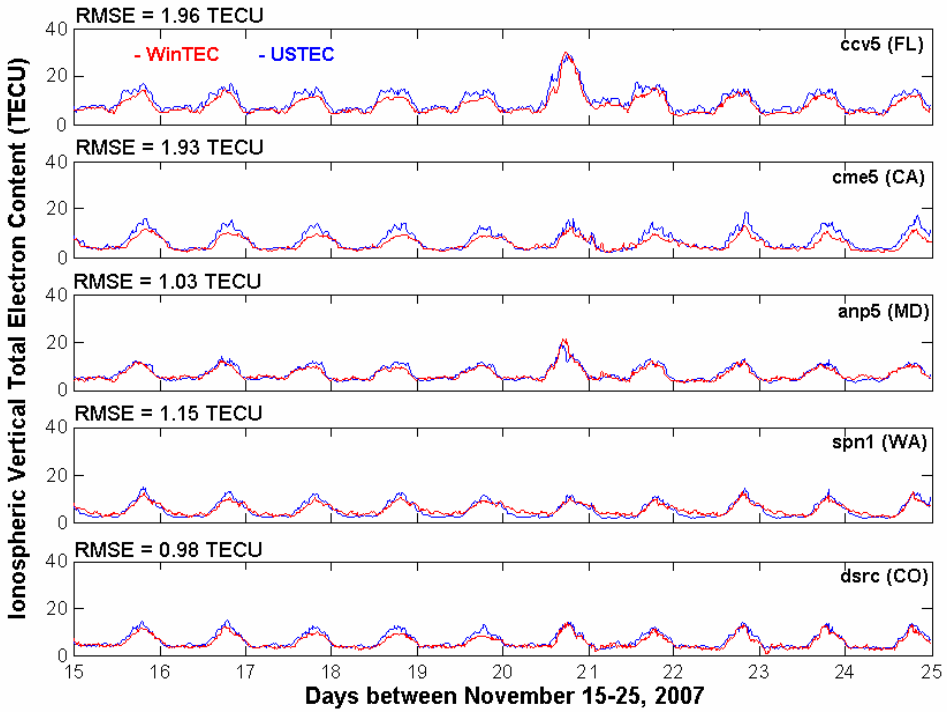

Figure 7.6: WinTEC and USTEC-estimated vertical TEC values at CCV5, ANP5, CME5 and SPN1, for 15-24 November 2007.

7.4.3 Comparative Results between WinTEC and WinTEC-IP

GPS measurements collected by three ground-based, dual frequency receivers located at different geomagnetic latitudes in the American sector are used to compare the WinTEC-IP results, with and without the plasmaspheric term included in the observation equation, for 15-24 November 2007. The three stations are MANA, CCV5, and DSRC, and are listed in Table 7.2. The purpose of this analysis is twofold: (1) to evaluate the effect of the plasmaspheric term on the estimated biases and TEC, and (2) to assess the performance of the newly developed algorithm in estimating both the ionospheric and plasmaspheric TEC for stations located in the American sector.

GPS Stations		*Latitude*	*Longitude*
MANA	(MANAGUA, Nicaragua)	12.08	273.86
CCV5	(CAPE CANAVERAL, FL, USA)	28.46	279.45
DSRC	(BOULDER, CO, USA)	39.99	254.74

Table 7.2: List of GPS stations used for the WinTEC - WinTEC-IP comparative analysis.

The discussion in this section is centered on Figure 7.7, which shows the WinTEC (upper row) and WinTEC-IP (bottom row) results, at a sampling time of 30 seconds, for the stations listed in Table 7.2. The plots were produced using a cutoff elevation angle of 10^{o}, an ionospheric shell height of 350 km, and a third order polynomial approximation for the vertical ionospheric TEC. To interpret the results shown in this figure, we consider the post-fit residuals and the stability of the estimated biases as indicators of modeling accuracy. As seen in this figure, at the low-latitude station MANA, the post-fit residuals are slightly larger than at CCV5 and DSRC, probably because at this station the estimated total and ionospheric TEC values are also larger at the other two stations, but there is still not a clear dependency of the residuals on latitude. It is also evident in this figure that, at all three stations, the changes in the residuals and their standard deviations are negligible when the plasmaspheric term is included in the observation equation compared to the case when it is not, and the instrumental biases estimated with the two algorithms are relatively constant over the entire interval. We can thus conclude that by explicitly accounting for the plasmasphere, the modeling accuracy of our technique is not affected, but there are slightly changes in the magnitudes of the estimated biases and total TEC.

Minor changes in the estimated biases can be observed in Figure 7.7, when the PEC is taken into account compared to the case when it is not, but they amount less than 3 TECU at MANA, about 1 TECU at DSRC, and are almost negligible at CCV3. At MANA, the WinTEC-estimated vertical TEC is also less by about 3 TECU than the vertical total TEC predicted by WinTEC-IP, the underestimation of the vertical TEC by WinTEC being most possibly caused by an overestimation of the biases at this station. Since WinTEC does not explicitly account for the PEC, at low latitudes, where PEC exhibits a relatively weak elevation angle dependency, the estimation algorithm distributes the plasmaspheric contribution between the biases and TEC, thereby leading to an overestimation of the biases and, in turn, to an underestimation of the total TEC. At CCV5 and DSRC, the vertical total TEC values predicted by WinTEC exceed those predicted by WinTEC-IP by about 1 TECU. Our results are consistent with those reported by Carrano et al. (2008), where they also found a decrease of about 3 TECU in the estimated vertical TEC at a low-latitude station and an increase of less than 1 TECU at two mid-latitude stations when the plasmaspheric term was not included compared to the case when it was included. In their studies, the receiver bias was also estimated to be 3.4 TECU higher at the low-latitude station and 0.7 TECU smaller at the most poleward of the three stations when the plasmaspheric term was not included compared to the case when it was included, but no clear changes in the estimated bias were observed at the other station.

Another aspect to be remarked in Figure 7.7 is that the vertical PEC predicted by WinTEC-IP (solid black lines) presents a latitudinal dependency, as it decreases with increasing geomagnetic latitude. The largest daytime vertical PEC values are

recorded at MANA with values around 2 TECU, while at CCV5 and DSRC the daytime vertical PEC values are about 1 TECU and 0.2 TECU, respectively. A small diurnal variation is also observed in the vertical PEC at all three stations, with a daytime minimum and an evening maximum, around 2100 LT, reaching values of about 4 TECU at MANA, 2 TECU at CCV5, and 0.5 TECU at DSRC. In percentage values, the vertical PEC represents about 10% of the daytime and about 50% of the nighttime vertical total TEC at MANA, while at CCV5 and DSRC the percentage contributions are slightly smaller. It is important to remark that, although the latitudinal and diurnal variations of the vertical PEC are mainly imposed by the background plasmaspheric model, our vertical PEC results are in reasonable agreement with results reported by previous experimental and modeling studies (e.g., Lunt et al., 1999a; Mazzella et al., 2002; Balan et al., 2002; Behelaki et al., 2004).

As shown in Figure 7.7, following the November 20 storm event, there is a slow decrease in the vertical PEC, which is more evident at MANA than at the other two stations. This seems to be in agreement with the fact that, following a storm event, magnetospheric convection currents erode the outer plasmasphere producing a depletion of the plasmaspheric flux tubes (e.g., Kersley and Klobuchar; 1980, Lunt et al., 1999a, c). Following the increase in the geomagnetic activity on November 20, a slight decrease in the evening plasma bulge at MANA can be also observed. However, our plots do not show any changes in the occurrence time of the plasma bulge as the geomagnetic conditions change, most probably because the background plasmaspheric model used here is more appropriate for quiet-time conditions. It is though possible that plasmaspheric models that take into account the geomagnetic

activity dependency of the plasmaspheric electron density distribution (e.g., Gallagher et al., 2000; Webb and Essex, 2004) might be more appropriate for studies focusing on the storm-time response of the plasmasphere, but this is beyond the purpose of our current research.

It can be also seen in Figure 7.7 that the estimated slant PEC at the three stations exhibits a meridional asymmetry, with larger PEC values on ray paths to the south than to the north, which is more evident at CCV5 and DSRC. The hemispheric asymmetry in the estimated PEC is mainly imposed by the background model and is associated with the geometry of the plasmaspheric flux tubes. At CCV5, the vertical PEC values are closer to the slant PEC values along ray paths to the north, which is consistent with the model results shown in Figure 7.1c. The daytime slant PEC varies between about 0.2-7 TECU depending on the elevation angle and on the north/south position of the satellite with respect to the station, but also on the geomagnetic conditions, as after the storm event on November 20, the daytime slant PEC decreases gradually to values below 6 TECU. At DSRC, which is the most poleward of the three stations, the daytime slant PEC reaches values of up to about 4 TECU during the pre-storm period, while after the storm it decreases to values below 2 TECU. Like at the CCV5 station, the vertical PEC values are also closer to the slant PEC values along ray paths to the north. The evening bulge is about 2 TECU during the pre-storm period, but drops to values below 1 TECU after the storm. At the low-latitude station MANA, the slant PEC is less dependent on the viewing angle than at mid-latitudes, which is consistent with Figure 7.1, and varies within the 0.5-4 TECU range around the vertical PEC, decreasing to values below 3 TECU following the increase in the

geomagnetic activity. In this case, the plasma bulge is about 2 TECU, but presents a small decrease after November 20. It can be also remarked in Figure 7.7 that, at all three stations, there is more variability in the slant PEC along ray paths to the south than to the north. The largest variability is predicted at DSRC possibly because at this site the slant PEC on ray paths to the south contains mostly contributions from upper plasmaspheric layers which are under direct influence of magnetospheric processes.

To summarize, our results show that the plasmaspheric contributions to the daytime vertical TEC at the three northern hemisphere stations listed in Table 7.2, during 15-24 November 2007, are about 0.2 TECU at DSRC, 1 TECU at CCV5, and 2 TECU at MANA, while the plasmaspheric contributions to the daytime slant TEC are about 4 TECU at DSRC, 7 TECU at CCV5, and 4 TECU at MANA. A small diurnal variation is observed in the PEC at all three stations, with a daytime minimum and an evening maximum around 2100 LT, which is mainly imposed by the background plasmaspheric model. It is also shown that by explicitly accounting for the PEC, there are no significant changes in the standard deviation of the post-fit residuals and the biases remain relatively constant throughout the entire period, which therefore indicates that there is no degradation in the modeling accuracy of our algorithm. However, there are small changes in the estimated biases and total TEC when the plasmaspheric term is include in the observation equation, particularly at low latitudes, but they amount less than about 3 TECU at MANA and are even smaller at higher latitudes. Overall, our results suggest that WinTEC-IP is a reliable tool for estimating both the ionospheric and plasmaspheric TEC, although further validation studies for different solar and geomagnetic conditions are still required.

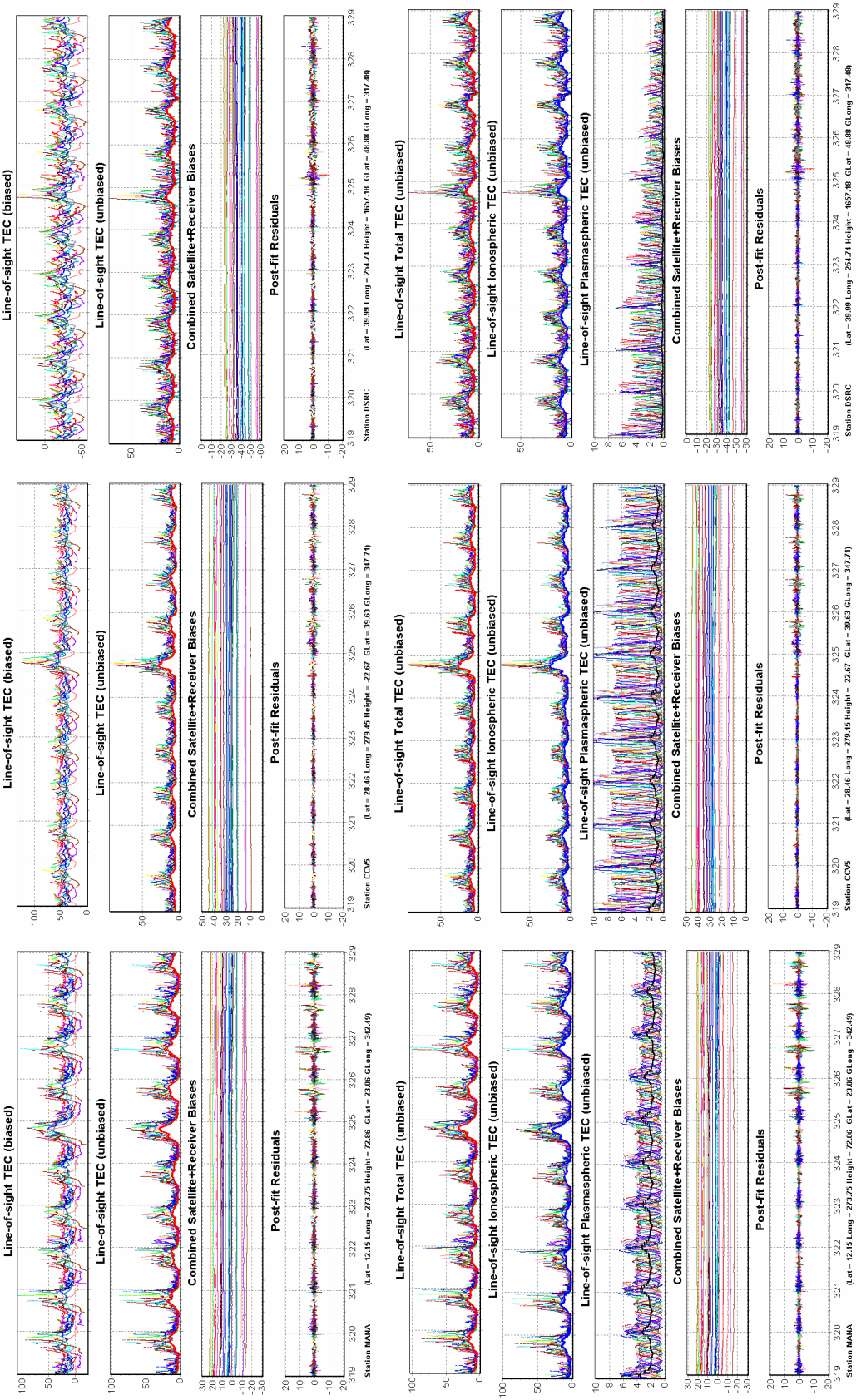

Figure 7.7: (upper panel) WinTEC and (lower panel) WinTEC-IP results at MANA, CCV5 and DSRC, for 15-24

7.4.4 Longitudinal Variability of the Plasmaspheric Electron Content

To assess the consistency of the plasmaspheric results obtained with our algorithm, we applied WinTEC-IP to twelve stations from the International Global Navigation Satellite System Service (IGS), Continuously Operating Reference Stations (CORS), and GPS Earth Observation Network (GEONET) networks, distributed roughly over four geomagnetic latitudes and three longitude sectors. The codes, names, and geographic coordinates of the stations are listed in Table 7.3, and their WinTEC-IP results for 15-24 November 2007 are shown in Figures 7.8 and 7.9. The first four stations in Table 7.3 (AREQ, MANA, CCV5, and GALB) are located within the 273^{o}-289^{o} longitude range and their WinTEC-IP results are displayed in the first row of plots in Figures 7.8 and 7.9. The next four stations (ADIS, DRAG, CRAO, and MOBN) are situated in the 34^{o}-39^{o} longitude range and their WinTEC-IP results are shown in the middle row of plots in Figures 7.8 and 7.9. Finally, the WinTEC-IP results for the last four stations (GUAM, AIRA, 001, and YAKT) listed in Table 7.3 and distributed over the 129^{o}-145^{o} longitude range are presented in the last row of plots in Figures 7.8 and 7.9. It should be remarked in this two figures that at all the stations considered here the estimated biases are relatively constant over the entire analyzed interval and the post-fit residuals have standard deviations less than 0.3 TECU, which indicate that there is a good modeling accuracy in each of the twelve cases.

GPS Stations		*Latitude*	*Longitude*
AREQ	(Arequipa, Peru) – IGS	-16.46	288.50
MANA	(Managua, Nicaragua) – CORS	12.08	273.86
CCV5	(Cape Cañaveral, FL, USA) – CORS	28.46	279.45
GALB	(Cincinnati, Ohio, USA) – CORS	39.12	275.71
ADIS	(Addis Ababa, Ethiopia) - IGS	9.03	38.76
DRAG	(Metzoki Dragot, Israel) – IGS	31.59	35.39
CRAO	(Simeiz, Ukraine) – IGS	44.41	33.99
MOBN	(Obninsk, Russian Federation) – IGS	55.11	36.56
GUAM	(Dededo, Guam) – CORS	13.58	144.84
AIRA	(Aira, Japan) – IGS	31.82	130.59
0001	(Japan) – GEONET	45.40	141.75
YAKT	(Yakutsk, Russian Federation) – IGS	62.03	129.68

Table 7.3: List of GPS stations used to study the longitudinal variability of the PEC.

Figure 7.8a shows the WinTEC-IP results for the AREQ, ADIS, and GUAM stations, which are located within the $\pm 5^{o}$ geomagnetic latitude range. At all three sites, the estimated slant PEC varies within a very narrow range around the vertical PEC, which is consistent with the model results illustrated in Figure 7.1d, and displays a diurnal variation with an evening plasma bulge at about 2100 LT. The maximum daytime PEC values vary between 1-4 TECU and the plasma bulge is about 1-2 TECU. Over the considered time interval, secular increasing and respectively decreasing trends can be distinguished in the estimated PEC at AREQ and ADIS, superimposed on the diurnal variation described by the Gallagher model, whereas there is more stability in the estimated PEC at GUAM. Different factors can be responsible for the observed trends in the estimated PEC at AREQ and ADIS. First, apart from the fact that AREQ is about -5^{o} south of the geomagnetic equator while ADIS and GUAM are about 0^{o} and 4^{o} north, respectively, the three stations are also separated by more than 100^{o} in longitude. It is thus possible that the slight differences between the estimated PEC patterns shown in Figure 7.8a may be

associated with the displacement between the geographic and geomagnetic equators, which can produce specific seasonal variations in the ionosphere and plasmasphere, and with local variations in the equatorial plasma drifts at these longitudes (e.g., Horvath and Essex, 2003). In addition, the trends in the estimated PEC patterns may be also associated with a reduction in the modeling accuracy of the algorithm, which is in general reflected by variations in the estimated biases. As shown in Figure 7.8a, there is indeed a small increasing trend in the estimated biases at ADIS and a small decreasing trend at AREQ, especially after November 20, which may indicate a possible reduction in the modeling accuracy. A reduction in the modeling accuracy can be due to a mismodeling of the storm-time equatorial ionosphere and also to the weak elevation angle dependency of the equatorial PEC predicted by the Gallagher model.

The WinTEC-IP results for the MANA, DRAG, and AIRA stations located within the 21^{o}-27^{o} geomagnetic latitude range are shown in Figure 7.8b. It can be observed in this figure that, over the entire analyzed period, the estimated PEC patterns at the three stations are very similar despite differences in the geometry of the GPS satellite configuration at these stations. The estimated, daytime slant PEC at these stations reaches maximum values of about 4 TECU on ray paths to the south and minimum values of about 0.5 TECU on ray paths to the north, and the evening plasma bulge amounts about 2 TECU. Also, the vertical PEC is about the same at all three stations, with values varying from about 2 TECU for the most part of the day to about 4 TECU at dusk. Similar results were reported by Otsuka et al. (2002). They used GPS-derived TEC observations and incoherent scatter radar electron densities

integrated in altitude between 100 km and 1000 km from Shigaraki, Japan (34.85^{o}N, 136.10^{o}E, geom. 27.8^{o}N), a site near AIRA and 0001, and determined an average vertical PEC of about 2 TECU during a period characterized by low solar and geomagnetic activity. At MANA, our results are in excellent agreement with those reported by Carrano et al. (2008) for Roatan, Honduras (16.29^{o}N, 273.42^{o}E, geom. 27^{o}N), where they determined a vertical PEC of about 3 TECU and a slant PEC varying from 1 to 5 TECU, depending on the viewing angle.

For the CCV5, CRAO, and 0001 stations, which are located within the 35^{o}-41^{o} geomagnetic latitude range, the WinTEC-IP results are displayed in Figure 7.9a. As shown in this figure, typical for these stations is a strong meridional asymmetry with larger PEC values on ray paths to the south than to the north. The estimated vertical PEC at these stations is about 1.5 TECU for most part of the day and reaches about 2.5 TECU at dusk. Slightly larger vertical PEC values are obtained at 0001, which are consistent with the results reported by Otsuka et al. (2002). At CCV5 and 0001, the estimated slant PEC varies between about 0.2 and 7 TECU, depending on the viewing angle, and reaches a maximum of about 10 TECU at dusk, while at CRAO the estimated slant PEC values on ray paths to the south are larger by about 3-5 TECU than at the other two stations. A gradual decrease in the estimated PEC can also be observed in all three cases following the increase in the geomagnetic activity on November 20. Overall, the estimated PEC patterns at these stations are quite similar indicating a consistency of our results within this geomagnetic latitude range.

The WinTEC-IP results for the GALB, MOBN, and YAKT stations located near 50^{o} geomagnetic latitude are presented in Figure 7.9b. As shown in this figure,

there is a strong latitudinal asymmetry in the estimated PEC at these stations, with larger PEC values along ray paths to the south than to the north. This is in agreement with the fact that, due to the geometry of the plasmaspheric flux tubes, the ray paths to the north from these stations encounter mostly flux tubes outside the plasmasphere, and consequently the PEC values along these ray paths are expected to be very low, while the ray paths to the south traverse long distances through a denser plasmasphere. The estimated vertical PEC at these stations is about 0.05 TECU and reaches values of 0.5 TECU at dusk, while the estimated slant PEC is as high as 10 TECU at GALB for most part of the day, with slightly smaller values at MOBN and YAKT, and displays an evening enhancement of about 3-5 TECU. It is also interesting to remark that the maximum slant PEC values predicted by WinTEC-IP at GALB are very similar with those at CRAO, although the estimated vertical PEC values at GALB are much smaller than at CRAO.

Our results at GALB, MOBN, and YAKT are in good agreement with those reported by other authors. Using concurrent GPS-TEC and Navy Ionospheric Monitoring System (NIMS)-derived TEC data, Lunt et al. (1999c) determined vertical PEC values at Aberystwyth, Wales (52.4^{o}N, 4.1^{o}W, geom. 49^{o}N) of about 0.05 TECU, and values of about 0.75 TECU around 2000 LT. However, they found only a small plasmaspheric contribution of 1-2 TECU along ray paths to the south from the station. Kersley and Klobuchar (1978) and Webb and Essex (2004) found at Aberystwyth, using observations from the ATS-6 satellite radio beacon, average slant PEC values of 5 TECU and respectively 7 TECU, which are consistent with our results. In a recent study, Carrano et al. (2008) estimated the vertical PEC for two

sites located near GALB, Westford (42.61^{o}N, 288.52^{o}E, geom. 52^{o}N) and Greensboro (36.08^{o}N, 280.23^{o}E, geom. 46^{o}N), to be about 0.7 and 1.3 TECU, respectively, which are higher than the values predicted by WinTEC-IP at GALB. Also, in both cases, the maximum slant PEC predicted by their algorithm is less by about 3 TECU than at GALB. A main cause for the observed differences could be that in our studies we use a different background plasmaspheric model than the one used by Carrano et al. (2008). However, it is also possible that there is an actual longitudinal variability in the slant PEC, as is the case at GALB (Figure 7.9b) and DSRC (Figure 7.7), where the estimated vertical PEC values are about the same, but there is a large difference of about 6 TECU between the estimated slant PEC at the two stations, which are only about 20^{o} apart in longitude.

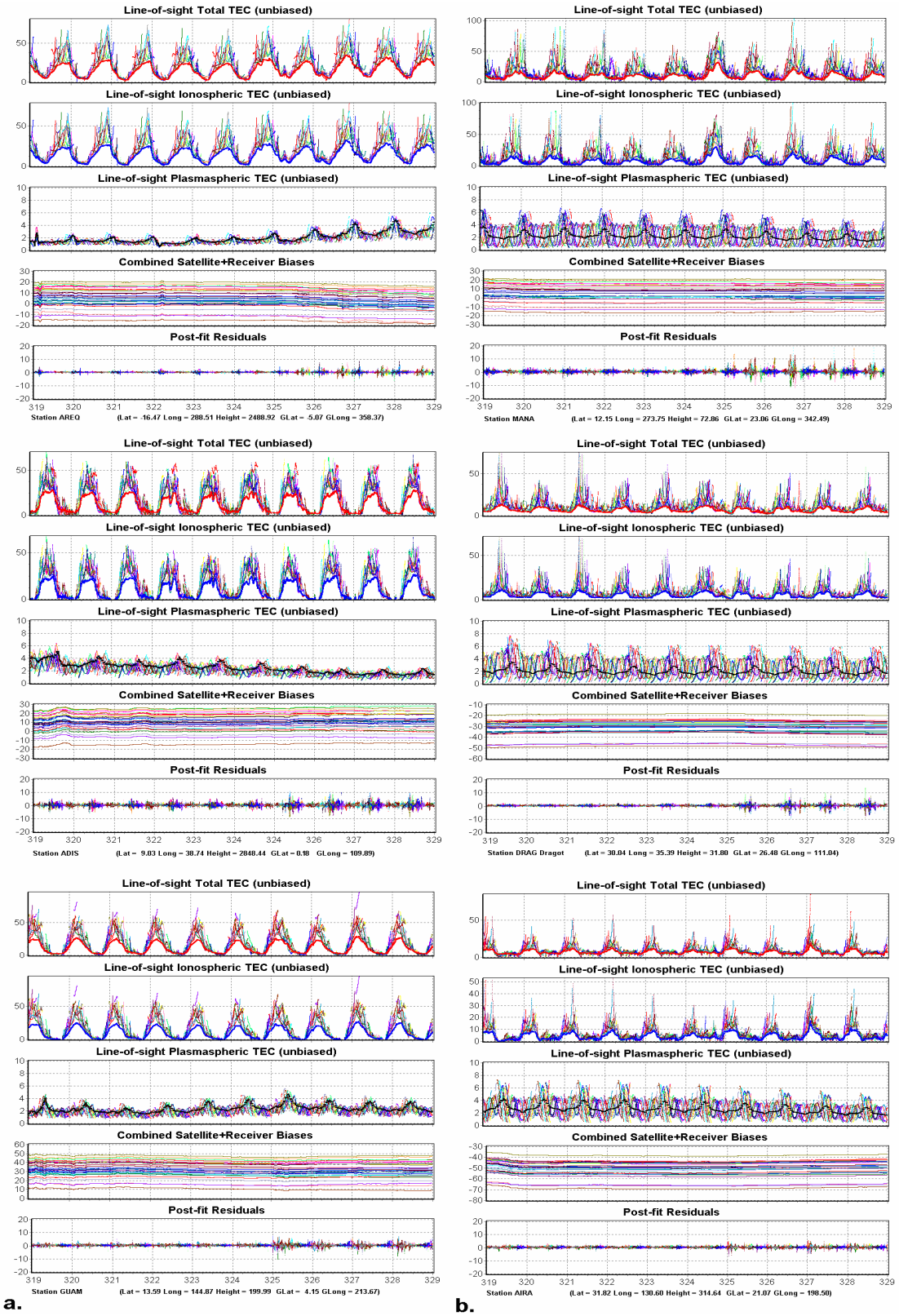

Figure 7.8: WinTEC-IP results for the six equatorial and low-latitude stations listed in Table 7.3, for 15-24 November 2007 (319-328).

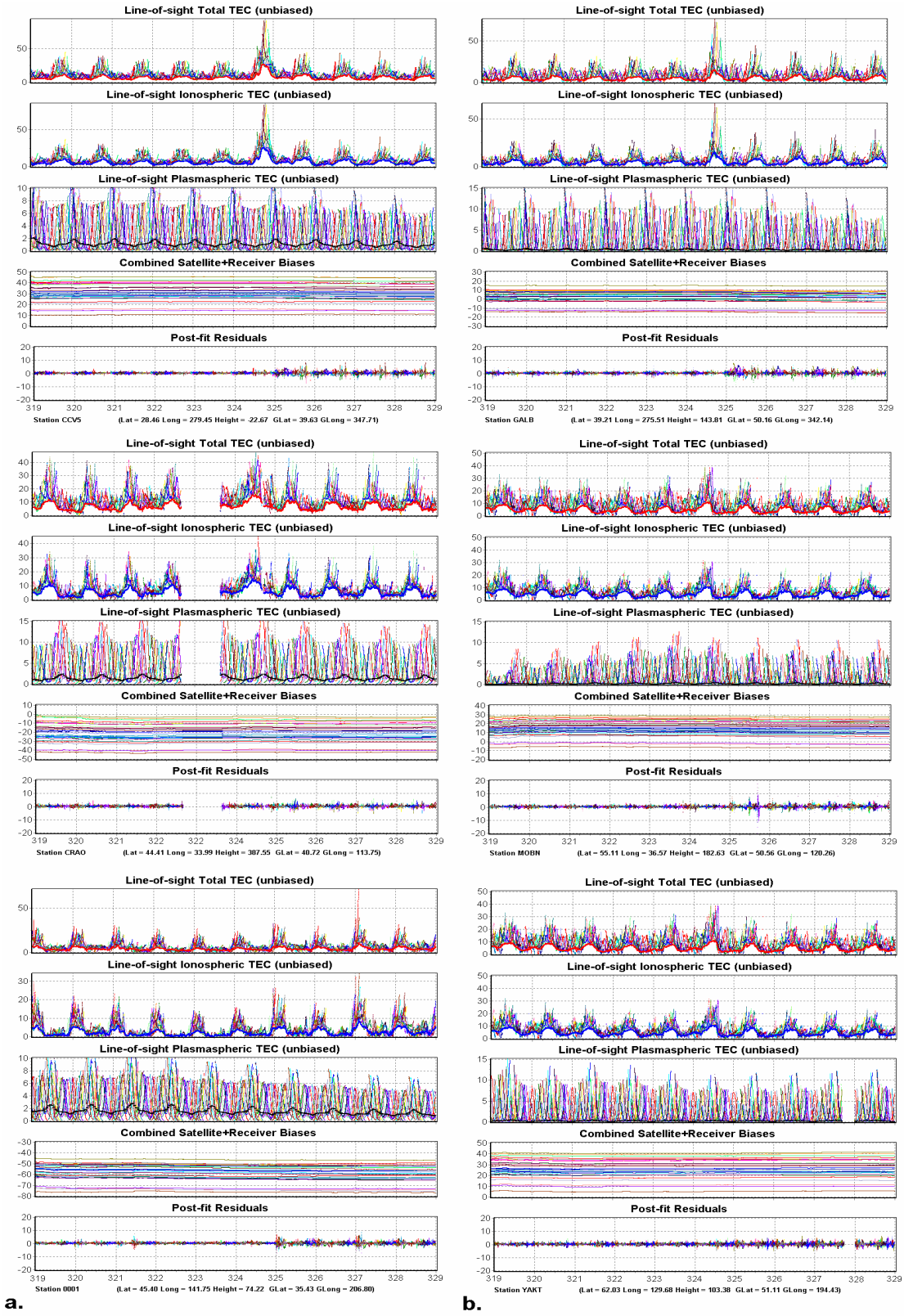

Figure 7.9: WinTEC-IP results for the six mid-latitude stations listed in Table 7.3, for 15-24 November 2007 (319-328).

7.5 Conclusions

Using the WinTEC algorithm, we have explored different ionospheric modeling techniques with the ionosphere approximated as a single-shell or multi-shell structure and the vertical TEC modeled as polynomials of different orders. We have found that out of the modeling approaches examined here, WinTEC produces the lowest post-fit residuals when the single-shell cubic approach is employed to represent the ionospheric TEC above the monitoring stations. Throughout the chapter, the post-fit residuals have been used as a measure of modeling accuracy together with the stability of the estimated biases, modeled as constants, as variations in the biases may indicate unmodeled systematic errors or ionospheric effects propagating into the bias solutions. To further test the performance of the algorithm for the cubic approach, we have also compared the TEC values predicted by WinTEC and USTEC at five North American stations during 15-24 November 2007, which is a relatively quiet solar minimum period, and have found an excellent agreement between the two algorithms with RMSEs less than about 2 TECU. Our validation results complement those reported in the previous chapter, where we have provided excellent comparative results between WinTEC and USTEC during three geomagnetically disturbed periods at the declining phase of the solar cycle 23.

Based on previous plasmaspheric studies (Mazzella et al., 2002, Carrano et al. 2008), we have developed the WinTEC-IP algorithm which explicitly accounts for both the ionospheric and plasmaspheric contributions to the GPS measurements of TEC by using the single-shell cubic approximation for the ionospheric TEC and the

Gallagher plasmaspheric model (Gallagher et al., 1988) as a background model for the PEC. Comparative results between WinTEC and WinTEC-IP have shown that by including the new data assimilation module to account for the PEC, there is no degradation in the performance and modeling accuracy of WinTEC-IP in terms of post-fit residuals and bias stability, although some minor changes in the estimated biases and total TEC can be observed, particularly at low-latitude stations. It has been shown that, for 15-24 November 2007, by not explicitly accounting for the PEC, the total vertical TEC is underestimated by about 3 TECU at MANA and overestimated by about 1 TECU at CCV5 and DSRC, while the changes in the estimated instrumental biases are less than 3 TECU at MANA, about 1 TECU at DSRC, and almost negligible at CCV3.

To further investigate the consistency of our plasmaspheric results obtained with WinTEC-IP, we have calculated the PEC patterns during 15-24 November 2007 at twelve stations distributed roughly over four geomagnetic latitudes and three longitude sectors, separated by about 100^{o}. Similar latitudinal PEC patterns have been obtained at each longitude sector consistent with the geometry of the plasmaspheric flux tubes and plasma distribution in the plasmasphere, but also with results reported by other authors (e.g., Lunt et al., 1999c; Mazzella et al., 2002; Otsuka et al., 2002; Carrano et al., 2008). Overall, our results suggest that WinTEC-IP is a reliable remote sensing technique for estimating the contribution to the GPS-TEC from both the ionosphere and plasmasphere. However, further investigations and validation studies still need to be carried out to test the potential of the method in estimating the PEC for different geophysical conditions and at different locations.

Chapter 8

Investigations of the Plasmasphere Morphology with GPS

8.1 Background

The ionosphere is a conductive, partially ionized region of the Earth's upper atmosphere that extends roughly within the 90-1000 km altitude range, with the bulk of plasma typically residing in a relatively thin altitude layer in the F-region, between about 200 and 400 km. The plasmasphere, on the other hand, is a doughnut-shaped plasma cloud confined by the Earth's magnetic field and located above the ionosphere in the inner magnetosphere. It surrounds the Earth at low and mid-latitudes and extends to equatorial distances of several Earth radii, from the O^+/H^+ transition height up to about 35,000 km. Together the ionosphere and plasmasphere form a dispersive medium for the Global Positioning System (GPS) signals, which must travel through the tenuous hydrogen-dominated plasma of the plasmasphere and oxygen-dominated plasma of the ionosphere on their way to the ground-based receivers. The two ionized

regions of the Earth's atmosphere affect the GPS signals by introducing a frequency dependent path delay proportional to the total electron content (TEC) along the propagation path from where valuable temporal and spatial information about the electron density distribution in both the ionosphere and plasmasphere can be retrieved. However, as shown in Chapter 7, to be able to determine the ionospheric and plasmaspheric electron contents (PEC) along the GPS signal paths, one needs to take into account the specific properties of the two media and make use of relevant knowledge about their specific dynamics and geometry.

Over the past two decades, several algorithms for estimating the ionospheric TEC from GPS observations have been developed and reported in the literature (e.g., Hernandez-Pajares et al., 1998; Spencer et al., 2004; Carrano et al., 2006; Rideout and Coster, 2006; Anghel et al., 2008). But, these algorithms implicitly assume that all the measured TEC is ionospheric in origin and employ background ionospheric models that do not correctly represent the plasmasphere. As a result, these algorithms tend to distribute the PEC between the instrumental biases and TEC, which can lead to inaccuracies in the biases and total TEC estimates. On the other hand, numerous studies have indicated that the contribution of the plasmasphere to the GPS measurements of TEC can become significant under certain conditions and should not be ignored (e.g., Law, 1999; Lunt et al., 1999a, b, c, d; Balan et al., 2002; Belehaki et al., 2002). Using GPS observations and model simulations, Mazzella et al. (2002, 2007) showed that more accurate TEC estimates can be obtained when the plasmasphere is also explicitly accounted for. Following on these ideas, Carrano et al. (2008) and Anghel et al. (2009a) extended the WinTEC algorithm presented in

Chapter 6 by incorporating a background plasmaspheric model and estimating an amplitude coefficient for the PEC predicted by the model.

In our current studies, we use the WinTEC-IP algorithm developed by Anghel et al. (2009a) and presented in Chapter 7. The algorithm estimates both the ionospheric and plasmaspheric electron content along GPS ray paths by combining GPS data from one or several ground-based, dual-frequency receivers with background information from the Gallagher's empirical plasmaspheric model (Gallagher et al., 1988) in a Kalman filter approach. To assess the performance of the algorithm, in the previous chapter, we applied WinTEC-IP to data obtained from several GPS receivers and showed that our results are consistent with results reported by others. Expanding on these studies, in an attempt to further validate our technique, here we examine the morphology of the plasmasphere by applying WinTEC-IP to data collected from four magnetically conjugate sites located at low and mid-latitudes within the 65^{o}-90^{o}W longitude range, for two quiet solar minimum periods in August and November 2007. We show that the estimated PEC displays a seasonal variation, with larger values in November than in August, and a hemispheric asymmetry (e.g., Park et al., 1978; Guiter et al., 1995; Clilverd et al., 1991, 2007) which originate from the measurements themselves and not from the background plasmaspheric model. We also show that the estimated PEC displays a diurnal variation, with a daytime minimum and an evening maximum, which is imposed by our selection of the Gallagher model and the manner it has been incorporated into our data assimilation scheme. Our results also indicate that the vertical PEC decreases with increasing geomagnetic latitude and that the slant PEC presents a meridional asymmetry with

larger values on ray paths towards the equator than towards the poles, these traits being also mainly inherited from the background plasmaspheric model.

The chapter is organized as follows: (1) in the next section, we provide relevant information about the plasmasphere, we then briefly (2) introduce the WinTEC-IP algorithm, (3) outline the ionospheric and plasmaspheric modeling techniques, and (4) review the Gallagher's empirical plasmaspheric model, and finally (5) present succinct results and conclusions.

8.2 Theoretical Considerations

The plasmasphere is the high-altitude extension of the ionosphere, with which is in a field-aligned diffusive equilibrium at the ends of the magnetic flux tubes. In consequence, since in the plasmasphere the production and loss processes are essentially absent, the plasmasphere is primarily populated by ionospheric plasma flows (Kersley and Klobuchar, 1978). Specifically, there is an exchange of plasma on a daily basis between the topside ionosphere and plasmasphere. During daytime, oxygen-dominated plasma from the underlying ionosphere diffuses upward along the magnetic field lines and charge exchanges with atomic hydrogen at some O^+/H^+ transition height, producing hydrogen-dominated plasma above this height. After the ionospheric sunset, hydrogen-dominated plasma from the plasmasphere returns along the field lines to lower altitudes and charge exchanges with atomic oxygen, producing oxygen-dominated plasma that contributes to maintaining the nighttime F layer. The O^+/H^+ transition height is usually defined as the altitude where the O^+ and H^+

densities are equal. Its position depends on the geomagnetic activity level and exhibits a diurnal, seasonal, solar cycle, latitudinal, and longitudinal variation (e.g., Marinov et al., 2004).

The plasmasphere thus acts as a reservoir of ionization, which is replenished during the day by upfluxes of ionospheric plasma and is capable of maintaining the F-region at night through downward plasma transport from plasmasphere, the coupling between ionosphere and plasmasphere in both cases involving a charge exchange between hydrogen and oxygen. At lower latitudes (L<3), the plasmasphere also facilitates a direct coupling between conjugate ionospheres through significant interhemispheric flows of thermal plasma that circulate along the magnetic flux tubes. Several features of the ionosphere and plasmasphere are linked with these flows of plasma (e.g., Bailey et al., 1987) including the hemispheric asymmetry of the plasmaspheric densities, which manifests mainly during the December solstice (Guiter et al., 1995). The interhemispheric flows are caused by differences in the atmospheric parameters and H^+ pressure across the equatorial plane, primarily due to different winter/summer conditions at the feet of the flux tubes, and are meant to maintain continuity in the plasma concentration within the plasmasphere. Hence, the flux tubes can be regarded as closed systems which interact with the underlying ionosphere in both local and conjugate hemispheres, variations in both local and conjugate ionospheres being thus expected to significantly affect the behavior of the plasmasphere that links them. Moreover, the ionosphere-plasmasphere interactions depend on the geomagnetic latitude of the footprints of the magnetic flux tubes, the short flux tubes with bases at low geomagnetic latitudes being in approximate

equilibrium with the underlying ionospheres in a diurnal average sense, while the large tubes with bases at higher geomagnetic latitudes being in a partial equilibrium with the ionosphere below.

The outer boundary of the plasmasphere, the plasmapause, encloses the magnetic flux tubes that corotate with the Earth and is characterized by a rapid decrease in the plasma density. To a first approximation, the plasmapause is considered to be circular in the magnetic equatorial plane, with a pronounced bulge of plasma at larger radial distances (L>3), at dusk. However the size, shape, and dynamics of the plasmasphere and plasmapause are strongly dependent on the geomagnetic conditions, geomagnetic latitude, and local time. In the absence of geomagnetic disturbances, the corotation dominates the near-Earth plasma flow, and the plasmapause moves outward to higher L-shells and becomes gradually saturated with ionospheric plasma. Conversely, during disturbed conditions, the plasmapause moves towards the Earth, causing the contraction of the plasmasphere. Meanwhile, the enhanced sunward convection of the magnetosphere erodes the outer plasmasphere and transports the plasma outward and sunward towards the magnetopause. In the period following the storm, the depleted flux tubes are gradually refilled by upflows of ionospheric plasma, a process that can last for several days. The recovery time of the plasmasphere depends on the L-shell value and ranges from about 2 days at L = 2 to about 8 days at L = 4 (e.g., Park et al., 1978; Kersley and Klobuchar, 1980; Lunt et al., 1999a).

Previous observational and modeling studies have shown that, in addition to a diurnal variation and geomagnetic activity dependency, the plasmasphere also

displays a seasonal variation at American longitudes, with larger plasma densities during the December solstice than during the June solstice by a factor of about 1.5-3 at L = 1.5-5, which increases with decreasing L values (e.g., Clilverd et al., 1991, 2007). As discussed by Guiter et al. (1995), possible mechanisms responsible for the seasonal variation of the plasmaspheric density include:

(1) the tilt of the Earth's magnetic dipole, which can lead to a seasonal variation in the total solar flux illuminating the conjugate ionospheres and different wind-induced vertical plasma drifts. This is especially true at American longitudes where the displacement between the geographic and geomagnetic equators is largest and where the ends of the flux tubes are thus longer exposed to sunlight in December than in June, as illustrated in Figure 8.1 which shows the geometric configuration of the magnetic flux tubes at ~70^{o} W.

(2) seasonal variations in the chemical equilibrium levels of H^{+} in the middle ionosphere;

(3) seasonal variations in the H^{+} scale height caused by seasonal variations in the plasmaspheric temperatures;

(4) seasonal variations in the production and/or loss rates of H^{+} in the upper atmosphere caused by seasonal variations in the neutral atmosphere and/or O^{+} levels;

(5) seasonal variations in the O^{+} levels in the upper ionosphere.

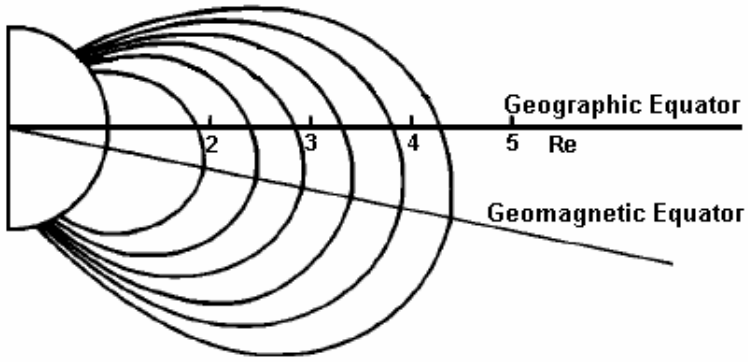

Figure 8.1: Configuration of the geomagnetic field lines at the American longitudes (~70^{o}W) (adapted from Kersley and Klobuchar, 1978).

8.3 The WinTEC-IP Algorithm

WinTEC-IP is a Borland C++ Builder application designed for estimating both the ionospheric and plasmaspheric TEC by processing GPS data from a single site or from several receivers simultaneously in a Kalman filter approach. In WinTEC-IP, the ionosphere is approximated as a set of thin spherical shells located at arbitrary fixed heights, and the vertical TEC on each shell is represented as polynomials of different orders. For our current studies, we used a single shell approximation for the ionosphere and a third order polynomial representation for the vertical TEC. More details about WinTEC-IP are provided in Chapter 7, where we compared four different ionospheric modeling techniques and showed that smaller post-fit residuals are obtained with the cubic approach than with the linear, quadratic and multi-shell linear approaches. Subsequently, we also tested the method for higher order polynomials and found that while the post-fit residuals decrease by increasing the order of the polynomial, the biases fail to remain constant as desired. This indicates that for polynomials of order greater than three the Kalman filter solution

becomes less well-conditioned in a numerical sense due to the large size of the state vector relative to the number of observations. However, while this is true when processing data from a single station, the situation may change when processing data from several receivers simultaneously as more observations become available.

As described in the previous chapter, to explicitly account for the plasmasphere, we included in the observation equation an additional term, *sPEC*, and a scaling factor for this term, a_p. The plasmaspheric term, *sPEC*, is obtained by integrating the electron density predicted by a plasmaspheric model along actual GPS ray paths from the O^+/H^+ transition height, taken here at 1000 km, up to the GPS orbital altitude of 20,200 km. The observation equation, at epoch k, for a receiver-satellite (R,S) pair is then given by:

$$TEC_{RS}^{k} = M\left(e_{RS}^{k},h\right)\cdot\begin{bmatrix} a_{0,R}^{k} + a_{1,R}^{k}\cdot\Delta\lambda_{RS,k} + a_{2,R}^{k}\cdot\Delta\varphi_{RS,k} + \\ a_{3,R}^{k}\cdot\Delta\lambda_{RS,k}^{2} + a_{4,R}^{k}\cdot\Delta\varphi_{RS,k}^{2} + a_{5,R}^{k}\cdot\Delta\varphi_{RS,k}\cdot\Delta\lambda_{RS,k} + \\ a_{6,R}^{k}\cdot\Delta\lambda_{RS,k}^{3} + a_{7,R}^{k}\cdot\Delta\varphi_{RS,k}^{3} + a_{8,R}^{k}\cdot\Delta\varphi_{RS,k}^{2}\cdot\Delta\lambda_{RS,k} + \\ a_{9,R}^{k}\cdot\Delta\varphi_{RS,k}\cdot\Delta\lambda_{RS,k}^{2} \end{bmatrix} + \tag{8.1}$$

$$a_{p}^{k}\cdot sPEC_{RS}^{k} + b_{R}^{k} + b_{S}^{k}$$

which is similar with Equation (7.5). In Equation (8.1), b_S and b_R are the satellite and receiver instrumental biases, $\{a_{j,R}\}_{j=0,..,9}$ are the coefficients of the polynomial fit to the ionospheric vertical TEC, $\Delta\lambda_{RS}$ is the difference between the longitudes of the ionospheric piercing point (IPP) and the mean sun, $\Delta\varphi_{RS}$ is the difference between the geomagnetic latitudes of the IPP and the station, *sPEC* is the slant PEC predicted by the background model, and a_p is the scaling factor for *sPEC*. $M(e_{RS},h)$ is given by

Equation (6.7) and represents a standard mapping function that relates the slant and the vertical TEC at the IPP, where e_{RS} is the elevation angle and h is the height of the ionospheric shell.

According to Equation (8.1), the state vector contains ten ionospheric coefficients, one plasmaspheric scaling factor, one receiver bias, and one bias for each satellite. For the multi-site case, in addition to the satellite biases, the state vector contains one receiver bias, one plasmaspheric scaling factor, and a set of ionospheric coefficients for each receiver. In WinTEC-IP, the biases and the plasmaspheric scaling factor(s) are approximated as constants, and the ionospheric coefficients as random walk processes.

8.4 Gallagher's Empirical Plasmaspheric Model

WinTEC-IP incorporates the empirical plasmaspheric model developed by Gallagher et al. (1988). As mentioned in Chapter 7, the model was developed from measurements taken by the Retarding Ion Mass Spectometer on the Dynamics Explorer 1 and consists of an analytical expression for the plasmaspheric electron density. The plasmasphere predicted by the model exhibits an approximate azimuthal symmetry at lower radial distances (L<3) and an extension at larger radial distances (L>3), at dusk (~2100 LT). Also, as discussed in Chapter 7, the vertical PEC predicted by the model decreases with increasing geomagnetic latitude, the slant PEC at low, mid, and high latitudes exhibits a latitudinal asymmetry with larger values on ray paths towards the equator than towards the poles, and the PEC at equatorial

latitudes is independent of the northward/southward viewing direction and displays a weak elevation angle dependency.

8.5 Results and Discussions

To investigate the morphology of the plasmasphere, we applied WinTEC-IP to the data collected from five low and mid-latitude stations located at magnetically conjugate points, within the 65^{o}-90^{o}W longitude range. A map showing the approximate locations of the stations used in this study is provided in Figure 8.2, and the codes, names, and geographic coordinates of the stations are listed in Table 8.1. We used data from both MANA and GUAT due to data availability, the two stations being located very close to each other. Two solar minimum periods are considered in our studies, 14-18 August 2007 and 15-19 November 2007, which are characterized by low geomagnetic activity levels. The daily Ap values for August and November 2007 are displayed in Figure 8.3. As shown in this figure, during the two periods of interest, marked with vertical dashed lines, the daily Ap was less than 10 and the geomagnetic activity was moderate prior to August 14 and low, for many days, prior to November 15. Having in view that the replenishment of the plasmasphere after disturbed periods can last for several days, this could be relevant to our studies, as it is possible that the plasmasphere was slightly depleted in August 14-18, especially at mid latitudes, and saturated with ionospheric plasma during November 15-19.

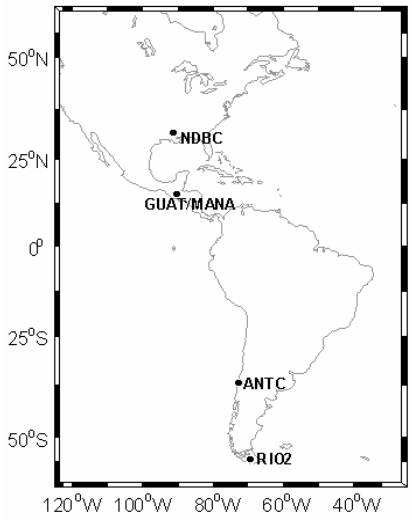

Figure 8.2: Map of the GPS stations used in the analysis

GPS Stations	*Geog. Lat.*	*Geog. Long.*	*Geom. Lat.*	*Geom. Long.*
NDBC, Mississippi, USA	30.21	89.36	40.99	337.21
MANA, Managua, Nicaragua	12.08	86.14	23.06	342.49
GUAT, Guatemala City, Guatemala	14.35	90.31	25.20	337.76
ANTC, Los Angeles, Chile	-37.20	71.31	-25.94	358.47
RIO2, Rio Grande, Argentina	-53.47	67.45	-42.39	1.64

Table 8.1: List of the GPS stations used in the analysis.

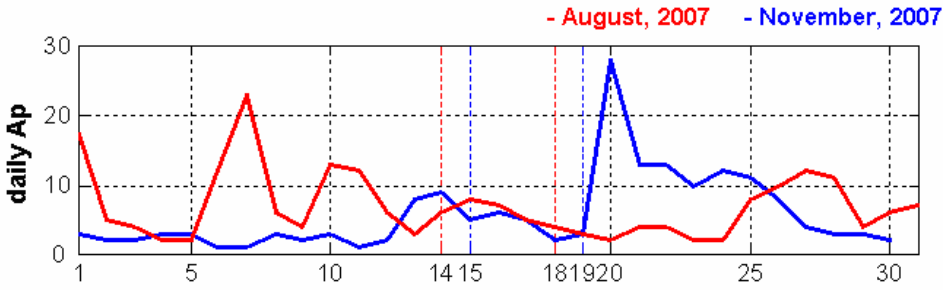

Figure 8.3: Daily Ap values for August and November 2007 as a function of day of the month.

Figure 8.4 illustrates the WinTEC-IP results, at a temporal resolution of 30 seconds, for RIO2, ANTC, MANA/GUAT, and NDBC, for August 14-18 (upper panel) and November 15-19 (lower panel), after one day of simulations to allow the Kalman filter to stabilize. The plots show, from top to bottom, the total (ionospheric+plasmaspheric) TEC, the ionospheric TEC, the plasmaspheric TEC, the combined satellite and receiver biases, and the post-fit residuals as a function of day of the year, in universal time (UT). In all these plots, the thick lines are the vertical TEC values and the thin lines are the slant TEC values. It is clear from these plots that the estimated biases are nearly constant over the two time intervals and the post-fit residuals have standard deviations less than 0.5 TECU, being slightly larger at the northern hemisphere stations than at the southern hemisphere stations. The post-fit residuals and the stability of the estimated biases are used here as a measure of the modeling accuracy, as variations in the biases and/or large post-fit residuals may indicate unmodeled errors in the estimation algorithm. In addition, the average values of the estimated scaling factors for the plasmaspheric term at the four latitudes, for both August and November, are given in Table 8.2. They can be used as correction factors for the Gallagher's plasmaspheric model.

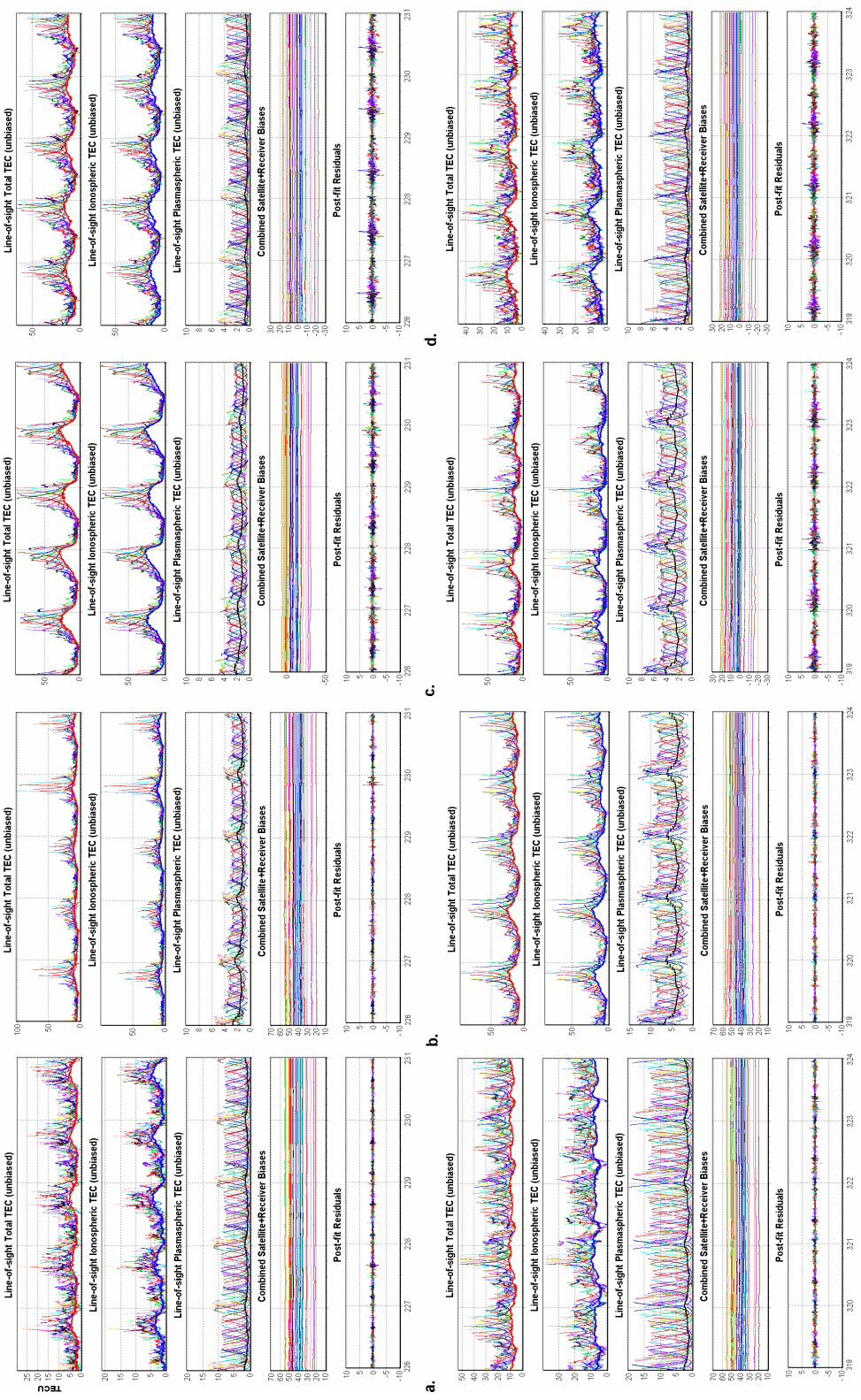

Figure 8.4: WinTEC-IP results for (upper panel) 14-18 August 2007 and (lower panel) 15-19 November 2007, as a function of the day of the year.

GPS Stations	**August**	**November**
NDBC	0.45	0.65
GUAT/MANA	0.40	0.78
ANTC	0.42	1.25
RIO2	1.10	1.85

Table 8.2: Estimated plasmaspheric scaling factors for August and November 2007.

Like in the previous chapter, to evaluate the effect of the plasmasphere on the GPS-TEC, we applied the algorithm, without the plasmaspheric term included in the observation equation, to the stations listed in Table 8.1 and found no evident changes in the post-fit residuals whether the plasmaspheric contribution was explicitly accounted for or not. The biases were also constant in the two cases, although small differences of about 1 TECU and 2-3 TECU could be observed between the biases estimated with the two algorithms at NDBC and respectively at MANA/GUAT, ANTC, and RIO2. The total and ionospheric vertical TEC values predicted in the two cases are plotted in Figure 8.5a, for August 14-18, and in Figure 8.5b, for November 15-19. As seen in Figure 8.5a, at NDBC and RIO2 the total vertical TEC values are larger by about 0.2 and 1.5 TECU, respectively, when the plasmaspheric term is not included in the observation equation compared to the case when it is included. Conversely, at GUAT and ANTC the total vertical TEC values are larger by about 1 TECU when the plasmaspheric contribution is explicitly taken into account compared to the case when it is not. As shown in Figure 8.5b, during November 15-19, the total TEC values at MANA and ANTC are larger by about 2-3 TECU when the plasmaspheric term is included compared to the case when it is not, while at NDBC and RIO2 they are larger by about 0.4 and 2 TECU, respectively, when the plasmaspheric term is not included compared to the case when it is included.

It can thus be concluded that, by not explicitly accounting for the plasmasphere, the total vertical TEC is underestimated by about 3 TECU at low latitudes and overestimated at mid latitudes in the northern and southern hemispheres by about 0.4 and 2 TECU, respectively, compared to the case when the plasmasphere is explicitly accounted for. These values are more characteristic for November and are slightly larger than the values obtained for August. Our results are in excellent agreement with those reported by Mazzella et al. (2007), where they also showed using model simulations that by not explicitly accounting for the plasmasphere the total TEC is underestimated at low latitudes and overestimated at mid latitudes. It can be also observed in Figure 8.5 that, at low latitudes, the vertical TEC estimated without explicitly accounting for the plasmasphere approximates quite well the ionospheric vertical TEC. This is in agreement with the fact that, since the PEC has a weak elevation angle dependency at equatorial and low latitudes, the estimation algorithm tends to attribute most of the PEC to the instrumental biases.

It is evident from Figures 8.4 and 8.5 that the ionospheric TEC displays a seasonal variation, with larger values in summer than in winter, which is also responsible for the observed hemispheric asymmetry in the ionospheric TEC, with larger values in the summer hemisphere than in the winter hemisphere. Also, as illustrated in these figures, the diurnal pattern of the ionospheric TEC at RIO2 presents some anomalies in November. This may be due to the fact that, during the December solstice, the completely sunlit Antarctic ionosphere has an abnormal behavior with relatively high plasma densities and reversed diurnal patterns, which in turn can affect the diurnal patterns of the plasmaspheric electron densities in both

local and conjugate hemispheres. As shown in Figure 8.4h, the estimated slant PEC at NDBC also displays a peculiar diurnal variation possibly associated with the anomalous behavior of the sub-Antarctic ionosphere in the conjugate hemisphere, at RIO2. In addition, the PEC values at NDBC are lower in August than in November although the ionospheric TEC values in August exceed those in November. A similar situation is encountered at low latitudes in the northern hemisphere, the PEC values at MANA in November being larger than those at GUAT in August, while the ionospheric TEC values at GUAT in August exceeding those at MANA in November. However, at the southern hemisphere stations the situation is different, as both PEC and ionospheric TEC values in November exceed those in August. These results suggest that at the southern hemisphere stations, the ionosphere-plasmasphere interactions in the local hemisphere tend to dominate the effects in the conjugate hemisphere, while at the northern hemisphere stations, the ionosphere-plasmasphere interactions in the conjugate hemisphere tend to dominate the effects in the local hemisphere, which is consistent with results reported by other authors (e.g., Kersley and Klobuchar, 1978).

It is thus clear from Figures 8.4 and 8.5 that the GPS-derived PEC presents a seasonal variation, with larger values in November than in August, similar with the seasonal variation of the predicted ionospheric TEC at the southern hemisphere stations. Although risky to imply seasonal trends on the basis of only 10 days of data, we suggest that the gross differences observed in the predicted PEC are primarily due to seasonal changes. We suggest that the main underlying physical mechanism responsible for the seasonal variation of the PEC may be the tilt of the Earth's

magnetic dipole, but, as discussed in Section 8.2, several other mechanisms may be also involved. Specifically, the southern hemisphere stations being located farther away from the geographic equator than the northern hemisphere stations due to the Earth's dipole tilt, the ionospheres above them were presumably longer exposed to sunlight in November than in August. This could then lead to substantial seasonal variations in the ionospheric plasma densities above them, which could then map into the plasmasphere as a consequence of the diffusive equilibrium, producing annual changes in the PEC.

It can also be observed in Figures 8.4 and 8.5 that the predicted PEC displays a significant hemispheric asymmetry in November, with larger values in the southern hemisphere than in the northern hemisphere. The hemispheric asymmetry of the PEC in November could be attributed to large interhemispheric plasma flows from the southern hemisphere to the northern hemisphere, probably caused by large differences in the atmospheric parameters and H+ pressure across the equatorial plane (e.g., Bailey et al., 1987). The fact that the hemispheric asymmetry of the predicted PEC is negligible in August may indicate that the plasma flows between hemispheres were low during this period. It is important to remark that, while the diurnal variation and the meridional asymmetry of the estimated PEC are imposed by the Gallagher's model, the seasonal variation and the hemispheric asymmetry of the PEC originate from the measurements themselves and are not imposed by the background plasmaspheric model.

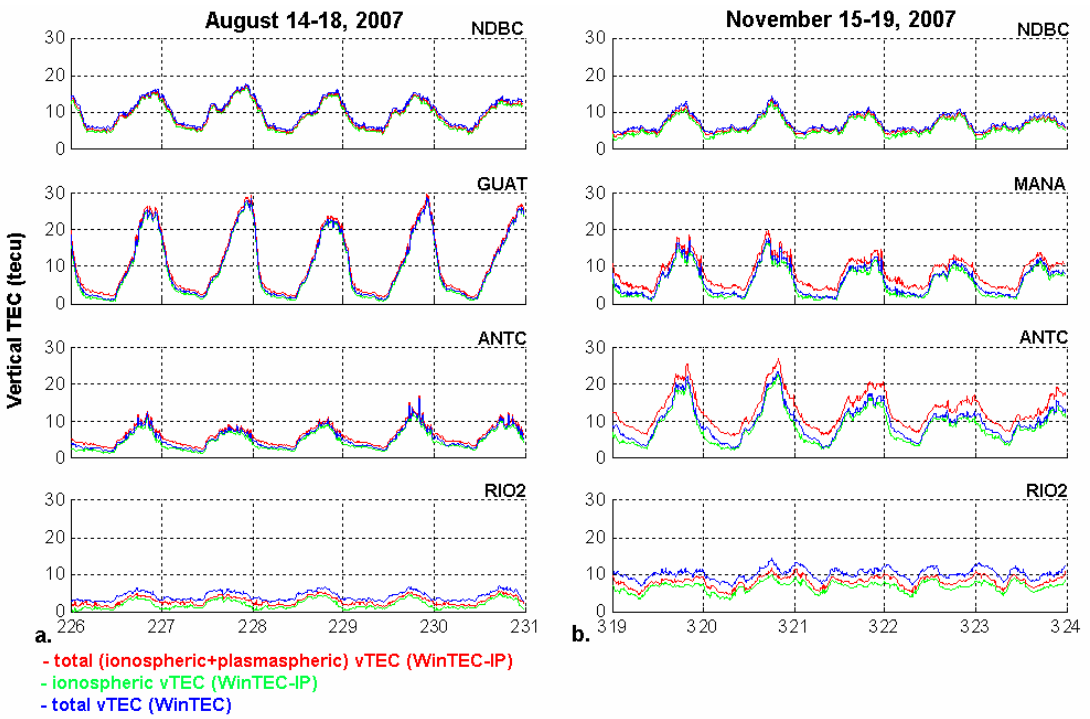

Figure 8.5: Vertical TEC estimates with and without the plasmaspheric term included in the observation equation for (left) 14-18 August 2007 and (right) 15-19 November 2007.

To better illustrate the seasonal variation of the GPS-derived PEC, the estimated vertical PEC values are also plotted in Figure 8.6. For each site, the ratio *r* between the average vertical PEC for November 15-19 and August 14-18 is indicated on the corresponding panel. As shown in these plots, the PEC ratios are greater at the southern hemisphere stations than at those in the northern hemisphere and decrease with increasing L-shell. At ANTC and MANA/GUAT the PEC ratios are about 3 and 2, respectively, while at RIO2 and NDBC the ratios are about 1.7 and 1.4, respectively. It is though possible that, at the mid-latitude stations, where the replenishment of the plasmasphere is expected to last for several days, the ratios may be slightly affected by the increased geomagnetic conditions prior to August 14. Although, in the current studies we use integrated electron densities on vertical ray

paths, our results are consistent with those reported by several other studies using equatorial plasmaspheric electron densities derived from whistler and satellite observations and from model simulations. For example, Clilverd et al. (2007) determined, using satellite observations, a December to June density ratio of about 2.7 at L = 2.5-3.5 for solar maximum conditions. Similar results were reported by Clilverd et al. (1991) using whistler measurements. They determined a density ratio of 3 (2) for solar minimum (maximum) conditions at L = 2.5. Based on numerical simulations, Guiter (1995) also reported a density ratio of 1.5 at L = 2 for solar minimum conditions. This further proves that our PEC estimation technique represents a valuable new approach for separating the ionospheric and plasmaspheric contributions to the GPS observations of TEC and for exploring the morphology of the plasmasphere.

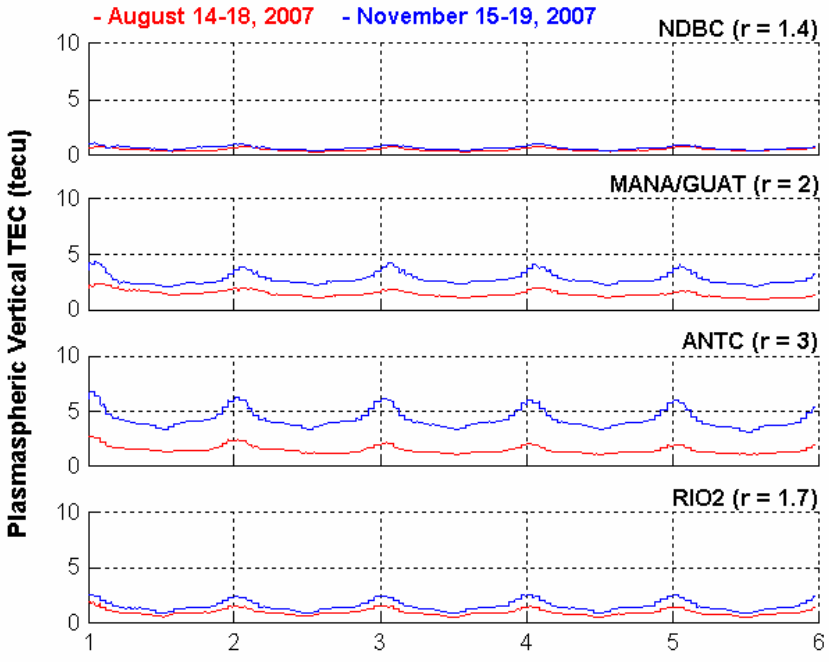

Figure 8.6: Estimated vertical PEC for 14-18 August and 15-19 November 2007.

8.6 Conclusions

In this chapter, we have presented a Kalman filter-based algorithm for estimating both the ionospheric and plasmaspheric electron content along GPS ray paths by combining GPS data with information from background ionospheric and plasmaspheric models. The estimation technique is thus able to distinguish between the ionospheric and plasmaspheric contributions to the GPS-TEC observations by exploiting the differences in the spatial distributions of electron densities in the two regions. In our algorithm, named WinTEC-IP, the ionosphere is approximated as a thin spherical shell located at the fixed height of 350 km and the ionospheric vertical TEC above the monitoring stations is represented as a third order polynomial. To explicitly account for the plasmasphere, we used the Gallagher's empirical plasmaspheric model and set the O^+/H^+ transition height at 1000 km. Having in view though that the O^+/H^+ transition height can display strong diurnal, seasonal, and latitudinal variations, we also tested the algorithm for a transition height of 600 km, but found no significant changes in the predicted PEC values. It is expected that by explicitly accounting for the plasmasphere, one can obtain more accurate estimates of the instrumental biases and ionospheric TEC, as clearly shown in the results reported by Mazzella et al. (2007) using model simulations.

Given the vast amount of GPS data readily available both globally and continuously, this new technique could offer ample new opportunities to remote sense the plasmasphere and hence to explore different aspects of the plasmasphere morphology including those which are difficult to identify using other techniques. As

an example of how our algorithm can be used to explore the morphology of the plasmasphere, here we have shown that the seasonal variation and the hemispheric asymmetry of the PEC can be inferred from GPS measurements and these inferences agree with results from previous investigators. This in turn supports the validity of our technique, although further validation studies still need to be carried out for different geophysiscal conditions using both absolute values of PEC and model simulations.

Chapter 9

Summary and Future Work

This thesis has covered a diverse set of topics and has introduced a variety of advanced signal processing techniques. Since the conclusions on individual studies have been included at the end of each chapter, here we simply provide a summary of our work, highlight some concluding remarks, and briefly summarize some future work that pertains to the ideas related in this thesis.

Geomagnetically forced periodicities in the thermosphere-ionosphere system

Using different wavelet-based techniques, we have shown that dominant oscillations with periods of 5.4, 6.75, 9, and 13.5 days, that appear as higher harmonics of the solar rotation period and persist for several solar rotations and even years, occur frequently in the thermosphere density, ionospheric TEC, and GUVI $\Sigma O/N_2$ ratios during 2004-2007, and correlate very well with similar periodicities in

the solar wind parameters and geomagnetic activity indices. Overall, our results provide compelling evidence that these periodicities are a direct response to recurrent geomagnetic activity and associated high-speed solar wind streams. We suggest that all these results regarding the geomagnetically forced periodic variations in different ionospheric and thermospheric parameters can be used to improve and validate the existing coupled magnetosphere-thermosphere-ionosphere models and to test their ability to replicate the observed variability.

In addition, our bispectral analysis results suggest that the periodic oscillations in the solar wind parameters, primarily rooted in rigidly rotating solar coronal holes, may also originate from nonlinear processes taking place in the solar wind, probably as a result of compression of the high-speed solar wind plasma and wave-shock interactions. However, further investigations are required to explain the origin of the observed phase-coherent couplings between different spectral components in the solar wind parameters.

Finally, we need to mention that additional data sources and model simulations are still needed to thoroughly examine the processes at play in modifying the state of the thermosphere and ionosphere in response to recurrent geomagnetic activity, and to evaluate the relative contribution of the periodicities in the neutral density, neutral composition, neutral temperature, neutral winds, and electric fields associated with recurrent geomagnetic activity in driving periodic oscillations in ionosphere.

Drift-Net algorithms

We have developed and presented several least-squares regression and neural network-based algorithms for estimating daytime, equatorial vertical ExB drifts from magnetometer observations. We have shown that although trained only with data from Peruvian longitudes, the models can be applied at any longitude where appropriately-placed magnetometers exist. We have also shown that the seasonal H and ΔH-inferred drift patterns present an excellent agreement at Peruvian and Indonesian longitudes, but at Indian and Philippine longitudes, the H-inferred drift patterns underestimated the ΔH-inferred drift patterns by about 2-5 m/s, mostly during the morning and noontime hours. However, further experimental and theoretical studies are needed to explain the observed differences between the seasonal H and ΔH-inferred drift patterns and to test the applicability of the algorithms at other longitude sectors. It is clear though that being able to estimate the ExB drifts using only the H component at the magnetic equator could be very important considering that, as shown by Richmond et al. (1973) and Fang et al. (2008a), the H component away from the equator is much more affected by zonal neutral winds than the H component at the magnetic equator. This could be also very useful at longitudes where a single equatorial magnetometer station is available, and could eliminate the uncertainty surrounding the position of the off-equatorial station.

Relating the periodic variations in the LLZEFs and IEF

The disturbed-time studies presented in Chapter 3, have demonstrated that we now have the capability to investigate the "weather" aspects of daytime, equatorial vertical ExB drifts at different longitudes, and to relate them to IEF conditions. In Chapter 4, we have used the continuous Morlet wavelet transform in order to relate the oscillation activity in the LLZEFs and IEF spectra at three longitude sectors, in the 10 min.-10 hour and 1.25-12 day period ranges, during time intervals of increased geomagnetic activity. For periods in the 10 min.-10 hour range, we have shown that the continuous wavelet analysis represents a powerful tool to study the frequency dependence of the two specific mechanisms of equatorial electric field variability which are dominant during disturbed conditions, namely penetration and disturbance dynamo. For periods in the 1.25-12 day range, we have found that there are significant periodicities that occur simultaneously in both LLZEF and IEF spectra and which are most probably caused by geomagnetic disturbances associated with enhanced geomagnetic activity. We suggest that further investigations using wavelet analysis in conjunction with physics-based models, ground-based and satellite data sets are needed to get a deeper understanding of the sources of periodicities in the LLZEF and of the system that links the IEF and the equatorial zonal electric fields.

Penetration electric fields

In Chapter 5 we have investigated the shielding effect of the ring current in both time and frequency domains, and have established quantitative relationships between IEF-Ey and the fluctuations in the equatorial zonal electric field at Peruvian and Indonesian longitudes. Several techniques based on neural networks, multiple regression analysis, and FIR filters have been employed for this purpose and have been discussed in this chapter. However, while the models work relatively well at both longitudes, the physical properties are still not understood, which suggests that further investigations of the penetration electric fields are needed. Further investigations are also needed to clarify the impact of the 6 and 8-hour periods, corresponding to the quarterdiurnal and terdiurnal tides, on interpreting the effects of the penetration electric fields at Indonesian longitudes. Additionally, our results have also indicated that the electic field penetration mechanism presents a longitudinal dependency which remains to be further investigated in future studies.

WinTEC algorithm

In Chapter 6, we have introduced the Kalman filter-based data assimilation algorithm, named WinTEC, developed for near real-time estimation of the ionospheric TEC using data from a single site or from a network of dual-frequency GPS receivers. In WinTEC, the ionospheric TEC and the combined satellite and receiver biases are estimated at the sampling rate of the GPS data (30 seconds) by

using hourly/daily RINEX observation and navigation files. The estimation procedure assumes a simple model for the ionosphere, approximated as a thin spherical shell at 350 km, and a first-order polynomial representation for the vertical TEC, in a solar-geomagnetic reference frame. Our excellent comparative results between WinTEC and USTEC reported in this chapter, have indicated that although based on a simple mathematical formalism, WinTEC is a powerful tool for ionosopheric studies that can reach the performance level of a more complex and computationally expensive algorithm, being able to retrieve accurate TEC values in near real-time during both quiet and disturbed periods.

In Chapter 7, we have explored different ionospheric modeling techniques with the ionosphere approximated as a single-shell or multi-shell structure at fixed heights and the vertical TEC modeled as polynomials of different orders. We have found that out of the different modeling techniques, WinTEC produces the lowest post-fit residuals when the cubic approach is employed to represent the ionospheric TEC above a monitoring station. For higher order polynomials, the size of the state vector increases considerably and, in the single site case, the Kalman filter becomes numerically unstable.

WinTEC-IP algorithm

In Chapter 7, we have presented the WinTEC-IP algorithm. WinTEC-IP explicitly accounts for both ionospheric and plasmaspheric contributions to the GPS-TEC measurements by using a single-shell cubic approximation for the vertical TEC

in ionosphere and the Gallagher model (Gallagher et al., 1988) as a background model for the plasmaspheric TEC. Comparative results between WinTEC and WinTEC-IP have shown that, by including the plasmaspheric term in the observation equation, there is no degradation in the performance and modeling accuracy of WinTEC-IP in terms of post-fit residuals and bias stability, although some minor changes in the estimated biases and total TEC can be observed, particularly at low-latitude stations. The estimation technique in WinTEC-IP is able to distinguish between the ionospheric and plasmaspheric contributions to the GPS-TEC observations by exploiting the differences in the spatial distributions of electron densities in the two regions. It is expected that by explicitly accounting for the plasmasphere, one can obtain more accurate estimates of the instrumental biases and total TEC. This was also clearly shown in the results reported by Mazzella et al. (2007) using model simulations and in the recent results by Carrano et al. (2009) using ALTAIR measurements.

To investigate the consistency of the plasmaspheric results obtained with WinTEC-IP, we have calculated the PEC patterns at twelve stations distributed roughly over four geomagnetic latitudes and three longitude sectors separated by about 100^{o}, during a quiet interval in November 2007. Similar latitudinal PEC patterns have been obtained at each longitude sector consistent with the geometry of the plasmaspheric flux tubes and plasma distribution in the plasmasphere, but also with results reported by other authors (e.g., Lunt et al., 1999c; Mazzella et al., 2002; Otsuka et al., 2002; Carrano et al., 2008). Overall our results suggest that WinTEC-IP is a reliable remote sensing technique for estimating the contribution to the total TEC

from both the ionosphere and plasmasphere. However, further investigations and validation studies need to be undertaken to test the potential of the method in estimating the PEC for different solar and geomagnetic conditions at different locations, in particular at equatorial and low latitudes.

Given the vast amount of GPS data readily available both globally and continuously, this new technique could offer ample new opportunities to remote sense the plasmasphere, and hence to explore different aspects of the plasmasphere morphology including those which are difficult to identify using other techniques. As an example of how our algorithm can be used to explore the morphology of the plasmasphere, we have shown that the seasonal variation and the hemispheric asymmetry of the PEC can be inferred from GPS measurements and these inferences agree with results from previous investigators. This in turn supports the validity of our technique, although further validation studies still need to be carried out for different geophysical conditions using absolute observations of PEC and numerical simulations. In the end, we also suggest that the algorithm in WinTEC-IP should be tested for different background plasmaspheric models and should be modified to estimate parameters in imposed plasmaspheric profiles.

BIBLIOGRAPHY

Abdu, M., P. Jayachandran, J. MacDougall, J. Cecile, and J. Sobral (1998), Equatorial F Region Zonal Plasma Irregularity Drifts Under Magnetospheric Disturbances, *Geophys. Res. Lett.*, 25(22), 4137-4140.

Abdu, M., T. Ramkumar, I. Batista, C. Brum, H. Takahashi, B. Reinisch, J. Sobral (2006), Planetary wave signatures in the equatorial atmosphere-ionosphere system and mesosphere - E- and F-region coupling, *J. Atmos. Solar-Terr. Phys.*, 68, 509-522.

Akasofu, S.-I. (1979), Interplanetary energy flux associated with magnetospheric substorms, *Planet. Space Sci.*, 27, 425–431.

Alex, S., and S. Mukherjee (2001), Local time dependence of the equatorial counter electrojet effect in a narrow longitudinal belt, *Earth Planets Space*, 53, 1151–1161.

Alken, P., S. Maus, J. Emmert, and D.P. Drob (2008), Improved horizontal wind model HWM07 enables estimation of equatorial ionospheric electric fields from satellite magnetic measurements, *Geophys. Res. Lett.*, 35, L11105.

Altadill, D. and E. Apostolov (2003), Time and scale size of planetary wave signatures in the ionospheric F region: Role of the geomagnetic activity and mesosphere/lower thermosphere winds, *J. Geophys. Res.*, 108 (A11), 1403.

Anderson, D. N., R.A. Heelis, J.P. McClure (1987), Calculated Nighttime Eastward Plasma Drift Velocities at Low Latitudes and their Solar Cycle Dependence, *Ann. Geophys.*, 5, 435.

Anderson, D., J. Forbes, and M. Codrescu, A Fully Analytic (1989), Low- and Middle-Latitude Ionospheric Model, *J. Geophys. Res.*, 94(A2), 1520-1524.

Anderson, D., A. Anghel, K. Yumoto, M. Ishitsuka, and E. Kudeki (2002), Estimating daytime vertical ExB drift velocities in the equatorial F-region using ground-based magnetometer observations, *Geophys. Res. Lett.*, 29(12), 1596.

Anderson, D., A. Anghel, J. Chau, O. Veliz (2004), Daytime vertical ExB drift velocities inferred from ground-based magnetometer observations at low latitudes, *Space Weather 2*, S11001.

Anderson, D., A. Anghel, J. Chau, K. Yumoto, (2006a), Global, low latitude, vertical ExB drift velocities inferred from daytime magnetometer observations, *Space Weather 4*, S08003.

Anderson, D., A. Anghel, E. Araujo, V. Eccles, C. Valladares, and C. Lin (2006b), Theoretically modeling the low-latitude, ionospheric response to large geomagnetic storms, *Radio Sci.*, 41, RS5S04.

Anghel, A., D.N. Anderson, N. Maruyama, J.L. Chau, K. Yumoto, A. Bhattacharyya, S. Alex (2007), Interplanetary electric fields and their relationship to low-latitude electric fields under disturbed conditions, *J. Atmos. Sol.-Terr. Phys.*, 69(10-11), 1147-1159.

Anghel, A., D. Anderson, J.L. Chau, K. Yumoto, A. Bhattacharyya (2008a), Relating the Interplanetary-induced electric fields with the low-latitude zonal electric fields under geomagnetically disturbed conditions, *AGU Monograph on Mid-latitude Ionospheric Disturbances and Dynamics*.

Anghel, A., A. Astilean, T. Letia, A. Komjathy (2008b), Near real-time monitoring of the ionosphere using dual-frequency GPS data in a Kalman filter approach, *Proceedings of the IEEE International Conference on Automation, Quality and Testing, Robotics*, Cluj-Napoca, Romania.

Anghel, A., C.S. Carrano, A. Komjathy, A. Astilean and T. Letia (2009a), Kalman filter-based algorithms for monitoring the ionosphere and plasmasphere with GPS in near-real time, *J. Atmos. Sol.-Terr. Phys.*, 71 (1), 158-174.

Anghel, A., C.S. Carrano, A.J. Gasiewski, A. Astilean, and T. Letia (2009b), Investigations of the plasmasphere morphology with GPS, accepted by *GPS Solutions*.

Anghel, A., C.S. Carrano, A.J. Gasiewski, A. Astilean, and T. Letia (2009c), Kalman filter-based algorithm for near real-time monitoring of the ionosphere using dual-frequency GPS data, *manuscript*.

Anghel, A. and A.J. Gasiewski (2009d), Drift-Net: A neural network-based algorithm for estimating the daytime, equatorial vertical ExB drift velocities using ground-based magnetometer observations, submitted to *J. Atmos. Sol.-Terr. Phys.*

Anghel, A. (2009e), Empirical models of the penetration electric fields at Peruvian and Indonesian longitudes, *manuscript*.

Anghel, A. (2009f), Periodic modulation of the thermosphere-ionosphere system by solar wind high-speed streams and corotating interaction regions at the declining and minimum phases of the solar cycle 23, *manuscript*.

Arnoldy, R.L. (1971), Signature in the Interplanetary Medium for Substorms, *J. Geophys. Res.*, 76(22), 5189–5201.

Arruda, D. C. S., J. Sobral, M. Abdu, V. Castilho, H. Takahashi, A. Medeiros, R. Buriti (2006), Theoretical and experimental zonal drift velocities of the ionospheric plasma bubbles over the Brazilian region, *Advances in Space Research*, 38 (11), 2610-2614.

Balan N., Y. Otsuka, T. Tsugawa, S. Miyazaki, T. Ogawa, K. Shiokawa (2002), Plasmaspheric electron content in the GPS ray paths over Japan under magnetically quiet conditions at high solar activity, *Earth Planets Space* 54, 71–79.

Bartels, J. (1932), Terrestrial-magnetic activity and its relations to solar phenomena, *Terr. Magn. Atmos. Electr.*, 37(1), 1–52.

Bartels, J. (1934), Twenty-seven day recurrences in terrestrial-magnetic and solar activity, 1923– 1933, *Terr. Magn.*, 39, 201.

Batista, I.S., R.T. deMedeiros, M.A. Abdu, J.R. deSouza, G.J. Bailey, E.R. dePaula (1996), Equatorial ionospheric plasma drift model over the Brazilian region, *J. Geophys. Res.*, 101, 10,887–10,892.

Bailey, G. J., P.A. Simmons, R.J. Moffett (1987), Topside and interhemispheric ion flows in the mid-latitude plasmasphere, *J. Atmos. Terr. Phys*., 49(6), 503-519.

Belehaki, A., N. Jakowski, B. Reinisch (2004), Plasmaspheric electron content derived from GPS TEC and digisonde ionograms, *Advances in Space Research*, 33(6), 833-837.

Bertoni, F., I.S. Batista, M.A. Abdu, B.W. Reinish, and E.A. Kherani (2006), A comparison of ionospheric vertical drift velocities measured by Digisonde and Incoherent Scatter Radar at the magnetic equator, *J. Atmos. Sol. Terr. Phys.*, 68, 669–678.

Bilitza, D. (1995), International Reference Ionosphere, http://nssdc.gsfc.nasa.gov/space /model/ionos/iri.html.

Bishop, C.M. (1995), Neural Networks for Pattern Recognition, *Oxford University Press*.

Blanc, M., and A. Richmond (1980), The Ionospheric Disturbance Dynamo, *J. Geophys. Res.*, 85(A4), 1669-1686.

Borries, C., N. Jakowski, C. Jacobi, P. Hoffmann, and A. Pogoreltsev (2007), Spectral analysis of planetary waves seen in ionospheric total electron content (TEC): First results using GPS differential TEC and stratospheric reanalyses, *J. Atmos. Sol. Terr. Phys.*, 69, 2442 – 2451, doi:10.1016/j.jastp.2007.02.004.

Borovsky, J. E., and M. H. Denton (2006), Differences between CME-driven storms and CIR-driven storms, *J. Geophys. Res.*, 111, A07S08, doi:10.1029/2005JA011447.

Bronshtén, V.A. (1960), The structure of the far outer of 19 June 1936, *Soviet Astronomy*, 3, 821.

Buonsanto, M.J. (1999), Ionospheric storms - A review, *Space Science Reviews*, 88, 563.

Burke, W.J., (2007), Penetration electric fields: A Volland Stern approach, *J. Atmos. Sol. Terr. Phys.*, 69(10-11), 1114-1126.

Burns, A. G., T. L. Killeen, G. R. Carignan, and R. G. Roble (1995), Large enhancements in the O/N2 ratio in the evening sector of the winter hemisphere during geomagnetic storms, *J. Geophys. Res.*, 100, 14,661–14,671.

Burton, R. K., R. L. McPherron, and C. T. Russell (1975), An empirical relationship between interplanetary conditions and *Dst*, *J. Geophys. Res.*, 80(31), 4204–4214.

Carrano, C. and K. Groves (2006), The GPS segment of the AFRL-SCINDA global network and the challenges of real-time TEC estimation in the equatorial ionosphere, paper presented at the *Institute of Navigation, National Technical Meeting*, Monterey, CA, January 18-20.

Carrano, C.S., R.A. Quinn, K.M. Groves, A. Anghel, M.V. Codrescu (2008), Kalman Filter Estimation of Plasmaspheric TEC using GPS, *Proceedings of the 12th International Ionospheric Effects Symposium*, Alexandria, VA, May 13-15.

Carrano, C.S., A. Anghel, R.A. Quinn, and K.M. Groves (2009), Kalman filter estimation of plasmaspheric total electron content using GPS, *Radio Sci.*, 44, RS0A10, doi:10.1029/2008RS004070.

Carpenter, D.L. and R.R. Anderson (1992) An ISEE/whistler model of equatorial electron density in the magnetosphere, , *J. Geophys. Res.*, 97(A2), 1097–1108.

Carpenter, D.L. (2004), Remote Sensing the Earth's Plasmasphere, *Radio Sci. Bulletin (URSI)*, 308, 13-29.

Chapman, S., and V.C.A. Ferraro (1931), A new theory of magnetic storms, Part 1, The initial phase, *Terrest. Magnetism and Atmospheric Elec.*, 36, 171-186.

Chapman, S., and J. Bartels (1940), Geomagnetism, *Oxford Univ. Press*, New York.

Chau, J.L. and R.F. Woodman (2004), Daytime, vertical and zonal velocities from 150-km echoes: Their relevance to F-region dynamics*, Geophys. Res. Lett.*, 10.

Chree, C. (1912), Some phenomena of sunspots and terrestrial magnetism at Kew observatory, *Phil. Trans. R. Soc. London*, A, 213, 75.

Christensen, A. B., et al. (2003), Initial observations with the Global Ultraviolet Imager (GUVI) in the NASATIMED satellite mission, *J. Geophys. Res.*, 108(A12), 1451, doi:10.1029/2003JA009918.

Ciraolo, L., and P. Spalla (1997), Comparison of ionospheric total electron content from the Navy Navigation Satellite System and the GPS, *Radio Sci.*, 32(3), 1071–1080.

Clilverd, M.A., A.J. Smith, N.R. Thomson (1991), The annual variation in quiet time plasmaspheric electron density, determined from whistler mode group delays, *Planetary and Space Science*, 39(7), 1059-1067.

Clilverd, M., N. Meredith, R. Horne, S. Glauert, R. Anderson, N. Thomson, F. Menk, R. Sandel (2007), Longitudinal and seasonal variations in plasmaspheric electron density: Implications for electron precipitation, *J. Geophys. Res.*, 112, A11210.

Crooker, N.U., and E.W. Cliver (1994), Postmodern View of M-Regions, *J. Geophys. Res.*, 99(A12), 23,383–23,390.

Crowley, G., A. Reynolds, J.P. Thayer, J. Lei, L.J. Paxton, A.B. Christensen, Y. Zhang, R.R. Meier, and D.J. Strickland (2008), Periodic modulations in thermospheric composition by solar wind high speed streams, *Geophys. Res. Lett.*, 35, L21106, doi:10.1029/2008GL035745.

Demuth, H. and M. Beale (2001), Neural Network Toolbox User's Guide, *The MathWorks Inc*.

Denton, M.H., J.E. Borovsky, R.M. Skoug, M.F. Thomsen, B. Lavraud, M.G. Henderson, R.L. McPherron, J.C. Zhang, and M.W. Liemohn (2006), Geomagnetic storms driven by ICME- and CIR-dominated solar wind, *J. Geophys. Res.*, 111, A07S07, doi:10.1029/2005JA011436.

Doumouya, V., J. Vassal, Y. Cohen, O. Fambitakoye, and M. Menvielle (1998), The equatorial electrojet: First results from magnetic measurements, *Ann. Geophys.*, 16, 658–676.

Dudok de Wit, T. and V.V. Krasnosel'skikh (1995), Wavelet bicoherence analysis of strong plasma turbulence at the Earth's quasiparallel bow shock, *Phys. Plasmas*, 2, 4307–4311.

Dungey, J.W., Interplanetary magnetic field and the auroral zones, *Phys. Rev. Lett., 6*, 47, 1961.

Earle, G.D. and M.C. Kelley (1987), Spectral studies of the sources of ionospheric electric fields, *J. Geophys. Res.*, 92, A1, 213-224.

Echer, E., W. D. Gonzalez, B. T. Tsurutani, and A. L. C. Gonzalez (2008), Interplanetary conditions causing intense geomagnetic storms (Dst ≤ −100 nT) during

solar cycle 23 (1996–2006), *J. Geophys. Res.*, 113, A05221, doi:10.1029/2007JA012744.

Elgar, S. and R.T. Guza (1988), Statistics of bicoherence, Transactions on Acoustics, Speech and Signal Processing, IEEE, 36, 1667-1668.

Emery, B.A., I.G. Richardson, D.S. Evans, and F.J. Rich (2009), Solar wind structure sources and periodicities of auroral electron power over three solar cycles, *J. Atmos. Solar Terr. Phys.*, 71(10-11), doi:10.1016/j.jastp.2008.08.005

Fagundes, P.R., V.G. Pillat, M. Bolzan, Y. Sahai, F. Becker-Guedes, J.R. Abalde, S.L. Aranha, and J.A. Bittencourt (2005), Observations of *F* layer electron density profiles modulated by planetary wave type oscillations in the equatorial ionospheric anomaly region, *J. Geophys. Res.*, 110, A12302.

Fang, T. W., A. D. Richmond, J. Y. Liu, and A. Maute (2008a), Wind dynamo effects on ground magnetic perturbations and vertical drifts, *J. Geophys. Res.*, 113, A11313, doi:10.1029/2008JA013513.

Fang, T.W., A.D. Richmond, J.Y. Liu, A. Maute, C.H. Lin, C.H. Chenb and B. Harperd (2008b), Model simulation of the equatorial electrojet in the Peruvian and Philippine sectors, *J. Atmos. Sol.-Terr. Phys.*, 70 (17), 2203-2211.

Fejer, B.G., W. Spiro, R. Wolf, J. Foster (1990) Latitudinal variation of perturbation electric fields during magnetically disturbed periods: 1986 SUNDIAL observations and model results, *Ann. Geophys*, 8, 441–454.

Fejer, B.G., E.R. dePaula, S.A. Gonzalez and R.F. Woodman (1991), Average vertical and zonal F region plasma drifts over Jicamarca*, J. Geophys. Res.*, 96, 13,901-13,906.

Fejer, B., E. de Paula, R. Heelis, and W. Hanson (1995), Global Equatorial Ionospheric Vertical Plasma Drifts Measured by the AE-E Satellite*, J. Geophys. Res.*, 100(A4), 5769-5776.

Fejer, B., and L. Scherliess (1995), Time Dependent Response of Equatorial Ionospheric Electric Fields to Magnetospheric Disturbances, *Geophys. Res. Lett.*, 22(7), 851-854.

Fejer, B.G. (1997), The electrodynamics of the low-latitude ionosphere: Recent results and future challenges, *J. Atmos. Solar-Terr. Phys.*, 59(13), 1465-1482.

Fejer, B.G., and L. Scherliess (1997), Empirical models of storm-time equatorial zonal electric fields, *J. Geophys. Res.*, 102, 24047.

Fejer, B., and L. Scherliess (1998), Mid- and Low-Latitude Prompt-Penetration Ionospheric Zonal Plasma Drifts, *Geophys. Res. Lett.*, 25(16), 3071-3074.

Fejer, B.G., J. de Souza, A.S. Santos, A.E. Costa Pereira (2005), Climatology of F region zonal plasma drifts over Jicamarca, *J. Geophys. Res.*, 110, A12310.

Forbes, J.M. (1981), The equatorial electrojet, *Rev. Geophys.*, 19, 469–504.

Forbes, J. M. (1996), Planetary waves in the thermosphere-ionosphere system, *J. Geomagn. Geoelectr.*, 48, 91– 98.

Forbes, J.F., S.E. Palo and X. Zhang (2000), Variability of the ionosphere, *J. Atmos. and Solar-Terr. Phys.*, 62(8), 685-693.

Fraser-Smith, A.C. (1972), Spectrum of the Geomagnetic Activity Index Ap, *J. Geophys. Res.*, 77, 4209-4220.

Fuller-Rowell, T.J., M.V. Codrescu, R.J. Moffett, and S. Quegan (1994), Response of the Thermosphere and Ionosphere to Geomagnetic Storms, *J. Geophys. Res.*, 99(A3), 3893–3914.

Fuller-Rowell, T., M. Codrescu, H. Rishbeth, R. Moffett, and S. Quegan (1996), On the seasonal response of the thermosphere and ionosphere to geomagnetic storms, J. Geophys. Res., 101(A2), 2343-2353.

Fuller-Rowell, T., M. Codrescu, N. Maruyama, M. Fredrizzi, E. Araujo-Pradere, S. Sazykin, and G. Bust (2007), Observed and modeled thermosphere and ionosphere response to superstorms, Radio Sci., 42, RS4S90, doi:10.1029/2005RS003392.

Gallagher, D.L., P.C. Craven, R.H. Comfort (1988), An empirical model of the Earth's plasmasphere, *Advances in Space Research,* 8, (8)15-(8)24.

Gallagher, D.L., P.D. Craven, R.H. Comfort, T.E. Moore (1995), On the azimuthal variation of the core plasma in the equatorial magnetosphere, *J. Geophys. Res.*, 100(A12), 23,597–23,605.

Gallagher, D.L., P.D. Craven, R.H. Comfort (2000), Global core plasma model, *J. Geophys. Res.*, 105(A8), 18,819–18,833.

Garrett, H. B., A. J. Dessler, and T. W. Hill (1974), Influence of Solar Wind Variability on Geomagnetic Activity, *J. Geophys. Res.*, 79(31), 4603–4610.

Gonzales, C.A., M.C. Kelley, B.G. Fejer, J.F. Vickrey, R.F. Woodman (1979), Equatorial electric fields during magnetically disturbed conditions. 2: implications of simultaneous auroral and equatorial measurements, *J. Geophys. Res.*, 84, 5803.

Gonzalez, W. D., J. A. Joselyn, Y. Kamide, H. W. Kroehl, G. Rostoker, B. T. Tsurutani, and V. M. Vasyliunas (1994), What is a Geomagnetic Storm?, *J. Geophys. Res.*, 99(A4), 5771–5792.

Gonzalez, W. D., E. Echer, A. L. Clua-Gonzalez, and B. T. Tsurutani (2007), Interplanetary origin of intense geomagnetic storms (*Dst* < −100 nT) during solar cycle 23, *Geophys. Res. Lett.*, 34, L06101, doi:10.1029/2006GL028879.

Grewal, M.S., L.R. Weill, A.P. Andrews (2007), Global Positioning Systems, Inertial Navigation and Integration, *John Wiley & Sons*, Hoboken, New Jersey, 2nd edition.

Guiter, S.M., C.E. Rasmussen, T.I. Gombosi, J.J. Sojka, and R.W. Schunk (1995), What is the source of observed annual variations in plasmaspheric density?, *J. Geophys. Res.*, 100(A5), 8013–8020.

Haldoupis, C., D. Pancheva, and N.J. Mitchell (2004), A study of tidal and planetary wave periodicities present in midlatitude sporadic *E* layers, *J. Geophys. Res.*, 109, A02302, doi:10.1029/2003JA010253.

Hale, G.E., and S.B. Nicholson (1925), The law of sun-spot polarity, *Astro-physical Journal*, 62, 270–300.

Hansen, A.J., T. Walter and P. Enge (1997), Ionospheric correction using Tomography, *Proceedings of ION GPS-97*, the 10th International Technical Meeting of the Satellite Division of the Institute of Navigation, Kansas City, MO, USA, 16-19 September, 249-257.

Harvey, K.L., and F. Recely (2002), Polar coronal holes during cycles 22 and 23, *Solar Phys.*, 211, 31-52.

Hauska, H., S. Abdel-Wahab, and E. Dyring (1973), A search for periodic variations in geomagnetic activity and their solar cycle dependence, *Phys. Scr.*, 7, 135– 140.

Haykin, S. (1994), Neural networks: A comprehensive foundation, *Macmillan College Publishing Company*, New York.

Haykin S. (2001), Kalman Filtering and Neural Networks, *John Wiley & Sons*.

Heelis, R.A. (2004), Electrodynamics in the low and middle latitude ionosphere: A tutorial, *J. Atmos. Solar-Terr. Phys.*, 66(10), 825-838.

Hernández-Pajares, M., J. M. Juan, J. Sanz, and J. G. Solé (1998), Global observation of the ionospheric electronic response to solar events using ground and LEO GPS data, *J. Geophys. Res.*, 103(A9), 20,789–20,796.

Hinich, M.J. and C.S. Clay (1968), The Application of the Discrete Fourier Transform in the Estimation of Power Spectra, Coherence and Bispectra of Geophysical Data, *Reviews of Geophysics*, 6(3), 347-363.

Hoffmann-Wellenhof, B., H. Lichtenegger, J. Collins (1998), GPS: Theory & Practice", *Springer-Verlag*.

Hocke, K. (2008), Oscillations of global mean TEC, *J. Geophys. Res.*, 113, A04302, doi:10.1029/2007JA012798.

Huang, C.S., J.C. Foster, M.C. Kelley (2005), Long duration penetration of the planetary electric field to the low- latitude ionosphere during the main phase of magnetic storms, *J. Geophys. Res.*, 110, A11309.

Huang, Ch. S., S. Sazykin, J.L. Chau, N. Maruyama, M.C. Kelley (2007), Penetration electric fields: Efficiency and characteristic time scale, *J. Atmos. Solar Terr. Phys.,* Vol. 69(10-11), 1135-1146.

Immel, T. J., H. Frey, S. Mende, and E. Sagawa (2004), Global observations of the zonal drift speed of equatorial ionospheric plasma bubbles, *Ann. Geophys.*, 22, 3099–3107.

Ishkov, V.N. (2005), Properties of the current 23-rd solar activity cycle, *Solar System Res.*, 39(6), 453-461, doi:10.1007/s11208-005-0058-6.

Izengaw, E., M.B. Moldwin, D. Galvan, B.A. Iijima, A. Komjathy, A. Mannucci (2008), The global plasmaspheric TEC and its contribution to the GPS TEC, *J. Atmos. Solar Terr. Phys.*, 70, 1541-1548.

Jaggi, R. K., and R. A. Wolf (1973), Self-consistent calculation of the motion of a sheet of ions through the magnetosphere, *J. Geophys. Res.*, 16, 2852.

Jensen, J.W. and B.G. Fejer (2007), Longitudinal dependence of middle and low latitude zonal plasma drifts measured by DE-2, *Ann. Geophys.*, 25(12), 2551-2559.

Juan, J.M., A. Rius, M. Hernández-Pajares, J. Sanz (1997), A two-layer model of the ionosphere using Global Positioning System data, *Geophys. Res. Lett.*, 24(4), 393–396.

Kalman, R. E. (1960), A New Approach to Linear Filtering and Prediction Problems, *Journal of Basic Engineering*, 82, 34-45.

Kamide, Y., et al. (1998), Current understanding of magnetic storms: Storm-substorm relationships, *J. Geophys. Res.*, 103(A8), 17,705–17,728.

Kane, R.P. (1973), A critical appraisal of the method of estimating equatorial electrojet strength, *Proceedings of the Indian Academy of Sciences*, 78 (A), 149–158.

Kan, J. R., and L. C. Lee (1979), Energy coupling function and solar wind-magnetosphere dynamo, *Geophys. Res. Lett.*, 6(7), 577–580.

Kataoka, R., and A. Pulkkinen (2008), Geomagnetically induced currents during intense storms driven by coronal mass ejections and corotating interacting regions, *J. Geophys. Res.*, 113, A03S12, doi:10.1029/2007JA012487.

Kelley, M.C., B.J. Fejer, C.A. Gonzales (1979), An explanation for anomalous equatorial ionospheric electric fields associated with a northward turning of the interplanetary magnetic field, *Geophys. Res. Lett.,* 6, 301–304.

Kelley, M.C. (1989), The Earth's Ionosphere: Plasma Physics and Electrodynamics, *Elsevier*, New York.

Kelley, M., J. Makela, J. Chau, M. Nicolls (2003), Penetration of the solar wind electric field into the magnetosphere/ ionosphere system, *Geophys. Res. Lett.*, 30 (4), 1158.

Kelley, M.C., M. Nicolls, D. Anderson, A. Anghel, J. Chau, R. Sekar, K. Subbarao, A. Bhattacharyya (2007), Multi-longitude case studies comparing the interplanetary and equatorial ionospheric electric fields using an empirical model, *J. Atmos. and Solar-Terr. Phys.*, 69(10-11), 1174-1181.

Kersley, L. and J. Klobuchar (1978), Comparison of protonospheric electron content measurements from the American and European sectors, *Geophys. Res. Lett.*, 5(2), 123–126.

Kersley, L. and J.A. Klobuchar (1980), Storm associated protonospheric depletion and recovery, *Planetary and Space Sciences*, 28, 453-458.

Kim, Y.C. and E.J. Powers (1979), Digital bispectral analysis and its applications to nonlinear wave interactions, *IEEE Trans. on Plasma Science*, 7, 120-131.

Kishore, H. M. and G.K. Mukherjee (2007), Equatorial F-region plasma drifts: a study using OI 630 mm emission all-sky images, *Current Science*, 93(4), 488-97.

Kivelson, M.G. and C.T. Russell (1995), Introduction to space physics, *Cambridge University Press*.

Komjathy, A. (1997), Global ionospheric total electron content mapping using the Global Positioning System, *Ph.D. dissertation*, University of New Brunswick.

Komjathy, A., B.D. Wilson, T. Runge, B.M. Boulat, A.J. Mannucci, L. Sparks, M.J. Reyes (2002), A new ionospheric model for wide area differential GPS: The multiple

shell approach, *Proceedings of the National Technical Meeting of the Institute of Navigation*, San Diego, CA, January 28-30.

Kotova, G.A. (2007), The Earth's plasmasphere: State of studies (a Review), *Geomagnetism and Aeronomy*, 47(4), 409-422.

Krieger, A. S., A. F. Timothy, and E. C. Roelof (1973), A coronal hole and its identification as the source of a high velocity solar wind stream*, Sol. Phys.*, 29, 505.

Kumar, P., and E. Foufoula-Georgiou (1997), Wavelet analysis for geophysical applications, Rev. of Geophysics, 35(4), 385-412.

Larsen, Y., A. Hanssen, B. Krane, H. L. Pécseli, and J. Trulsen (2002), Time-resolved statistical analysis of nonlinear electrostatic fluctuationsin the ionospheric *E* region, *J. Geophys. Res.*, 107(A1), 1005, doi:10.1029/2001JA900125.

Laštovička, J. (2006), Forcing of the ionosphere by waves from below, *J. Atmos. and Solar-Terr. Phys.*, 68, 479-497.

Lavraud, B., M.F. Thomsen, J.E. Borovsky, M.H. Denton, and T.I. Pulkkinen (2006), Magnetosphere preconditioning under northward IMF: Evidence from the study of coronal mass ejection and corotating interaction region geoeffectiveness, *J. Geophys. Res.*, 111, A09208, doi:10.1029/2005JA011566.

Law, K.M. (1999), Validation of the Gallagher Protonospheric Model, M.S. thesis.

Lei, J., J.P. Thayer, J.M. Forbes, E.K. Sutton, and R.S. Nerem (2008a), Rotating solar coronal holes and periodic modulation of the upper atmosphere, *Geophys. Res. Lett.*, 35, L10109.

Lei, J., J.P. Thayer, J.M. Forbes, E. K. Sutton, R.S. Nerem, M. Temmer, and A.M. Veronig (2008b), Global thermospheric density variations caused by high-speed solar wind streams during the declining phase of solar cycle 23, *J. Geophys. Res.*, 113, A11303.

Lei, J., J.P. Thayer, J.M. Forbes, Q. Wu, C. She, W. Wan, and W. Wang (2008c), Ionosphere response to solar wind high-speed streams, *Geophys. Res. Lett.*, 35, L19105.

Longden, N., M.H. Denton, and F. Honary (2008), Particle precipitation during ICME-driven and CIR-driven geomagnetic storms, *J. Geophys. Res.*, 113, A06205, doi:10.1029/2007JA012752.

Lunt, N., L. Kersley, G.J. Bailey (1999a), The influence of the protonosphere on GPS observations: Model simulations, *Radio Sci.*, 34(3), 725–732.

Lunt, N., L. Kersley, G.J. Bishop, A.J. Mazzella, Jr., G.J. Bailey (1999b), The effect of the protonosphere on the estimation of GPS total electron content: Validation using model simulations, *Radio Sci.*, 34(5), 1261–1271.

Lunt, N., L. Kersley, G.J. Bishop, A.J. Mazzella, Jr. (1999c), The contribution of the protonosphere to GPS total electron content: Experimental measurements, *Radio Sci.*, 34(5), 1273–1280.

Lunt, N., L. Kersley, G.J. Bishop, A.J. Mazzella, Jr., G.J. Bailey (1999d), The protonospheric contribution to GPS total electron content: Two-station measurements, *Radio Sci.*, 34(5), 1281–1285.

Manju, G., S. Ravindran, C.V. Devasia, S.V. Thampi, R. Sridharan (2008), Plasmaspheric electron content (PEC) over low latitude regions around the magnetic equator in the Indian sector during different geophysical conditions, *J. Atmos. and Solar-Terr. Phys.*, 70(7) 1066-1073.

Manoj, C., H. Lühr, S. Maus, and N. Nagarajan (2006), Evidence for short spatial correlation lengths of the noontime equatorial electrojet inferred from a comparison of satellite and ground magnetic data, *J. Geophys. Res.*, 111, A11312, doi:10.1029/2006JA011855.

Mannucci, A.J., B. D. Wilson, D. N. Yuan, C. H. Ho, U. J. Lindqwister, and T. F. Runge (1998), A global mapping technique for GPS-derived ionospheric total electron content measurements, *Radio Sci.* 33(3):565-582.

Mansilla, G.A. (2007), Thermosphere–ionosphere response at middle and high latitudes during perturbed conditions: A case study, *J. Atmos. and Solar-Terr. Phys.*, 70(11-12), 1448-1454

Manson, A.H., C.E. Meek, T. Chshyolkova, S. K. Avery, D. Thorsen, J.W. MacDougall, W. Hocking, Y. Murayama, and K. Igarashi (2005), Wave activity (planetary, tidal) throughout the middle atmosphere (20-100km) over the CUJO network: Satellite (TOMS) and Medium Frequency (MF) radar observations, *Ann. Geophys.*, 23, 305-323.

Marinov, P., I. Kutiev, I., S. Watanabe (2006), Empirical model of O^+ H^+ transition height based on topside sounder data, *Advances in Space Research*, 34(9), 2021-2025.

Maruyama, N., S. Sazykin, R. Spiro, D. Anderson, A. Anghel, R. Wolf, F. Toffoletto, T. J. Fuller-Rowell, M. Codrescu, A.D. Richmond (2007), Modeling storm-time electrodynamics of the low-latitude ionosphere-thermosphere system: Can long lasting disturbance electric fields be accounted for?, *J. Atmos. and Solar-Terr. Phys.*, 69 (10-11), 1182-1199.

Masters, T. (1993), Practical Neural Network Recipes in C++, *Academic Press, Inc*.

Maunder, W.E. (1904), Magnetic disturbances, 1882 to 1903, as recorded at the Royal Observatory, Greenwich, and their association with sunspots, *Mon. Not. R. Astron. Soc.*, 65, 2.

Mazzella, A. J., Jr., E. Holland, A. Andreasen, C. Andreasen, G. Rao, and G. Bishop (2002), Autonomous estimation of plasmasphere content using GPS measurements, *Radio Sci.*, 37(6), 1092.

Mazzella, A. J., Jr., G. S. Rao, G. J. Bailey, G. J. Bishop, L. C. Tsai (2007), GPS Determinations of Plasmasphere TEC, *International Beacon Satellite Symposium*.

McIlwain, C.E. (1961), Coordinates for Mapping the Distribution of Magnetically Trapped Particles, *J. Geophys. Res.*, 66(11), 3681–3691.

McIlwain, C.E. (1961), Coordinates for Mapping the Distribution of Magnetically Trapped Particles, *J. Geophys. Res.*, 66(11), 3681–3691.

Meier, R.R., G. Crowley, D.J. Strickland, A.B. Christensen, L.J. Paxton, D. Morrison, and C.L. Hackert (2005), First look at the 20 November 2003 superstorm with TIMED/GUVI: Comparisons with a thermospheric global circulation model, J. Geophys. Res., 110, A09S41, doi:10.1029/2004JA010990.

Mendillo, M. and K. Schatten (1983), Influence of solar sector boundaries on ionospheric variability, *J. Geophys. Res.*, 88(A11), 9145–9153.

Mendillo, M. (2006), Storms in the ionosphere: Patterns and processes for total electron content, *Rev. Geophys.*, 44, RG4001, doi:10.1029/2005RG000193.

van Milligen, B.Ph., C. Hidalgo, and E. Sánchez (1995), Nonlinear phenomena and intermittency in plasma turbulence, *Phys. Rev. Lett.*, 74, 395 - 398

Minter, C.F., D. Robertson, P. Spencer, A. Jacobson, T. J. Fuller-Rowell, E.A. Araujo-Pradere, and R. Moses (2007), A comparison of Magic and FORTE ionosphere measurements, *Radio Sci.*, 42, RS3026, doi:10.1029/2006RS003460.

Mlynczak, M. G., F. J. Martin-Torres, C. J. Mertens, B. T. Marshall, R. E. Thompson, J. U. Kozyra, E. E. Remsberg, L. L. Gordley, J. M. Russell III, and T. Woods (2008), Solar-terrestrial coupling evidenced by periodic behavior in geomagnetic indexes and the infrared energy budget of the thermosphere, *Geophys. Res. Lett.*, 35, L05808, doi:10.1029/2007GL032620.

Mohinder S. Grewal, L.R. Weill, and A.P. Andrews (2007), Global Positioning Systems, Inertial Navigation, and Integration, Second edition, *John Wiley & Sons*.

Mursula, K., and B. Zieger (1996), The 13.5-day periodicity in the Sun, solar wind, and geomagnetic activity: The last three solar cycles, *J. Geophys. Res.*, 101(A12), 27,077–27,090.

Nayar, S. R., V. Sanalkumaran Nair, V. N. Radhika, and K. Revathy (2001), Short-period features of the interplanetary plasma and their evolution, *Sol. Phys.*, 201, 405– 417.

Newell, P.T., T. Sotirelis, K. Liou, C.-I. Meng, and F.J. Rich (2007), A nearly universal solar wind-magnetosphere coupling function inferred from 10 magnetospheric state variables, *J. Geophys. Res.*, 112, A01206, doi:10.1029/2006JA012015.

Nicolls, M.J., M.C. Kelley, J. Chau, O. Veliz, D.N. Anderson, A. Anghel (2007), The spectral properties of low latitude daytime electric fields inferred from magnetometer observations, *J. Atmos. and Solar-Terr. Phys.*, 69(10-11), 1160-1173.

Nikias, C.L. and M.R. Raghuveer (1987), Bispectrum estimation: a digital signal processing framework, Proc. IEEE, 75, 867-891.

Onwumechili, C.A. (1997), The equatorial electrojet, *Gordon and Brea*ch, New York.

Otsuka, Y., T. Ogawa, A. Saito, T. Tsugawa, S. Fukao, S. Miyazaki (2002), A new technique for mapping of total electron content using GPS network in Japan, *Earth Planets Space*, 54, 63-70.

Oyekola O.S. and C. C. Oluwafemi (2007), Morphology of F-region vertical E×B drifts in the African sector using ionosonde measurements, *Ann. Geophys.*, 50(5).

Pancheva, D. (2000), Evidence for nonlinear coupling of planetary waves and tides in the lower thermosphere over Bulgaria, *J. of Atmos. and Solar-Terr. Phys.*, 62 (2), 115-132.

Pancheva, D., and P. Mukhtarov (2000), Wavelet analysis of transient behaviour of tidal amplitude fluctuations observed by meteor radar in the lower thermosphere above Bulgaria, *Ann. Geophys.*, 18, 316-331.

Pancheva, D., N. Mitchell, R. Clark, J. Drobjeva, J. Lastovicka (2002), Variability in the maximum height of the ionospheric F2-layer over Millstone Hill (September 1998-March 2000): influence from below and above, *Ann. Geophys.*, 20(11), 1807-1819.

Pancheva, D.V., and N.J. Mitchell (2004), Planetary waves and variability of the semidiurnal tide in the mesosphere and lower thermosphere over Esrange (68°N, 21°E) during winter, *J. Geophys. Res.*, 109, A08307, doi:10.1029/2004JA010433.

Pancheva, D., et al. (2006), Two-day wave coupling of the low-latitude atmosphere-ionosphere system, *J. Geophys. Res.*, 111, A07313, doi:10.1029/2005JA011562.

Papitashvili, V.O., N.E. Papitashvili, and J.H. King (2000), Solar cycle effects in planetary geomagnetic activity: Analysis of 36-year long OMNI dataset, *Geophys. Res. Lett.*, 27, 2797.

Perreault, W.K., and S-I. Akasofu (1978), A study of geomagnetic storms, *Geophys. J. R. Astron. Soc.*, 54, 547.

Parish, H.F., J.M. Forbes, F. Kamalabadi (1994), Planetary wave and solar emission signatures in the equatorial electrojet*, J. Geophys. Res.*, 99, 355-368.

Park, C. G., D. L. Carpenter, and D. B. Wiggin (1978), Electron density in the plasmasphere: Whistler data on solar cycle, annual, and diurnal variations, *J. Geophys. Res.*, 83(A7), 3137–3144.

Pavlov, A. V. and N. M. Pavlova (2008), The zonal ExB plasma drift effects on the low latitude ionosphere electron density at solar minimum near equinox, *J. Atmos. Sol.-Terr. Phys.*, 70, 11.

Picone, J. M., A. E. Hedin, D. P. Drob, and A. C. Aikin (2002), NRLMSISE-00 empirical model of the atmosphere: Statistical comparisons and scientific issues, *J. Geophys. Res.*, 107(A12), 1468, doi:10.1029/2002JA009430.

Preble, A.J., D.N. Anderson, B.G. Fejer, P.H. Doherty (1994), Comparison between calculated and observed F region electron density profiles at Jicamarca, Peru, *Radio Sci.*, 29, 857–866.

Prölss, G.W. (1997), Magnetic storm associated perturbations of the upper atmosphere, *Magnetic Storms, Geophys. Monogr. Ser.*, 98, edited by B. T. Tsurutani et al., 227–241, AGU, Washington, D. C.

Prölss, G.W. (2004), Physics of the Earth's space environment, Springer.

Pulkkinen, T.I., N. Partamies, K.E.J. Huttunen, G.D. Reeves, and H.E.J. Koskinen (2007), Differences in geomagnetic storms driven by magnetic clouds and ICME sheath regions, *Geophys. Res. Lett.*, 34, L02105, doi:10.1029/2006GL027775.

Rastogi, R.G. and J.A. Klobuchar (1990), Ionospheric electron content within the equatorial F2 layer anomaly belt, *J. Geophys. Res.*, 95, 19,045–19,052.

Reddy, C. A. (1989), The equatorial electrojet, *Pure Appl. Geophys.*, 131, 485.

Reigber, C., H. Lühr, and P. Schwintzer (2000), CHAMP mission status and perspectives, *Eos Trans. AGU*, 81(48), Fall Meet. Suppl., Abstract G52A-01.

Rho, H. and R.B. Langley (2002), Assessment of WAAS Correction Data in Eastern Canada, *Proceedings of Ionospheric Effects Symposium, IES 2002*, Alexandria, Virginia, 7-9 May 2002, 131-138.

Rideout W., and A. Coster (2006), Automated GPS processing for global total electron content data, *GPS Solutions*, 10(3), 219-228.

Roberts, R.A. and C.T. Mullis (1987), Digital signal processing, *Addison-Wesley*.

Richmond, A.D. (1973), Equatorial electrojet: I. Development of a model including winds and instabilities, *J. Atmos. Terr. Phys.*, 35, 1082.

Richmond, A.D., M. Blanc, B.A. Emery, R.H. Wand, B.G. Fejer, R.F. Woodman, S. Ganguly, P. Amayenc, R.A. Behnke, C. Calderon, J.V. Evans (1980), An empirical model of quiet-day ionospheric electric fields at middle and low latitudes, *J. Geophys. Res.*, 85 (A9), 4658–4664.

Richmond, A.D. (1989), Modeling the ionospheric wind dynamo: A review, *Pure Appl. Geophys.*, 131, 413.

Richmond, A.D. and J.P. Thayer (2000), Ionospheric electrodynamics : A tutorial, in *Magnetospheric Currents Systems*, American Geophysical Union.

Rishbeth, H., T.J. Fuller-Rowell and A.S. Rodger (1987), F-layer storms and thermospheric composition, *Phys. Scr.*, 36 327-336, doi: 10.1088/0031-8949/36/2/024.

Rishbeth, H. and M. Mendillo (2001), Patterns of F2-layer variability, *J. Atmos. Sol.-Terr. Phys.*, 63(15), 1661-1680.

Russell, C.T. (2001), Solar wind and interplanetary magnetic field: A tutorial, *Space Weather, Geophys Mono. Series*, 125, ed. by P. Song, H. J. Singer, and G. L. Siscoe, 73-89.

Sakharov, Y., M. Nikitin, O. Smirnov (1989), Response of low-latitude electric fields to the action of a magnetospheric source, *Geomagnetism and Aeronomy*, 29, 344–349.

Sardon, E., A. Riusand N. Zarraoa (1994), Estimation of the Transmitter and Receiver Differential Biases And The Ionospheric Total Electron Content From Global Positioning System Observations, *Radio Sci.*, 29, 577-586.

Senior, C., and M. Blanc (1984), On the control of magnetospheric convection by the spatial distribution of ionospheric conductivities, *J. Geophys. Res.*, 89, 261-284.

Scherleiss, L. and B.G. Fejer (1997), Storm time dependence of equatorial disturbance dynamo zonal electric fields, *J. Geophys. Res.*, 102, 24,037–24,046.

Scherliess, L. and B.G. Fejer (1999), Radar and satellite global equatorial F region vertical drift model, *J. Geophys. Res.*, 104, 6829–6842.

Schunk, R.W and A.F. Nagy (2000), Ionospheres: physics, plasma physics, and chemistry, *Cambridge University Press*.

Schunk, R.W and L. Zhu (2008), Response of the ionosphere-thermosphere system to magnetospheric processes, *J. Atmos. Sol.-Terr. Phys.*, 70(18), 2358-2373.

Siscoe, G.L. (1982), Energy coupling between region 1 and 2 Birkeland current systems, *J. Geophys. Res.*, 87, 5124.

Snyder, C.W., M. Neugebauer, and U.R. Rao (1963), The solar wind velocity and its correlation with cosmic-ray variations and with solar and geomagnetic activity, *J. Geophys. Res.*, 68, 6361.

Spencer, P., D.S. Robertson, G.L. Mader (2004), Ionospheric data assimilation methods for geodetic applications, *Proceedings of IEEE PLANS*, Monterey, CA, 510-517.

Stauning, P., and O. A. Troshichev (2008), Polar cap convection and PC index during sudden changes in solar wind dynamic pressure, *J. Geophys. Res.*, 113, A08227, doi:10.1029/2007JA012783.

Sutton, E.K., R.S. Nerem, and J.M. Forbes (2007), Density and winds in the thermosphere deduced from accelerometer data, *J. Spacecr. Rockets*, 44(6), 1210–1219, doi:10.2514/1.28641.

Svalgaard, L. and J.W. Wilcox (1975), Long term evolution of solar sector structure, *Sol. Phys.*, 41, 461–475.

Tascione, T. (1994), Introduction to the Space Environment, *Krieger Publishing Company*, 2nd Edition.

Tapley, B.D., B.E. Schutz, G.H. Born (2004), Statistical orbit determination, *Academic Press*.

Teitelbaum, H., F. Vial, A.H. Manson, R. Giraldez, and M. Massebeuf (1989), Non-linear interaction between the diurnal and semidiurnal tides: Terdiurnal and diurnal secondary waves, *J. Atmos. Terr. Phys.*, 51, 627–634.

Temmer, M., B. Vršnak, and A.M. Veronig (2007), Periodic appearance of coronal holes and the related variation of solar wind parameters, *Sol. Phys.*, 241, 371– 383.

Thayer, J.P., J. Lei, J.M. Forbes, E.K. Sutton, and R.S. Nerem (2008), Thermospheric density oscillations due to periodic solar wind high-speed streams, *J. Geophys. Res.*, 113, A06307, doi:10.1029/2008JA013190.

Torrence, C. and G.P. Compo (1998), A practical guide to wavelet analysis, *Bulletin of the American Meteorological Society*, 79, 61-78.

Tsurutani, B. T., C. M. Ho, J. K. Arballo, B. E. Goldstein, and A. Balogh (1995), Large Amplitude IMF Fluctuations in Corotating Interaction Regions: Ulysses at Midlatitudes, *Geophys. Res. Lett.*, 22(23), 3397–3400.

Tsurutani, B.T., and C.M. Ho (1999), A Review of Discontinuities and Alfvén Waves in interplanetary space: Ulysses Results, *Rev. Geophys.*, 37(4), 517–541.

Tsurutani, B. T., et al. (2006a), Corotating solar wind streams and recurrent geomagnetic activity: A review, *J. Geophys. Res.*, 111, A07S01, doi:10.1029/2005JA011273.

Tsurutani, B.T., R.L. McPherron, W.D. Gonzalez, G. Lu, J.H.A. Sobral, and N. Gopalswamy (2006b), Introduction to special section on corotating solar wind streams and recurrent geomagnetic activity, *J. Geophys. Res.*, 111, A07S00, doi:10.1029/2006JA011745.

Verma, V.K. (2001), On the periodicity of high speed solar wind streams, *Space Sci. Rev.*, 97, 205– 210.

Verma, V. K., and G. C. Joshi (1994), On the occurrence rate of high-speed solar wind events, *Sol. Phys.*, 155, 401– 404.

Vršnak, B., M. Temmer, and A. Veronig (2007), Coronal holes and solar wind high-speed streams: I. Forecasting the solar wind parameters, *Sol. Phys.*, 240, 315– 330.

Vsekhsvjatsky, S.K. (1963), The structure of the solar corona and the corpuscular streams, in *The Solar Corona* (J.W. Evans, ed.), 271, *Academic Press*, New York.

Webb, P.A., E.A. Essex (2004), A dynamic global model of the plasmasphere, *J. Atmos. Sol.-Terr. Phys.*, 66, 1057-1073.

Wilcox, J.M., and N.F. Ness (1965), Quasi-Stationary Corotating Structure in the Interplanetary Medium, *J. Geophys. Res.*, 70(23), 5793–5805.

Wolf, R.A. (1975), Ionosphere–magnetosphere coupling, *Space Science Review*, 17, 4677–4698.

Woodman, R. F., J. L. Chau, and R. R. Ilma (2006), Comparison of ionosonde and incoherent scatter drift measurements at the magnetic equator, *Geophys. Res. Lett.*, 33, L01103, doi:10.1029/2005GL023692.

Xie, H., N. Gopalswamy, P.K. Manoharan, A. Lara, S. Yashiro, and S. Lepri (2006), Long-lived geomagnetic storms and coronal mass ejections, *J. Geophys. Res.*, 111, A01103, doi:10.1029/2005JA011287.

Yao, D. and J.J. Makela (2007), Analysis of equatorial plasma bubble zonal drift velocities in the Pacific sector by imaging techniques, *Ann. Geophys.*, 25(3), 701-709.

Yacob, A. (1977), Internal induction by the equatorial electrojet in India examined with surface and satellite geomagnetic observations, *J. Atmos. Terr. Phys.*, 39, 601–606.

Yue, X., W. Wan, J. Lei, and L. Liu (2008), Modeling the relationship between ExB vertical drift and the time rate of change of hmF2 (ΔhmF2/Δt) over the magnetic equator, *Geophys. Res. Lett.*, 35, L05104, doi:10.1029/2007GL033051.

Yumoto, K. (2001), Characteristics of Pi 2 magnetic pulsations observed at the CPMN stations: a review of the STEP results, *Earth Planets Space*, 53, 981–992.